TECHNISCHE
UNIVERSITÄT
WIEN
Vienna University of Technology

Cavity QED experiments with a whispering-gallery-mode bottle resonator

DISSERTATION

zur Erlangung des akademischen Grades

Doktor der technischen Wissenschaften

eingereicht von

Danny O'Shea
Matrikelnummer 1129901

an der
Fakultät für Physik der Technischen Universität Wien

Betreuung: Univ. Prof. Dr. Arno Rauschenbeutel

Diese Dissertation haben begutachtet:

(Titel Vorname Nachname) (Titel Vorname Nachname)

Wien, TT.MM.JJJJ

(Danny O'Shea)

TECHNISCHE
UNIVERSITÄT
WIEN
Vienna University of Technology

Cavity QED experiments with a whispering-gallery-mode bottle resonator

DISSERTATION

submitted in partial fulfillment of the requirements for the degree of

Doktor der technischen Wissenschaften

by

Danny O'Shea
Registration Number 1129901

to the Faculty of Physics
at the Vienna University of Technology

Advisor: Univ. Prof. Dr. Arno Rauschenbeutel

The dissertation has been reviewed by:

(Titel Vorname Nachname)

(Titel Vorname Nachname)

Wien, TT.MM.JJJJ

(Danny O'Shea)

Erklärung zur Verfassung der Arbeit

Danny O'Shea
Musterplatz 1, 1111 Wien

Hiermit erkläre ich, dass ich diese Arbeit selbständig verfasst habe, dass ich die verwendeten Quellen und Hilfsmittel vollständig angegeben habe und dass ich die Stellen der Arbeit - einschließlich Tabellen, Karten und Abbildungen -, die anderen Werken oder dem Internet im Wortlaut oder dem Sinn nach entnommen sind, auf jeden Fall unter Angabe der Quelle als Entlehnung kenntlich gemacht habe.

(Ort, Datum)

(Unterschrift Danny O'Shea)

Abstract

The interaction of a two-level atom with the mode of a quantized electromagnetic field constitutes one of the most fundamental systems investigated in quantum optics. We have pursued such an investigation where rubidium atoms are strongly coupled to the modes of a whispering-gallery-mode (WGM) resonator that is itself interfaced with an optical fiber. In order to facilitate studies of this atom-light interaction, an experimental apparatus was constructed around a novel type of WGM resonator developed in our group. Compared to typical single-mode resonators, the spectral and spatial mode structure of this resonator yields a qualitatively different atom-light response arising principally because the resonator supports two frequency-degenerate modes.

This thesis reports on high resolution experiments studying the transmission and reflection spectra of high-Q modes ($Q \sim 10^7 - 10^8$) in a WGM resonator. Light is coupled into and out of WGMs by frustrated total internal reflection using an optical nanofiber. Single-atoms are clearly observed transiting the evanescent field of the resonator modes with a duration of a few microseconds. A high-speed experimental scheme was developed to firstly detect the coupling of individual atoms to the resonator and secondly to perform time-resolved spectroscopy on the strongly coupled atom-resonator system.

Spectral measurements clearly resolve an atom-induced change in the resonant transmission of the coupled system ($\sim 65\%$ absolute change) that is much larger than predicted in the standard Jaynes-Cummings model (25% absolute change) and has thus far not been observed. To gain further insight, we experimentally explored the properties of the interaction and performed supporting simulations.

Spectroscopy was performed on the atom-resonator system using two nanofibers to in- and out-couple light for probing/observing the system. Using this setup, we find an asymmetric response in the fraction of reflected light from the empty resonator mode. The coupling of atoms to a mode similarly produces asymmetric transmission and reflection spectra that critically depend on the direction of light propagation in the mode. Possible explanations for the spectral properties are identified and possible routes to verifying the exact nature of the atom-light interaction are suggested.

The observation of directional asymmetries and large atom-induced changes in the transmission and reflection spectra provide important new perspectives on the fundamental dynamics of atom-light coupling with whispering-gallery-mode resonators. Moreover, our novel resonator design features four-port functionality using two optical fibers as well as very low intrinsic losses, which altogether makes the system a versatile platform for fundamental studies of open quantum systems.

Contents

Introduction **1**

1 Theory of Whispering Gallery Modes in a Bottle Microresonator **7**
- 1.1 Introduction 7
- 1.2 Optical Properties of Bottle Microresonators 7
  - 1.2.1 Whispering gallery modes 8
  - 1.2.2 Axial wave equation 14
  - 1.2.3 Optical mode spectrum 16
- 1.3 Optical nanofibers 17

2 Quantitative Description of Coupling Single Atoms to WGMs **21**
- 2.1 The Fabry-Pérot resonator 21
  - 2.1.1 A single mode light field 21
  - 2.1.2 A two-level atom 22
  - 2.1.3 Coupled atom–cavity system 22
- 2.2 The WGM resonator 24
  - 2.2.1 WGMs of light 24
  - 2.2.2 Coupled atom-cavity system 25
  - 2.2.3 Input-output formalism 29

3 Characteristics of the Microresonator Design **31**
- 3.1 Fabrication of bottle microresonators and ultra-thin optical fibers 31
  - 3.1.1 Sub-micron tapered optical fibers 32
  - 3.1.2 Bottle microresonators 33
  - 3.1.3 Techniques for estimating the curvature of bottle microresonators . . . 33
- 3.2 Properties of Tapered Optical Fiber Couplers 35
  - 3.2.1 Mode matching of resonator and coupling fiber 36
  - 3.2.2 Coupling regimes 37
- 3.3 Resonator properties 40
  - 3.3.1 Quality factor and Finesse 40
  - 3.3.2 The role of mode-splitting on resonator Q-factor 45
  - 3.3.3 Imaging the axial mode structure 47
  - 3.3.4 Full tunability of WGMs 48

3.4 Bottle resonators designed for cavity QED 52
  3.4.1 Atomic Rubidium as a quantum emitter 52
  3.4.2 Resonator size and cavity QED parameters 53
  3.4.3 Axial and radial resonator modes, polarization and coupling strength . . 53

4 Characterization of the Atom Delivery System 57
4.1 Atomic Fountain Apparatus 57
4.2 Experimental Setup 60
  4.2.1 Vacuum system 60
  4.2.2 MOT setup – magnetic coils and camera imaging 69
  4.2.3 Fountain performance 72
  4.2.4 Resonator imaging 73
  4.2.5 Fiber positioning system 74
  4.2.6 Vibration isolation 76
4.3 Laser systems 77
  4.3.1 Cooling laser 78
  4.3.2 Repump laser 80
  4.3.3 Resonator laser 80

5 Realization of Frequency and Distance Stabilization of Ultra-high-Q Modes 85
5.1 Active frequency stabilization 86
  5.1.1 Introduction 86
  5.1.2 Principle of Pound-Drever-Hall stabilization 87
  5.1.3 Setup of the resonator frequency stabilization 87
  5.1.4 Stabilization performance in air 89
  5.1.5 Thermal bistability 93
  5.1.6 Mode-splitting 94
  5.1.7 Stabilization performance in vacuum 95
  5.1.8 Thermal response in vacuum 96
  5.1.9 Summary 98
5.2 Distance stabilization of evanescent coupling 100

6 Optical Fiber Network and Experimental Control 103
6.1 Optical Fiber Network 103
  6.1.1 Network layout 103
  6.1.2 Photon detection 104
6.2 Experimental Control and Data Acquisition System 105
  6.2.1 Motivation 105
  6.2.2 Experimental control 107
  6.2.3 Experimental Sequence 108
  6.2.4 Realtime data processing 108

7 Observation of the Rabi Spectrum of a Coupled Atom–WGM-Resonator System 113
7.1 Characterization of the atom detection schemes 114

7.1.1 Realtime performance: Single atom detection scheme 115
7.1.2 Realtime performance: Double atom-detection scheme 117
7.1.3 Observation of single atom events 119
7.1.4 Photon detection probability 121
7.2 Spectroscopy of single atoms coupled to a high-Q WGM resonator 122
7.2.1 Conditional selection of strongly interacting atoms 122
7.2.2 Rayleigh scattering in a strongly-coupled atom-resonator system 124
7.3 Spectroscopy with a fiber-coupled three-port resonator 128
7.4 Forces and velocity effects on atomic motion 129
7.4.1 Theory 131
7.4.2 Experimental results 134
7.4.3 Properties of atom transits and dipole forces 139
7.5 Light scattering effects in WGMs 144
7.5.1 Asymmetries in the atom-resonator interaction 144
7.5.2 Asymmetric WGM mode structure 145
7.6 Summary and outlook 148

8 Summary & Outlook – Switching Photons in a Four-Port Device 151
8.1 Thesis Summary 151
8.2 Future Applications: Atom-controlled optical switching 153
8.2.1 Single-atom switching in a bottle resonator 154

Appendices 157

A Electric Fields in Optical Fibers 159

B Trapping and Cooling Atoms 161
B.1 Magneto-optical trap 161

Bibliography 169

Introduction

Single Atoms and Photons

The interaction of a quantized electromagnetic field with atoms is the subject area of quantum electrodynamics (QED). Its success as a quantum theory is evidenced by a number of extremely accurate predictions and corresponding experiments in both high and low energy physics, in which, for example, the value of the fine structure constant has been independently compared to give a value that is precise to 0.4 parts-per-billion [1]. One of the earliest successes of QED was the measurement of the Lamb shift (i.e., the interaction of an electron and vacuum) for the hydrogen atom [2], and its subsequent theoretical verification by Bethe in 1947 [3]. Around the same time, theoretical advancements in the field led to the explanation of spontaneous emission [4], calculations of the electron g-factor [5], and the prediction by Purcell of inhibited and enhanced spontaneous emission of an atom depending on the mode density of a surrounding physical structure [6]. The latter effect is particularly relevant in the context of this thesis because the surrounding structure can be an electromagnetic resonator. One possible realization of this effect is to place an atom between two reflecting mirrors that trap light in an optical mode – commonly referred to as a Fabry-Pérot resonator. (As an alternative to using a resonator, it is possible to use a photonic crystal optical fiber with properly designed boundary conditions that form optical band-gaps at discrete energies [7]).

The work of Purcell [6] shows that spontaneous emission is not just an intrinsic and fixed property of an atom but is also a property of the radiated field and, as such, can be engineered. Indeed, enhanced spontaneous emission was first experimentally demonstrated in Ref. [8] using a Fabry-Pérot resonator and alkali atoms. The spontaneous emission of an atom in a resonator is $\Gamma_{\text{res}} = \Gamma_{\text{free}} \cdot \lambda^3 Q/(4\pi^2 V)$, where Γ_{free} is the spontaneous emission in free space, λ is the wavelength of that atomic transition, V is the mode volume in the resonator, $Q = c/(2\pi\lambda\kappa)$ is the quality factor of the resonator mode, c is the speed of light in vacuum, and κ is the energy decay rate of the resonator. In principle, the two resonator parameters — Q and V — can therefore be freely chosen to control spontaneous emission. The work in this thesis focuses on the interaction of atoms and light in a resonator with a very high Q/V ratio and is formed within the framework of *cavity* QED.

Modern cavity QED experiments have evolved over the last 40 years due to increased levels of sophistication and control of optical fields at the single photon level in numerous photonic devices, ranging from Fabry-Pérot resonators, semiconductor systems, photon-bandgap structures, superconducting systems, and recently to whispering-gallery-mode (WGM) systems (for a review, see Refs. [9–11]). Indeed, the importance of the field of cavity QED has recently been confirmed through the award of half of the 2012 Nobel Prize in Physics for work performed by Serge Haroche [12]. Complementing these developments, atomic and atomic-like systems now come in a variety of forms, such as quantum dots in semiconductors, Rydberg atoms, superconducting qubits, and alkali atoms. Compared to traditional nonlinear optical physics, cavity QED launches atomic and optical physics into a new regime where single photons interact with single atoms. The coupling of a single atom to a resonator mode can induce strong nonlinear responses from the system even at the single photon level, which can be exploited to manipulate quantum states [13]. In the setting of cavity QED, photon blockade — i.e., the routing of single photons one-by-one into a resonator that is also coupled to an atom — is a very prominent example of a nonlinear photon-photon interaction demonstrated recently in Ref. [14] using a Fabry-Pérot resonator and a trapped cesium atom. The effect is enabled through a quantum mechanical phenomenon that strongly regulates the energy conservation of the combined system of resonator mode and atom. Unlike in a classical interaction of light and matter where the photon statistics are always poissonian, the photon statistics of this cavity QED interaction are inherently nonclassical and were observed to be strongly sub-poissonian and anti-bunched. Properties such as photon blockade, afforded by a cavity QED system, can form the basis for applications in a quantum network in which photonic qubits must be processed and routed.

Cavity QED experiments typically rely on the strong interaction of an atomic dipole with an electromagnetic mode. Here, a strong interaction is taken to mean that the atomic interaction with the resonator mode is strong relative to the interaction with radiation modes. The spontaneous emission of a photon from an atom into a radiation mode leads to dissipation of the composite atom-cavity system, while spontaneous emission into a resonator mode is reversible because the photon can be re-absorbed by the atom many times as the photon bounces back and forth between the mirrors. The interaction strength is characterized by the amplitude of the mode at the position of the atom, which can be very large in a resonator with large Q/V due to the resonant enhancement of light at discrete frequencies. Since modes that radiate into free space are numerous and not spatially confined, the amplitude of an individual mode relative to the totality of modes is very small.

The most elementary quantum system where the interaction of light and matter occurs consists of a single two-state atom coupled to a single electromagnetic mode, and was originally theoretically investigated by Jaynes and Cummings in 1963 [15]. Despite having initially developed a model to just study spontaneous emission of atoms in terms of classical physics, the work of Jaynes and Cummings was later found to provide a fully soluble quantum mechanical model of an atom coupled to a mode of a light (see Ref. [16] for a review). This ideal one-atom system has been experimentally realized in the domain of cavity QED at microwave frequencies in a micromaser [17], and at optical frequencies in a Fabry-Pérot resonator [18, 19]. At optical frequencies, one pioneering experiment with a Fabry-Pérot resonator was performed by dropping laser-cooled atoms over a resonator and then observing the transits through an intra-cavity probe field [18]. This method allowed the coherent and reversible exchange of energy between the atom and resonator mode on a timescale long enough to achieve strong coupling, and marks an important milestone in optical cavity QED.

In order to realize the regime where strong coupling between light and an atom is possible, several stringent requirements must be fulfilled. Firstly, the atomic system must have two energy states — a ground and excited state — that can couple to a mode of light. Furthermore, the energy exchange rate between the atom and mode, g, must be larger than the spontaneous emission rate between the two energy states, γ. In the absence of a resonator, this condition is difficult to satisfy because the coupling between an atomic system and a propagating light beam is typically very low due to the scale of the cross-section of the light beam (wavelength λ) and the atomic absorption cross-section (approximately λ^2). On the other hand, it is possible to enhance g in a very small resonator and thus achieve the condition $g \gg \gamma$. The function of the resonator is to simultaneously store light for extended periods of time and to also confine the light in a microscopic volume such that the probability of an atom–light interaction is greatly enhanced. As stated already in relation to the Purcell effect, resonators have imperfections that lead to light loss that is characterized by a cavity decay rate, κ. Therefore, in order to achieve strong coupling the condition $g \gg \kappa$ must also be fulfilled, i.e., the coherent exchange of energy between the atom and resonator mode must be at a rate that is much greater than the energy dissipation. The above conditions can be combined into a single criterion for the strong coupling regime of cavity QED given by $\eta = g^2/\kappa\gamma \gg 1$, where η is called the cooperativity parameter [10]. The cooperativity can be equivalently written in terms of the mode volume V and quality factor Q as $\eta = 3/4\pi \cdot \lambda^3 \cdot Q/V$.

The observation of normal mode splitting in the energy level structure of a cavity QED system is generally regarded as a decisive confirmation of operation in the strong coupling regime [18, 19]. Normal mode splitting can be explained classically as a consequence of the dispersion properties of a single atom acting as refractive perturbation of the resonator mode [20], or instead modeled as a system of coupled oscillators. In a fully quantized description the splitting arises from the Jaynes-Cummings model. However, unlike in the classical situation, the level splitting is anharmonic. Furthermore, the photon statistics of the new mode-split resonances are non-classical and can exhibit a sub-poissonian or super-poissonian photon distribution. Under optimal conditions in a Fabry-Pérot resonator with single atoms, another striking feature of the new resonances is the asymmetry in their linewidth and amplitude, which depends on the detuning of the free-space atomic resonance from the empty resonator resonance [18]. This behavior is a direct consequence of attractive and repulsive dipole forces acting on the motion of the atom in the mode, and can be exploited to trap single atoms with single intra-cavity photons [21, 22].

During the course of this thesis, a new experimental apparatus was constructed to study the strong coupling of single ^{85}Rb atoms to the modes of a WGM resonator having $Q/V \approx 6 \times 10^4\ (\lambda/n)^{-3}$, where λ is the optical wavelength and n is the refractive index of the resonator material. The observation of normal mode splitting (or Rabi splitting) for single atoms resonant with the mode of a WGM resonator for the first time is a central result of this thesis. Spectroscopy of the coupled atom-resonator system reveals split resonances indicating operation in the strong coupling regime. The combined effects of dipole and surface forces strongly modify both the spectral features and atom-light interaction time. The use of two optical fibers for in/out-coupling of light to the resonator in these spectroscopic measurements greatly aids our ability to probe the operation of the system.

Whispering-Gallery-Modes and Optical Fibers

Numerous ground-breaking experiments have demonstrated the clear potential of cavity QED through the successful demonstration of quantum non-demolition measurements of the state of single intra-cavity photons [23], non-linear photon-photon interactions by photon blockade [14], atom-light entanglement, as well as many others (see Ref. [11] for a review). While high-Q optical Fabry-Pérot resonators have been employed in many of these proof-of-principle experiments, they suffer from technical drawbacks that limit their deployment on a wider scale. For example, these high-Q resonators tend to have centimeter-scale dimensions that make them bulky, costly optical coatings must be applied to the mirror surfaces so as to achieve high quality at a fixed wavelength region, absorption and scattering in the mirrors limit the effective transmission to a few tens of percent, and passive frequency stability tends to be worse compared to monolithic WGM designs [24]. On the other hand, WGM resonators offer major advantages on each of these points; these resonators can be fabricated with micronscale dimensions from standard optical glass fibers or on solid-state microchips using well established techniques [10, 25], optical coatings are not required because the optical surfaces can be produced with sub-nanometer roughness, high-Q resonances are available across the full transparency window of the resonator material (e.g., silica transparency: $\sim 350 - 2000$ nm), light can be in/out-coupled from the resonator with greater than 99% efficiency using optical fibers [26], and the passive frequency stability is very good due to their monolithic construction from a single dielectric material. To date, the highest Q/V-ratios have been reached with WGM resonators [27]. Therefore, WGM resonators are an advantageous platform that is highly suited for cavity QED experiments.

WGM resonators are monolithic dielectric structures and generally have a circular cross-section that guarantees the confinement of light. Light is guided in high-Q modes near the curved surface by total internal reflection [28]. Light is coupled into and out of WGMs by frustrated total internal reflection [29]. In this thesis, coupling is performed with an ultra-thin optical glass fibers placed adjacent to the WGM resonator.

The concept of whispering-gallery-modes is widely known in the micro-optics and photonics communities, but it's origins are actually in the acoustic domain. In 1910, Lord Rayleigh explained what was a well known, but poorly understood, phenomenon observed in the dome of St. Paul's Cathedral (see Fig. 1). This is where a person's whisper near the wall at any point is audible to a listener near the wall at other points around the 31 m diameter gallery [30]. Lord Rayleigh's wave description of acoustic modes in a gallery can be equally applied to optical modes propagating in a dielectric microresonator. The experiments in this thesis use silica glass microresonators with a cross-section of around 35 μm and a quality factor of $\gtrsim 1 \times 10^8$, corresponding to over one hundred thousand circular revolutions of the field.

Optical fibers are typically made from long silica wires and are widely used in communication infrastructure to guide optical signals over long distances. More recently, optical fiber-based quantum optics experiments are now emerging as realistic systems for future quantum technologies. Recent work in this field has successfully integrated a two-color dipole trap for an atomic ensemble together with an ultra-thin optical fiber (500 nm diameter) [31]. The atoms are trapped in the evanescent field of the laser light at a distance on the order of 200 nm from the fiber surface, thus greatly enhancing the atom-light interaction time compared to untrapped atoms. Such

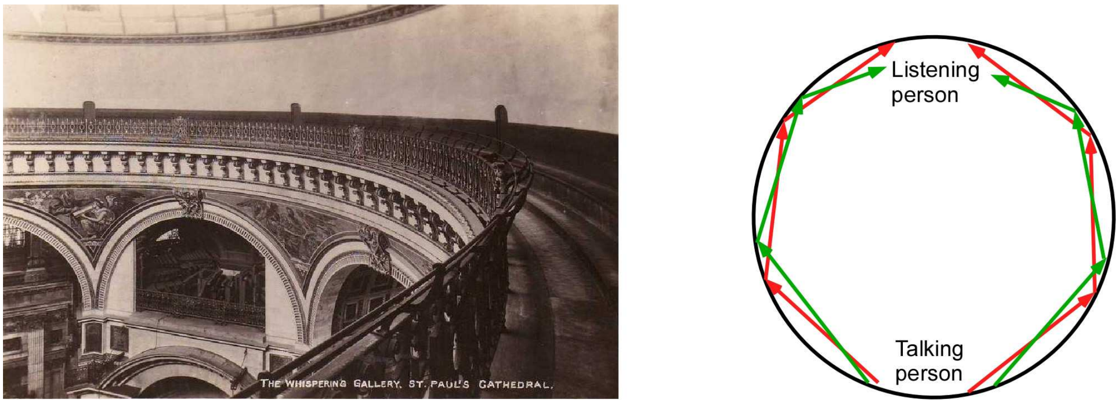

Figure 1: Acoustic whispering modes in the gallery at St. Paul's Cathedral in London. Acoustic waves from people whispering near the wall are efficiently transmitted by continuous specular reflections around the gallery wall despite its 31 m diameter.

an atom-light interface may also function as a quantum memory in the DLCZ quantum communication protocol [32] and thus benefit from the high optical density of the ensemble and its inherently efficient coupling to a single mode field. The evanescent field of an ultra-thin optical fiber can also efficiently interface individual quantum emitters, such as nanodiamonds containing nitrogen vacancy defect centers. Using this scheme, work in Ref. [33] demonstrated a single photon source having the highest rate of single photon emission into a single-mode fiber, to date.

Scope of the thesis

In this thesis, an experiment is presented where laser-cooled atoms interact with the evanescent field of a WGM microresonator. The rotational symmetry of the resonator means that two frequency-degenerate modes can co-exist — a clockwise and anti-clockwise mode — similar to the situation in a ring resonator [34]. Specifically, the experiments involve a novel WGM resonator design, termed a bottle resonator, that can be interfaced by either one or two ultra-thin optical fibers. (Coincidentally, the resonator itself is also fabricated from an optical fiber). The work in this thesis can be broadly divided into two sections; (a) the development of new techniques to allow an ultra-high Q bottle resonator to be used in a cavity QED experiment (Chapters 4, 5, 6), (b) the actual demonstration and investigation of the strong coupling regime of cavity QED with a bottle resonator (Chapter 7).

The experiment features several innovations; light is in- and out-coupled from the resonator with near unity efficiency using up to two optical nanofibers, a vacuum apparatus offers excellent optical access to the setup (Chapter 4), a variety of different optical mode geometries in the resonator are selected to study the atom-light interaction, the optical frequency and intra-cavity power of the resonator mode is actively stabilized (Chapter 5), and, finally, a high-speed experimental control setup was developed to study the interaction on a sub-microsecond timescale (Chapter 6). The work also builds on earlier work with bottle resonators in our group [35–38] through the construction of a compact, in-vacuum setup with two optical fibers coupled to a bottle resonator. While the research is principally experimental, it is supported by theoretical modeling of the atom-light coupling and also modeling of the dynamics of atomic motion near the dielectric surface of the resonator.

In the cavity QED experiment, the transmission and reflection of a weak probe light reveals the spectral responses of the empty resonator (classical) and coupled atom-resonator (quantum) system. The general spectral features correspond well with previous theoretical and experimental results using a single atom strongly coupled to a single-mode Fabry-Pérot resonator [18, 19], or an ensemble of atoms in a ring resonator [34]. However, since the experiment involves two WGM modes that can be frequency degenerate, the experimental results significantly differ from the predicted model. This model is based on a simple extension of the standard Jaynes-Cummings model for a single atom interacting with a single mode of light to a model that includes two modes [39]. The principle difference is the appearance of two clearly defined resonances whereas three resonances are theoretically predicted. Equally important, this also means that single atoms have a much larger effect on the resonant transmission of the system than would otherwise be possible.

In order to gain further knowledge of the atom-light interaction, the spectra of the system is observed under different experimental conditions; positive and negative atom-cavity detunings, controlled variations of the velocities of atoms entering the resonator mode, and Rabi spectra are studied using two modes having different spatial geometries and properties. The underlying mechanism can be attributed to an asymmetry in the atom-light interaction, and several causes are proposed and investigated in Chap. 7. The presence of this new physics is highly beneficial because it enables single atoms to switch optical fields between two optical fibers with much higher extinction than predicted in the standard Jaynes-Cummings model for an ideal WGM resonator.

CHAPTER 1

Theory of Whispering Gallery Modes in a Bottle Microresonator

1.1 Introduction

Optical microresonators have proven to be a powerful tool in studies requiring strong light-matter interaction [10]. The light inside such resonators can be strongly confined spatially and stored for an extended period of time. Consequently, very high intra-cavity intensities are obtained with only moderate optical powers coupled into the resonator. For example, just 1 μW of in-coupled power can yield very high power densities of 1 MW/cm^2.[1] This makes optical microresonators ideal tools for efficiently coupling light and matter.[2] The spatial and temporal confinement of light in microresonators is characterized by their mode volume V and their quality factor Q. The ratio Q/V thus relates the coupling strength between light and matter to the dissipation rates of the coupled system. Record values of Q/V have been reached with photonic crystal microcavities [40] and toroidal WGM microresonators [27]. Recently, a conceptually new type of WGM microresonator was demonstrated both theoretically [41, 42] and experimentally [43, 44] with Q/V ratios rivalling the best demonstrated to date [25].

In this chapter I describe the necessary physical principles and theoretical basis underpinning bottle resonators.

1.2 Optical Properties of Bottle Microresonators

WGM microresonators are monolithic dielectric structures in which the light is guided near the surface by continuous total internal reflection [28]. The versatile properties of WGM microresonators have found wide-spread service in optics and photonics. They are found in experiments ranging from microlasers [45–47] to cavity quantum electrodynamics [48] and nonlinear optics [37,49,50] where they greatly enhance light-matter and light-light interactions, respectively.

---

[1] With 1 μW of in-coupled power in the resonator, the intra-cavity intensity is over three hundred million times the saturation intensity of the so-called D$_2$ cycling transition in ^{85}Rb ($|F = 3\rangle \rightarrow |F' = 4\rangle$) for π-polarized light.

[2] Intra-cavity intensity $I_{\rm cav}$ scales linearly with quality factor $I_{\rm cav} = I_0 Q\lambda/(\pi^2 nR)$, where I_0 is the free space intensity, R is the resonator radius, and λ/n is the wavelength in a resonator material of refractive index n.

Light can be coupled into and out of WGM resonator modes with high efficiency by frustrated total internal reflection using the evanescent field of a sub-micron diameter tapered optical fiber coupler [26, 29]. Most notably, the coupling can be performed with near 100% efficiency [26, 36], thereby exceeding the coupling efficiencies of all other types of optical microresonators. Efficient in- and out-coupling of light is a universal property of silica WGM microresonators and has been demonstrated in microspheres, microtoroids, microdisks, and bottle microresonators [25, 51].

Due to the small dimensions and monolithic construction of traditional WGM microresonators, however, they exhibit a large frequency spacing between resonances and a limited tuning range. This poses a large obstacle for a wide range of applications which require a resonance of the microcavity to coincide with a predetermined frequency like, e. g., an atomic transition in cavity quantum electrodynamics or a given channel of a wavelength division multiplexed signal in optical communication. The fiber-coupled bottle microresonators presented in this work combines an ultra-high Q-factor of up to 3.6×10^8, a small mode volume of $\sim 1200\ \mu\text{m}^3$, and near lossless coupling, characteristic of whispering-gallery-modes, with a customizable mode structure and the ease of tuning of a Fabry-Pérot resonator. These properties identify the bottle microresonator as a powerful tool that opens numerous exciting perspectives for a broad area of applications and studies that were previously limited to Fabry-Pérot resonators.

Recently it was shown in the Rauschenbeutel group that the mode geometry of the bottle resonator offers access to the resonator's light field with two coupling fibers without the spatial constraints inherent to equatorial WGMs [38]. This facilitates the use of the bottle microresonator as a four-port device in a so-called *add–drop configuration*. In communication technology, such devices are used for (de)-multiplexing optical signals. By judicious placement of the coupling fibers at the resonator caustics, the power transfer efficiency between the bus fiber and the drop fiber is as high as 93% while, simultaneously, the device bandwidth is as narrow as 49 MHz [38]. Importantly, these properties are compatible with strong coupling in a cavity quantum electrodynamic experiment with neutral rubidium atoms.

In the following section I will give an introduction to the theory describing the properties and structure of the electric field modes of bottle resonators.

1.2.1 Whispering gallery modes

The electromagnetic modes in a whispering gallery mode resonator are described by Maxwell's equations. In the absence of charges and currents, these equations are given by,

$$\boldsymbol{\nabla} \times \mathbf{E} = -\mu \frac{\partial \mathbf{H}}{\partial t}\,, \tag{1.1}$$

$$\boldsymbol{\nabla} \times \mathbf{H} = \varepsilon \frac{\partial \mathbf{E}}{\partial t}\,, \tag{1.2}$$

$$\boldsymbol{\nabla} \cdot \mathbf{E} = 0\,, \tag{1.3}$$

$$\boldsymbol{\nabla} \cdot \mathbf{H} = 0\,, \tag{1.4}$$

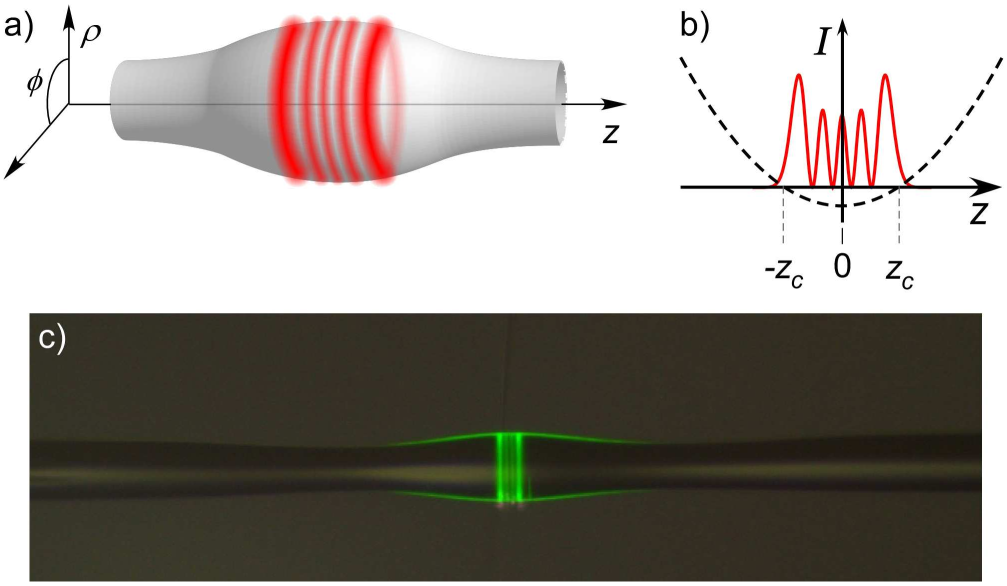

Figure 1.1: Concept of the bottle resonator and mode profile. (a) Light (red) circulates in a path within a solid glass fiber which forms the resonator. Total internal reflection of light ensures that modes with high angular momentum are confined near the glass surface. (b) The weak parabolic curvature of the glass fiber along the z-axis defines an effective harmonic potential for the light, thereby providing axial confinement. Fiber curvature exaggerated. (c) Microscope image of a WGM mode in a bottle resonator. The resonator is doped with Erbium ions that emit green fluoresce when excited at the absorption wavelength. Image taken from the Er-doped resonator presented in Refs. [25, 36, 52].

where $\mathbf{E}$ is the electric field vector, $\mathbf{H}$ is the magnetic field vector, $\mu = \mu_r\mu_0$ is the magnetic permeability of the material, $\varepsilon = \varepsilon_r\varepsilon_0$ is the electric permittivity of the material of refractive index n, $\mu_r = 1$ and $\varepsilon_r = n^2$ in silica, and μ_0 and ε_0 are the vacuum permeability and vacuum permittivity, respectively. Taking the curl of Eq. (1.1) and substituting Eq. (1.2) we get

$$\boldsymbol{\nabla} \times \boldsymbol{\nabla}\mathbf{E} = -\frac{\varepsilon}{c^2}\frac{\partial^2\mathbf{E}}{\partial t^2} \,, \tag{1.5}$$

where c is the speed of light in vacuum. This equation can be simplified to yield a wave equation which satisfies both field vectors $\mathbf{E}$ and $\mathbf{H}$:

$$\boldsymbol{\nabla}^2\mathbf{E} - \frac{\varepsilon}{c^2}\frac{\partial^2\mathbf{E}}{\partial t^2} = 0 \,. \tag{1.6}$$

Here, the electromagnetic wave varies with a time dependence $\exp(-i\omega t)$, where t is time and $\omega = kc/n = 2\pi c/n\lambda$ is the angular frequency of the wave with wavevector k. In the frame of the rotating wave, the above wave equation transforms into a vector Helmholtz equation,

$$\boldsymbol{\nabla}\mathbf{E} + k^2\mathbf{E} = 0 \,, \tag{1.7}$$

and an equivalent equation also holds for $\mathbf{H}$. This equation can be solved with three scalar components given in cylindrical coordinates, which is a valid approximation given the near cylindrical profile of the resonator as shown in Fig. 1.1. For the z component of the field the Helmholtz equation then becomes

$$\left(\partial_\rho^2 + \frac{1}{\rho}\partial_\rho + \frac{1}{\rho^2}\partial_\phi^2 + \partial_z^2 + k^2\right)\psi = 0, \quad \text{with} \quad \psi = E_z, H_z. \tag{1.8}$$

Using the assumption that the resonator is cylindrically symmetric, the solution to Eq. (1.8) is translationally invariant along the z-axis and we can set the z-axis term in Eq. (1.8) as $\partial_z^2\psi = 0$. Also, we note that the angular component varies sinusoidally as $\exp(-im\phi)$, where m is the angular momentum quantum number. The equation is now in the general form of a Bessel differential equation

$$x^2\partial_x^2 y + x\partial_x y + (x^2 - n^2)y = 0 \ , \tag{1.9}$$

which can be re-written using the substitutions $y = \psi$, $x = k\rho$, and $n = m$, as

$$\rho^2\partial_\rho^2\psi + \rho\partial_\rho\psi + ((k\rho)^2 - m^2)\psi = 0 \ , \tag{1.10}$$

where for the case of a WGM resonator we consider only non-negative integer values $m = 0, 1, 2, 3\ldots$ This is a second-order differential equation with two independent solutions — the Bessel function of the first kind, J_m, and the Bessel function of the second kind, Y_m (also known as the Hankel function).

$$\psi(k\rho) = c_1 J_m(k\rho) + c_2 Y_m(k\rho) \ . \tag{1.11}$$

The function Y_m diverges for $k\rho \ll 1$, but since this is not physically allowed the constant c_2 is set to zero for fields within the resonator. However, the function Y_m exhibits a fast decay towards zero over a short distance correctly describing the field outside the resonator and therefore the constant c_1 is set to zero in this region. The mode number m counts the number of wavelengths around the resonator circumference with $m \sim k\rho$.

The z-components of the E-field are defined as [53]

$$E_z(\rho, z) = AJ_m(k_0 n\rho)\exp\left[i(m\phi - \omega t)\right] \ , \qquad \text{for } \rho \leq R \ , \tag{1.12}$$

$$E_z(\rho, z) = BY_m(k_0\rho)\exp\left[i(m\phi - \omega t)\right] \ , \qquad \text{for } \rho > R \ . \tag{1.13}$$

And similarly for the H-field:

$$H_z(\rho, z) = CJ_m(k_0 n\rho)\exp\left[i(m\phi - \omega t)\right] \ , \qquad \text{for } \rho \leq R \ , \tag{1.14}$$

$$H_z(\rho, z) = DY_m(k_0\rho)\exp\left[i(m\phi - \omega t)\right] \ , \qquad \text{for } \rho > R \ . \tag{1.15}$$

In addition to the axial z-components of the field, the radial ρ- and angular ϕ-components can be obtained from Eq. (1.1) and Eq. (1.2)

$$\begin{aligned} E_\rho &= \frac{-i}{\epsilon\omega\rho}\partial_\phi H_z \ , \\ E_\phi &= \frac{i}{\epsilon\omega}\partial_\rho H_z \ , \\ H_\rho &= \frac{i}{\mu\omega\rho}\partial_\phi E_z \ , \\ H_\phi &= \frac{-i}{\mu\omega}\partial_\rho E_z \ . \end{aligned} \tag{1.16}$$

Here, as mentioned earlier, we neglect z-derivatives. We also assume there is no mode propagation in the z direction so that $\exp(i\beta z)$ plays no role. Modes where $E_\rho = 0$ are signified as transverse electric (TE) modes while modes where $H_\rho = 0$ are signified as transverse magnetic (TM) modes. Using the requirement that the amplitude of the tangential field components at the resonator surface $\rho = R$ must obey the following equalities,

$$TM \begin{cases} E_z^{\text{in}} = E_z^{\text{out}}, \\ H_\phi^{\text{in}} = H_\phi^{\text{out}} \end{cases} \quad TE \begin{cases} H_z^{\text{in}} = H_z^{\text{out}}, \\ E_\phi^{\text{in}} = E_\phi^{\text{out}} \end{cases} \tag{1.17}$$

we find the relations,

$$\begin{aligned} TM: &\qquad n\frac{\partial J_m(k_0 n\rho)}{J_m(k_0 n\rho)} = \frac{\partial Y_m(k_0\rho)}{Y_m(k_0\rho)}, \\ TE: &\qquad \frac{\partial J_m(k_0 n\rho)}{J_m(k_0 n\rho)} = n\frac{\partial Y_m(k_0\rho)}{Y_m(k_0\rho)} \ . \end{aligned} \tag{1.18}$$

Equation (1.18) therefore defines the boundary conditions at the position of the resonator caustic at $z = z_c$ (see Fig. 1.1) and is termed a *characteristic equation.* Solutions to the characteristic equations are eigen-wavenumbers k_m for allowed oscillations in the resonator. The imaginary part of the solution quantifies the radiative losses and can be used to calculate a radiative quality factor $Q_{\text{rad}} = \text{Re}(k_m)/2\text{Im}(k_m)$. Equation (1.18) can be readily solved numerically using software such as Mathematica as described in Ref. [53].

For completeness, if we return to Eq. (1.16) we find for TE-polarized modes,

$$E_\rho = \begin{cases} \frac{m}{\epsilon\omega\rho} C J_m(k_0 n\rho) \exp\left[i(m\phi - \omega t)\right], & \text{for} \rho \leq \text{R} \ , \\ \frac{m}{\epsilon\omega\rho} D Y_m(k_0\rho) \exp\left[i(m\phi - \omega t)\right], & \text{for} \rho > \text{R} \ , \end{cases} \tag{1.19}$$

$$E_\phi = \begin{cases} \frac{i}{\epsilon\omega} C \exp\left[i(m\phi - \omega t)\right] \partial_\rho J_m(k_0 n\rho), & \text{for} \rho \leq \text{R} \ , \\ \frac{i}{\epsilon\omega} D \exp\left[i(m\phi - \omega t)\right] \partial_\rho Y_m(k_0\rho), & \text{for} \rho > \text{R} \ , \end{cases} \tag{1.20}$$

and for TM-polarized modes we find,

$$H_\rho = \begin{cases} \frac{-m}{\mu\omega\rho} A J_m(k_0 n\rho) \exp\left[i(m\phi - \omega t)\right], & \text{for} \rho \leq \text{R} \ , \\ \frac{-m}{\mu\omega\rho} B Y_m(k_0\rho) \exp\left[i(m\phi - \omega t)\right], & \text{for} \rho > \text{R} \ , \end{cases} \tag{1.21}$$

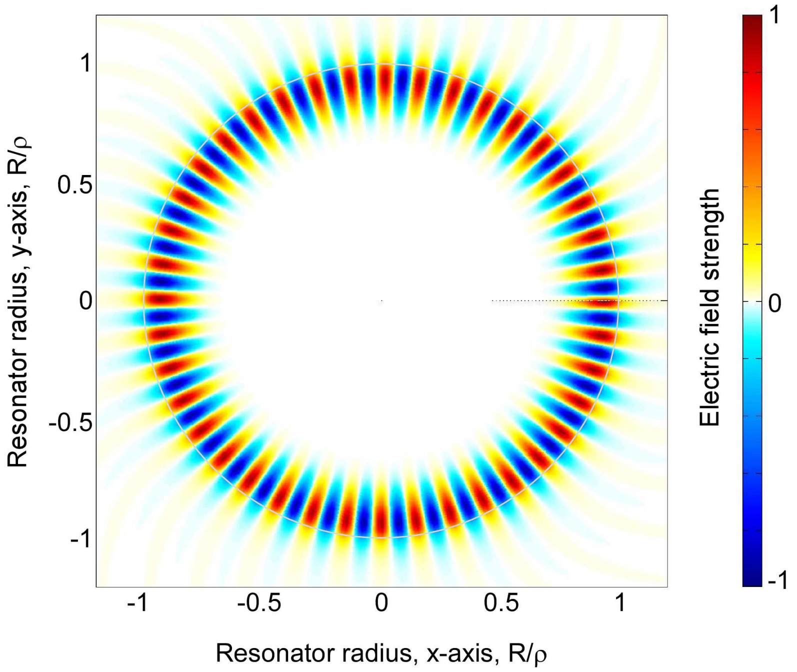

Figure 1.2: Cross-section of the TM field of the fundamental resonator radial mode for quantum number $m = 40$. The field near the surface at $R/\rho = 1$ is the evanescent field. At large distances from the resonator surface measuring more than several wavelengths, the electric field pattern exhibits a distinct spiral shape unique to WGM resonators. The spiral originates from the fact that the phase velocity of the field far from the surface exceeds the phase velocity of the field in/near the resonator due to the circular propagation of the fields. The field far from the surface is not guided by the resonator and is lost to free space, thus corresponding to radiative losses. Radiative loss is unique to WGMs and does not exist in Fabry-Pérot resonators.

$$H_\phi = \begin{cases} \frac{-i}{\mu\omega} A \exp\left[i(m\phi - \omega t)\right] \partial_\rho J_m(k_0 n \rho), & \text{for} \rho \leq \text{R} \ , \\ \frac{-i}{\mu\omega} B \exp\left[i(m\phi - \omega t)\right] \partial_\rho Y_m(k_0 \rho), & \text{for} \rho > \text{R} \ , \end{cases} \tag{1.22}$$

The azimuthal cross-section of the solution to the electric field for a TM-polarized WGM is plotted in Fig. 1.2. Antinodes in the figure correspond to light reflecting off the glass surface via total internal reflection given in the ray-optics interpretation, i.e., there are 20 reflections. Outside the resonator, the electric field is seen to have an exponential-like decay due to the Hankel function, and this part of the field is termed the *evanescent field*.

We note the wavevector deep inside the resonator, $k_1 = \omega\sqrt{\mu_1\varepsilon_1}$, is different to the wavevector far outside the resonator, $k_2 = \omega\sqrt{\mu_2\varepsilon_2}$. The difference in phase velocity of the mode in these regions causes the faint spiralling wave outside the resonator far from the surface. See Sec. 9.2 in Ref. [54] for further details.

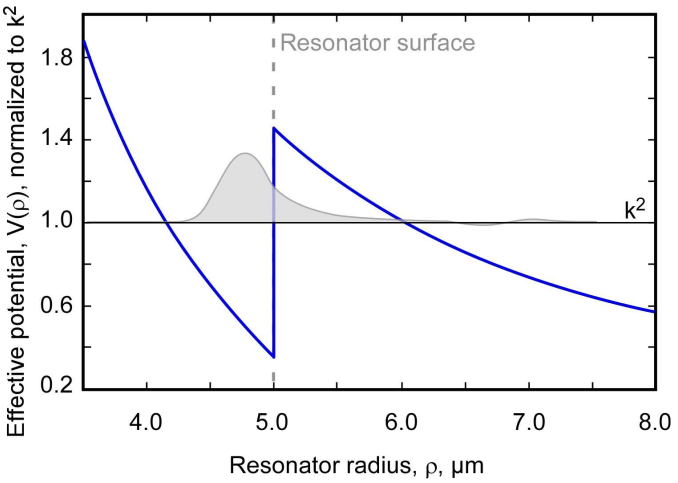

Figure 1.3: Sketch of the effective radial potential. In analogy to a particle trapped in a potential well, photons in a WGM resonator are trapped in an effective potential well (solid blue line) behind the resonator surface. The wavefunction (grey shaded) decays exponentially beyond the surface into the evanescent region. A fraction of the wavefunction tunneling beyond the potential well is no longer trapped, corresponding to radiative losses. These losses are significant for very small resonators of a few microns in radius due to the large fraction of the wavefunction extending past the resonator surface.

Radiative tunneling of radial modes

Interestingly, the Bessel differential equation Eq. (1.10) is analogous to the Schrödinger equation for a particle of mass M in a potential well V with energy E [55],

$$\left[-\frac{h^2}{2M}\frac{\partial^2}{\partial\rho^2}+V(\rho)-E\right]\psi(\rho)=0. \tag{1.23}$$

where $E = h^2k^2/2M$. The radial potential ensures that circulating photons remain confined behind a potential barrier at the resonator surface. Classically, the photon is in a bound state and cannot propagate into the forbidden regions when it's energy is below the barrier height. This analogy can be further extended by considering that the wavefunction has a non-zero probability beyond the potential well, which can result in significant radiative tunneling of light out of the resonator. The effective potential is a function of the radial position, refractive index, and wavelength and is given by

$$V(\rho)=\begin{cases} k^2(1-n^2)+m^2/\rho^2, & \text{for } \rho \leq R\ , \\ m^2/\rho^2, & \text{for } \rho > R\ , \end{cases} \tag{1.24}$$

where R is the position of the resonator surface. The part of the wavefunction extending just outside the resonator surface is evanescent and bound, see the sketch in Fig. 1.3.

With the radial solutions to the field now at hand, we next focus on the axial solutions.

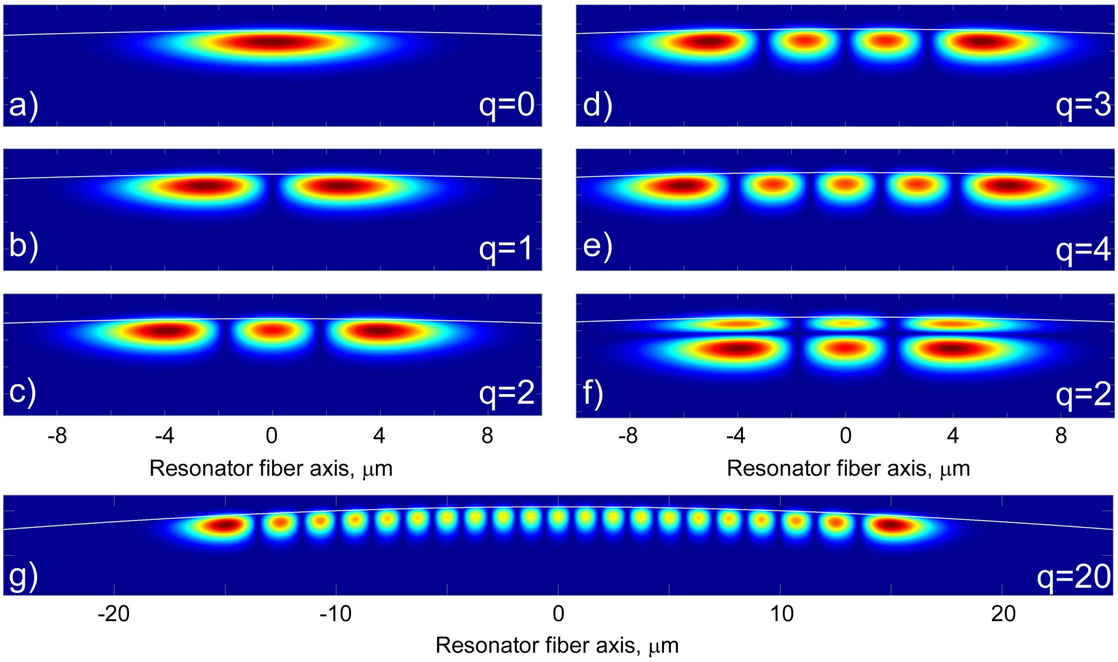

Figure 1.4: Absolute electric field, $|E_{\rho,z}|$, for cross-sections of the resonator axial modes ranging from quantum number $q = 0 - 4$ (a – f) and $q = 20$ (g), with TE polarization. Higher order radial modes push the field maximum deeper into the resonator as can be seen by comparing (c) and (f). The radial field pattern in the glass is described by Bessel functions while the axial field is described by a Hermite polynomial. The electric field is substantially enhanced at the extremal anti-nodes of the Hermite polynomial, which are termed the *caustic* positions.

1.2.2 Axial wave equation

The spectral properties of WGM microresonators are typically determined by their geometry. Traditional WGM resonators, like the microtoroid, microdisk, and microsphere [10], are generally considered 2D resonators that confine light in an equatorial plane with their spectral properties defined by their diameter. In contrast, as shown in Fig. 1.1, bottle resonators are intrinsically 3D in design and their spectral properties are defined by their diameter as well as their curvature along the fiber axis [41]. The resonator radius R along the resonator axis z is assumed to have a parabolic profile

$$R(z) = R_0 \left(1 - (\Delta k z)^2 / 2\right) . \tag{1.25}$$

Here, R_0 is the maximum radius of the resonator at the position $z = 0$ and Δk denotes the curvature of the resonator profile.

Due to the prolate shape of the bottle resonator there is only a small variation in its radius along z, meaning that $dR/dz \ll 1$ in the central region of the structure, for example, see Fig. 1.4. This motivates the so-called *adiabatic approximation*, where the radial component

$k_\rho = (dR/dz)\, k_z$ of the wave vector can be neglected[3] with respect to the axial and azimuthal components k_z and k_ϕ

$$k \approx \sqrt{k_z^2 + k_\phi^2} \approx \frac{2\pi n}{\lambda} \,, \tag{1.26}$$

where λ is the wavelength of light in vacuum. The resonators used in this work have a diameter $D_0 = 2R_0$ of around 35–50 μm and a typical curvature of $\Delta k = 0.012\ \mu\text{m}^{-1}$. The bottle modes experimentally investigated are typically located in a region $|z| \leq 10\ \mu$m. With these values one finds $|k_\rho(z)| \leq 2.5 \times 10^{-2} |k_z(z)|$.

In the adiabatic approximation, the wave function is written as a product of the axial wave function $Z(z)$ and the radial wave function $\Phi(\rho, R(z))$. The latter only exhibits a weak z dependency via the adiabatic variation of the resonator radius. The wave equation thus reads as

$$(\nabla^2 + k^2)\Phi\,(r, R(z))\, Z(z) e^{im\phi} = 0 \,, \tag{1.27}$$

where the exponential component derives from the cylindrical symmetry of the azimuthal part. The radial wave equation for the component was solved in Sec. 1.2.1.

The axial wave equation only depends on the z coordinate

$$\left(\partial_z^2 + k_z^2\right) Z(z) = 0 \,. \tag{1.28}$$

Using Eq. (1.26) and eliminating k_ϕ via $k_\phi(z) = kR_c/R(z) = m/R(z)$, where R_c is the radius at the caustic, one can solve the axial wave equation. For the parabolic radius profile of Eq. (1.25), the axial wave equation is well approximated by

$$\partial_z^2 Z + \left[\underbrace{k^2 - \left(\frac{m}{R_0}\right)^2}_{E} - \underbrace{\left(\frac{m\Delta k}{R_0}\right)^2 z^2}_{V(z)}\right] Z = 0 \,. \tag{1.29}$$

This differential equation is equivalent to the harmonic oscillator $\partial_z^2 Z + (E - V(z))\, Z = 0$, with kinetic energy E and potential energy $V(z)$, as discussed in Ref. [41].

The resonance condition dictates that the optical path length has to be an integer multiple of the wavelength of the light coupled into the resonator, which is satisfied only for certain caustic radii, R_c. The mode spectrum is determined by the allowed eigenvalues for the wave number and is given by

$$k_{m,q} = \frac{m}{R_c} = \sqrt{\frac{m^2}{R_0^2} + (q + 1/2)\, \frac{2m\Delta k}{R_0}} \,, \tag{1.30}$$

with $\Delta E_m = 2m\Delta k/R_0$. The axial quantum number $q \in \mathbb{N}$ (nonnegative integer) gives the number of antinodes in the axial intensity distribution. The solutions for Z are given by a product of a Hermite Polynomial, H_q, and a Gaussian,

$$Z_{m,q}(z) = H_q\left(\sqrt{\frac{\Delta E_m}{2}} z\right) \exp\left(-\frac{\Delta E_m}{4} z^2\right) \,. \tag{1.31}$$

---

[3] Since light is circling in the bottle, we can set $k_\rho = 0$, because the wavevector is proportional to the curvature, $\frac{dR}{dz} = \frac{k_\rho}{k_z}$.

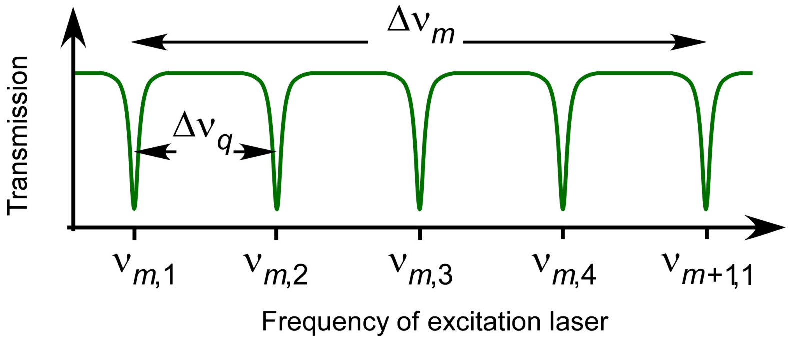

Figure 1.5: Resonator spectrum illustrating axial and azimuthal modes. Taking advantage of the customizable spectral mode structure of our resonator design, the large gap of one azimuthal FSR can be sub-divided with a set of fundamental axial modes. Four axial modes — $\{\nu_{m,1}, \nu_{m,2}, \nu_{m,3}, \nu_{m,4}\}$ — are equally spaced within one azimuthal free spectral range $\Delta\nu_m$ and we assume a design where $\Delta\nu_m = 4\Delta\nu_q$. The tuning range of any single axial mode is greater than $\Delta\nu_q$ — the spacing between the axial modes. The axial quantum number, q, counts the number of axial rings of the mode and the azimuthal quantum number, m, counts the number of wavelengths that fit into one full revolution around the resonator circumference.

It is instructive to consider the influence of a change in axial mode number on the spatial and spectral properties of the resonator. For example, we consider a resonator with a curvature of $\Delta k = 0.012\ \mu\mathrm{m}^{-1}$, a radius of $R_0 \approx 17.5\ \mu$m, a resonant wavelength of around 850 nm, and an azimuthal quantum number of $m = 180$, see Fig. 1.1 (b) for a plot of the axial mode structure. Increasing the axial quantum number causes the caustic position to shift to larger z and thus R_c decreases due to the resonator profile. At the same time, the resonance frequencies of the higher order modes shift to larger values.

1.2.3 Optical mode spectrum

The axial and azimuthal free spectral range $\Delta\nu_q = \nu_{m,q+1} - \nu_{m,q}$ and $\Delta\nu_m = \nu_{m+1,q} - \nu_{m,q}$ can be derived from the eigenvalues $k_{m,q}$ of the wave equation $\left(\nabla^2 + k^2\right)\mathbf{E} = 0$. To a good approximation, they can be written as [41]

$$\Delta\nu_m = \frac{c}{2\pi n}(k_{m+1,q} - k_{m,q}) \approx \frac{c}{2\pi n R_0} \tag{1.32}$$

and

$$\Delta\nu_q \approx \frac{c\Delta k}{2\pi n}\,, \tag{1.33}$$

where c/n is the speed of light in a medium with refractive index n. For a typical bottle microresonator considered in this work with radius $R_0 = 17.5\ \mu$m and curvature $\Delta k = 0.012\ \mu\mathrm{m}^{-1}$ the above formula yields an axial FSR of $\Delta\nu_q = 0.4$ THz while the azimuthal FSR is $\Delta\nu_m = 1.9$ THz, see Fig. 1.5. The benefit of a customizable mode spectrum is described further in Sec. 3.3.4 in the context of frequency tunability of WGMs.

1.3 Optical nanofibers

Several technologies exist for coupling light into WGM resonators, such as, prism couplers, polished half-block couplers, angle-polished fibers, and tapered optical nanofibers [51]. When using tapered optical nanofibers for this purpose, the coupling can be performed with near 100% efficiency [26, 36, 37], thereby exceeding the coupling efficiencies of all other types of coupling techniques. The work in this thesis uses an optical nanofiber to couple light into WGM resonators by frustrated total internal reflection. This technique, originally shown in Ref. [29], relies on the overlap of evanescent field on the mode of the nanofiber with evanescent field of the resonator. For an extensive review of the guiding properties of optical fibers, see the work of Snyder and Love [56], or other theses from our group [53, 57, 58]. Here we limit our scope and focus on the basic properties of optical fibers.

A nanofiber is produced from standard optical glass telecommunication fiber that has been specially shaped to have a small diameter of a few hundred nanometers, as shown in Fig. 1.6. Standard single-mode optical fiber is composed of a core with a diameter of several microns and cladding with typical diameter of 125 μm.

Light is mostly localized and guided in the core because its refractive index is marginally higher. The propagation of light in the fiber is mathematically described by a Helmholtz equation usually written in cylindrical coordinates, and is very similar to that of the bottle resonator. Likewise with the bottle resonator, the mode within the core is mathematically described by a Bessel function of the first kind, while the mode outside the core (i.e., in the cladding region) is described by a Bessel function of the second kind. This latter field is again termed an evanescent field.

In order to access the evanescent field with a WGM resonator, it is necessary to taper the fiber profile so that the outer cladding has a diameter of around 0.5–1 μm and the core effectively vanishes. On this scale, the wavelength of the guided light is comparable to, or larger than, the fiber diameter. This strongly confines the field to small cross-section where a large fraction of the field is outside the fiber in the ambient air or vacuum, as shown in Figs. 1.6 (a) and 1.7. (See appendix A for the mathematical description of the electric field in a nanofiber). The coupling strength between the nanofiber and resonator is defined by the overlap integral of the fields of both structures. Since the evanescent field decays over a short distance of around 200 nm, the resonator must be placed within a distance of a few hundred nanometers of the fiber.

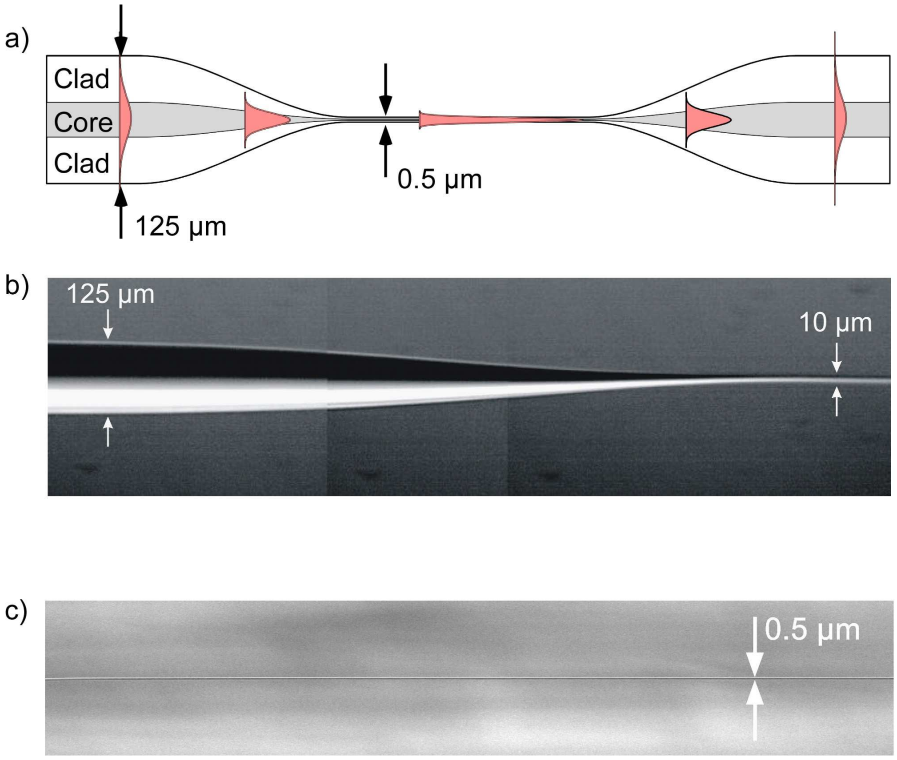

Figure 1.6: Profile of a tapered optical fiber. (a) Schematic of light propagation in a tapered optical fiber. Light in the unprocessed part of the fiber is guided by the glass core, which has a slightly higher refractive index than the surrounding cladding. A core diameter of 4 μm is typical for single mode fibers at an operating wavelength of 780 nm, and a cladding diameter of 125 μm is standard on all optical fibers. An adiabatic reduction of the cladding fiber diameter down to a typical size of 500 nm causes a spatial compression of the guided mode, greatly enhancing the intensity. Light in the 500-nm–diameter part propagates to a second adiabatic fiber region where it is guided into the fiber core. (b) SEM images of a tapered optical fiber. (c) SEM image of a nanofiber waist with a diameter of 500 nm. Adapted from Ref. [57].

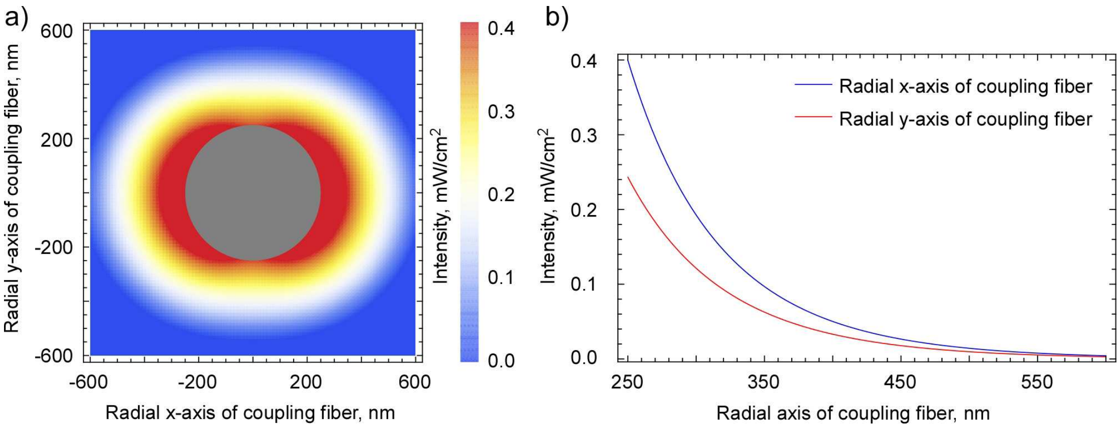

Figure 1.7: Radial light intensity in an optical nanofiber. (a) The radial intensity profile is plotted for a linearly polarized HE_{11} mode in the waist of a 500-nm–diameter optical nanofiber (grey disk) with 1 pW of power. The evanescent field decays exponentially with a characteristic decay length of approximately $\lambda/2\pi/\sqrt{n^2-1} = 118$ nm, where $\lambda = 780$ nm is the light wavelength and $n = 1.45$ is the refractive index of silica. (b) A cross section through the intensity profile along both fiber axes reveals an intensity of up to 0.4 mW/cm^2 at the fiber surface. As a comparison, this value is almost one eight the saturation intensity of the rubidium atoms used in our cavity QED experiment (3.13 mW/cm^2, D$_2$ transition of a ^{85}Rb atom: $F = 3 \rightarrow F' = 4$).

CHAPTER 2

Quantitative Description of Coupling Single Atoms to WGMs

The theoretical basis of cavity quantum electrodynamic (cavity QED) experiments with a bottle resonator and rubidium atoms is described in this chapter. First, the master equation is derived for the simple case of a single-mode Fabry-Pérot resonator interacting with a two-level atom. Indeed, the validity of this master equation is borne out in numerous experiments with Fabry-Pérot resonators (see for example Refs. [13,18,19,59]). Building on this model, we finally derive the master equation for a two-mode WGM resonator and two-level atom and then calculate the expected spectral properties of the strongly coupled system.

2.1 The Fabry-Pérot resonator

2.1.1 A single mode light field

The quantization of electromagnetic fields centers on the description of a single mode light field in analogy to a quantum mechanical harmonic oscillator. Here we consider the Hamiltonian of a mode of the electromagnetic field, as can be realized in cavity, for example, which is

$$\hat{H}_c = \hbar\omega_c(\hat{a}^\dagger\hat{a} + \frac{1}{2}). \tag{2.1}$$

By setting the ground state energy to zero the equation simplifies to $\hat{H}_c = \hbar\omega\hat{a}^\dagger\hat{a}$. The parameters can be attributed with physical meaning as follows: ω_c is the cavity resonance frequency, $\hat{a}$ is the photon annihilation operator and $\hat{a}^\dagger$ is the photon creation operator. These operators obey the boson commutator relation $\left[\hat{a}, \hat{a}^\dagger\right] = 1$, and can be applied to number states giving

$$\hat{a}^\dagger|n\rangle = \sqrt{n+1}|n+1\rangle \ , \tag{2.2}$$

and also

$$\hat{a}|n\rangle = \sqrt{n}|n-1\rangle \ . \tag{2.3}$$

2.1.2 A two-level atom

For a single uncoupled two-level atom, the Hamiltonian is

$$\hat{H}_a = \frac{\hbar\omega_a}{2}\hat{\sigma}_z \ , \tag{2.4}$$

where $\hat{\sigma}_z$ is the Pauli spin matrix $\hat{\sigma}_z = |e\rangle\langle e| - |g\rangle\langle g|$ and ω_a is the atomic transition frequency between states $|g\rangle$ and $|e\rangle$ with energies $E_g = -\hbar\omega_a/2$ and $E_e = \hbar\omega_a/2$, and we exclude the zero-point energy. The atomic raising operator is $\hat{\sigma}_+ = |e\rangle\langle g|$ and the atomic lowering operator is $\hat{\sigma}_- = |g\rangle\langle e|$.

2.1.3 Coupled atom–cavity system

The Hamiltonian of a coupled atom-cavity system is significantly different to that of the individual atom or cavity, and is quantum mechanical in nature. The interaction of a field and a two-level atom is given in the dipole approximation by

$$\hat{H}_{ac} = -\hat{d}\hat{E} \ , \tag{2.5}$$

where the WGM field is $\hat{E} \propto \hat{a} + \hat{a}^\dagger$, and the $\hat{d} = e\hat{r}$ is the atomic dipole operator of an atom. Expressing the dipole operator using the atomic basis states we get

$$\hat{d} = d|g\rangle\langle e| + d^*|e\rangle\langle g| = d(\hat{\sigma}_- + \hat{\sigma}_+), \tag{2.6}$$

where $\langle e|\hat{d}|g\rangle = \hat{d}$. The Hamiltonian of a two-level atom interacting with a quantized single-mode field in the rotating wave approximation is thus

$$\hat{H}_{ac} = \hbar g(\hat{a}^\dagger\hat{\sigma}_- + \hat{a}\hat{\sigma}_+) \ , \tag{2.7}$$

where the atom-cavity coupling strength is g given by

$$g = \sqrt{\frac{\omega_c}{2\hbar\varepsilon V}}d \ , \tag{2.8}$$

where ω_c is the frequency of the cavity and ε is the electric permittivity [16]. The coupling strength scales with the square root of the mode volume and linearly with the dipole matrix element $\hat{d}$ for the transition $|g\rangle \rightarrow |e\rangle$. The total atom-cavity Hamiltonian is finally the sum of the individual parts, $\hat{H}_0 = \hat{H}_{\text{ac}} + \hat{H}_a + \hat{H}_c$,[1]

$$\hat{H}_0/\hbar = \Delta\omega_{\text{al}}\hat{\sigma}_+\hat{\sigma}_- + \Delta\omega_{\text{cl}}\hat{a}^\dagger\hat{a} + (g\hat{a}^\dagger\hat{\sigma}_- + g^*\hat{a}\hat{\sigma}_+) \ , \tag{2.9}$$

where $\Delta\omega_{\text{cl}} = \omega_c - \omega_l$ is the detuning between cavity and laser, and $\Delta\omega_{\text{al}} = \omega_a - \omega_l$ is the detuning between atom and laser. This is the unitary Jaynes-Cummings Hamiltonian for a closed quantum system. The model and excitation spectrum are illustrated in Fig. 2.1.

---

[1] All terms have units of s^{-1} since the left-hand side of the equation is in units of $J/(J\ s)$.

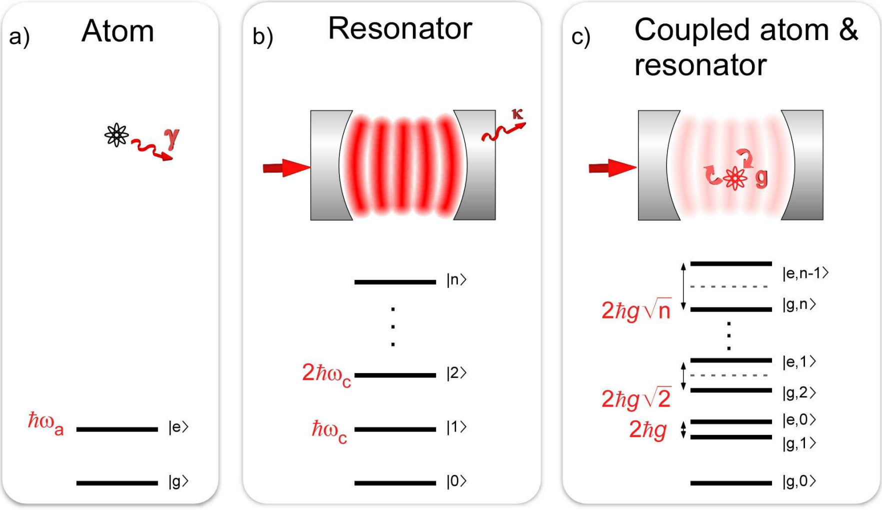

Figure 2.1: Jaynes-Cummings model for a single atom strongly coupled to a single mode Fabry-Pérot resonator. (a) Eigenstates of the free two-level atom with a ground state $|g\rangle$ and excited state $|e\rangle$ with a transition frequency $\hbar\omega_a$. (b) Eigenstates of the resonator with atom. Photon number states in the resonator are labeled $|n\rangle$, where n is $1, 2, 3 \ldots$. The photons have energy $\hbar\omega_c$ where ω_c is the resonance frequency of the resonator. Dissipation is included in the model via the terms κ resonator losses due to mirror transmission and intrinsic mechanisms such as absorption and scattering, and the transverse atomic decay rate is γ. (c) The eigenstates of the coupled atom-resonator system exhibits an anharmonic energy spacing, $2\hbar g\sqrt{n}$, that is dependent on the number of excitations, which is a distinctly quantum mechanical feature.

Master equation and dissipation

In the presence of dissipation of energy to the environment and pumping from an external driving field, the density matrix models the evolution of what is now an open quantum system. The evolution of the atom-cavity density matrix operator ρ is defined in a master equation using the Hamiltonian H_0' [16], where the master equation is written as

$$\begin{aligned}\frac{d\hat{\rho}}{dt} &= -i\left[\hat{H}_0', \hat{\rho}\right] + \kappa(2\hat{a}\hat{\rho}\hat{a}^\dagger - \hat{a}^\dagger\hat{a}\hat{\rho} - \hat{\rho}\hat{a}^\dagger\hat{a}) \\ &\quad + \frac{\Gamma}{2}(2\hat{\sigma}_-\hat{\rho}\hat{\sigma}_+ - \hat{\sigma}_+\hat{\sigma}_-\hat{\rho} - \hat{\rho}\hat{\sigma}_+\hat{\sigma}_-)\ ,\end{aligned} \tag{2.10}$$

where the Hamiltonian is

$$\begin{aligned}\hat{H}_0'/\hbar &= \Delta\omega_{\mathrm{al}}\hat{\sigma}_+\hat{\sigma}_- + (g\hat{a}^\dagger\hat{\sigma}_- + g^*\hat{a}\hat{\sigma}_+) \\ &\quad + \Delta\omega_{\mathrm{cl}}\hat{a}^\dagger\hat{a} + \left(\mathcal{E}\hat{a}^\dagger + \mathcal{E}^*\hat{a}\right)\ .\end{aligned} \tag{2.11}$$

The cavity field is now driven by an amplitude $\mathcal{E}$, while dissipation is included in the density matrix by the cavity loss term κ arising from out-coupling of light through the mirror as well as absorption and scattering at the mirror. Equation (2.10) can be solved numerically to study the dynamics of the coupled system and is valid for any combination of g, κ, and Γ. While it is convention to use lower case letters ($\hat{a}$) to describe the standing wave mode in a Fabry-Pérot cavity, for the following section on WGM cavities uses the standard convention of lower case letters for traveling wave modes, and upper case letters ($\hat{A}$) for standing wave modes.

2.2 The WGM resonator

2.2.1 WGMs of light

Apart from being relevant to Fabry-Pérot resonators, the previous discussion can also be applied to a resonator with two counter-propagating waves, such as in a ring resonator or a whispering gallery mode resonator. Considering waves counter-propagating along a common z-axis, the positive frequency field is [16]

$$E^{+} = \mathcal{E}_t \left(\hat{a} \exp^{ikz} + \hat{b} \exp^{-ikz} \right) \exp^{-i\omega t} \,, \tag{2.12}$$

where $\mathcal{E}_s = \sqrt{2}\mathcal{E}_t = [\hbar\omega/\varepsilon V]^{1/2}$ is the relation comparing the electric field per photon for standing and traveling waves, and $\hat{a}$ and $\hat{b}$ identify the two running wave modes. The resonator has a mode volume V and electric permittivity ε. Alternatively, standing wave operators $\hat{A}$ and $\hat{B}$ can be defined as

$$\hat{A} = \frac{\hat{a} + \hat{b}}{\sqrt{2}} \tag{2.13}$$

and

$$\hat{B} = \frac{\hat{a} - \hat{b}}{\sqrt{2}} \tag{2.14}$$

and give

$$E^{+} = \mathcal{E}_s \left(\hat{A} \cos(kz) + i\hat{B} \sin(kz) \right) \exp^{-i\omega t} \,, \tag{2.15}$$

where the operator $\hat{A}$ obeys the commutator relation $\left[\hat{A}, \hat{A}^{\dagger}\right] = 1$, and similarly for $\hat{B}$. The standing wave operators act on the number state $|n_A n_B\rangle$ giving

$$\hat{A}|n_A n_B\rangle = \sqrt{n_A}|n_A - 1, n_B\rangle \,, \tag{2.16}$$

and

$$\hat{B}|n_A n_B\rangle = \sqrt{n_B}|n_A, n_B - 1\rangle \,, \tag{2.17}$$

where n_A (n_B) is the number of photons in standing wave mode A (B).

The Hamiltonian for the WGM in terms of the traveling wave operators is trivially

$$\hat{H}_c = \hbar\omega(\hat{a}^{\dagger}\hat{a} + \hat{b}^{\dagger}\hat{b}) \,, \tag{2.18}$$

where we have set the ground state energy to zero.

While the choice of traveling or standing wave operators is irrelevant for calculating the atom-cavity density matrix discussed in the later sections of this chapter, it does however have a

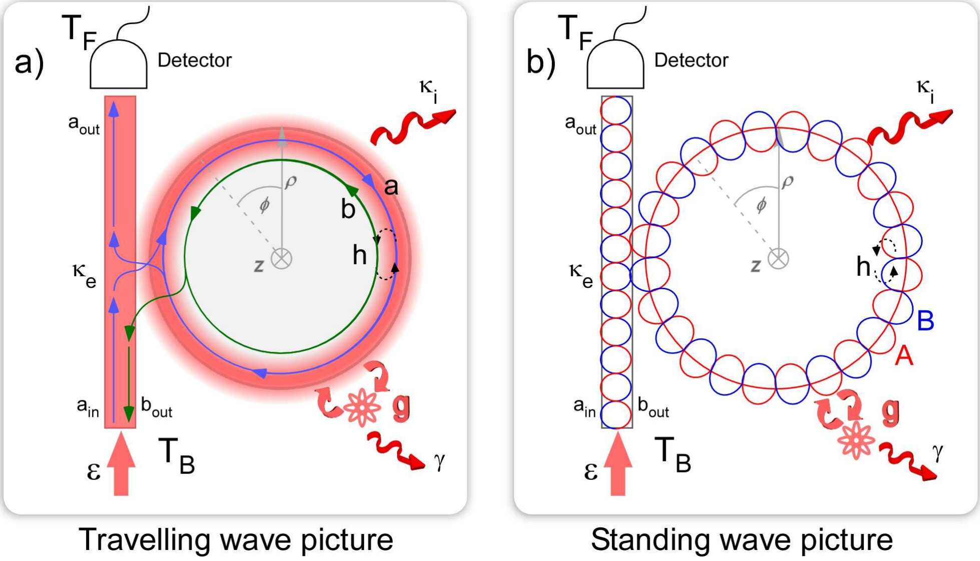
a)
T_F
Detector
a_{out}
κ_e
a_{in}
b_{out}
ε
T_B
κ_i
ρ
ϕ
a
b
h
z
g
γ
Travelling wave picture
b)
T_F
Detector
a_{out}
κ_e
a_{in}
b_{out}
ε
T_B
κ_i
ρ
ϕ
z
h
B
A
g
γ
Standing wave picture

Figure 2.2: Schematic cross-section through the bottle resonator and input coupling fiber. Light with drive strength $\mathcal{E}$ is coupled into the whispering gallery mode bottle resonator using a sub-wavelength diameter optical fiber. (a) Travelling wave picture: Light couples between the fiber and resonator at a rate κ_e while modes a and b couple at a rate h. (b) Standing wave picture: Travelling waves can be decomposed into a combination of standing waves A and B, as described in the main text.

further meaning when momentum exchange and light forces are taken into account in the few-photon regime as pointed out by Shore *et al.* [60]. With running waves, it is possible to identify which wave exchanges momentum with the atom by observing the atomic motion, for example. A quantum standing wave in a Fabry-Pérot resonator, in contrast, has zero average momentum because the mirrors act as "infinite sinks and sources of momentum," restoring the field after every resonator round-trip [60]. It is therefore not possible to identify which *traveling* wave exchanges momentum with the atom.

2.2.2 Coupled atom-cavity system

The interaction Hamiltonian of a two-level atom interacting with quantized WGM field modes in the traveling wave picture is

$$\hat{H}_{ac}/\hbar = (g_t^* \hat{a}^\dagger \hat{\sigma}_- + g_t \hat{a} \hat{\sigma}_+) + (g_t \hat{b}^\dagger \hat{\sigma}_- + g_t^* \hat{b} \hat{\sigma}_+) \,, \tag{2.19}$$

where g_t is assumed to be equal for both traveling wave modes $\hat{a}$ and $\hat{b}$ and has a phase with respect to each. A schematic of the interaction between an atom and traveling wave modes is shown in Fig. 2.2 (c).

The total atom-cavity Hamiltonian, in the rotating frame of the laser field, is again the sum of the individual parts, $\hat{H}_0' = \hat{H}_{\mathrm{ac}} + \hat{H}_a + \hat{H}_c$, [61]

$$\begin{aligned}\hat{H}_0'/\hbar = {} & \Delta\omega_{\mathrm{al}}\hat{\sigma}_+\hat{\sigma}_- + \left(g_t^*\hat{a}^\dagger\hat{\sigma}_- + g_t\hat{a}\hat{\sigma}_+\right) + \left(g_t\hat{b}^\dagger\hat{\sigma}_- + g_t^*\hat{b}\hat{\sigma}_+\right) \\ & + \Delta\omega_{\mathrm{cl}}\hat{a}^\dagger\hat{a} + \Delta\omega_{\mathrm{cl}}\hat{b}^\dagger\hat{b} + h\left(\hat{a}^\dagger\hat{b} + \hat{b}^\dagger\hat{a}\right) \\ & + \left(\mathcal{E}\hat{a}^\dagger + \mathcal{E}^*\hat{a}\right) \ ,\end{aligned} \tag{2.20}$$

Each parameter is described as follows: h is the coupling strength between modes a and b for an empty resonator (e.g., due to coherent Rayleigh scattering from surface roughness) and is assumed to be equal between both modes $a \to b$ and $b \to a$.[2] This term in Eq. (2.20) is phenomenological and is a product of h and the operators $\hat{a}$ and $\hat{b}$ and describes the cycling of energy between the modes at a rate h. If h is larger than the other rates in the system, it can lead to a breaking of the frequency degeneracy of modes a and b: see the next chapter for further details. The detuning between cavity and laser is $\Delta\omega_{\mathrm{cl}} = \omega_c - \omega_l$ and the detuning between atom and laser is $\Delta\omega_{\mathrm{al}} = \omega_a - \omega_l$. The first two lines are the unitary Jaynes-Cummings Hamiltonian while the third line is a driving term. The model and excitation spectrum is illustrated in Fig. 2.3. The resonator is driven with a strength $\mathcal{E} = i\sqrt{2\kappa_e P_{\mathrm{in}}/(\hbar\omega_l)}$ which is assumed to drive only mode a, where κ_e is the coupling rate between the resonator and the neighboring coupling fiber, $P_{\mathrm{in}} = \hbar\omega_l|\langle a_{\mathrm{in}}\rangle|^2$ is the input power in the coupling fiber, and $|\langle a_{\mathrm{in}}\rangle|^2$ is the input photon flux. We define the traveling wave coupling strength as $g_t = g_t^0\psi(\rho, z)\exp^{\pm i\phi}$, dependant on the radial (ρ) and azimuthal (z) and angular (ϕ) position of the atom in both clockwise (+) and counter-clockwise (-) traveling modes, c.f. Fig. 2.2.

Each term in Eq. (2.20) can be intuitively understood as follows: The first term is the energy of the free atom, given by the atomic raising and lowering operators. The first part of the second term in brackets describes the reversible exchange of energy between the atom and traveling resonator mode a by emission of a photon from the atomic excited state into the mode at a rate g_t. Conversely for the other term in brackets, light is absorbed by the atom from mode a. The last term on the first line similarly describes energy exchange for mode b.

The first two terms in the second line describe the energy of the free photon fields in modes a and b, respectively, while the last two terms describe the exchange of energy between the resonator modes at a rate h mediated by Rayleigh scattering. On the third line, a complex driving term $\mathcal{E}$ acts on mode a.

---

[2] Here we assume h to be real without affecting a loss of generality. The solution of the master equation only requires the phase difference between g and h.

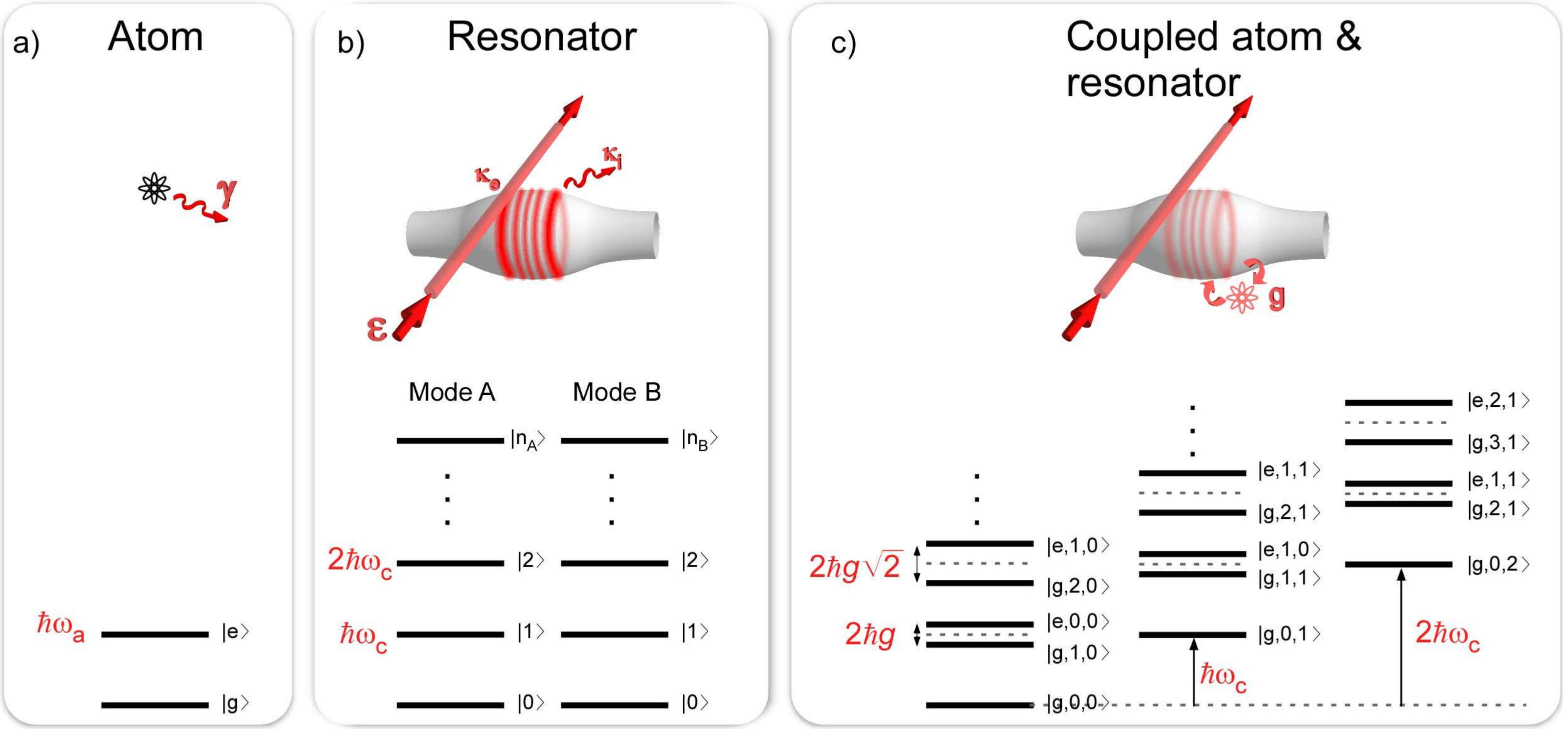
a)
Atom
γ
$\hbar\omega_a$
|e⟩
|g⟩
b)
Resonator
κ_e
κ_i
ε
Mode A
Mode B
$|n_A\rangle$
$|n_B\rangle$
$2\hbar\omega_c$
|2⟩
|2⟩
$\hbar\omega_c$
|1⟩
|1⟩
|0⟩
|0⟩
c)
Coupled atom & resonator
g
$2\hbar g\sqrt{2}$
$2\hbar g$
|e,1,0⟩
|g,2,0⟩
|e,0,0⟩
|g,1,0⟩
|g,0,0⟩
|e,1,1⟩
|g,2,1⟩
|e,1,0⟩
|g,1,1⟩
|g,0,1⟩
$\hbar\omega_c$
|e,2,1⟩
|g,3,1⟩
|e,1,1⟩
|g,2,1⟩
|g,0,2⟩
$2\hbar\omega_c$

Figure 2.3: Jaynes-Cummings model in the standing wave picture for a single atom strongly coupled to a WGM resonator. (a) Eigenstates of the free atom. (b) Resonator: Eigenstates of the resonator without atom. Two standing wave resonator modes, A and B, each have a ladder of photon states, $|n_{A(B)}\rangle$, with energy $\hbar\omega_c$, where ω_c is the cavity resonance frequency which we assume is equal for both modes. (c) Coupled atom and resonator: The eigenstates of the coupled system are written as as $|\mathrm{Atom}, \mathrm{Mode\ A}, \mathrm{Mode\ B}\rangle$. In the sketch we assume that the atom couples to mode A, giving lowest energy states $|g, n_A = 0, (n_B = 0, 1, 2, 3\ldots)\rangle$. Photons that populate mode B do not couple to the atom, thus resulting in an offset in the lowest energy states of $n_B\hbar\omega_c$, where n_B is the number of photons in mode B. Therefore, the Jaynes-Cummings ladder of states is two-dimensional. Dissipation is included in the model via the terms κ_i and κ_e describing the resonator losses due to intrinsic mechanisms such as absorption and scattering while extrinsic mechanisms arise from coupling to the neighboring nanofiber.

Master equation

The master equation describing the time evolution of the density matrix is modified from the case of the Fabry-Pérot resonator to include the second mode

$$\begin{aligned}\frac{d\hat{\rho}}{dt} &= -i\left[\hat{H}_0', \hat{\rho}\right] \\ &+ \kappa(2\hat{a}\hat{\rho}\hat{a}^\dagger - \hat{a}^\dagger\hat{a}\hat{\rho} - \hat{\rho}\hat{a}^\dagger\hat{a}) \\ &+ \kappa(2\hat{b}\hat{\rho}\hat{b}^\dagger - \hat{b}^\dagger\hat{b}\hat{\rho} - \hat{\rho}\hat{b}^\dagger\hat{b}) \\ &+ \frac{\Gamma}{2}(2\hat{\sigma}_-\hat{\rho}\hat{\sigma}_+ - \hat{\sigma}_+\hat{\sigma}_-\hat{\rho} - \hat{\rho}\hat{\sigma}_+\hat{\sigma}_-)\ ,\end{aligned} \tag{2.21}$$

where $\hat{\rho}$ is the density matrix operator, $\kappa = \kappa_e + \kappa_i$ is the total field decay rate, and $\Gamma = 2\gamma_\perp$ is the atomic spontaneous emission rate and $\gamma_\perp$ is the transverse atomic decay rate. The rate κ_e characterizes the coupling rate between light in the optical fiber and resonator mode, which is due to frustrated total internal reflection at the coupling region. The rate κ_i characterizes the intrinsic loss of light from the resonator mode into free space, which is due to its finite ability to store light.

In the standing wave mode basis described in Sec. 2.2.1, the master equation becomes

$$\begin{aligned}\frac{d\hat{\rho}}{dt} &= -i\left[\hat{H}_0', \hat{\rho}\right] \\ &+ \kappa(2\hat{A}\hat{\rho}\hat{A}^\dagger - \hat{A}^\dagger\hat{A}\hat{\rho} - \hat{\rho}\hat{A}^\dagger\hat{A}) \\ &+ \kappa(2\hat{B}\hat{\rho}\hat{B}^\dagger - \hat{B}^\dagger\hat{B}\hat{\rho} - \hat{\rho}\hat{B}^\dagger\hat{B}) \\ &+ \frac{\Gamma}{2}(2\hat{\sigma}_-\hat{\rho}\hat{\sigma}_+ - \hat{\sigma}_+\hat{\sigma}_-\hat{\rho} - \hat{\rho}\hat{\sigma}_+\hat{\sigma}_-)\ ,\end{aligned} \tag{2.22}$$

with the Hamiltonian

$$\begin{aligned}\hat{H}_0' = \Delta\omega_{\mathrm{al}}\hat{\sigma}_+\hat{\sigma}_- &+ g_A(\hat{A}^\dagger\hat{\sigma}_- + \hat{A}\hat{\sigma}_+) - ig_B(\hat{B}^\dagger\hat{\sigma}_- - \hat{B}\hat{\sigma}_+) \\ &+ (\Delta\omega_{\mathrm{cl}} + h)\,\hat{A}^\dagger\hat{A} + (\Delta\omega_{\mathrm{cl}} - h)\,\hat{B}^\dagger\hat{B} \\ &+ \frac{1}{\sqrt{2}}\left[\mathcal{E}^*\left(\hat{A} + \hat{B}\right) + \mathcal{E}\left(\hat{A}^\dagger + \hat{B}^\dagger\right)\right]\ ,\end{aligned} \tag{2.23}$$

In this normal mode representation the coupling strength is sinusoidally modulated and is given by $g_A = \sqrt{2}g_t\psi(\rho, z)\cos(\phi)$ and $g_B = \sqrt{2}g_t\psi(\rho, z)\sin(\phi)$. The coupling of the atom to modes A and B shows a $\sin^2(\phi)$ behavior when calculating the intra-cavity photon flux. For a fixed atom, the coupling can be dominated by either mode A or mode B. This can be readily seen by plotting the spectrum for different laser and resonator detunings as shown in Fig. 2.4. The spectrum in Fig. 2.4 (a) shows a characteristic anti-crossing with the diagonal resonator mode only weakly coupled to the atom. This results in the transmission and reflection at $\Delta\omega_{\mathrm{cl}} = \Delta\omega_{\mathrm{ac}} = 0$ changing by $\sim 25\%$ compared to the empty resonator case as shown in Fig. 2.4 (b). An explanation for this observation of equal power in both ports of the coupling fiber is given in Sec. 2.2.3.

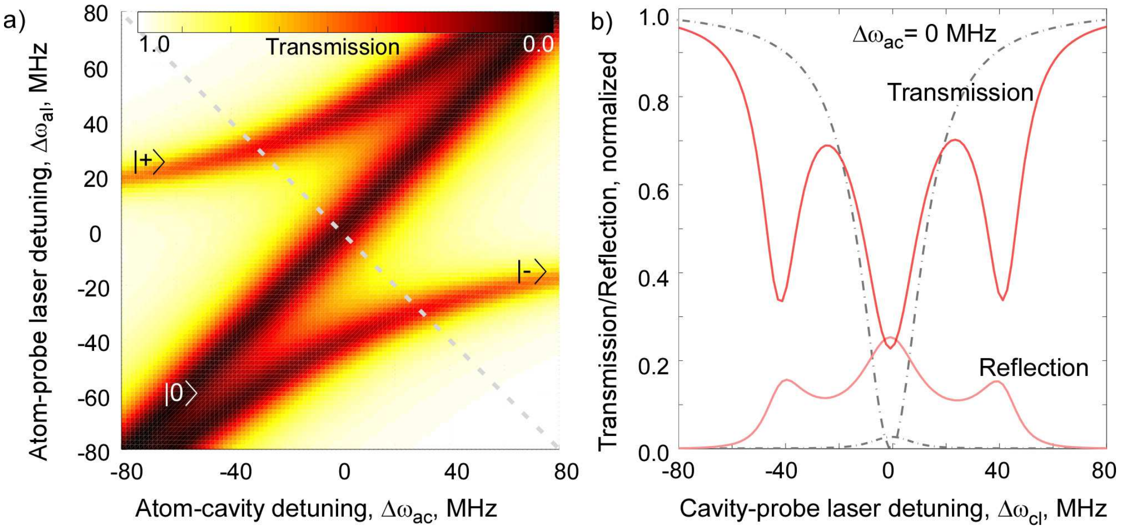

Figure 2.4: Theoretical transmission spectrum of a rubidium atom strongly coupled to a bottle resonator mode observed through a coupling fiber. (a) The black/red lines indicate the three resonances, two of which are the coupled resonances, $|\pm\rangle$, while the third resonance, $|0\rangle$, is uncoupled. (b) Transmission and reflection spectra as a function of probe laser detuning, $\Delta\omega_{\mathrm{l}}$, with $\omega_a = \omega_c$ (see diagonal dashed line in (a)). Typical values expected in the experiment: the split resonances are separated by $2\sqrt{2}g_t^0 = 84$ MHz with $g_t^0/2\pi = 30$ MHz, $\kappa/2\pi = 13$ MHz, and $\gamma/2\pi = 3$ MHz, $h/2\pi = 2$ MHz, $\phi = \pi/4$. Dash-dot lines: empty resonator. Atomic transition: ^{85}Rb, $5^2S_{1/2} \rightarrow 5^2P_{3/2}$, π-polarized light for transition ($F = 3, m_F = 0 \rightarrow F' = 4, m_F = 0$).

2.2.3 Input-output formalism

The operator for the fields coupled out of a resonator, $\hat{a}_{\mathrm{out}}$, can be written in terms of the input field operator, $\hat{a}_{\mathrm{in}}$, and the intra-cavity field operator [62],

$$\hat{a}_{\mathrm{out}} = \hat{a}_{\mathrm{in}} + i\sqrt{2\kappa_e}\hat{a}(t) = \hat{a}_{\mathrm{in}} + i\sqrt{\kappa_e}\left[\hat{A}(t) + \hat{B}(t)\right] , \tag{2.24}$$

$$\hat{b}_{\mathrm{out}} = \hat{b}_{\mathrm{in}} + i\sqrt{2\kappa_e}\hat{b}(t) = \hat{b}_{\mathrm{in}} + i\sqrt{\kappa_e}\left[\hat{A}(t) - \hat{B}(t)\right] . \tag{2.25}$$

The normalized transmission, T_F, and back-reflection, T_B, in the coupling fiber is therefore

$$T_F = \frac{\langle \hat{a}^\dagger_{\mathrm{out}} a_{\mathrm{out}} \rangle}{|\mathcal{E}|^2/2\kappa_e} , \tag{2.26}$$

$$T_B = \frac{\langle \hat{b}^\dagger_{\mathrm{out}} b_{\mathrm{out}} \rangle}{|\mathcal{E}|^2/2\kappa_e} , \tag{2.27}$$

The output photon fluxes $\langle \hat{a}^\dagger_{\mathrm{out}} a_{\mathrm{out}} \rangle$ and $\langle \hat{b}^\dagger_{\mathrm{out}} b_{\mathrm{out}} \rangle$ can be determined from the density matrix formalism in the previous section.

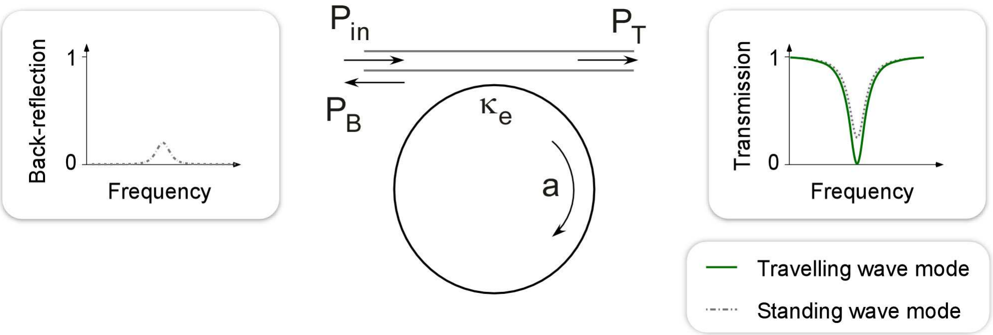

Figure 2.5: Model of a coupling fiber and single-mode WGM resonator. The left fiber port (P_{in}) is taken as the input port which couples evanescently to the resonator. The transmission and back-reflection characteristics of each port are sketched for the cases of traveling and standing wave cavities.

On-resonance transmission

Prior to an atom coupling to the resonator, both WGM modes are frequency degenerate at $\Delta\omega_{\mathrm{cl}} = 0$ MHz, see Fig. 2.4 (b). Suppose, for example, an atom strongly couples to standing wave mode A where it firstly creates two new eigenstates of the coupled system, thus forming the left-most and right-most dips in the Rabi-spectrum in Fig. 2.4 (b). Secondly, mode B remains an eigenstate of the resonator because it does not couple to the atom, thus forming the central dip on resonance. However, this dip is not unchanged from the case prior to the atom coupling to mode A: the transmission and reflection are both ~ 0% before the atom couples and ~ 25% after the atom couples. The difference is explained in the following.

For traveling wave modes, resonant light enters the input port of the fiber in Fig. 2.5, couples to the resonator, and couples out to the fiber again and propagates to the right-hand output port. Assuming the fiber and resonator are critically coupled such that the cavity decay rate equals κ_e, the transmission and reflection is zero on resonance.

Contrasting the previous situation is the case of standing wave modes where light exits through both fiber ports rather than just one port.[3] Since the resonator mode forms a standing wave, the field will decay equally to both left and right ports. In this case, the cavity field amplitude a is reduced by 50%, corresponding to a 25% reduction in the transmitted power and a 25% increase in the back-reflected power. Therefore, if the presence of an atom or nano-particle fixes a standing wave, we expect to observe equal power in both ports at $\omega_c = \omega_l = \omega_a$.

---

[3] A resonator with a traveling wave can be reconfigured as a standing wave resonator if a strongly coupled scatter is introduced, such as a nano-particle or atom.

CHAPTER 3

Characteristics of the Microresonator Design

In this chapter I describe the basic properties of the bottle microresonator enabling its potential for cavity QED experiments. Recent results from our group demonstrate a number of important physical properties of the resonators such as ultra-high quality-factors and full frequency tunability [25]. The ability to tune the behavior of the resonator (i.e., quality factor, intra-cavity power, mode structure) using a tapered optical fiber coupler distinguishes it from Fabry-Pérot resonators. More importantly, a tapered optical fiber enables the near lossless in- and out-coupling of light to a resonator mode.

Before describing the properties of the bottle resonator, I first outline the fabrication of the bottle resonator and optical coupling fiber. Finally, particular emphasis is given to optimization of the resonator geometry in relation to the cavity QED experiments described later.

3.1 Fabrication of bottle microresonators and ultra-thin optical fibers

Both sub-micron optical fibers and bottle microresonators are produced from commercial glass fibers using the heat-and-pull technique [63, 64]. For the work presented in this thesis, the sub-micron coupling fiber is a step-index single mode fiber with an operation wavelength of 830 nm (Newport, F-SF), cladding diameter of 125 μm, and a mode field diameter of 5.6 μm. The resonators used in this chapter and Sec. 5.1.4 are also made of this fiber, while all other resonators are made using a Ceramoptik GmbH solid glass fiber (model PWF 200 T) with a diameter of 200 μm. Before processing the fibers, the polyacrylate buffer is removed and the fiber surface is cleaned with acetone (Uvasol). The heat-and-pull technique is implemented using a home-made fiber pulling rig, which is schematically shown in Fig. 3.1 and described in detail in Ref. [53].

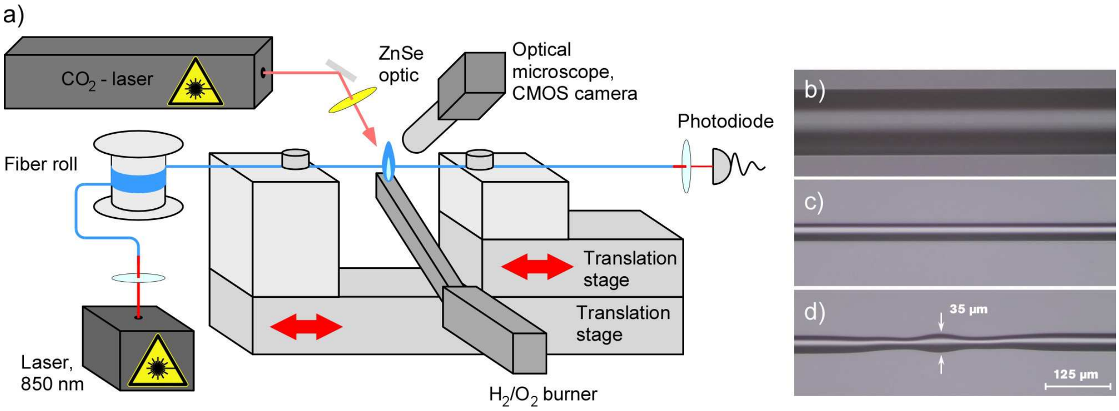

Figure 3.1: Fabrication of ultra-thin optical fibers and bottle microresonators. (a) Schematic of the fiber pulling rig (see main text). (b–d) Steps in bottle microresonator fabrication. (b) First, a commercial 125–200–μm-diameter optical step-index fiber is prepared by stripping away the buffer material and then cleaning with Uvasol grade acetone (Merck Millipore). (c) A section of fiber is then heated with a focussed CO_2-laser beam being stretched to yield the desired resonator diameter, which is 35 μm in the figure. (d) Finally, the laser beam is again used to form two so-called "microtapers" on the fiber separated by approximately 150 μm. The resulting bulge between the microtapers forms a bottle microresonator of diameter 35 μm. Adapted from Refs. [25, 35–37].

The machine consists of a pair of stacked translation stages onto which a fiber is clamped before heating with a hydrogen/oxygen flame (flame width = 1 mm). Fibers are heated and stretched in a computer-controlled process in order to reduce the fiber diameter from an initial value of 125 μm down to typical values of around 100–500 nm, depending on application. Alternatively, a focused CO_2-laser beam with a maximum power of 30 W (Series 48-2, Synrad Inc.) can be used as a heat source. The laser beam is focused with a ZnSe lens and only heats a 100–150 μm wide section of the fiber and therefore allows the production of a much smaller structure. A microscope attached to a color CMOS camera images the fibers. The transmission of the sub-micron coupling fiber is monitored using either a diode laser ($\lambda = 850$ nm) or a white light source ($\lambda = 400 - 900$ nm). The typical transmission after fabrication is greater than 95–99% in the 780–850 nm wavelength range.

3.1.1 Sub-micron tapered optical fibers

Optical fibers with sub-micron diameters down to 100 nm can be produced with the flame as the heat source, while the minimal diameter achievable with the CO_2-laser is around 2–3 μm. (This difference in final diameter is due to the quadratic scaling of radius and light absorption in the CO_2-laser technique compared to the linear scaling of surface heating and radius with the flame technique. The CO_2-laser technique involves absorption of light in the fiber, while the flame technique involves heating the surface of the fiber). Therefore, only the flame heat source is used to produce the required coupling fibers where a typical waist diameter of around 500 nm is required to phase match the fiber mode with the resonator mode.

A central feature of the fiber pulling rig is its ability to reproducibly fabricate fibers with any desired shape and taper profile. Scanning electron microscope measurements (not shown) and second-harmonic generation measurements [65] both confirm a fabrication tolerance of around ±3% of the target waist diameter. The taper region between the unprocessed fiber and the final processed fiber waist can be designed to have the required profile using a custom *trajectory calculator* program. The fiber waist can have an arbitrary length up to several centimeters while the taper region can also have arbitrary length and the taper profile can be tailored to have, for example, a linear taper profile. The calculated fiber profile is then used in the control of the fiber pulling rig in a computer-automated process.

3.1.2 Bottle microresonators

Resonator fabrication also employs the heat-and-pull process using a standard glass fiber, with an initial diameter of 125–200 μm, and a CO_2-laser as a heat source. Figure 3.1 (b)–(d) shows the fiber profile after each step in the fabrication process.

First, the fiber is tapered down to the desired diameter of the resonator using the heat-and-pull technique described previously in Fig. 3.1 (b). In the work presented here, this step is usually accomplished using the CO_2-laser light, however, the hydrogen/oxygen flame can be equally well employed. The second and final step involves forming the resonator curvature along the fiber axis so that the resonator yields the required spectral mode spacing, as described in Sec. 1.2.2. This is achieved by sequentially microtapering two sections on the fiber by again using the heat-and-pull technique with the CO_2-laser. The CO_2-laser is operated with a power of $\sim$2 W — this is high enough to soften the glass but low enough to not melt the glass and cause appreciable evaporation of silica. The central zone between the microtapers exhibits a parabolic variation of the fiber diameter over a length of a several tens of microns and forms the bottle microresonator. The curvature of the resonator can be precisely tailored by adjusting the CO_2-laser beam spot size, the microtaper separation, and the microtaper elongation length. An additional strategy successfully employed for achieving highly curved resonators ($\Delta k \gtrsim 0.020$ μm^{-1}) is to undertake a third step where the central resonator region is heated above the glass melting point, thereby allowing the glass to contract under surface tension. In this work, the final resonator diameter is typically in the 30–40 μm range and the curvature is in the range $\Delta k = 0.009$–0.020 μm^{-1}.

3.1.3 Techniques for estimating the curvature of bottle microresonators

The radius of the highly prolate central region of the bottle around $z = 0$ is well approximated by a parabolic profile

$$R(z) \approx R_0 \left(1 - (\Delta k z)^2 /2\right) \ .$$

Following fabrication of the resonator, the curvature is measured with the aid of either an optical microscope and CCD camera image of the resonator itself ($\Delta k \gtrsim 0.009$ μm^{-1}) or far-field diffraction of a laser beam ($\Delta k \lesssim 0.009$ μm^{-1}).

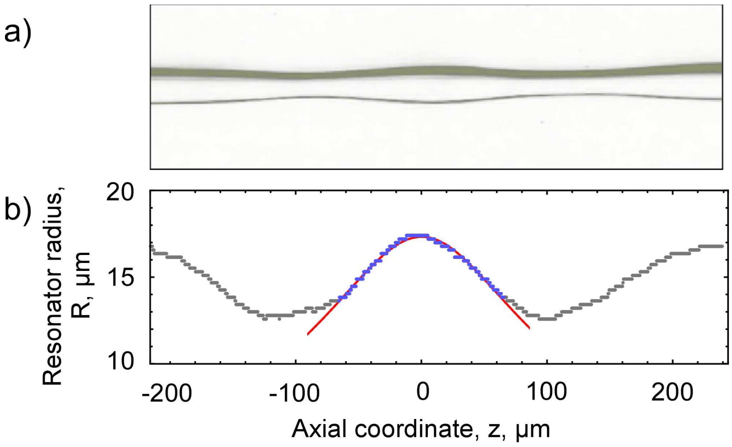

Figure 3.2: Reconstructing the profile of a bottle microresonator. (a) Microscope picture of a bottle microresonator with the edges highlighted in grey. (b) The reconstructed radius profile of a typical resonator used in this work agrees well with a parabolic fit (red) (see Eq. (1.25)) in the central region around $z = 0$. The fit yields $R_0 = 17.4$ μm and $\Delta k = 0.012$ μm^{-1}. Measurement tolerance: R_0 : ± 2.0 μm, Δk : ± 0.001 μm^{-1}.

A typical microscope image of a resonator and the inferred radius profile is shown in Fig. 3.2. The images are analyzed with a customized image analysis software. The program successively scans the pixels of each vertical line of the image and automatically estimates the fiber edges. From this data, the profile can be calculated using the conversion factor 0.42 μm/pixel. This method allows us to determine the local diameter with a precision of ± 2 μm and Δk with a precision of ± 0.001 μm^{-1}. The accuracy is mostly limited by the resolution of the optical microscope and any saturation in the image.

The profile of bottle microresonators can also be reconstructed from a diffraction pattern (see Ref. [53] and references therein). This is obtained by shining a collimated laser beam perpendicular to the resonator which, due to its small curvature, can be locally approximated as a cylinder. The dependency of the scattered intensity on the scattering angle and the fiber radius can then be easily calculated from Refs. [66–68]. The diffraction pattern is formed by Mie scattering of light occurring when the incident light excites resonances in the resonator, as well as interference of the transmitted, diffracted and reflected light rays.[1] The resulting diffraction pattern is shown in Fig. 3.3 (b) and is obtained in the Fraunhofer regime. The diffraction pattern is the coherent sum of light refracted and scattered by the fiber. This method provides a radial resolution of better than 100 nm [66] and is applicable to resonators having a curvature of up to 0.009 μm^{-1}.

---

[1] In general, the measurement technique requires the fiber-under-test to be transparent, and will not, for example, provide a diffraction pattern for translucent or metallic fibers [68].

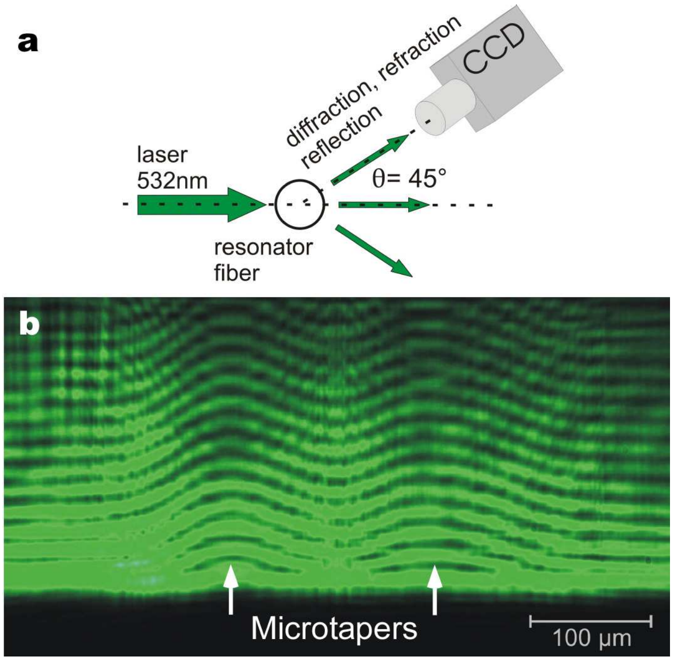

Figure 3.3: Setup of the scheme for determining the radius and curvature of bottle microresonators with low curvature ($\Delta k \lesssim 0.009\ \mu\mathrm{m}^{-1}$). (a) The resonator is illuminated with laser light at a wavelength of 532 nm and the resulting far-field diffraction is collected with a microscope at an angle of 45° relative to the incident beam. The microscope objective has a numerical aperture of 0.28 corresponding to a detection angle of 16°. (b) The measured diffraction pattern reveals two regions where the diffraction pattern is modulated, indicating the microtapers on either side of the resonator. The difference in radius between the resonator region and the microtaper region is 330 nm while the curvature is $\Delta k = 0.0040\ \mu\mathrm{m}^{-1}$. Reproduced from Ref. [35].

3.2 Properties of Tapered Optical Fiber Couplers

In this work, we use the evanescent field of a tapered optical glass nanofibers to efficiently couple light to and from the resonator mode. Other techniques such as free-space coupling, half-block couplers, angle-polished fibers and prism couplers are common in the literature [28]. For example, pioneering works on WGMs in liquid and aerosol droplets almost exclusively employed focussed laser beams to excite modes [28]. While being successful in exciting WGMs, the method is very inefficient because mode matching is hampered by inefficient in-coupling of light from the far-field. In small resonators with diameters below $\sim 20\ \mu$m, light predominantly escapes the mode by emission into free space in a spiralling pattern (i.e. radiative losses, c.f. Fig. 1.2). Reversing this process and focussing a beam onto the mode is a non-trivial task because a spiralling (high angular momentum) beam profile is required. Due to the high Q-factor of WGMs, very little light is lost from the mode into free space, and therefore very little light can be coupled into the mode from a free space beam. Silica resonators larger than $\sim 25\ \mu$m in diameter experience a few tens of orders of magnitude less radiative loss compared to absorption and scattering losses.

Other couplers such as prisms and angle-polished fibers achieve much greater coupling efficiency because they operate in the near-field. However, these couplers are inherently based on free-space optics and they tend to be bulky, which is an issue for fiber-based systems. Tapered optical fibers are the most appealing couplers because they can readily achieve very efficient and near loss-less coupling to a majority of different WGM microresonators, and they permit a fully fiber-based and very compact setup.

3.2.1 Mode matching of resonator and coupling fiber

The coupling strength between between the coupling fiber mode and resonator fiber mode is proportional to the evanescent field overlap of the two modes. This parameter is controlled through spatial alignment of the fibers. Efficient coupling also relies on the phase matching of the two modes. The propagation constant of a resonator mode is fixed by the resonator geometry and is given as $\beta_{\rm res} = m/R_0$, where m is the azimuthal quantum number and R_0 is the radius of the resonator. The propagation constant of the coupling fiber is a function of fiber diameter and rapidly approaches 1 for very small diameters of a few hundred nanometers. This scaling is due to the increased overlap of the mode with ambient air/vacuum. Since the coupling fiber diameter varies smoothly in the tapered region from an initial value of around 125 μm down to sub-micron dimensions, phase matching can be achieved by translating the resonator to different points on the coupling fiber until the efficiency is maximized.

Mode selectivity: One of the tangible benefits of phase matching is the possibility of selectively exciting one particular mode while suppressing all other modes. This is possible when the phase of the mode in the coupling fiber exactly matches the phase of the resonator mode. In practice, this is achieved by aligning the fibers as described above and, in particular, also involves maintaining a gap between the fiber and resonator. This gap serves to control the coupling strength between the modes. Figure 3.4 shows a typical mode spectrum measured over 900 GHz where axial modes $q = 1, 2$ are selectively optimized: both modes are believed to belong to the same mode family and have the same propagation constant. For the experiments described in Chaps. 7 and 8, the phase matching is not optimal but the mode spectrum nevertheless is generally free of unwanted modes over the frequency range of interest, e.g. a 1 GHz range. We note that we can always operate in the regime of critical coupling by increasing the coupling between the fiber and resonator (See next section for details). A poorly phase-matched setup, in contrast, would show several hundred resonance dips over the same 900 GHz span in the spectrum.

Probing the mode profile: Tapered coupling fibers also serve as a useful tool for identifying axial modes in the bottle resonator [25]. By physically translating the fiber along the axis of the resonator fiber the coupling fiber will probe different spatial regions of the mode. If the transmission spectrum of a particular mode is recorded simultaneously, the coupling efficiency will be observed to modulate. The number of modulations provides a direct measurement of the number of nodes in the axial mode, e.g. a $q = 2$ mode exhibits three oscillations since is has three bands of light, c.f. Fig. 3.11.

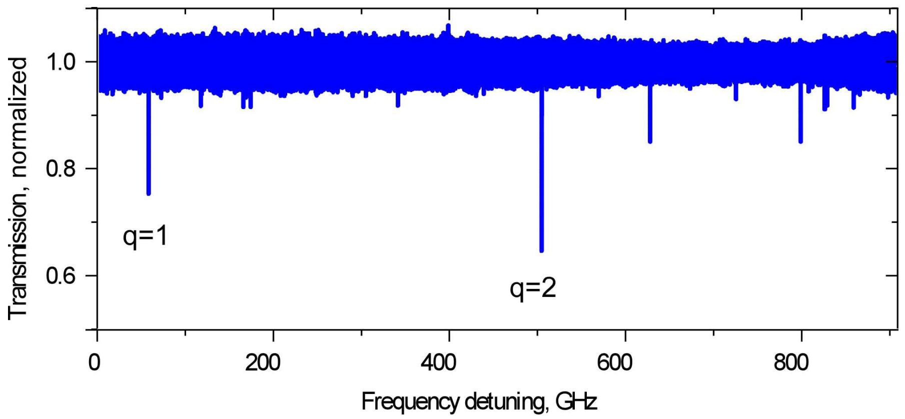

Figure 3.4: Transmission spectrum of a bottle resonator with a well-phase matched coupling fiber. By careful selection of the coupling point on the coupling fiber so that the propagation constant matches that of the resonator it is possible to excite only the desired modes (in this case $q = 1, 2$). For demonstration purposes in this particular measurement, the coupling fiber is aligned so that it couples to both modes simultaneously. Two smaller mode dips from other modes appear between 600–800 GHz because the coupling fiber is not optimally aligned to the spatial positions of the $q = 1, 2$ modes — this misalignment is purposeful because it allows both $q = 1, 2$ modes to appear on the same spectrum. Optimal spatial alignment to a single mode would reveal a cleaner spectrum. Data taken from Fig. 3.12 (b).

3.2.2 Coupling regimes

The ability to control the coupling rate between the resonator and fiber is one of the great advantages of evanescently coupled WGM resonators. Such a system enables the coupling rate to be varied over a wide range by judicious adjustment of the gap between the resonator and the coupling fiber. The equivalent behavior in a conventional high-Q Fabry- Pérot microresonator would require a mirror with a tunable reflectivity — this is something that has not been achieved to date due to the difficult technical requirements. In the following we consider a single fiber coupled to the bottle resonator, and examine the transmission characteristics.

Coupling losses in the context of a WGM resonator can be parameterized in a single variable, K, as [26]

$$K \equiv \frac{\kappa_e}{\kappa_p + \kappa_0} \,, \tag{3.1}$$

where κ_p accounts for all parasitic losses such as coupling to higher order modes (if present) of the coupling fiber, and the other terms are described in Sec. 2.2.2. The equation gives the ratio of coupling to the fundamental fiber mode and the coupling to parasitic and intrinsic loss channels. In practice, we find $\kappa_p \approx 0$, after which Eq. (3.1) then becomes $K \equiv \kappa_e/\kappa_0$ [36]. Maximizing K corresponds to maximizing the coupling rate to the desired fiber mode, and is therefore related to the mode overlap.

The coupling parameter K also affects the intracavity field. On resonance, the cavity field amplitude of a single mode is [37]

$$a = i \cdot \frac{2a_{\rm in}\sqrt{\kappa_e}}{\kappa_{\rm tot}} \,, \tag{3.2}$$

where $a_{\rm in}$ The intracavity photon number is simply the square modulus of the field amplitude,

$$n_{\rm cav} = |a|^2 = \frac{a_{\rm in}^2}{\kappa_{\rm tot}} \frac{4K}{(1+K)} = \frac{a_{\rm in}^2}{\kappa_0} \frac{4K}{(1+K)^2} \,. \tag{3.3}$$

Combining the above equation with Eq. (2.24), assuming a single mode, the resonant transmission for an empty resonator can be written in terms of K as

$$T_F = \left| \frac{a_{\rm out}}{a_{\rm in}} \right|^2 = \left| \frac{1-K}{1+K} \right|^2 \,. \tag{3.4}$$

This equation is minimized when $K = 1$, a point commonly referred to as the critical coupling point because it represents where the fiber-resonator coupling rate, κ_e, is equal to the intrinsic loss rate of the resonator, κ_0, causing zero transmission. At this point the resonator is mode matched and all the light is coupled from the fiber into the resonator.

The resonant transmission is plotted as a function of the fiber–resonator gap in Fig. 3.5 (a) for the same resonator as in Fig. 3.4. For large gaps, light in the coupling fiber does not interact with the resonator and is transmitted. At reduced distances of several hundred nanometers the transmission decreases because κ_e increases, but is still less than κ_0.[2] Fig. 3.5 (b) shows K as a function of gap size. The plot has an exponential response of the form $K_0 \exp(-x/\gamma_0)$, where γ_0 ≈130 nm is the decay length of the evanescent field away from the resonator, and x is the gap. For gaps smaller than the critical coupling gap at $\sim$ 700 nm, the coupling parameter K increases to a value of 98; the estimated value of K is a lower bound based on the assumption that parasitic losses are negligible, which is reasonable. The transmission increases to near unity as a direct consequence of large fiber–resonator coupling, $\kappa_e > \kappa_0$,

Intracavity power: The scaling of K with the fiber–resonator gap also affects the scaling of intra-cavity photon number. From Eq. 3.3 we see that the intra-cavity photon number is maximized when $K = 1$, i.e. at critical coupling. Intuitively this behavior is expected because at critical coupling ($K = 1$) all the light is coupled into the resonator. When the gap is very large (under-coupling), little light couples into the resonator, while when the gap is very small (over-coupled) the quality factor of the mode is reduced, thus reducing the build-up of power. We see evidence for this prediction in the data points in Fig. 3.5 (a, b). Around critical coupling we observe a deviation of the data from the fitted curves. These points are highlighted to indicate the presence of a thermal nonlinearity [28, 69, 70] in the resonator which affects the mode transmission spectrum (data not shown, see Sec. 5.1.5 for more discussion on thermal nonlinearities). The nonlinearity is only observed for points around critical coupling where the

---

[2] On resonance with $\omega = \omega_0$, the transmission coefficient is [37]

$$a_{\rm out} = 1 - 2\frac{\kappa_e}{\kappa_{\rm tot}} \,, \tag{3.5}$$

where $\kappa_{\rm tot} = \kappa_0 + \kappa_e$.

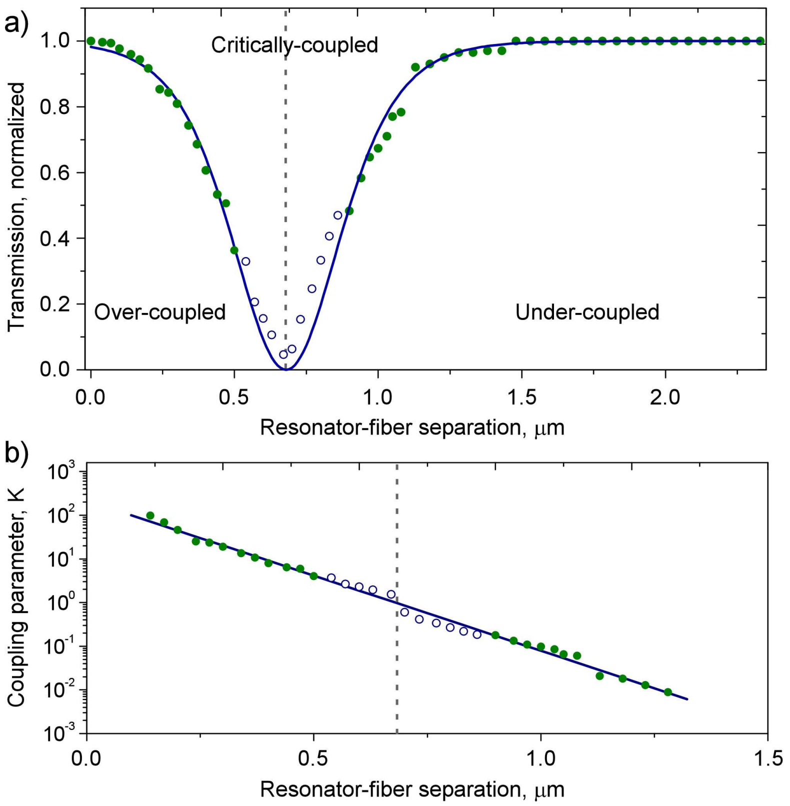

Figure 3.5: Measured and calculated coupling behavior of the resonator-fiber system as a function of physical separation. (a) Three distinct coupling regimes can be identified which correspond to different ratios of fiber coupling rate κ_e to the intrinsic coupling rate of the resonator κ_0. Under-coupling: $\kappa_\mathrm{e} < \kappa_0$, critical-coupling: $\kappa_\mathrm{e} = \kappa_0$, over-coupling: $\kappa_\mathrm{e} > \kappa_0$. The data points around critical coupling (highlighted as blue circles) deviate from the expected response (solid line) due to the onset of thermal bistability of the mode. The effect of the bistability is greatest near critical critical coupling and diminishes outward from this point. (b) Coupling at the fiber–resonator junction as quantified by the coupling parameter K (see main text). The exponential trend (note the logarithmic y-axis) indicates negligible loss at the coupling junction. Adapted from Ref. [37].

intra-cavity power is maximal; the thermal nonlinearity is proportional to the intra-cavity power. This behavior disappears in our resonators when the power in the coupling fiber is reduced below $\sim 30 - 50\ \mu$W.

Fiber controlled shifting of the cavity resonance frequency: The optical resonance frequency of a mode scales inversely with the effective refractive index of the mode. An increase in the effective refractive index of the resonator mode due to the presence of the coupling fiber causes the resonance frequency to be red shifted. As shown in Fig. 3.6, changing the fiber-resonator gaps from under-coupling to critical coupling (i.e., shaded region at zero position) we

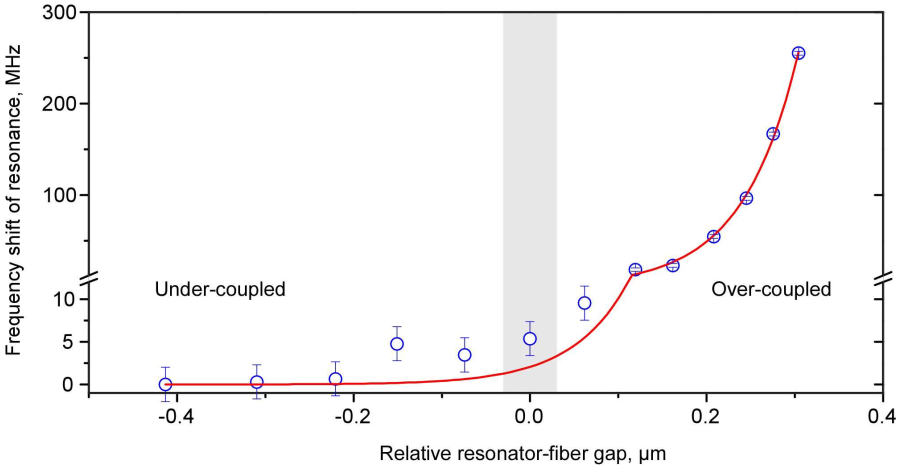

Figure 3.6: Red-shift of optical resonance frequency as a function of coupling fiber loading. The solid line is an exponential fit arising from the exponential dependence of the overlap between the resonator and coupling fiber modes. Error bars: ±2 MHz.

observe a maximum shift of 5 MHz which rapidly increases to 300 MHz when the fiber further approaches and we enter the deeply over-coupled regime. This can be an important issue to consider when interfacing a dipole emitter with the resonator.

3.3 Resonator properties

3.3.1 Quality factor and Finesse

Quality factor is a critical performance parameter of a resonator that defines its ability to store energy. In general, the Q-factor is simply given as

$$Q = 2\pi \frac{\text{Energy stored}}{\text{Power dissipated per revolution}} \equiv \frac{\tau}{T} \,, \tag{3.6}$$

where τ is the $1/e$ decay time of the resonator field and T is the time is takes for the light field to make one full revolution around the resonator. The Q-factor therefore defines the photon storage time.

Resonator loss mechanisms

Photon storage in silica resonators is limited by several factors arising from internal and external loss mechanisms: internal losses include radiative/WGM losses (see radiative losses in Fig. 1.2) and material losses such as Rayleigh scattering, water absorption and bulk material absorption, while external losses include coupling to the adjacent nanofiber [47]. It will be prudent to consider and quantify the factors limiting the quality factor so as to gain an understanding of how to maximize the Q-factor.

In an impressive experiment by Gorodetsky *et al.* [71] it was found that the Q-factor rapidly degrades within the first two to three minutes after fabrication of a microsphere. The formation of monolayers of water adsorbed on the glass surface were identified as the culprit when they found that the adsorption was found to be partially reversed by heating the resonator to 400°C for thirty seconds. As a consequence, resonator fabrication should ideally be performed in a vacuum environment, or, alternatively, the water monolayers can be removed by reheating in a vacuum environment. The absorption of water scales as

$$Q_w \approx \sqrt{\frac{2R\pi}{8\lambda n^3}}\frac{1}{\delta\alpha_w} , \tag{3.7}$$

where monolayer of water has a thickness of $\delta \approx 0.2$ nm, α_w is the absorption coefficient of water, λ is the light wavelength, n is the refractive index of silica, and R is the resonator radius. We see there is a square root dependence of Q-factor on radius.

Bulk absorption of silica, on the other hand, only depends on wavelength and refractive index and is given by the formula [72]

$$Q_{\text{bulk}} = \frac{2\pi n}{\alpha_s\lambda} , \tag{3.8}$$

where we use the phenomenological expression

$$\alpha_s \approx \left[(0.7\mu\text{m}^4) + 1.1\times10^{-3}\exp(4.6\mu\text{m}/\lambda) + 4\times10^{12}\exp(-56\mu\text{m}/\lambda)\right]\ \text{dB/km} .$$

Analyzing this equation we see that bulk absorption is minimal in the 1.5 μm wavelength band but rapidly increases for shorter wavelengths; absorption is a factor of 10 higher at $\lambda = 0.85$ μm and 15 higher at $\lambda = 0.78$ μm compared to the absorption at $\lambda = 1.5$ μm.

While our bottle resonators have nanometer smoothness as determined from atomic force microscope measurements, minute irregularities on the glass surface can give rise to significant surface scattering. Measurements by Kippenberg *et al.* [27] found a sharp decrease in Q-factor for small microtoroids due to scattering of light out of the resonator but also backscattering into the counter-propagating WGM. Intuitively this is expected because as the resonator dimensions are reduced the fraction of the evanescent field increases, thus enhancing the effect of surface irregularities. Empirical evidence suggests that the surface scattering Q_{ss} factor scales linearly with the resonator radius and is given by the formula [72]

$$Q_{\text{ss}} = \frac{K_{\text{TE(TM)}}}{1+K_{\text{TE(TM)}}}\frac{3\lambda^3 R}{8n\pi^2B^2\sigma^2} , \tag{3.9}$$

where $K_{\text{TE(TM)}}$ is a suppression coefficient defined as the ratio of total scattered power to the power scattered into the TE(TM) mode scattering angle. The parameters B and σ are the statistical correlation length and RMS surface roughness, respectively, and are given in Ref. [73].

Each of the above contributions combine together to yield a total Q-factor given as

$$Q_{\text{total}}^{-1} = \underbrace{Q_{\text{ss}}^{-1} + Q_{\text{w}}^{-1} + Q_{\text{bulk}}^{-1}}_{Q_{\text{material}}^{-1}} + Q_{\text{WGM}}^{-1} + Q_{\text{coupling}}^{-1} . \tag{3.10}$$

WGM resonator losses are dependent on the resonator diameter and markedly increase when the dimensions are scaled down to several microns. Figure 3.7 shows a comparison between theory and the current state-of-the-art in terms of Q-factor of optical WGM microresonators.

The role of resonator size on resonator Q-factor

The highest Q-factor demonstrated in any type of optical resonator was in a millimeter-scale WGM resonator made from calcium fluoride with $Q = 3 \times 10^{11}$ at a wavelength of 1.5 μm [74]. Micro-scale WGM resonators made from silica feature quality factors in the 10^8 range, which is still at least a factor of two less than the theoretical limit. The record Q-factor of for a microtoroid [27] resonator (Symbol in Fig. 3.7: ●) is $4.0{\times}10^8$ with a diameter of 29 μm at a wavelength of 1550 nm. The record Q-factor for a microdisk resonator is $5{\times}10^5$ with a diameter of 2.1 μm and a wavelength of 1.4 μm and made from AlGaAs [75]. More recently, a silicon-on-insulator microdisk resonator (▲) was demonstrated with a Q-factor of $3.0{\times}10^6$ having a diameter of 20 μm and a wavelength of 1530 nm [76]. The newly developed microbubble resonator from Sumetsky *et al.* is formed from a glass capillary and is capable of Q-factors in excess of 10^6 with a 220 μm diameter and a wavelength of 1.5 μm [77].

Early work with bottle resonators yielded moderate Q-factors of around $4{\times}10^5$ in a resonator with a 19–μm-diameter and wavelength around 850 nm [53]. Other work found a slightly higher Q-factor of $4{\times}10^5$ in a 185–μm-diameter resonator at a wavelength of 1.5μm [78]. In comparison, our recent work with these resonators has demonstrated that it is possible to achieve Q-factors as high as $3.6{\times}10^8$ in a 35–μm-diameter resonator operating at a wavelength of around 850 nm. The bottle resonators in Fig. 3.7 (★) have a Q-factor that is a factor of 2–2.5 below the maximum theoretical value over a range of diameters from 36 μm to 105 μm.

Figure 3.7 clearly defines two distinct regions that meet at a critical resonator radius of about 18 μm. Smaller resonators experience a pronounced quality roll-off of almost three orders of magnitude when the radius is reduced to half the critical radius. This roll-off in Q-factor is correlated with a significant increase in the fraction of the field that is evanescent. Consequently, surface scattering and absorption losses from water adsorbed to the surface become more important. Earlier work observed that the Q-factor scales with the square root of the resonator radius when losses due to surface scattering and surface water absorption are present, identifying these as dominant loss mechanisms [73]. Furthermore, the mode spectra reveal a sudden onset of large mode splitting for radii below the critical radius. In this case, surface scattering is strong enough to couple light into the counter-clockwise propagating mode, therefore causing the Q-factor at critical coupling to decline [79].[3] Additionally, for very small resonators, radiative losses also become increasingly important. In stark contrast is the right-hand region where the Q-factor remains essentially constant for large radii.

For a recent review comparing the Q/V ratio for WGM, photonic crystal, and Fabry-Pérot resonators, see Ref. [37].

Experimental determination of ultra high quality factor

The quality factor of a resonator can be determined by measuring the photon lifetime τ and then using the equation $Q = \omega\tau$, where $\omega = 2\pi\nu$ is the angular optical frequency. For this purpose, we use a cavity ringdown technique to determine τ: by first critically coupling the

---

[3] Critical coupling is a regime where the rate of coupling from the in-coupler to the resonator is equal to the loss rate of the resonator. When a coupling fiber is used for in-coupling, the transmission drops to zero due to power conservation.

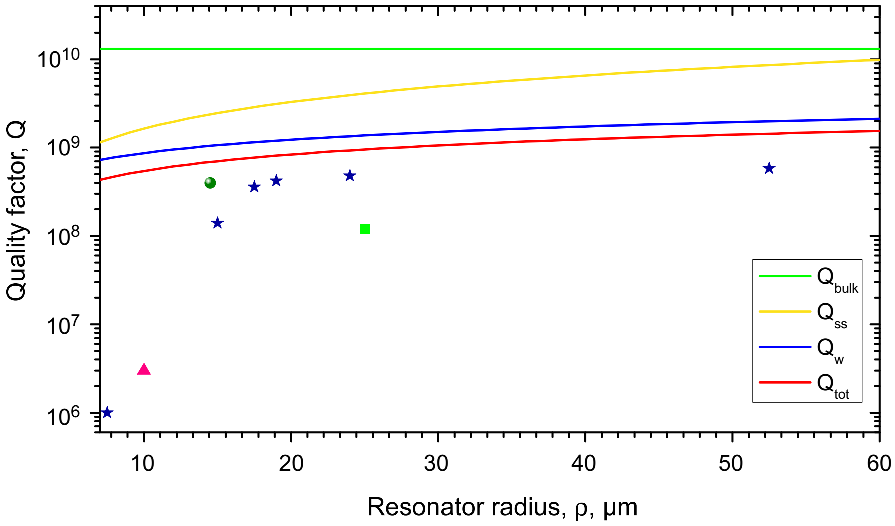

Figure 3.7: Size dependence of quality factor in WGM resonators. The theoretically calculated contributions to the total Q-factor – bulk absorption, surface scattering and water absorption – is indicated by the solid lines. The markers are data points from our own experiments and others mentioned in the literature: Bottle resonator (this work) measured at 850 nm wavelength: ★ Refs. [35, 37, 52], Toroid resonator measured at 1550 nm: ● Ref. [27], Toroid resonator measured at 850 nm: ■ Ref. [80], Microdisk resonator measured at 1550 nm: ▲ Ref. [76]. Theory plot parameters: $\lambda = 850$ nm. Refractive index estimated from the Sellmeier equation, $n = 1.45$. The solid lines show the Q-factors that would be achievable if only the mentioned loss mechanism would be present. See main text.

resonator, we resonantly excite the bottle mode under investigation with the 850 nm probe laser. After switching off the probe beam within 35 ns using an acousto-optical modulator, the exponential decay of the intra-cavity power is monitored through the output port of the coupling fiber. This measurement, shown in Fig. 3.8 (a), is taken on a 35–μm-diameter resonator with $\Delta k = 0.012\ \mu\text{m}^{-1}$ and yields a photon lifetime at critical coupling of $\tau_{\text{crit}} = 82$ ns. Critical coupling is accomplished when the incident optical power is entirely dissipated in the resonator and the transmission of the coupling fiber at resonance drops to zero. We thus obtain a lower bound for the intrinsic photon lifetime in the uncoupled resonator of $\tau_0 = 2\tau_{\text{crit}} = 164$ ns and an intrinsic Q-factor in excess of $Q_0 = 3.6 \times 10^8$.

This ultra-high intrinsic Q-factor is comparable to the values reported for other WGM microresonators of the same diameter [27]. We note that at critical coupling, required for many applications including the cavity QED experiment described in Chaps. 7 and 8, our Q-factor of $Q_{\text{crit}} = \omega\tau_{\text{crit}} = 1.8 \times 10^8$ is about one order of magnitude larger than what has previously been reported in a suitable WGM microsonator [27]. This ring-down measurement is independently confirmed by measuring the mode spectrum in a scheme wherein the frequency of the probe laser is scanned across the mode while recording the transmission. Several measurements on different resonators all show similar Q-factors. The spectrum of a second resonator with similar

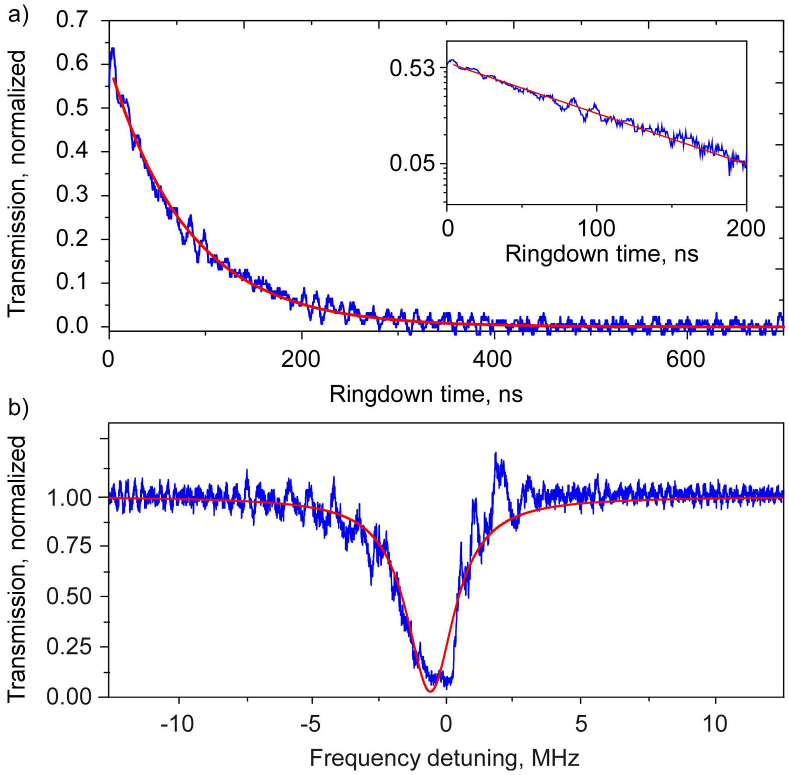

Figure 3.8: Cavity ringdown measurment on a $q = 2$ resonator mode with ultra-high Q-factor. The exponential decay with a time constant of 82 ns measured at critical coupling reveals a loaded Q-factor of 1.8×10^8 and indicates an intrinsic Q-factor of 3.6×10^8. The inset shows a plot with the same data on a logarithmic scale. Measurements on several resonators all show similar results and are independent of the choice of the cavity ringdown technique or the resonator spectroscopy technique. (b) Resonator spectroscopy: For example, the spectrum of a separate bottle microresonator obtained at critical coupling shows a FWHM linewidth of 2.2 MHz (solid line is a Lorentzian fit), corresponding to an intrinsic quality factor in excess of $Q_0 = 3.3 \times 10^8$. The measured line is slightly asymmetric and broadened probably due to a combination of both thermal effects and interference between the cavity light and the quickly scanned laser frequency [28, 81]. This interference might also explain the ringing on the positive frequency side of the resonance. Refs. [25, 35, 37, 52].

dimensions yields a quality factor of $Q_0 = 3.3 \times 10^8$ and is shown in Fig. 3.8 (b).

3.3.2 The role of mode-splitting on resonator Q-factor

Experiments normally consider the situation where only one of the two travelling resonator modes — clockwise or counter-clockwise — is pumped by laser light. However, light can unintentionally be coupled to the unpumped mode when there is surface roughness, which coherently scatters light from the pumped mode to the other mode. The coupling strength between the modes is dependent on the amount of surface roughness and is quantified by the parameter h. When the inter-modal coupling strength $h/2\pi$ exceeds the mode linewidth $\tau_0^{-1}/2\pi$, where τ_0 is the lifetime of a photon in the resonator, the two normally degenerate modes become visibly non-degenerate by an amount $2h/2\pi$, as shown in the under-coupled regime in Fig. 3.9 (a). As a comparison, a mode where $h = 0$ MHz is shown in Fig. 3.9 (b) where both resonator modes are degenerate.

As can be seen from the figure, the loaded Q-factor can be substantially different to the intrinsic Q-factor, dependent on the value of h. For a given input power, the intra-cavity power of the modes in Fig. 3.9 (a) will be less than in Fig. 3.9 (b) since intra-cavity power is proportional to the loaded Q-factor. Therefore, the most relevant quantity to consider is the loaded Q-factor because it includes the effect of light scattering between the clockwise and counter-clockwise propagating modes. More quantitatively, this is expressed through the mode coupling parameter Γ_{res} defined as

$$\Gamma_{\text{res}} \equiv 2h\tau_0 \ , \tag{3.11}$$

where $\tau_0^{-1}/2\pi$ is equal to the intrinsic cavity linewidth and $2h/2\pi$ is the frequency splitting of the mode. This parameter can reach very high values of $\Gamma_{\text{res}} = 31$ [27] in microtoroids and other high-Q WGM resonators, but is typically very small ($\Gamma_{\text{res}} < 1$) in the bottle resonators used in this work.

The usual definition of Q-factor can be re-arranged to give a relation between intrinsic quality factor, Q_0, critical coupling quality factor, Q_{crit}, and mode splitting, giving [27]

$$Q_0 = \omega\tau_0 = \omega\frac{2}{\tau_{\text{crit}}}\left(\frac{1}{\tau_{\text{crit}}^2} - h^2\right)^{-1} \ , \tag{3.12}$$

where $\tau_{\text{crit}}^{-1}/2\pi$ is equal to the mode linewidth measured at critical coupling. An examination of Eq. (3.12) reveals a slightly surprising result where for a given τ_{crit} the intrinsic Q-factor actually increases with h.

This point can be better appreciated by considering the example of the mode in Fig. 3.8 (a). Here, the cavity ringdown measurement was performed a few hours after manufacture and yielded an ultra-high Q. After storing the resonator in ambient conditions for three days the measurement was repeated and, as expected, τ_{crit} showed a marked degradation from 82 ns to 36 ns, see Fig. 3.10 (a). The corresponding Q-factor is then $Q_{\text{crit}} = 0.8 \times 10^8$. The cause of the degradation as seen in the mode spectrum in Fig. 3.10 (b) is clearly due to surface scattering losses: during storage, dust apparently collected on the resonator surface causing light to be coherently scattered between the two counter-propagating resonator modes. The mode coupling rate is 3.1 MHz and breaks the degeneracy of the resonator modes. Nevertheless, the intrinsic

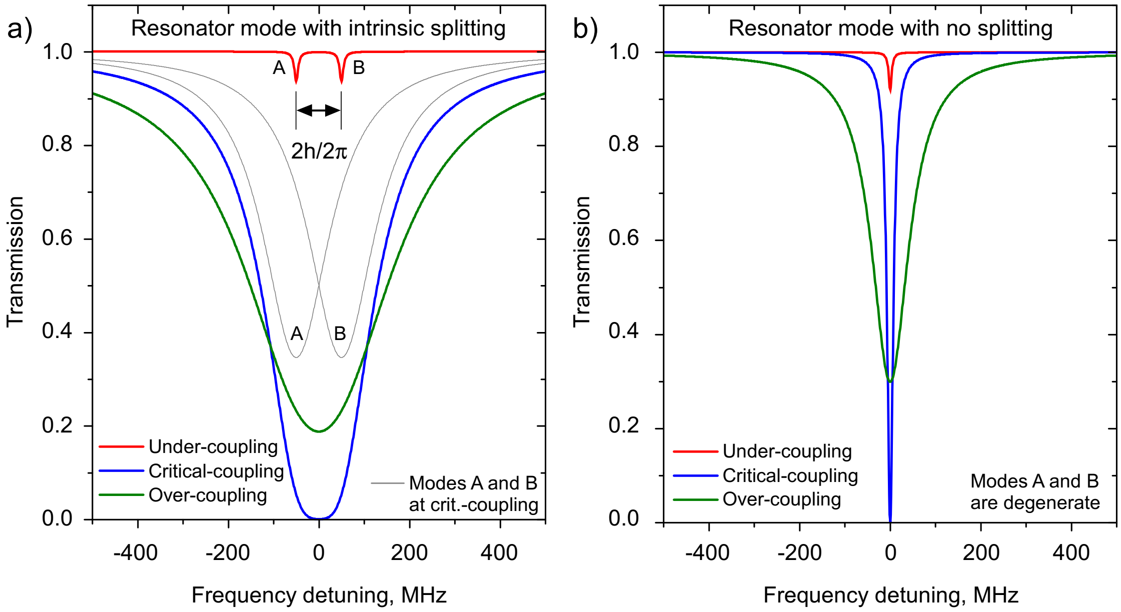

Figure 3.9: Role of mode splitting in resonator coupling. The spectra of two resonator modes with the same intrinsic quality factor of 4×10^7 are schematically plotted in three coupling regimes: under-coupling, critical-coupling, and over-coupling. (a) Shown is a resonator mode with intrinsic mode splitting due to, e.g., surface scattering which couples clockwise and counter-clockwise propagating modes, which are labeled A and B. The mode splitting can be seen in the under-coupled regime and measures $(\omega_B - \omega_A)/2\pi = 2h/2\pi = 100$ MHz and the mode splitting parameter is $\Gamma_{\text{res}} = 10$, defined in Eq. (3.11), which are typical values found in the literature. At critical-coupling, defined as when all light is coupled into the resonator and the transmission is zero in the coupling fiber, both modes partially overlap and the loaded quality factor reduces by about a factor of 20 to $\sim 4 \times 10^6$. The non-degeneracy of the modes A and B at critical coupling is visible when plotted they are individually, as shown by the grey curves. In the over-coupled regime the mode continues to rapidly broaden. (b) In contrast to (a), a mode with no intrinsic mode splitting can have a loaded quality factor of 2×10^7 at critical coupling, and is a factor of 10 greater than for the other mode. Similar to the mode in (a), the mode here starts to rapidly broaden in the over-coupled regime.

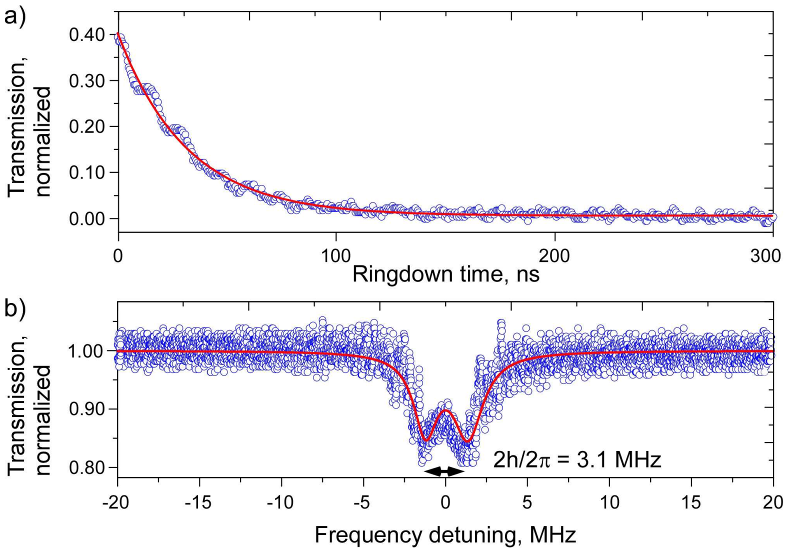

Figure 3.10: Cavity ringdown measurement and mode spectrum for a $q = 2$ resonator mode with ultra-high quality factor. The mode is the same as in Fig. 3.8 (a) but measured 3 days after manufacture whereas the data in Fig. 3.8 (a) was measured a few hours after manufacture. (a) The time constant of the exponential decay is $\tau_{\text{crit}} = 36$ ns corresponding to a critically loaded Q-factor of 0.8×10^8. (b) The under-coupled mode shows mode splitting of 3.1 MHz while the linewidth of the individual modes have a Q-factor of $\sim 2.5 \times 10^8$. Data acquired from the 38–μm-diameter resonator presented in Refs. [25, 35, 37].

Q-factor remains unchanged from Fig. 3.8 (a) at about 3.6×10^8. Therefore, while it is possible to have an ultra-high intrinsic Q-factor, mode coupling can strongly dictate the loaded Q-factor.

This observation is important to consider when selecting a resonator mode for the work described in Chaps. 5–8. Most modes with ultra-high Q-factor in our bottle resonators show negligible mode scattering due to the very clean fabrication process. It is also essential to keep a newly fabricated resonator in a clean environment before mounting and sealing it in the vacuum chamber, and this should ideally take no more than two hours between fabrication and the beginning of vacuum chamber evacuation.

3.3.3 Imaging the axial mode structure

A direct comparison between the theoretical predictions regarding the axial mode structure of the bottle resonator presented in Chap. 1 and experimental measurements is critical to verifying our understanding of the resonator. The axial mode has an intensity profile described by a Hermite polynomial, c.f. Eq. (1.31). Direct visual observation of the mode structure in a silica glass resonator is difficult without the aid of, for example, a fluorescent coating on the glass surface or doping the glass bulk with fluorescing atoms. Earlier work in our group succeeded in observing part of the mode structure in a silica glass resonator having low quality factor via the tangentially scattered light from the edge of the resonator [53].

Further developments have since improved this measurement by doping the glass with Erbium ions, revealing the full mode structure via the fluorescence emission rather than the directional scattering. In this scheme, Erbium ions undergo two-photon absorption of the excitation laser light propagating in the resonator mode and emit single green photons [46, 47, 82] in a random direction, see Fig. 3.11. Therefore it is possible to image the full spatial profile of the mode in the resonator rather than part of the mode at the resonator edge [83]. The technique makes it a simple task to observe different axial modes ranging from the lowest mode $q = 0$ to $q = 11$ as shown in Fig. 3.11 (a), and can potentially image modes up $q \sim 100$ if there is sufficient imaging resolution. Different modes were excited by slowly tuning the frequency of a distributed feedback diode laser (850nm DFB, Toptica Photonics AG) while maintaining an air gap between the coupling fiber and the resonator. Each image is produced from a stack of around a dozen images taken at varying object planes and then reconstituted using a software program (CombineZM), well known within the photography community. The software helps overcome the limited depth of focus of the imaging microscope ($\times$ 20 objective Mitutoyo Inc., 1.6 μm depth of focus, Pixelink color CCD camera) and effectively increase it to around 20 μm, thus generating sharp images of the modes.

As predicted from the theory in Sec. 1.2.2, the axial modes have a profile given by a Hermite-polynomial with the highest intensity regions located at the outermost bands while the middle section shows narrow bands with less intensity. The locations of the field maxima also agree very well with the theory predictions as shown in Refs. [37, 52].

3.3.4 Full tunability of WGMs

A key requirement for cavity QED applications involving the interfacing of single emitters with a resonator mode is the ability to tune the resonance frequency to any desired frequency. This task necessitates a mechanism to tune the resonance frequency of the resonator by at least an amount equal to the free spectral range (FSR). The FSR of a resonator, $\Delta\nu$, is inversely proportional to the resonator (optical path) length, L, and is given by

$$\Delta\nu = \frac{c}{L}\,, \tag{3.13}$$

where c is the speed of light. For a Fabry-Pérot resonator L is the optical path length between the mirrors while for a WGM resonator $L \approx 2\pi n R_0$, where n is the refractive index of the resonator and R_0 is the resonator diameter. In the case of small WGM resonators the azimuthal FSR is typically very large and can reach a few tera-hertz. For example, a typical resonator diameter of 35 μm considered in this work gives an azimuthal FSR of 2 THz (~2 nm), i.e., about one percent of the optical frequency. While tuning a Fabry-Pérot resonator over this range involves the straightforward task of changing the mirror separation by one wavelength, similar tuning behavior has, until recently, been impossible with WGM microresonators [25]. For a recent review of tunable WGM resonators see Ref. [37].

Frequency tuning via resonator elongation is much more favorable than, e.g., temperature tuning via the temperature-dependent refractive index of the resonator material and temperature-dependent size change of the resonator. Firstly, resonator elongation can be performed with substantially greater bandwidth of a few tens of kilo-hertz, compared to several hertz for tempera-

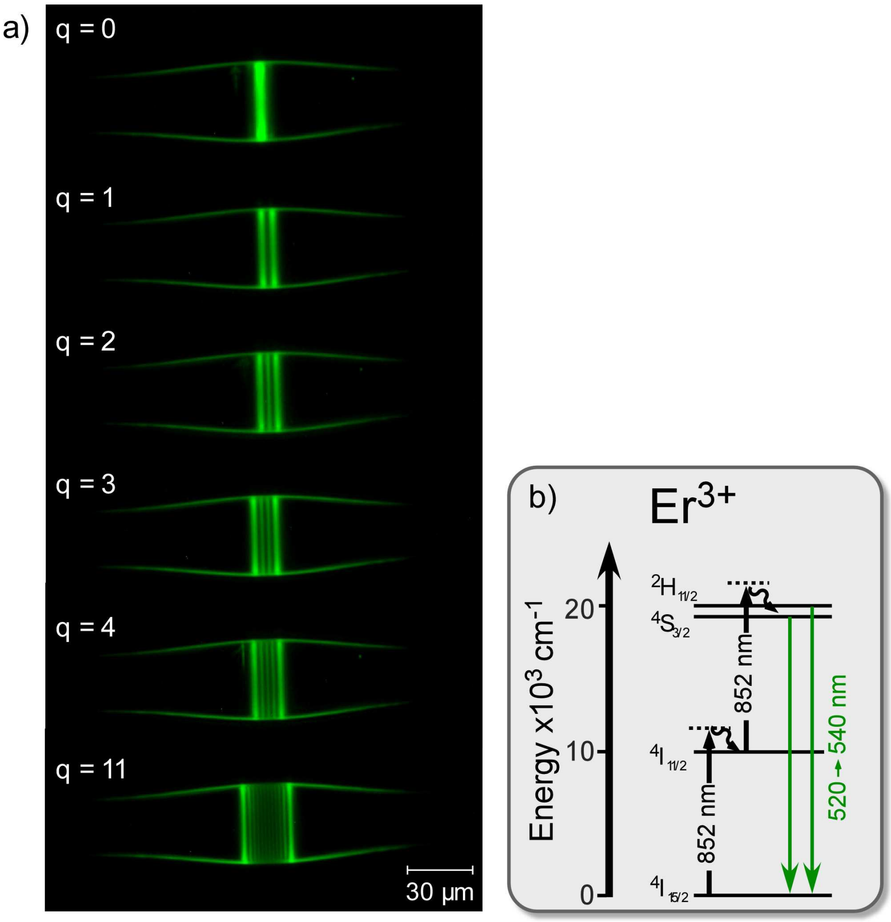
a)
q = 0
q = 1
q = 2
q = 3
q = 4
q = 11
30 μm
b)
Er3+
Energy x10³ cm⁻¹
20
10
0
2H11/2
4S3/2
4I11/2
4I15/2
852 nm
852 nm
520 → 540 nm

Figure 3.11: Fluorescence emission from an Er^{3+}–doped bottle microresonator. (a) Optical microscope images of the $q = 1 - 4$ and $q = 11$ bottle modes in a 36–μm-diameter microresonator with a curvature $\Delta k = 0.015\ \mu\text{m}^{-1}$. The Q-factor at the excitation wavelength is 10^7. (b) The bottle mode is off-resonantly excited with several tens of microwatts at a wavelength of 852 nm and visualized via the two-photon, upconverted green fluorescence of dopant Erbium ions. The upconversion mechanism is verified by the quadratic dependence of fluorescence emission with pump power (data not shown). Adapted from Refs. [25, 36, 37, 52].

ture tuning [84]. Secondly, temperature tuning of a resonator mode over a full azimuthal FSR of 2 THz requires a temperature change of $\sim 400°$C, which is technically difficult to achieve.[4]

In Ref. [25] it was shown that a bottle resonator can circumvent this problem: the axial FSR only depends on the curvature of the resonator profile (Eq. (1.33)) and can thus be engineered to be significantly smaller than its azimuthal FSR, which is 2 THz in the example above. So rather than tune the resonator over a full azimuthal FSR, it is sufficient to tune the bottle microresonator over one axial FSR. In addition, the axial mode closest to the desired absolute operating frequency must be chosen, just as in the case of the Fabry-Pérot resonator. (We note that the $q = 0$ mode is typically used in these resonators).

The resonance frequencies $\nu_{m,q}$ and $\nu_{m+1,q}$ of modes differing by one in the azimuthal quantum number m are spaced by $\Delta\nu_m = 1.92$ THz in a 35–μm-diameter resonator. This frequency interval can thus be bridged by four consecutive axial modes, making any arbitrary frequency accessible by using the set of modes $\{\nu_{m,1}, \nu_{m,2}, \nu_{m,3}, \nu_{m,4}\}$ with m properly chosen, c.f. Fig. 1.5. The tuning scheme is implemented by elastically deforming the resonator through mechanical strain, thereby changing its diameter by ΔR and the refractive index of the medium by Δn. The fractional change in frequency is given as

$$\frac{\Delta\nu_0}{\nu_0} \approx -\frac{\Delta R}{R_0} - \frac{\Delta n}{n} \,. \tag{3.14}$$

Piezo-electric shear actuators located on both ends of the resonator fiber were used to elastically elongate the resonator. This elongation, ΔL, is proportional to the reduction in the resonator radius ($\Delta R/R_0 = \sigma_{\text{glass}}\Delta L/L$) with the proportionality constant $\sigma_{\text{glass}} = 0.17$, which is the Poisson coefficient for silica glass [37]. Resonator elongation similarly causes a proportional decrease of the refractive index via the electro-optic effect; the proportionality constant is only 0.04 for TM polarization and 0.14 for TE polarization [37, 41].

To verify our tuning scheme, we study the same ultra-high Q resonator presented in Fig. 3.8 (a), which has a FSR of 2 THz and an axial mode spacing of 425 GHz [25]. In the setup both fiber ends supporting the resonator are attached to piezoelectric bending actuators offering an elongation of up to 160 μm. The resonance frequency can thus be shifted by applying a voltage to the actuator which mechanically strains the resonator. The tuning of two modes with axial quantum numbers $q = 1$ and $q = 2$ over 700 GHz is presented in Fig. 3.12 and represents a tuning range of 1.7 times the axial mode spacing, or equivalently, 700,000 linewidths. In terms of tuning range relative to FSR, this tuning scheme exceeds all others reported for monolithic microresonators by at least a factor of two [37] and is limited here by the travel range of the bending actuators. The mechanical strain applied to the fiber never exceeds about 0.7 GPa, which is 14% of the tensile strength of silica fiber [85]. This corresponds to a frequency shift of 0.2% of the

---

[4] The temperature dependent frequency change, $\delta\nu$, due to a temperature change, δT is given by [47]

$$\frac{1}{\nu}\frac{\delta\nu}{\delta T} = \left(\frac{1}{n}\frac{dn}{dT} + \frac{1}{R}\frac{dR}{dT}\right) = 1.34 \times 10^{-5}/^{\circ}C \,,$$

where the first term in the brackets is the temperature dependent refractive index change (silica: $\sim 1.28 \times 10^{-5}$/°C) and the second term is temperature dependent size change of the resonator radius (silica: $\sim 5.5 \times 10^{-7}$/°C), where n is taken as 1.45 and R is taken as 36 μm. .

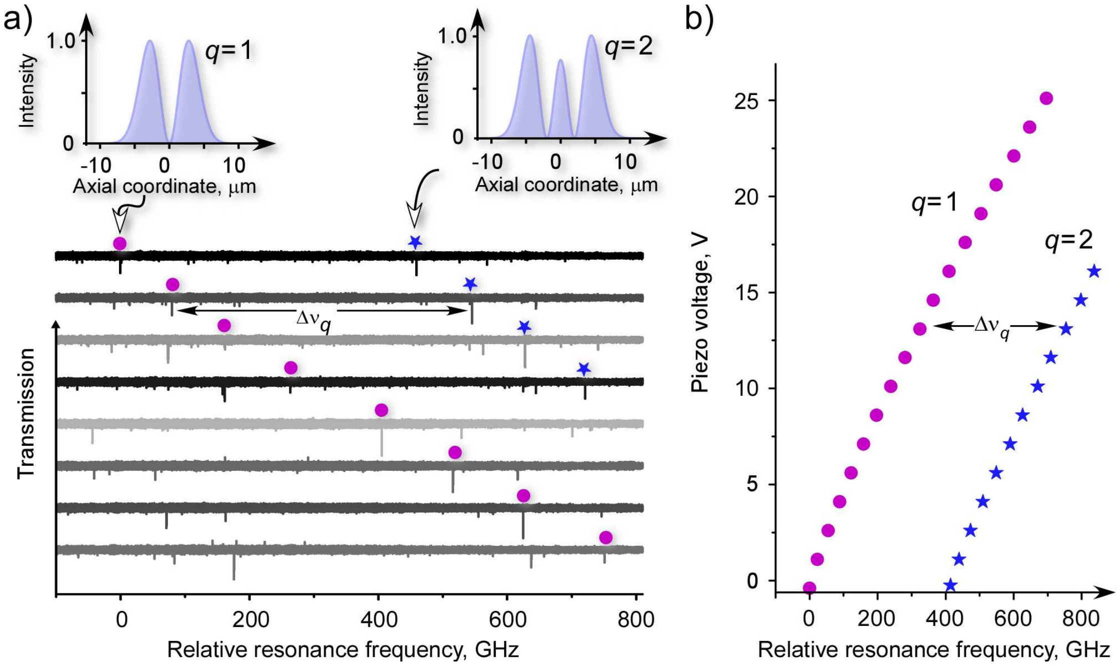

Figure 3.12: Tuning the bottle microresonator. (a) Mechanically straining the resonator shifts the resonator mode spectrum to higher frequencies. Consecutive spectra (from top to bottom) are recorded with increasing strain, realized by linearly incrementing the voltage applied to the bending piezo which pulls on the end of the resonator fiber. The calculated axial intensity distributions are for modes with axial quantum numbers $q = 1, 2$ and azimuthal quantum number $m = 180$. The calculated resonance wavelengths are 852.0 nm and 850.8 nm, respectively. (b) Two TM-polarized bottle modes $q = 1$ and $q = 2$, shown in (a), can be strain tuned over a range of 700 GHz, which exceeds the free spectral range (FSR) of $\Delta\nu_q = \nu_{m,q+1} - \nu_{m,q} \approx c\Delta k/2\pi n = 397$ GHz between bottle modes of adjacent q quantum numbers, where c/n is the speed of light in the resonator material of refractive index n. The observed axial FSR of $\Delta\nu_q = 425$ GHz is in good agreement with the theoretical value. The data was acquired from the same resonator used in Fig. 3.8 (a) [25, 35, 37, 52].

optical frequency. Repeated tuning of the resonator over this range is therefore possible without damage to the glass.

Recently, Sumetsky *et al.* demonstrated strain tuning of a WGM over 2.2 azimuthal FSRs (0.35% of the optical frequency) in a novel microbubble resonator with a diameter of 220 μm [77]. Currently, UHQ modes have not yet been observed and the small mode volume discussed in the present work has not yet been realized with this resonator.

Apart from optimizing the resonator radius discussed here and the spectral mode spacing discussed in Sec. 1.2.2, it is also possible to accurately control the tuning response of the resonator. This issue is particularly relevant when designing the resonator fiber to operate with particular piezo actuators having a fixed travel range. The tunability of resonator modes is governed not only by the resonator itself, but also by the supporting fiber. For a given fiber elongation, δ_{tot}, the applied strain, P, and thus the tuning range, is inversely proportional to the length of the support fiber, L, and proportional to the support fiber cross-section, A. (Ideally, the strain on the support fiber should be small compared to the strain on the resonator, which is possible by having a very large diameter support fiber). We therefore have $P = \delta_{tot} EA/L$ where E is the Young's modulus of the fiber material. Using a suitable design for the resonator fiber, we are able to exploit this extra degree of customizability using our fiber pulling rig to manufacture very short, non-exponential fiber profiles [53]. Short fibers have the advantage of increasing the sensitivity of the resonator frequency to fiber elongation, which is particularly important for the cavity QED experiments described in Chap. 7 due to the limited travel range of the employed piezo actuators. On the other hand, long fibers reduce the sensitivity of the resonator frequency to fiber elongation, which improves the ability of the frequency stabilization scheme to reduce frequency fluctuations.

3.4 Bottle resonators designed for cavity QED

For a given in-coupled power, the ratio of Q/V is proportional to the intra-cavity intensity and thus describes the enhancement of light–matter interactions. For the investigation of cavity QED systems, the choice of Q and V is therefore of the utmost importance (see Refs. [10, 51]). As discussed in Sec. 2.1.3 (Eq. (2.8)) the atom–cavity coupling strength depends on the mode volume according to $g \propto V^{-1/2}$, indicating the cavity should be as small as possible. The observation of strong coupling requires g to dominate the atomic dipole decay rate, $\gamma_\perp$, and the cavity field decay rate, κ, with $Q = \omega_l/2\kappa$, giving the condition $g \gg (\gamma_\perp, \kappa)$. On the other hand, the coupling strength can be related to the saturation photon number, n_0, and the critical atom number, N_0. The saturation photon number is the number of photons required to saturate a coupled atom, scaling as $n_0 = \gamma_\perp^2/2g^2$, while N_0, the number of atoms required to have a noticeable influence on the cavity transmission, scales as $N_0 = 2\gamma_\perp\kappa/g^2$. Examining the parameter n_0 reveals that $n_0 \propto V$, and similarly for N_0 we find that $N_0 \propto V/Q$. Therefore, the resonator geometry and Q-factor govern the scaling of important parameters of the atom–cavity system.

3.4.1 Atomic Rubidium as a quantum emitter

This thesis describes the design of a cavity QED experiment where we chose rubidium as a quantum emitter. Rubidium is used here because commercial lasers, optical components, and detectors with a high detection efficiency of up to 60% are readily available at the transition wavelength. A second reason is that the coupling strength between single Rb atom coupling in the evanescent field of the bottle resonator is sufficiently large to put the coupled system well into the strong coupling regime.

Rubidium is an alkali metal with one optically active valance electron in the outer shell and another 36 electrons in the inner shells. Only the D_2 line ($^5S_{1/2} \rightarrow ^5P_{3/2}$ transition in Fig. 4.14) can be used for cooling and trapping because it has a closed transition, unlike the D_1 line which has no closed transition. However, either line can be used for quantum optics experiments. In this experiment we use the D_2 line of the isotope ^{85}Rb, which has a transition wavelength of 780.2 nm, a transverse decay rate of $\gamma_\perp = 2\pi \times 3.03$ MHz, and a ground state hyperfine doublet due to LS coupling with a splitting of $2\pi \times 3.03$ GHz. The isotope ^{87}Rb has a similar doublet but with a splitting of $2\pi \times 6.8$ GHz.

3.4.2 Resonator size and cavity QED parameters

In order to quantify the performance of our bottle microresonators, we characterized several resonators with radii ranging from 7–53 μm in terms of Q-factor and the predicted coupling strength for the D_2 transition of a ^{85}Rb atom.

For the 18–μm-radius resonator considered in Sec. 3.3.1, the inferred coupling strength in Fig. 3.13 (a) is found to be high enough to place the atom–cavity system deep into the strong coupling regime. Smaller resonators yield higher g due to the tighter confinement of the resonator mode, but at the expense of lower Q-factor. Plotting the critical atom number for different radii in Fig. 3.13 (b) shows a minimum of 2.4×10^{-2} for a radius of 19 μm, corresponding to the radius where the ratio Q/V is maximized. The strong quality factor roll-off mentioned in Sec. 3.3.1 dominates the critical atom number for smaller radii which rapidly increases to large values for a radius of 7 μm. Larger resonators only show a weak increase in critical atom number which remains a factor of 5 below unity even for a 53–μm-radius resonator. The saturation photon number, shown in Fig. 3.13 (c), can be as low as 5×10^{-4} for a 7 μm radius resonator with a corresponding mode volume of 330 μm^{-3}, a coupling strength of 94 MHz, and a moderately high Q-factor of 0.5 million. For the 18 μm radius resonator the saturation photon number is still 3×10^{-3} and even for the largest resonator the saturation photon number is a factor of 50 below unity.

A more relevant quantity to optimize in nonlinear optics applications is Q^2/V — the use of Q^2 instead of Q accounts for processes such as frequency mixing and other nonlinear process where two wavelengths are used (e.g. signal and idler) and each has a particular Q-factor. Taking the data in Fig. 3.13 (a), we find this ratio is as high as 2.1×10^{13} $(\lambda/n)^{-3}$ for a radius of about 19 μm. This value is among the highest realized for optical microresonators [22, 27, 40].

3.4.3 Axial and radial resonator modes, polarization and coupling strength

In order to understand the effects of mode geometry on the coupling strength g, we perform calculations varying the radial and axial mode numbers as well as the polarization. In the calculations we fix the resonator to a diameter of 18 μm and a curvature of ($k = 0.014$ μm^{-1}), similar to that used in Chaps. 7 and 8.

The coupling of a field and a two-level (rubidium) atom is given in the dipole approximation by the term $\hat{d}\hat{E}$, where $\hat{E}$ is the electric field operator, and $\hat{d}$ is the atomic dipole operator (see Eq. (2.5)). Using the radial field equations for the bottle resonator and the dipole matrix elements of $\hat{d}$, this coupling can be calculated as a function of radial position, as shown in Fig. 3.14. As expected, the maximum coupling strength is inside the resonator and close to the glass/vacuum interface. For the TE-polarized mode this is 112 MHz at a position 400 nm inside the resonator. However, the coupling remains as high as 43 MHz at the surface, decaying over a length of around 118 nm. The TM-polarized mode on the other hand, has a maximum of 110 MHz inside

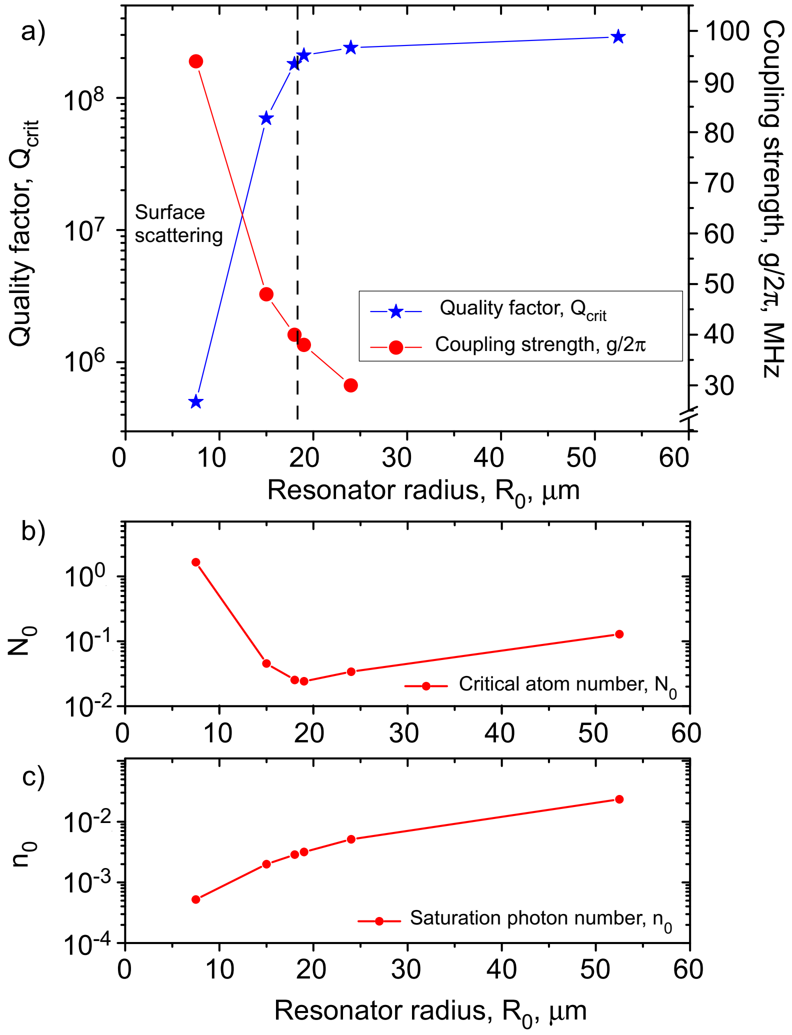

Figure 3.13: (a) Measured quality factor at critical coupling as a function of resonator radius (same data as in Fig. 3.7). The right-hand y-axis indicates the expected coupling strength for the D_2-transition of a ^{85}Rb atom with a $q = 1$ resonator mode at the resonator surface. Resonators with radii below a critical radius of around 18 μm experience significant losses, believed to be primarily due to scattering from irregularities on the glass surface. (b) Critical atom number calculated from the data in (a). (c) Saturation photon number calculated from the data in (a). See main text for details. Reproduced from Ref. [35], and adapted from data presented in Ref. [52].

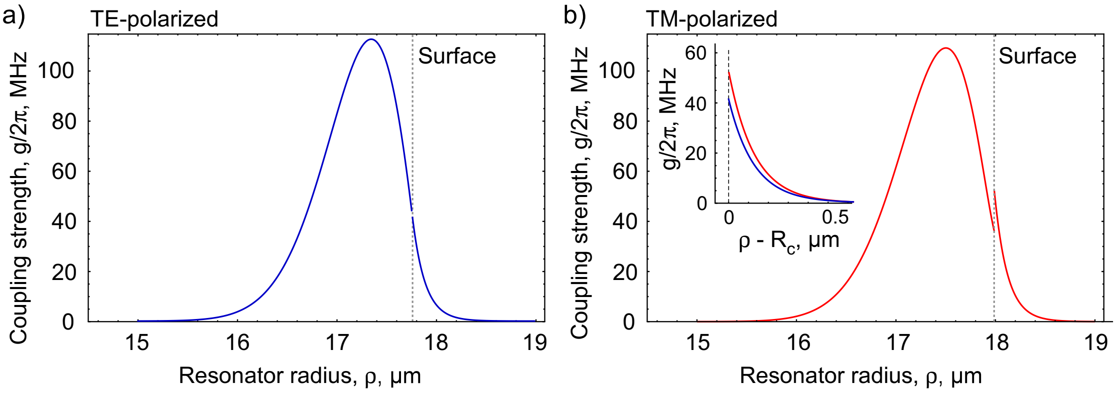

Figure 3.14: Coupling strength as a function of radial position. (a) TE-polarized fundamental radial mode with the electric field parallel to the surface. The coupling strength reaches a maximum of 112 MHz within the resonator and is 43 MHz at the surface (dashed line), decaying over a characteristic length of $\sim \lambda/(2\pi\sqrt{n^2-1}) = 118$ nm. Resonator radius at $z = 0$: $R_0 = 17.8$ μm. (b) TM-polarized fundamental mode with the electric field perpendicular to the surface. Again the maximum field reaches a maximum of 110 MHz with 52 MHz at the surface. Inset: comparison of the coupling strength for TE- and TM-polarized evanescent fields. Resonator radius at $z = 0$: $R_0 = 18.0$ μm. Parameters: Resonator curvature: $k = 0.014$ μm^{-1}, angular quantum number: $m = 200$, axial quantum number: $q = 1$, refractive index: $n = 1.467$. Atomic transition: ^{85}Rb, $5^2S_{1/2} \to 5^2P_{3/2}$, π-polarized transition ($F = 3, m_F = 0 \to F' = 4, m_F = 0$).

the resonator, but there is sharp discontinuity at the surface due to the boundary conditions for the magnetic field component of the field, giving a coupling strength of 52 MHz. This represents 47% of the maximum coupling strength.

The axial field distribution of the resonator is described by a Hermite polynomial, as shown in the inset to Fig. 3.15 where the normalized intensity $Z^2_{m,q}(z)/\max\left[Z^2_{m,q}(z)\right]$, defined in Eq. (1.31), is plotted. The plot has a maximum at the two caustics ($z = \pm 29$ μm), which is the position where we consider the atom to couple to the mode since the field is greatly enhanced at this point. Varying the axial quantum number q in the range 0–60 in the main figure, the coupling strength correspondingly changes from 49 MHz to 29 MHz for the fundamental (first) radial mode. Even with a $q = 60$ mode, with its large spatial extension along the resonator axis, the coupling strength at the caustics remains large enough to put the coupled atom–resonator system well into the strong coupling regime.

For ultra-high Q WGM resonators in general, the experimental identification of the radial mode order is difficult because the spatial mode structure is not visible in optical images and all modes appear spectrally are similar. As shown in Fig. 3.15, there is only around a 5% reduction in coupling strength when changing the radial mode order from one to two. This fact, taken together with the weak dependence of coupling strength on q, demonstrates the bottle resonator as a robust system capable of very good operation over a wide range of parameters.

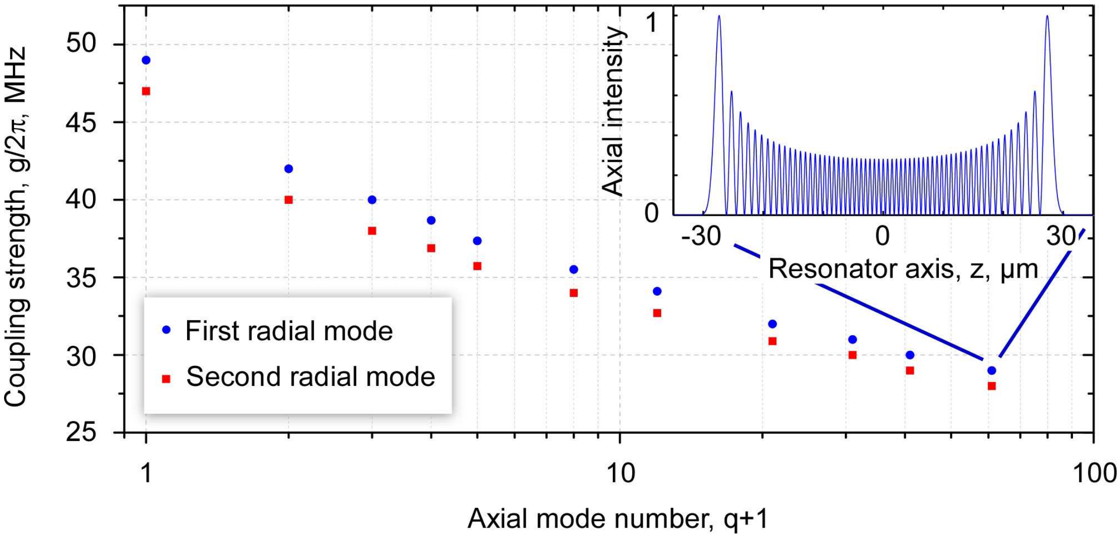

Figure 3.15: Coupling strength as a function of axial and radial mode numbers. The coupling strength between a Rb atom and TE-polarized light at the resonator caustic is seen to approximately follow a logarithmic scaling with axial mode number q over a wide range of values. Incrementing the radial quantum number from one (fundamental) to two reduces the coupling strength by $\sim$ 5%. Inset: Normalized axial intensity distribution for a mode with an axial quantum number $q = 60$ and the first radial quantum number. The simulation parameters are identical to Fig. 3.14. Caustic radius for the first radial mode and $q = 0$ axial mode $R_c = 17.7$ μm, caustic radius for the second radial mode and $q = 0$ axial mode $R_c = 18.5$ μm.

CHAPTER 4

Characterization of the Atom Delivery System

The central goal of the atom delivery system is to transport cold ^{85}Rb atoms to the location of the resonator, enabling studies of the atom-resonator interactions. Trapping and cooling of neutral atoms greatly slows the atomic motion compared to thermal atomic velocities and is essential to studies requiring atoms to have long interaction times in an experimental region, i.e., the resonator's evanescent field. This work uses a magneto-optical trap (MOT) for trapping and cooling as well as an atomic fountain for the subsequent transport of the cold atoms to the experimental region. Atomic fountains are finding increasing application outside the traditional domain of atomic fountain clocks and into new areas such as in the cavity QED experiments of a number of international groups [13, 86]. This thesis adds to this existing body of work: the use of an atomic fountain for delivering cold atoms to the location of a bottle resonator is now a well established technique within our laboratory. The experimental setup, performance, as well as the principles involved in an atomic fountain and MOT, are described in following sections.

Much of the setup was initially designed and constructed in the Johannes Gutenberg Universität-Mainz in the context of this thesis. There, a majority of the performance and optimization measurements were conducted, which, in particular, includes several of the measurements in the present chapter and Chap. 5. Since moving the experiment to the Technische Universität Wien, there have been several improvements concerning the bottle resonator and fiber distance stabilization, fountain launch control, atom detection, real-time control, experimental control protocols, and the laser systems. The current setup and characterisation will be described here. Details of the early stages of the setup can be found in Refs. [52, 87, 88].

4.1 Atomic Fountain Apparatus

The atomic fountain apparatus delivers cold atoms to the location of the resonator where they can interact with the evanescent field. This task facilitates the strong coupling of atoms with the resonator mode if the following condition is satisfied:

$$g \gg \left(\kappa, \gamma, T_{\text{int}}^{-1}\right) \ . \tag{4.1}$$

As discussed in Chap. 2, the atom-resonator coupling strength g must be greater than the dissipation rates of the system, but also the inverse of the interaction time T_{int}^{-1}, where the atom is sufficiently close to the resonator, must be sufficiently long. It is therefore obvious that the atomic source should, firstly, not degrade the resonator dissipation rate κ and secondly, it should enable the longest possible interaction time, short of actually trapping the atoms.

Atom trapping in Fabry-Pérot resonators is now a well-understood process and has been achieved in numerous experiments [32, 89, 90]. The long interaction time between the trapped atom and the light in the resonator allows one to perform complex operations such as feedback cooling and quantum control. This level of control is not yet possible with WGM resonators principally because the resonator is a partially closed structure, unlike a Fabry-Pérot which has a mode volume that can be more easily accessed by free-space beams, and as such, requires the development of new experimental techniques. Therefore, current experiments must be performed during the brief and random atom transits through the evanescent field.

The interaction time should ideally be limited by the thermal velocity of the atom and as few atoms as possible should be adsorbed on the resonator surface over time in order to preserve the resonator quality factor. Two options exist: a single vacuum chamber setup in which atoms are dropped onto the resonator from a background-gas-loaded 3D-MOT, or a differentially pumped two-chamber setup with the resonator chamber containing a low background pressure and the second chamber containing a high rubidium background pressure. Concerning adsorption of rubidium on the resonator surface, the latter design is preferable. In this case, several schemes for delivering atoms from the second chamber to the resonator exist: loading a 3D-MOT in the resonator chamber from a 2D$^+$-MOT in the second chamber and then dropping the atoms on the resonator, or loading a 3D-MOT in the second chamber, transporting the atoms into the resonator chamber using an optical conveyor belt [89], and then dropping the atoms, or finally, an atomic fountain might be used in order to launch atoms on a parabolic trajectory towards the resonator. Dropping the atoms on the resonator, suffers from a fundamental drawback. Assuming the atoms are dropped from a height, h, of more than 160 μm, the velocity acquired by the falling atoms, $v_{\text{grav}} = \sqrt{2gh} > 5.6$ cm s^{-1}, will already be comparable to atoms having the same average thermal velocity in the direction of the resonator [91],

$$v_{\text{therm}} = \sqrt{\frac{9\pi k_B T}{8 m_{\text{Rb}}}} = 5.6 \text{ cm s}^{-1} \ , \tag{4.2}$$

where g is the gravitational constant, k_B is Boltzmann's constant, m_{Rb} is the atomic mass of rubidium, and T is the atomic temperature, assumed to be 10 μK. Experimentally, atoms ($T = 10 - 100$ μK) can only be dropped from a height of more than several hundred microns above the resonator due to geometry constraints [48, 92]. This already sets severe limitations on the minimum speed of the atoms and thus on the obtainable interaction times.

Alternatively, an atomic fountain can launch a sub-Doppler cooled atomic cloud such that the heights of the turning points of the atomic trajectories on average coincide with the position

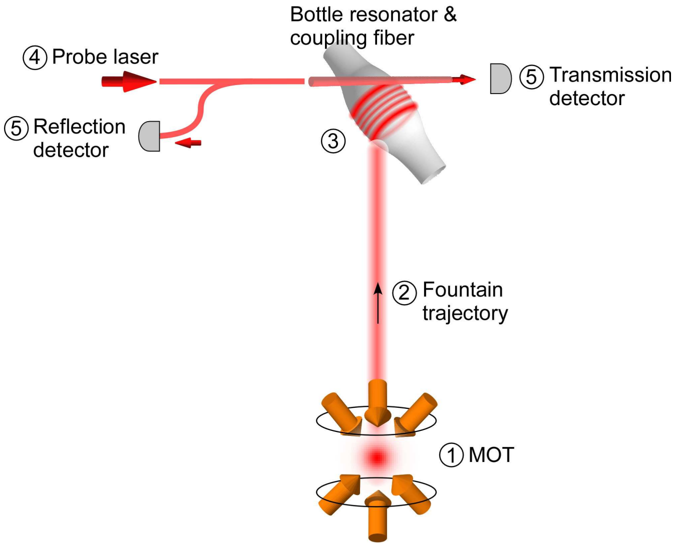

Figure 4.1: Experimental concept of the atomic fountain and resonator apparatus. ① Atoms are first trapped and cooled in a MOT. ② These atoms are then launched in a vertical trajectory to the location of the resonator about 31 cm above the MOT. ③ After reaching the resonator position, atoms can then interact with the resonator mode and subsequently modify the transmission and reflection of a weak probe laser light. ④ The probe light is sent through an optical fiber which couples into the resonator mode and ⑤ is detected on photon detectors.

of the resonator, thereby yielding the longest atom–field interaction time. In addition, it is also possible to set the average velocity of the atoms to well defined values to compensate, for example, repulsive dipole forces of the resonator light field. For these reasons, we chose an atomic fountain as the means of delivering the atoms to the resonator, the concept of which is shown in Figure 4.1.

MOT Parameters

Earlier work documented in Ref. [88] contains a full account of the parameters and characteristics of the MOT apparatus used in this work. See Appendix B for background details to atom trapping and cooling. These results are briefly summarized here:

Up to a maximum of 10^8 atoms are loaded and cooled to around 5 μK in 1–2 seconds using a combination of Doppler and polarization gradient cooling. This requires the rubidium partial pressure in the MOT vacuum chamber to be around 1×10^{-9} mBar while the background gas pressure is $\sim 1 \times 10^{-10}$ mBar. Higher background pressures lead to a lower steady state atom number in the MOT due to atomic collisions of Rb with the background gas. A magnetic field gradient of 5 G cm^{-1} is used for the MOT. This yields a MOT diameter of 1-2 mm and the atomic density is $\sim 3.5 \times 10^{10}$ atoms cm^{-3}, limited by collision losses from the background gas. A physically small, cold atomic cloud with high-density is desirable in order to increase the number of atoms interacting with the resonator mode, and we find these experimental parameters satisfy this goal well.

Atomic fountain principle

The atomic fountain was originally developed by Ramsey and Zaharias [93] as a technique for overcoming the problems caused by varying trapping potentials in atom traps which hindered measurements of the exact transition frequencies of atoms and molecules. Today, cesium (primary standard) and rubidium (secondary standard) atomic fountains provide the international frequency standard based on the clock transition between the two $m_F = 0$ levels of the hyperfine ground states, and have a relative uncertainty of better than 10^{-14}. In general, the principle of an atomic fountain is to first trap and cool atoms in a MOT and then briefly accelerate the atoms (now in an optical molasses) vertically in a parabolic trajectory to the interrogation zone. The maximal height of the parabolic flight is determined by the starting velocity and gravity.

A schematic of the fountain used in this work is shown in Fig. 4.1 and the operating principle is shown in Fig. 4.2. A Rb-dispenser provides a source of hot ^{85}Rb atoms that are trapped and cooled in a six-beam MOT. The cooling laser beams are arranged in a 1–1–1 configuration with three beams pointing downward at an angle $\theta = \cos\left(1/\sqrt{3}\right)^{-1} = 54.7^\circ$ and three opposing beams pointing upward also at 54.7°. After the loading stage, the magnetic field of the MOT is switched off and the atoms are transferred into an optical molasses with a vertical velocity, v_z, set by the detuning, $\Delta\omega$, between the upward and downward pointing sets of beams.

$$v_z = \sqrt{3}\frac{\Delta\omega}{k} \ , \tag{4.3}$$

where the factor of $\sqrt{3}$ is due to the 1–1–1 configuration and accounts for the angle of the beams.

4.2 Experimental Setup

4.2.1 Vacuum system

Transporting cold Rb-atoms to the evanescent field of the bottle resonator is only possible in an ultra-high vacuum (UHV) environment with pressures on the order of 10^{-10} mBar. Collisions between the background gas and atoms in the MOT increase the loss rate of the MOT and thus reduce the storage time. As a consequence, the repetition rate of the experiment is reduced because the steady state atom number in the MOT decreases: if fewer atoms are launched to the resonator, there will be fewer atom–resonator coupling events. To mitigate these problems, special attention must be paid to the choice of materials, types of vacuum pumps, resonator design and gas flow rates, while also observing best preparation and cleaning practices. Since atoms are not currently trapped at the location of the resonator, it is sufficient to operate the resonator at a pressure of 10^{-9} mBar. Useful information on reaching UHV pressures can be found in Refs. [88, 94] and references therein.

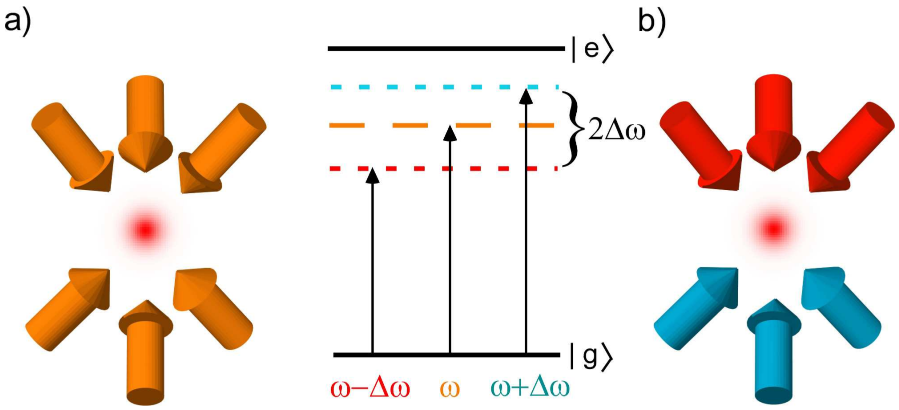

Figure 4.2: Operating principle of an atomic fountain in the 1–1–1 configuration. Three pairs of mutually orthogonal laser beams are arranged so that each beam forms an angle of 54.7° with the vertical axis. (a) Initially all beams have the same frequency ω and are detuned from the cooling transition. (b) The reference frame of the molasses is transferred from a stationary frame to a moving frame by red-detuning the three upper laser beams with respect to the lower laser beams by an amount $2\Delta\omega$, all while still cooling the molasses. The starting velocity v_z in the vertical direction is proportional to detuning, and is given by $v_z = \sqrt{3}\Delta\omega/k$. Adapted from Ref. [88].

MOT chamber

The vacuum chamber setup shown in Fig. 4.3 is produced from 304L and 316L non-magnetic stainless steels. Both MOT and science chambers are CNC machined by Kimball Physics Inc. from solid blocks of steel and achieve a port alignment precision of < 0.1 degree. Port alignment is a major issue for the MOT chamber (Expanded Spherical Cube, MCF275-ESC608) because past experience of other groups have found that deviations of a few degrees in the parallelism of opposing ports shifts the fountain launch angle by a few degrees: such an error is critical to the transmission of the cloud through the differential pumping tube. In addition, all ports have ConFlat (CF) flanges and all surfaces have a mirror finish.

The MOT viewports (CF40, silica glass, all viewports are produced by Kurt J. Lesker Company/Torr Scientific Ltd.) have a V-band anti-reflection coating at a wavelength of 780 nm on both optical surfaces ($< 0.1\%$ reflectance at 780 nm, $< 0.5\%$ in the wavelength range 730–840 nm) and have a parallelism of 3 arc minutes. Two additional ports (CF16) in the MOT chamber are fitted with electrical feedthroughs (EFT0123052, Kurt J. Lesker Company) capable of carrying at least 3 A of current required for heating two Rb dispensers (RB/NF/7/25 FT 10 + 10, SAES Getters). The dispensers are aligned so that the emitting surface is directed towards the chamber wall rather than towards the MOT, otherwise the MOT lifetime may be degraded. Various other CF16 flanges are used for MOT imaging, mechanical support (bottom flange), differential pumping (top flange), vacuum pumping, and a viewport for the repump-light. CF16 silica and zinc-selenide viewports produced by Torr Scientific Ltd. have a non-standard thickness for the metal part, and some viewports are particularly prone to leakage at the glass-metal brazed seal. It is therefore critical to identify the leaking viewports at the assembly and testing

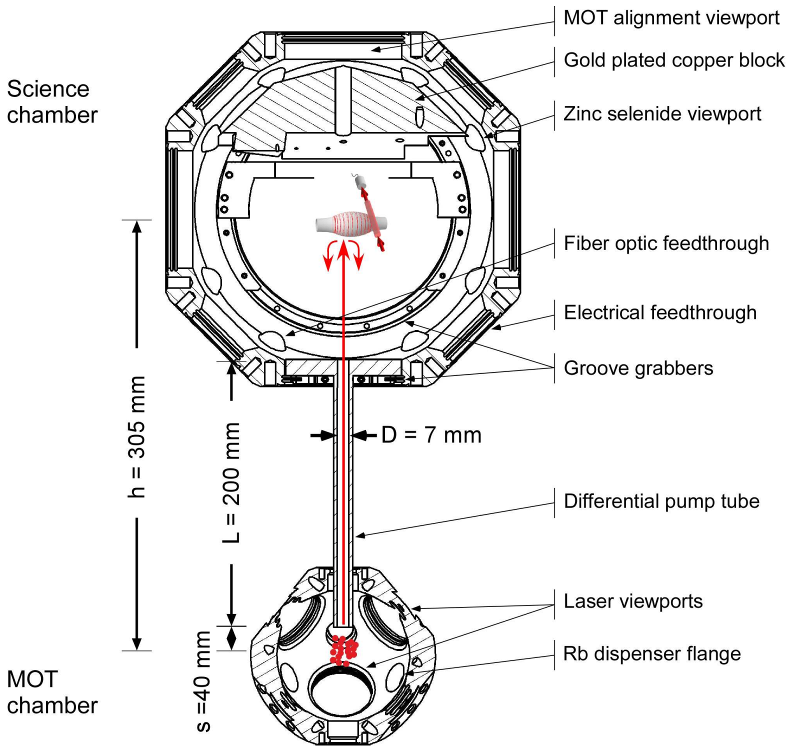
MOT alignment viewport
Gold plated copper block
Zinc selenide viewport
Science chamber
Fiber optic feedthrough
Electrical feedthrough
Groove grabbers
h = 305 mm
L = 200 mm
D = 7 mm
Differential pump tube
Laser viewports
Rb dispenser flange
MOT chamber
s =40 mm

Figure 4.3: Cross-section through the vacuum apparatus. Rubidium is cooled in a magneto-optical trap in the lower chamber. The atomic cloud is then launched through a differential pumping tube into the upper chamber where it reaches the resonator at a height of around 305 mm.

stage with the aid of a Helium leak detector.

The complete setup of the MOT chamber vacuum system is shown in Fig. 4.4. Attached to the spherical-square MOT chamber is a conical reducer flange and a custom-made four-way-cross which connects a Pirani/Cold cathode pressure gauge, ion getter pump, and turbo pump. The pressure gauge (PKR 251, Pfeiffer Vacuum GmbH) operates in the range 10^3 mBar–5×10^{-9} mBar and is used for diagnostic purposes. Directly across from the MOT chamber is a 30 l s^{-1} ion getter pump (VacION Plus Starcell 40, Agilent Technologies Inc./Varian Deutschland GmbH). The dry turbo pump (TMU 071 P, Pfeiffer Vacuum GmbH) is part of a pump-stand unit (TSU-071E) which uses a membrane backing pump (MVP 015-2). The PVC connection tube between the two pumps was replaced with a corrugated metal hose to enable the use of a Helium leak detector: helium readily leaks through PVC giving the false indication of a leak. Any possible back-streaming from the membrane pump into the turbo pump is blocked by a ball-valve (KF16 fitting, Pfeiffer Vacuum GmbH/Trinos GmbH). An all-metal right-angle UHV valve (540 series, VAT GmbH) placed after the turbo pump is closed when the base pressure of the turbo pump is reached ($<5\times10^{-9}$ mBar), at which time the ion pump is turned on.[1] Dual operation of the ion and turbo pumps is not possible because the mechanical vibration of the turbo blades is efficiently transmitted to the resonator coupling setup, which in turn causes transmission noise in the optical fibers.

---

[1] The viton-sealed version of this type of valve (28436-GE01-0001) is not compatible with these pressures despite

Differential pumping

The vacuum system is based on a two-chamber design where one chamber is dedicated to trapping and cooling atoms in a MOT, while a second chamber houses the resonator setup. A differential pumping tube connecting the chambers maintains a very low Rb pressure in the resonator chamber so as to minimize the buildup of a metal Rb coating on the resonator, thereby prolonging the useful lifetime of the resonator. The dimensions of the differential pumping tube in Fig. 4.3 were carefully chosen to meet two competing constraints. Firstly, the tube should be long and have a small bore diameter so that the gas conductance though the tube is minimized. Secondly, the tube should be short enough and have a large bore diameter to allow the atomic cloud to pass unhindered on its way to the resonator.

The atomic cloud is located a distance s directly below the differential pumping tube of length L. The initial cloud diameter is d_0 and the bore diameter is D. The gas conductance C of the differential pumping tube for rubidium is (see Ref. [88] and references therein)

$$C_{\mathrm{Rb}} = 6.95 \frac{D^3}{L + (4/3)D} \quad \text{in l s}^{-1} \text{ with } L \text{ and } D \text{ in cm} , \tag{4.4}$$

assuming the gas is air at 23°C.[2] The pressure ratio across the differential pumping tube is $\Delta = P_{\mathrm{MOT}}/P_{\mathrm{science}} = S/C$, where P is the pressure in the MOT/Science chambers, S is the pump rate of the vacuum pump in the science chamber, and C is the gas conductance of the tube. Using this relation and Eq. (4.4), the criteria for the minimum length of the tube to obtain a pressure difference Δ in Fig. 4.3 is therefore

$$L \geq 6.95 \frac{\Delta}{S} D^3 - \frac{4}{3} D . \tag{4.5}$$

Considering the atomic cloud as a solid object, the motion of the cloud after being launched in the atomic fountain is described by the equation

$$v(t) = v_0 t - {}^1\!/\!_2 g t^2 , \tag{4.6}$$

where $v(t)$ is velocity at time t, v_0 is the initial velocity, and $g = 9.81$ m s^{-2} is the acceleration due to gravity. Using this equation, a similar criteria to Eq. (4.5) can be obtained for the expansion of the cloud as it passes through the tube.

$$L \leq v_0 \frac{D - d_0}{v_{\mathrm{exp}}} - \frac{g}{2} \left(\frac{D - d_0}{v_{\mathrm{exp}}} \right)^2 - s . \tag{4.7}$$

---

being rated for pressures in the 10^{-10} mBar range: according to VAT customer service, pressures in the 10^{-10} mBar range are only possible with their viton-sealed valve if there is a sufficiently large pump rate on the vacuum side to counter the high leak rate of viton.

[2] When considering another gas this formula scales with a factor $\sqrt{M_{\mathrm{Rb}}/M}$, where M is the mass [88].

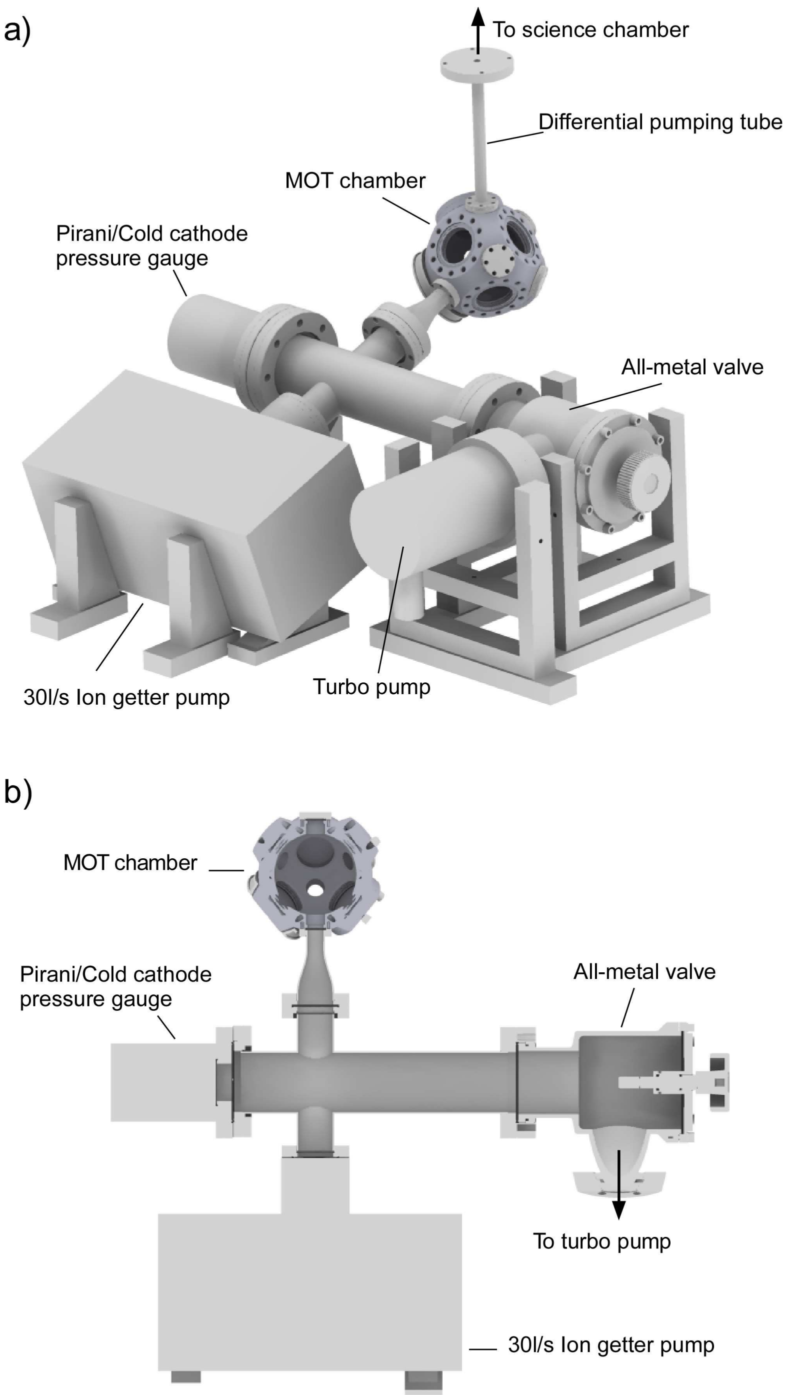
a)
To science chamber
Differential pumping tube
MOT chamber
Pirani/Cold cathode pressure gauge
All-metal valve
30l/s Ion getter pump
Turbo pump
b)
MOT chamber
Pirani/Cold cathode pressure gauge
All-metal valve
To turbo pump
30l/s Ion getter pump

Figure 4.4: Overview of the lower vacuum chamber. (a) Atoms trapped and cooled in a MOT in the spherical-cube chamber are vertically launched through a differential pumping tube to the science chamber. (b) Cross-section through the setup showing the layout of the ion pump, all-metal right angle valve connected to a turbo pump, and pirani/cold cathode pressure gauge for measuring pressures down to 3×10^{-9} mBar. Adapted from Ref. [88].

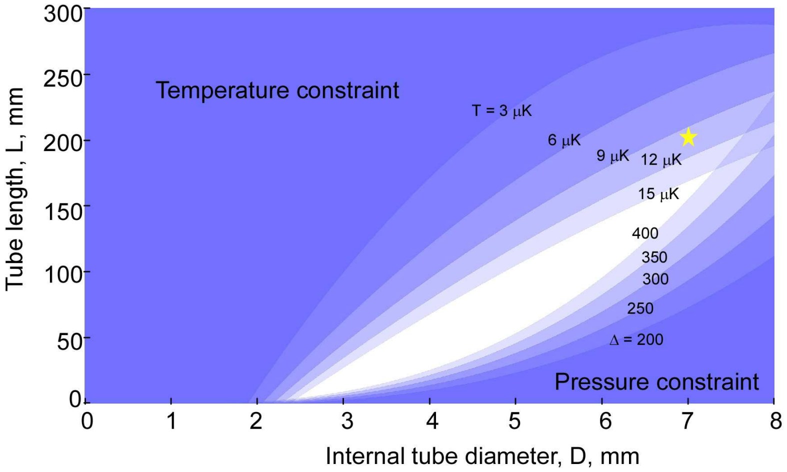

Figure 4.5: Differential pumping constraints diagram. The differential pressure ratio (lower right shaded regions, Eq. (4.5)) and atom cloud temperature (upper shaded regions, Eq. (4.7)) constrain the dimensions allowed for a differential pumping tube between the MOT chamber and the science chamber (see main text). The star ★ indicates the selected tube dimensions. The dimensions are compatible with atomic temperatures below 10 μK and a differential pressure ratio of around $\Delta = 600$ or less. Parameters: initial cloud diameter, $d_0 = 1.5$ mm, effective pumping rate of the science chamber = 58 l s^{-1}, distance between initial cloud position and tube entrance $s = 4$ cm, maximum fountain launch height $h = 328$ mm (slightly above the resonator position), and the corresponding launch velocity $v_0 = 2.53$ m s^{-1}.

The cloud expansion velocity is $v_{\exp} = \sqrt{2k_B T/M}$, where T is the atomic temperature and M is the atomic mass. The launch velocity of the atomic cloud is $v_0 = \sqrt{2hg}$, where h is the maximum height of the parabolic trajectory.

Equations (4.7) and (4.5) both have a functional dependence on the tube length and diameter: a long tube with a small diameter increases the maximum possible pressure difference (Eq. (4.5)), while a short tube with a large diameter enables the cloud to have a higher temperature (Eq. (4.7)). Figure 4.5 shows this tradeoff between the temperature of the atomic cloud (upper curves, Eq. (4.7)) and the pressure difference across the tube (lower right curves, Eq. (4.5)). The chosen dimensions in the current experiment (see star) are compatible with temperatures below $T = 10$ μK and a differential pressure ratio of around $\Delta = 600$ or less, assuming air is the background gas.

Science chamber

The science chamber houses the bottle resonator and coupling fibers and is connected to the MOT chamber via the differential pumping tube. Several features of the science chamber (Spherical Square, MCF800-SS204040.16, Kimball Physics Inc.) make it a flexible housing for the experimental setup:

- **Feedthroughs:** A total of 16 CF16 flanges and a further four CF40 flanges arranged symmetrically around the chamber can be chosen for electrical and optical feedthroughs. Some of these flanges are indicated in Fig. 4.3.

  Two CF16 flanges with CF-to-$1/4$-inch swagelok adapters (Vacom GmbH) and teflon ferrules are used to feed through four optical fiber ends (for details, see Ref. [57] and references therein). The teflon ferrules are first mounted on the swagelok with the optical fibers attached before tightening the locking nut by hand until it is finger tight. Approximately two further full revolutions of the nut should be sufficient to seal the feedthrough but further tightening is needed during and after baking of the chamber. Special attention should be given to the limited temperature range of teflon and the maximum temperature should not exceed 100°C. Tightening of the nut should only ever be performed while monitoring the transmission through the fibers.

  Two sub-C electrical feedthroughs (IFDJG091052K, Kurt J. Lesker Company) are mounted on CF16 flanges and are used for controlling bending piezos attached to the coupling fibers. A sub-D electrical feedthrough (IFDGG091053, Kurt J. Lesker Company) is used for controlling the bottle resonator shear piezos. All three feedthroughs have PEEK connectors on the vacuum side.

  In addition to these feedthroughs, a pair of opposing CF16 flanges are fitted with zinc selenide viewports which are transmissive for a CO2-laser beam at a wavelength of 10.6 μm. This laser beam passes freely through the center of the chamber and can be used to heat the bottle resonator in order to evaporate rubidium or water adsorbed on the resonator surface.

- **Internal mounting:** So-called *groove grabbers* enable the complete resonator setup to be securely mounted inside the chamber, see Fig. 4.3. The groove grabbers consist of a system of metal rings that mechanically clamp onto grooves machined into the chamber and are concentric with the flanges. Screws in the metal rings are used to clamp the rings into place. Two custom designed groove grabbers attached to two CF160 flanges are used to hold a 2-kg gold-plated copper block (OFHC copper, nickel-free gold plated) in the top section of the chamber. The copper block serves as a platform for the resonator setup while also acting as a vibration sink (see Sec. 4.2.6).

  A third groove grabber provides support for the differential pumping tube which is attached to a CF60 port at the bottom of the chamber. A custom-made reducer flange (CF60 to CF16, not shown) connecting the two chambers is mounted independently of the differential pumping tube, i.e., there is no direct contact between the two parts.

- **Access ports:** A large CF160 flange on the front provides unhindered optical access to the experimental setup for various imaging optics and free space laser light. A light sheet passes through the flange which is fitted with a viewport (VPZL-800LDIO, silica glass) having a V-band anti-reflection coating at a wavelength of 780 nm on both optical surfaces for light incident perpendicular to the glass. (A CF160 flange on the back of the science chamber is connected to another section of the vacuum system). The fluorescence from atoms passing through the light sheet is detected with a photo-multiplier tube using a lens imaging system mounted near the left CF60 viewport at 90° to the beam path (see Sec. 4.2.3).

There is an additional optical access through the top viewport (CF60) down to the MOT chamber. By using a vari-focus lens and CCD camera (F131B, AVT Marlin GmbH) mounted to the viewport using an adapter plate, this port is particularly useful for aligning the resonator/copper block with the differential pumping tube and also for aligning the MOT. There is a hole through the copper block for this purpose.

The complete setup of the science chamber vacuum system is shown in Fig. 4.6. The chamber rests on a custom-made breadboard that is suspended over the MOT chamber with 18 steel posts (1 1/2-inch diameter, Thorlabs Inc.) that are clamped to an optical table. The stability of the breadboard is aided by an aluminum support frame glued (Scotch Weld DP760, 3M) to the underside of the breadboard covering about 10% of the surface area, and thin steel plates also glued (VHB tape 4959, 3M) to the underside of the breadboard covering about 70% of the surface area, see Fig. 4.7. The purpose of the steel sheets is to act as dampers that reduce the quality factor of the vibration modes in the breadboard. The breadboard and plates act as two coupled oscillators that each have an individual vibration spectrum – vibrational modes in one oscillator are damped by coupling to the other oscillator, and visa versa.

A large 5-way cross (CF160, C5-0800, Kurt J. Lesker Company) connects an ion pump (VacION Plus Starcell 300, Agilent Technologies Inc./Varian Deutschland GmbH) at right angles to the science chamber. An electrical feedthrough attached to the top flange of the 5-way cross connects to piezoelectric translators used for moving the coupling fibers into place with the resonator. The back flange of the cross is fitted with an AR coated viewport (VPZL-800LDIO, silica glass) and gives access to the light sheet beam sent through the front viewport of the science chamber. The remaining flange of the cross is connected to a reducer 4-way cross which is in turn connected to an all-metal UHV valve (48236-CE01-0001, VAT Deutschland GmbH) having a very low leakrate compatible with pressures $<10^{-10}$ mBar. A second turbo pump which is connected to the valve is arranged in the same manner as the other turbo pump mentioned earlier in Sec. 4.2.1 for the MOT chamber. The 4-way cross allows for a pirani/cold cathode pressure gauge to be connected.

Figures 4.7 and 4.8 show how the resonator setup is suspended upside down in the science chamber in order to maximize the available space. The resonator holder is fixed to a gold-plated copper block while the coupling fibers are mounted onto holders that attach to piezo-electric translation stages (ANPx101/NUM and ANPz101/NUM, Attocube GmbH). All three fibers are glued to piezos used for tensioning: the coupling fibers are tensioned with bending piezos (PL112.10, PI Ceramic) while two multi-layer shear piezos (PAXY+049, vacuum version: P141.10, Physik Instrumente GmbH & Co. KG) can tension both ends of the resonator fiber for resonance frequency tuning and stabilization. Vacuum compatible PTFE wire leads (see the red wires in Fig. 4.8) are bonded to the piezos from Physik Instrumente GmbH using an electrically conducting silver-filled epoxy (H21D, Epotek Technology Inc.) and baked in a vacuum oven to 100°C. The Kapton-sealed electrical wires for the Attocube translation stages come pre-assembled.

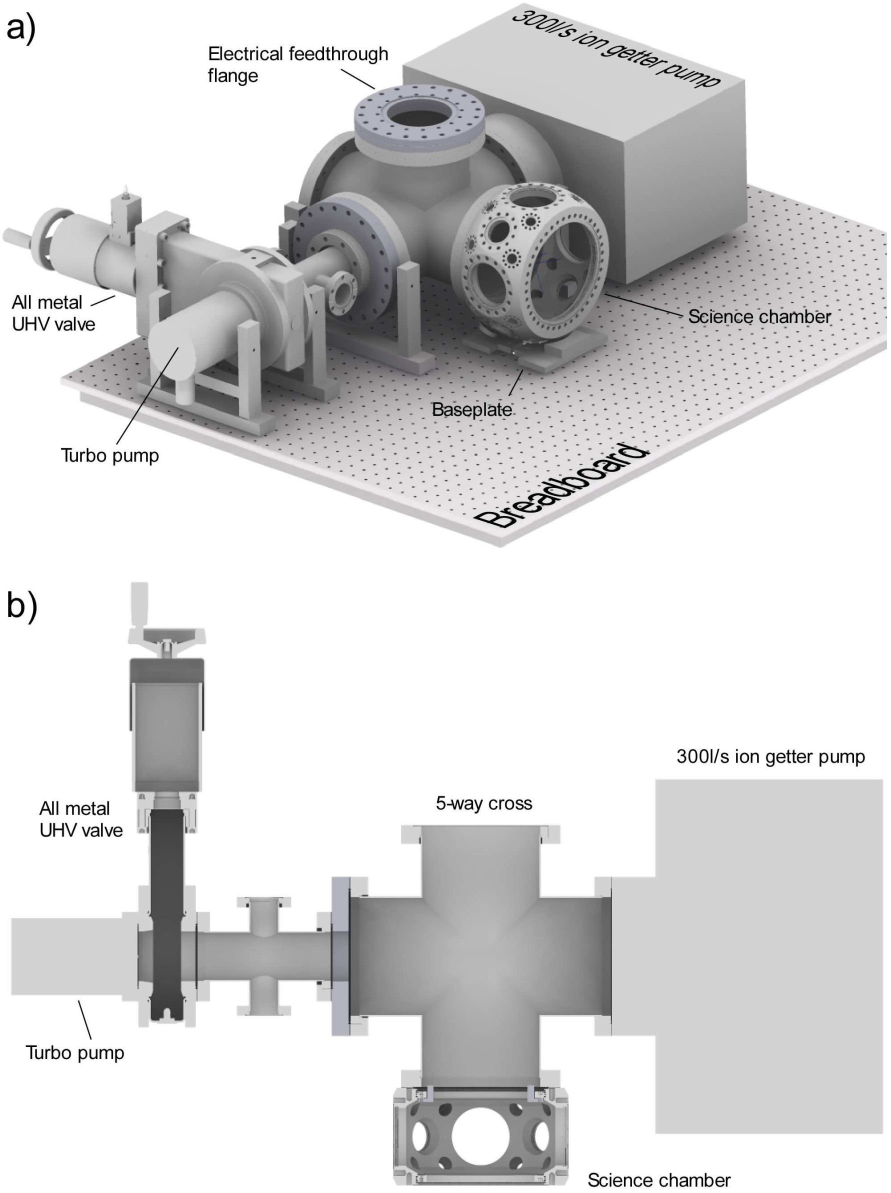
a)
Electrical feedthrough
flange
300l/s ion getter pump
All metal
UHV valve
Science chamber
Baseplate
Turbo pump
Breadboard
b)
300l/s ion getter pump
5-way cross
All metal
UHV valve
Turbo pump
Science chamber

Figure 4.6: Overview of the upper vacuum chamber. (a) The fiber coupling setup is mounted in a spherical octagonal chamber which connects to the lower vacuum chamber via a differential pumping tube. Large CF180 and CF60 viewports on the chamber give excellent optical access to the fibers for imaging and fountain diagnostics. In addition, two small CF16 ZnSe viewports have clear optical access for a CO2-laser beam for cleaning the resonator. (b) A cross-section through the setup shows the layout of the ion pump and the all-metal valve connecting to a turbo pump. A pirani/cold cathode pressure gauge can be optionally connected to the four-way cross. Adapted from Ref. [88].

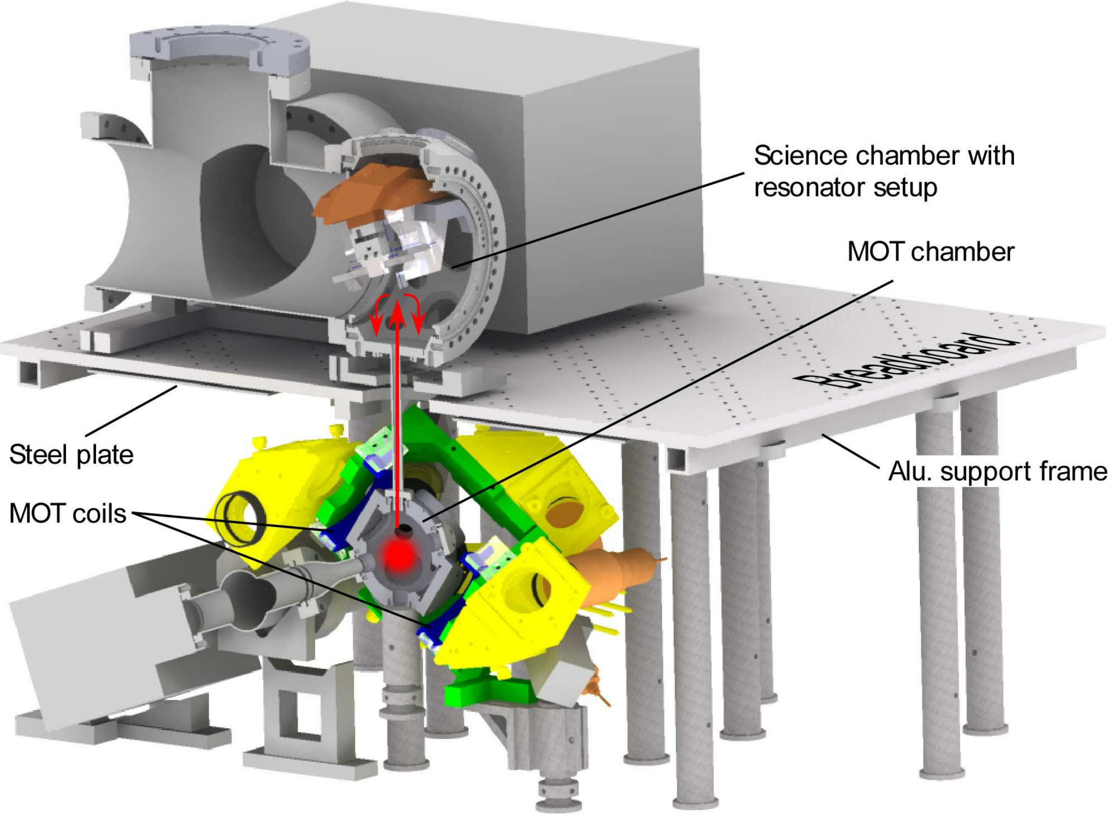

Figure 4.7: Cross-section through the atomic fountain apparatus. Atoms are trapped and cooled in the lower MOT chamber and subsequently launched to the upper science chamber where the resonator setup is mounted. The opto-mechanics and magnetic coils necessary for the MOT are highlighted. Adapted from Ref. [88].

Full details of the procedures and characteristics of vacuum pumping, baking, leak testing and gas flow rates are documented in Ref. [88] for interested readers.

4.2.2 MOT setup – magnetic coils and camera imaging

A magneto-optical trap requires a magnetic field with a constant gradient and a field minimum at the center of the atomic cloud, as described in Appendix A. Such a field can be constructed using two coils in a so-called *anti-Helmholtz* configuration. The arrangement of the coils with respect to the MOT chamber is shown in Fig. 4.9.

The coils are each constructed from 60 windings (6 windings radially and 10 windings laterally) of enamel-coated copper wire with a diameter of 1.5 mm around a circular aluminum frame with an internal radius of 47 mm. Due to geometry constraints, the shortest distance between the coils is about 130 mm, which is a factor of almost three greater than the optimal spacing where the gradient is maximized, however this is not a problem for the MOT. With a current of 13 A

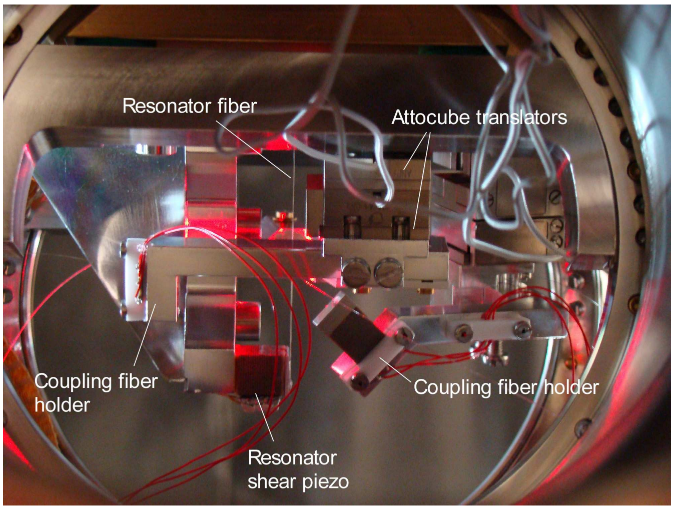

Figure 4.8: Picture of the setup in the science chamber. The atomic fountain enters from the bottom of the picture. Adapted from Ref. [87].

supplied to the coils, the magnetic field gradient at the trap center is 10 G cm^{-1} along the z-axis which passes through the center of the coils, and 5 G cm^{-1} along the perpendicular axes. We currently operate the MOT with 6 A because the atom number is maximized at this value [88].

A highly stable power supply (TOE 8815, Toellner GmbH) supplies current to the coils, which is quickly turned off during the experimental sequence on the microsecond timescale using a homemade MOSFET (IRFP460LC, International Rectifier Inc.) and diode-based (20ETF06PbF, Vishay Inc.) switching circuit. A TTL signal from the experiment control center is sent to an opto-isolator that opens and closes the circuit. The total inductance of both coils is calculated as $L = 2(N^2)r_{\mathrm{coil}}\mu_0\left[\ln\left(8r_{\mathrm{coil}}/a\right) - 2\right] = 2.1$ mH, where N is the number of coils, r_{coil} is the coil radius, μ_0 is the free-space magnetic permeability, and a is the radius of one wire. This inductance sets a bound to the switch-off speed at $\tau = LI/V = 25$ μs, where V is the reverse breakdown voltage of the MOSFET (500 V), and I is the current in the coil. The total power in the coils and MOSFET is quite high as estimated from the product of the current and voltage as $VI = 6$ A$\times$15 V $= 90$ W: the large voltage is required for operation of the MOSFET. Passive cooling of the coils is achieved by gluing (heat conductive glue, Arctic Silver Inc.) them to a large support cage surrounding the MOT chamber which acts as a heatsink (see the green parts in Fig. 4.7). In tests under realistic conditions with a high current of 13 A, we have found a maximum temperature of 43°C, which is well within acceptable limits.

Six additional coils arranged orthogonally in a Helmholtz configuration are used to adjust the position of the magnetic field minimum of the MOT quadrupole field created by the two anti-Helmholtz coils. These coils provide a homogeneous magnetic field that compensates the effect of the Earth's magnetic field, stray fields from the ion pumps, and non-optimal alignment of the anti-Helmholtz coils. It is critically important to ensure that the magnetic field minimum is precisely in the center of the six cooling laser beams. Sub-optimal alignment makes polarization gradient cooling less effective at best and may even prevent the formation of a MOT at worst. To overcome this problem, the six coils are placed concentrically with the six laser viewports onto which they are clasped in place, see Fig. 4.9 (a). Each pair of opposing coils is independently controlled with a stable power supply (EA-PS 3016-10B, EA Elektro-Automatik GmbH) that supplies up to 1 A of current. The center of the MOT can be shifted several millimeters along each axis by changing the current in each coil. The inner radius of a coil is 36 mm and the distance between each pair of coils is about 100 mm. The coil wires are constructed from ribbon cable with 3 windings radially and 7 windings laterally and can safely sustain a maximum current of 4 A.

There are two common strategies for optimizing the current to the compensation coils; both rely on a camera imaging system. Both strategies involve following the motion of the MOT when the magnetic field is turned off but with the laser light still turned on. Two CCD cameras (PL-B741EF, Pixellink) shown in Fig. 4.9 (a) image the MOT through CF16 viewports. A third CCD camera images the MOT from the top viewport of the science chamber along the axis co-linear with the fountain launch direction.

- The first approach is to monitor the spatial distribution/motion of the atomic cloud while slowly decreasing the magnetic field from the anti-Helmholtz coils. The expansion of the atomic cloud along each axis should be homogeneous and the center of mass should not change while the MOT is repeatedly loaded every 0.5–1 seconds. A special experimental control sequence performs this task automatically. By appropriately varying the current in each set of compensation coils it is possible to center the magnetic field minimum.
- The second approach is to simply cool the atoms in a MOT before suddenly turning off the current to the anti-Helmholtz coils and observing the direction in which the molasses moves. If there is a misalignment in the magnetic field minimum with respect to the laser beams, the cloud will rapidly move when the field is switched off. This happens because of an imbalance in the radiation pressure on the molasses. The rapid movement appears as a momentary streak across the camera image which is acquired at a rate of 30 frames per second. Perfect compensation of the magnetic field minimum is achieved when the molasses does not move along any axis. These steps are repeated every 0.5–1 seconds.

MOT chamber cage

The so-called *cage* surrounding the MOT chamber in Fig. 4.9 (b) provides cooling to the anti-Helmholtz coils, but more importantly, it also mechanically supports the opto-mechanics for the laser light and helps ensure their accurate alignment. In this way, the optics and coils are detached from the vacuum chamber and can be independently moved so that it is a straightforward procedure to optimally position the MOT under the differential pumping tube. Each of the six beam paths include a modular unit that attaches to the cage: this is composed of two right-angle mirror holders (KCB2, Thorlabs) for 50 mm diameter mirrors (MirHR mirror, $s = p$ for 780 nm at 45°, Lens Optics GmbH) and a laser-beam collimator (60FC-Q780-4-M150-37, Schäfter & Kirchhoff GmbH) with a free space beam diameter of 27 mm. Laser light from the laser table is fiber coupled into polarization maintaining fibers and transported to the vacuum chamber table where it is sent into two fiber clusters (Schäfter & Kirchhoff GmbH). The outputs from each fiber cluster connect to the collimators.

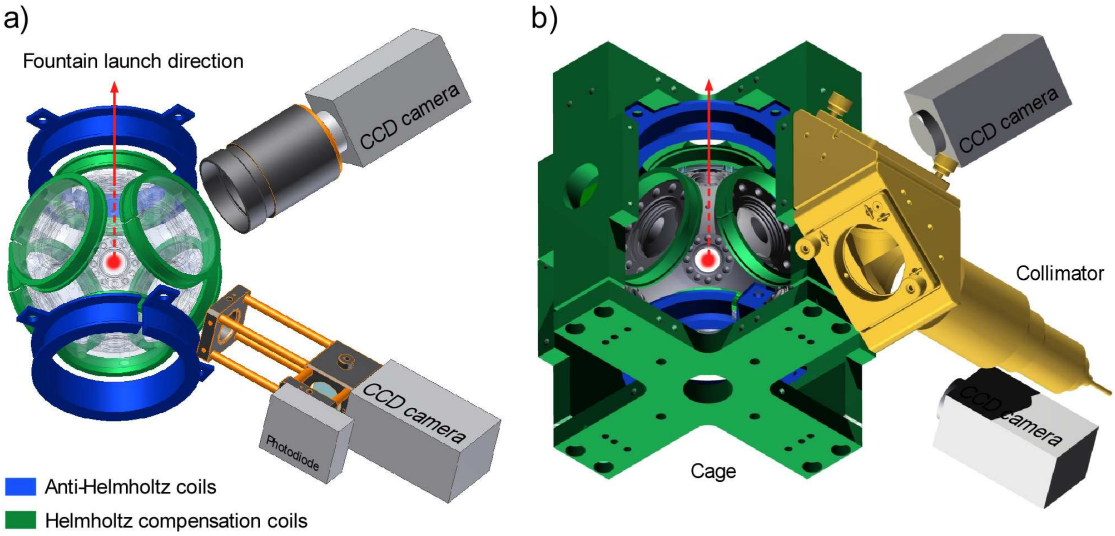

Figure 4.9: The MOT vacuum chamber and components. (a) Arrangement of the anti-Helmholtz trapping coils, compensation coils, and imaging system around the MOT chamber (semi-transparent). A third camera (not shown) images the MOT from the top viewport of the science chamber at a distance of about 0.5 m. Fluorescence from the atoms is detected on a photodiode. (b) A cage (green) surrounds the vacuum chamber and supports the mounted anti-Helmholtz coils and opto-mechanics used for the six cooling laser beams. The mirror holders and collimator for only one beam are shown for clarity. Adapted from Ref. [88].

The alignment procedure for each beam involves passing the light through four diaphragms having a 2 mm diameter hole: one diaphragm is mounted directly in front of the collimator and a second is mounted on the cage directly before the viewport, and the same for the opposing viewport and collimator. By using four diaphragms it is possible to ensure that all beams are exactly collinear. Once aligned, the beam from one collimator couples into the opposing collimator, which takes several hours of work for all six collimators. The procedure is aided by using a finger camera (Conrad Electronic SE) and the CCD cameras indicated in Fig. 4.9.

Since finishing the re-assembly and alignment of the experimental setup at the Atominstitut around the start of 2011, the MOT has run stably and has not required any further adjustments and nor has the performance degraded: the temperature of the atoms after being launched in the atomic fountain is consistently around 5 μK.

4.2.3 Fountain performance

The performance of the fountain is analyzed by fluorescence detection of the atomic cloud in the science chamber. This allows us to perform time-of-flight measurements in order to determine the atomic velocity and temperature. For this purpose, we launch a light sheet [88, 95], resonant with the atoms, through the science chamber a few centimeters below the resonator position and detect the atomic fluorescence with a photo-multiplier tube (PMT) (Hamamatsu Photonics

Deutschland GmbH, H 6780-20).

A typical time-of-flight measurement is shown in Fig. 4.10. The vertical trajectory and expansion of the atomic cloud, $f(t)$, can be modeled as a Gaussian distribution [88, 95]

$$f(t) = \frac{N}{\sigma(t)\sqrt{2\pi}} \left[1 - \exp\left(-\frac{\rho^2}{2\sigma^2(t)}\right)\right] \exp\left[-\frac{(h - v_z t + \frac{1}{2}gt^2)^2}{2\sigma^2(t)}\right] . \tag{4.8}$$

The term N is the total number of atoms in the launched cloud, ρ is the lateral width of the light sheet, h is the distance between the light sheet and the MOT, v_z is the initial vertical launch velocity, and $g = 9.81$ m s^{-2} is the gravitational constant. The cloud has a temperature T which results in a spatial expansion over time approximately given by

$$\sigma(t) = \sqrt{D^2 + \frac{k_B T}{m} t^2} , \tag{4.9}$$

where $\sigma(t)$ is the spatial variance in time t, D is the diameter of the cloud in the MOT, and m is the atomic mass of Rb. The first exponential term in Eq. (4.8) accounts for the fact that the atomic fluorescence will decrease over time since the cloud size may become greater than the lateral width of the light sheet, particularly when the cloud starts to fall down around $t_2 = 360$ ms in Fig. 4.10. This is evidenced in the broader peak width at t_2 compared to t_1, in agreement with Eq. (4.8).

Using this simple model describing the velocity and spatial distribution of the measured signal in terms of temperature, starting velocity, as well as light-sheet beam size and position, several properties can be determined from the data. Based on the width of the peaks it is possible to extract the temperature, which is around 6 μK. The arrival time of the atomic cloud is checked against the expected arrival time determined from the launch velocity, v_z, enabling us to verify the correct operation of the atomic fountain.

Having verified the delivery of cold atoms to the resonator chamber, we next demonstrate the ability to place the cloud at an exact, predetermined height by controlling the launch velocity. The top viewport of the resonator chamber acts as a known reference position. Atoms that collide with the viewport are lost from the cloud and do not contribute to the fluorescence signal which is recorded on the downward trajectory. Figure 4.11 shows several launches where the turning point of the cloud is incrementally moved closer to the viewport. It can be seen that an increasingly large fraction of the cloud is lost on the viewport, causing the fluorescence signal to be truncated. This demonstrates our ability to control the launch velocity of the cloud and thus to make the turning point of the cloud coincide with resonator position.

4.2.4 Resonator imaging

In addition to the MOT imaging systems described already, there is also a long working distance imaging system for imaging the bottle resonator. This is a commercial lens system with a variable zoom lens (1-50486, Optometron GmbH/Navitar Inc.) and has a long working distance of 86 mm, which is necessary since the resonator is located in the center of the science chamber. The variable zoom lens makes it convenient for aligning the coupling fibers with the resonator.

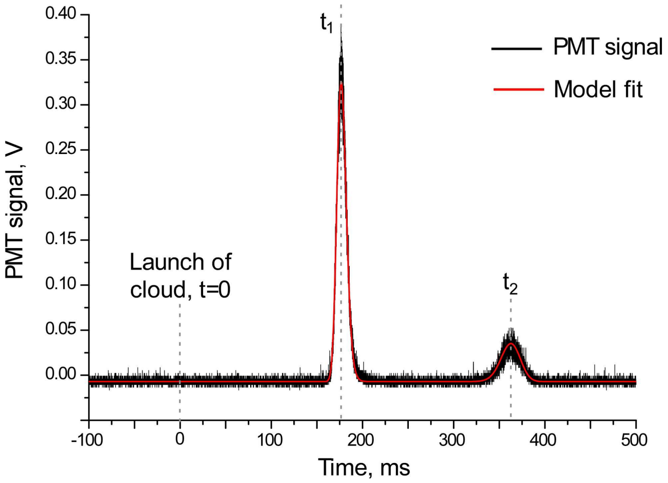

Figure 4.10: Fluorescence signal of an atomic cloud reaching a resonant light sheet placed at the position of the resonator (with the resonator removed). The data is a concatenation of two measurements: Data around the first peak at t_1 shows the cloud reaching the light sheet on its upward trajectory and data around the second peak at t_2 shows the cloud falling down after reaching its maximum height. The temperature estimated from a time-of-flight model is around 6 μK. Parameters: Light sheet lateral width $\rho = 18$ mm and vertical width of 0.5 mm, distance between MOT and light sheet $h \approx 310$ mm, diameter of the cloud in the MOT $D \approx 1.5$ mm, launch velocity $v_z = 2.62$ m s^{-1}.

Despite the long working distance, reasonably good quality images can be recorded and are sufficient for the purpose of aligning the coupling fibers, see Fig. 4.12. Several modulations in the tapered section of the fiber are visible and are a byproduct of making the taper transition very short: the tapers are about 3 mm long instead of a typical length of 30–40 mm commonly used in other tapered fibers. The short taper transition amplifies the affect of the shear piezos used for frequency tuning the resonator mode, as described in Sec. 3.4.

4.2.5 Fiber positioning system

Two coupling fibers are aligned with respect to the resonator mode using piezo-electric translation stages (ANPx101/NUM and ANPz101/NUM, Attocube GmbH). Each coupling fiber can be manipulated along two axes over a maximum travel range of 5 mm and with sub-nanometer resolution, see Fig. 4.13 for the layout. Such a large travel range is possible when operating in the so-called *slip-stick* mode, however the step-size is greater than 50 nm, which is too coarse for aligning the fiber to the critical coupling position. Another issue is that slip-stick movement necessarily requires a sudden shift of the piezo which, unfortunately, imparts a large momentum kick on the coupling fiber. This results in fiber vibrations with an amplitude of more than 2 μm lasting for a few seconds. Therefore, for very precise alignment of the fiber, it is necessary to use the standard piezo operation, where a continuous movement over a travel range of 3.5–5.0 μm is obtained by applying a DC voltage of up to 70 V. Only by using both types of piezo movement

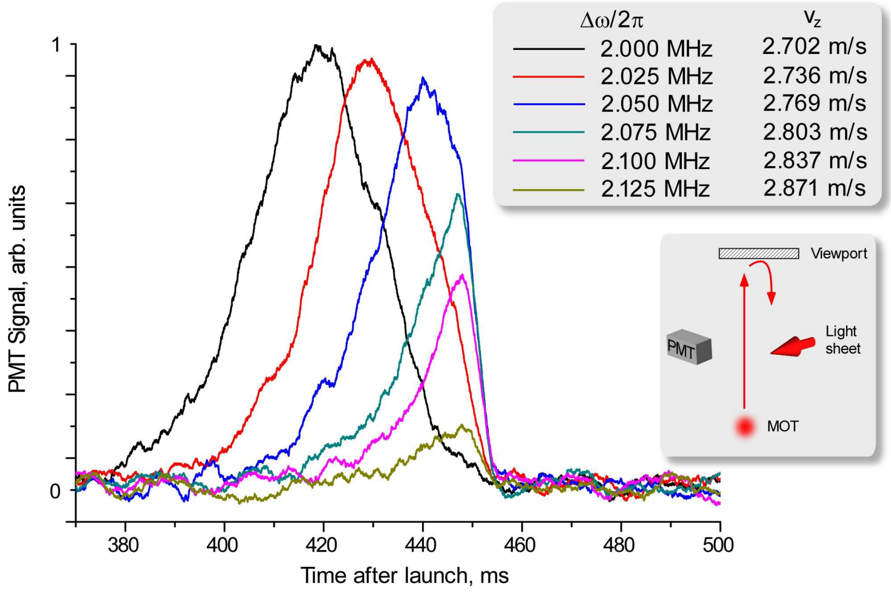

Figure 4.11: Precision control of the fountain launch height. Several atomic clouds are launched to various heights where the maximum turning point of the cloud is chosen to be progressively closer to the top viewport of the science chamber. The cloud is detected after it falls down again by probing it with a resonant light sheet and recording fluorescence with a PMT (see lower inset). The right flank of the fluorescence signals is abruptly cut off for fast launch velocities, v_z, revealing that atoms in a faster velocity class collide with the viewport and are lost. The upper inset lists the MOT light detunings (see Eq. (4.3)). Adapted from Ref. [88].

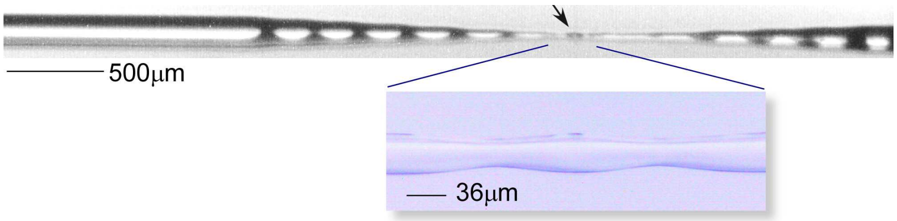

Figure 4.12: Optical microscope images of the resonator and supporting fiber used in experiments in Chaps. 7 and 8. The diameter of the unprocessed fiber is 200 μm and the resonator diameter is 36 μm. Both images were obtained through the front viewport of the science chamber using a variable zoom imaging system with a working distance of 90 mm. Adapted from Ref. [96].

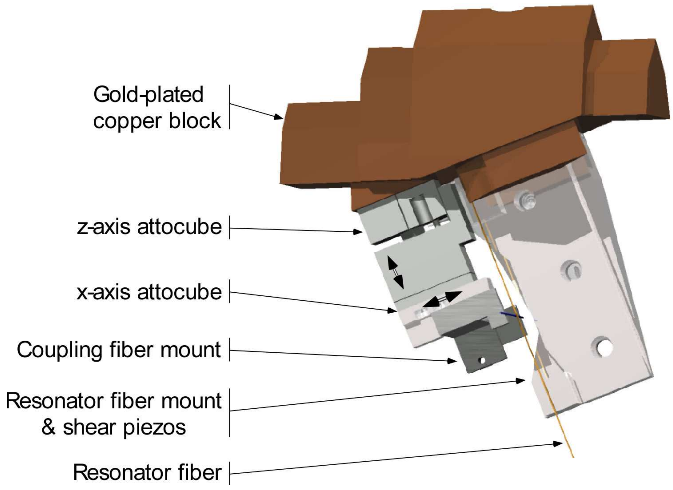

Figure 4.13: Side-view of the fiber translation stages and the resonator setup. The coupling fiber axis is perpendicular to both the resonator fiber axis and image plane. Only the translation stages for one coupling fiber are shown for clarity.

it is possible to align the coupling fiber. Mechanically, the coupling setup in Fig. 4.13 is very stable in a vacuum environment with good temperature stabilization of the vacuum chamber. We observe a drift of around 500 nm in the relative separation of the coupling fiber and resonator over approximately one week (see Sec. 5.2 for details).

A problem noted by several research groups is the issue of baking the Attocube translation stages and piezo-seizing. The piezo slip-stick motion may sieze during baking even if the maximum temperature during the bake is about 135°C, which is less than the maximum rated temperature of 150°C. In this situation, it may be possible to fix the problem by increasing the velocity and step-size to the maximum values and trying to move the piezo with the ANC350 controller, but only when confident that the piezo is at room temperature — piezo movement at elevated temperatures is not advised. Precautions should be taken to ensure that no translation stage is at the limit of the slip-stick travel range when baking. The voltage on the ANC350 stepper drive should be set to 0 V while baking. Apart from baking, the translation stages should be (dis)mounted on the copper block with the utmost care, and attention should be paid to the amount of force applied to all moveable parts. When these guidelines are closely followed, we have generally not experienced problems with their operation.

4.2.6 Vibration isolation

Mechanical vibrations transmitted through the vacuum chamber to the coupling fibers must be minimized because the coupling gap to the resonator must not drift by more than approximately ten nanometers, otherwise the fiber–resonator coupling would significantly change. Acoustic vibrations transmitted through air, on the other hand, are not a major problem since the fiber setup is in a vacuum environment, however the absence of air damping increases the quality factor of mechanical vibration modes. The fiber setup in Fig. 4.13 is attached to a 2 kg copper block which rests on four viton toroidal rings. These viton rings provide the only direct contact with the vacuum chamber and are therefore a critical design element. Here, several details of the design are outlined.

A single viton ring can be modelled as a spring with a spring constant k and a damping constant C. Measurements from an experiment verifying Hooke's law for the viton rings yield the value $k = 82$ kN m^{-1} per ring, which is very similar to the results in Refs. [97, 98]. The damping constant for a ring with a length of about 4.5 cm and diameter of 3 mm supporting a mass of $m = 2/4$ kg $= 0.5$ kg is $C \approx 50$ N s m^{-1} [98]. With a single level of damping, the setup is described as a first order system which can be written as [97]

$$s^2 mX + sCX + kX = (k + sC)Y \ , \tag{4.10}$$

where X is the response following a perturbation Y. We have made the transformation $s \to i\omega$, as is convention. The transfer function is then

$$\frac{X}{Y} = \frac{k + sC}{s^2 m + sC + k} \ , \tag{4.11}$$

which has so-called *zeros* at $s = -2 \times 10^3$ Hz and *poles* at $s = 5.1 \pm 110.5i$ Hz. Finally, the transfer function with all the data for a single ring is then

$$\frac{X}{Y} = \frac{50s + 0.8 \times 10^5}{4.9s^2 + 50s + 0.8 \times 10^5} \ . \tag{4.12}$$

The frequency response of this function for four rings can be straight-forwardly calculated with $k = 0.3 \times 10^6$ N m^{-1}, $m = 2$ kg, and a larger damping coefficient of $C = 100$ N s m^{-1} [98]. Analyzing this we find a mechanical resonance at 20 Hz and a roll-off of 20 dB/decade for higher frequencies, as expected for a first order system. At 2 kHz there is more than 40 dB of noise suppression, which is effective in the vertical direction of motion, and partially effective in lateral motion.

Vibrations originating from within the fiber setup should also be damped. By using a massive copper block, onto which the setup is attached, vibrations will be attenuated because a large amount of energy is required to move the block. In addition, structural vibrations of the building should be attenuated by the optical table. The center-of-mass of the complete setup of vacuum chamber and optical table is calculated to be about 5 cm above the surface of the table and has the maximum possible distance to each of the four legs supporting the table, thus ensuring the best stability.

We find that it is possible to work normally on the vacuum chamber table and to even drop metal tools on the table surface without appreciably disturbing the resonator frequency or distance stabilization schemes. Therefore, we conclude the vibration isolation measures are effective.

4.3 Laser systems

The observation of strong coupling between a ^{85}Rb atom and a bottle mode requires a number of lasers to firstly cool the atoms and launch them to the resonator, but also to probe the interaction.

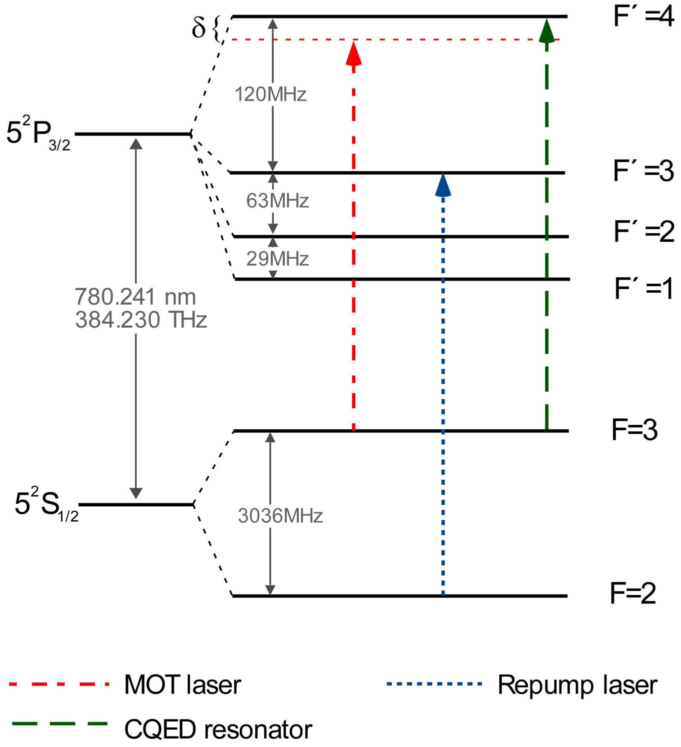

Figure 4.14: Hyperfine structure of the $^5S_{1/2} \rightarrow ^5 P_{3/2}$ transition for ^{85}Rb and frequencies of the experiment laser light (after passing through AOMs).

Three diode lasers in either Littrow or Littman-Metcalf configuration serve these purposes and are described in the following.

4.3.1 Cooling laser

Laser light from a Littman-Metcalf diode–tapered-amplifier laser system (MOPA, Sacher Lasertechnik GmbH) is set to a frequency that is red-detuned from the $F = 3 \rightarrow F' = 4$ cooling transition as shown in Fig. 4.14. The system is composed to a diode laser (labelled *master*) with an output power of 20 mW which seeds a tapered amplifier with an output power of 1 W (labelled *slave*). A fraction of the light from the slave laser is sent to a Rb Doppler-free saturated absorption spectroscopy unit (CoSy, TEM Messtechnik GmbH) using a pellicle beamsplitter (BP108, Thorlabs).

Figure 4.15 shows the layout of the laser system for producing the six beams for the MOT and for stabilization. Light for frequency stabilization of the master laser is sent through an acousto-optic modulator (AOM) in a double pass cat-eye configuration using the -1 diffraction order light (3200-124, 200 MHz, Crystal Technology LLC/ EQ Photonics GmbH). Several hundred microwatts of light is then fiber coupled in a polarization maintaining (PM) fiber and sent to the CoSy unit. Fiber coupling is especially important for this device in order to ensure the light correctly propagates through the Rb gas cell and optics.

The laser frequency is stabilized using frequency modulation spectroscopy (also known as dither locking). First, a weak 400 kHz signal from a function generator is applied to a frequency-tunable AOM driver (1200AF-AEF0-2.5, Crystal Technology LLC/ EQ Photonics GmbH) using a bias-tee. From the frequency modulated light, the CoSy unit generates a Doppler-free error signal which is pre-amplified (ZFC-500-LN+, Mini-circuits) and mixed with the signal from the function generator. After low pass filtering, the output signal from the mixer is sent to a proportional-integral (PI) controller which controls the master laser piezo. The advantages of performing frequency stabilization using modulation spectroscopy instead of the simpler side-of-fringe stabilization are two-fold: (a) the error signal has a dispersive shape that allows the frequency to be stabilized at a well-defined value, and (b) drifts in laser power will not affect the frequency, to first approximation. We use the cross-over peak of the transitions $F = 3 \rightarrow F' = 3$ and $F = 3 \rightarrow F' = 4$ for frequency stabilization because it provides the largest signal-to-noise ratio.[3] In initial experiments using side-of-fringe stabilization, we find a slow increase in the temperature of the cooled atomic cloud over a period of several hours, but this problem was eliminated once we switched to using modulation spectroscopy.

The output from the slave laser is used for the MOT and is split equally between two identical arms using a high power non-polarizing beamsplitter. Light in each arm is sent through a double-pass AOM and the -1 order light is fiber coupled into a 10-m–long polarization maintaining fiber connected to fiber clusters. The power in each fiber cluster is power stabilized using an internal photodiode that provides a measurement signal to a PI controller. The resulting correction signal is sent to the amplitude modulation port of the AOM driver to control the power. The stabilization loop corrects for fluctuations in the laser power and fiber coupling drifts and gives a standard deviation of 2.5×10^{-3} in the power. An important feature of the controller is that the power setpoint can be computer-controlled to, e.g., switch power for the polarization gradient cooling (see Appendix A) and fountain launching stages.

The frequency of the light going to the MOT is

$$\nu_{\mathrm{MOT}} = \nu_{\mathrm{CoSy}} + 2(\nu^{\mathrm{AOM}}_{\mathrm{SatAbs}} - \nu^{\mathrm{AOM}}_{\mathrm{Cooling}}) \ , \tag{4.13}$$

where $2\nu_{\mathrm{CoSy}}$ is the frequency of the light in the CoSy unit, $\nu^{\mathrm{AOM}}_{\mathrm{SatAbs}}$ is the driving frequency of the AOM for frequency stabilization, $\nu^{\mathrm{AOM}}_{\mathrm{Cooling}}$ is the driving frequency of the AOM in either of the cooling beam paths. The frequency of the light coming from the Slave (and Master) is

$$\nu_{\mathrm{laser}} = \nu_{\mathrm{CoSy}} + 2\nu^{\mathrm{AOM}}_{\mathrm{SatAbs}} \ . \tag{4.14}$$

Therefore, if all three AOMs are driven at the same center frequency, the frequency of the light going to the MOT chamber will be the same as the frequency of the atomic transition/cross-over peak used in the frequency stabilization path. Such an AOM configuration is advantageous because it allows us to use AOMs with high center frequency and large bandwidth: AOMs with low center frequency tend to have a small bandwidth, i.e., they have limited tunability. All the AOMs used in this work operate at a center frequency of 200 MHz and have a relatively large bandwidth of 50 MHz.

---

[3] Cross-over peaks are located midway between two transitions and are an artefact of laser spectroscopy of multiple transitions in atomic gases [99].

The AOM operating frequency in the frequency stabilization path is set by a voltage controlled oscillator (VCO), while the operating frequency for the other two AOMs for the lower and upper MOT beams is set by two individual 1-channel direct digital synthesizers (DDS, Crystal Technology LLC/EQ Photonics GmbH). The output from each DDS is frequency doubled to around 200 MHz and amplified to around 2 W before connecting to the AOMs. The extremely high frequency resolution (sub-hertz) of the DDS greatly improves the stability of the fountain launch compared to a VCO-controlled system.

Another important factor in the fountain operation is the power balance of the six cooling beams. An improperly balanced setup will firstly cause the MOT to be shifted off-center due to radiation pressure, and secondly, will cause a deviation in angle from the desired fountain launch direction. To overcome this problem we use a fiber cluster, which is a modular unit consisting of two half-wave plates and two polarizing beamsplitters that split the incoming light into three fiber-coupled output ports.[4] There is an additional 1/99 beamsplitter for sampling the incoming light which is measured on a passive photodiode and used for intensity stabilization. Using this setup, the power in each output fiber from the cluster is set equal to an accuracy of 0.2 mW with a maximum output power of 25 mW. The typical output power measured at the vacuum chamber is 20 mW.

4.3.2 Repump laser

The repump laser (DL 100, Toptica Photonics AG) is stabilized to the $F = 2 \rightarrow F' = 3$ transition. This laser is required because there is a small but significant probability of off-resonantly exciting the atom on the $F = 3 \rightarrow F' = 3$ transition with the cooling laser light, which after a spontaneous emission event can decay to the $F = 2$ state, which is a dark state. Since the atomic scattering rate for the repump laser on is almost negligible compared to the cooling laser, the polarization of the repump light is not important.

Figure 4.16 shows the setup of the laser system. As with the cooling laser, the -1 diffraction order light from both AOMs is used with each operating at a center frequency of around 200 MHz. The signal for $F = 2 \rightarrow F' = 3$ transition from the saturated absorption spectroscopy is used to stabilize the laser frequency by controlling the AOM driver frequency. However, unlike the cooling laser, side-of-fringe stabilization is used because a small detuning from the transition is acceptable, and also because the scheme is simple to implement. This scheme is improved by stabilizing the power going to the saturated absorption spectroscopy using an internal photodiode in the CoSy unit and a PI controller that feeds a correction signal back to the AOM in the arm labeled frequency stabilization. About 5 mW of power in the repump light is sent through a CF16 viewport and intersects the cooling lasers at the MOT position.

4.3.3 Resonator laser

The resonator laser system (DL Pro, Toptica Photonics AG) fulfills three main tasks: (a) probing the spectral properties of the atom-light interaction, (b) stabilizing the resonator frequency and in-coupled power, and (c) performing fountain diagnostics. Figure 4.17 shows the setup, which

---

[4] The collimators at the MOT chamber have an internally mounted quarter-wave plate for producing $\sigma^{\pm}$ light.

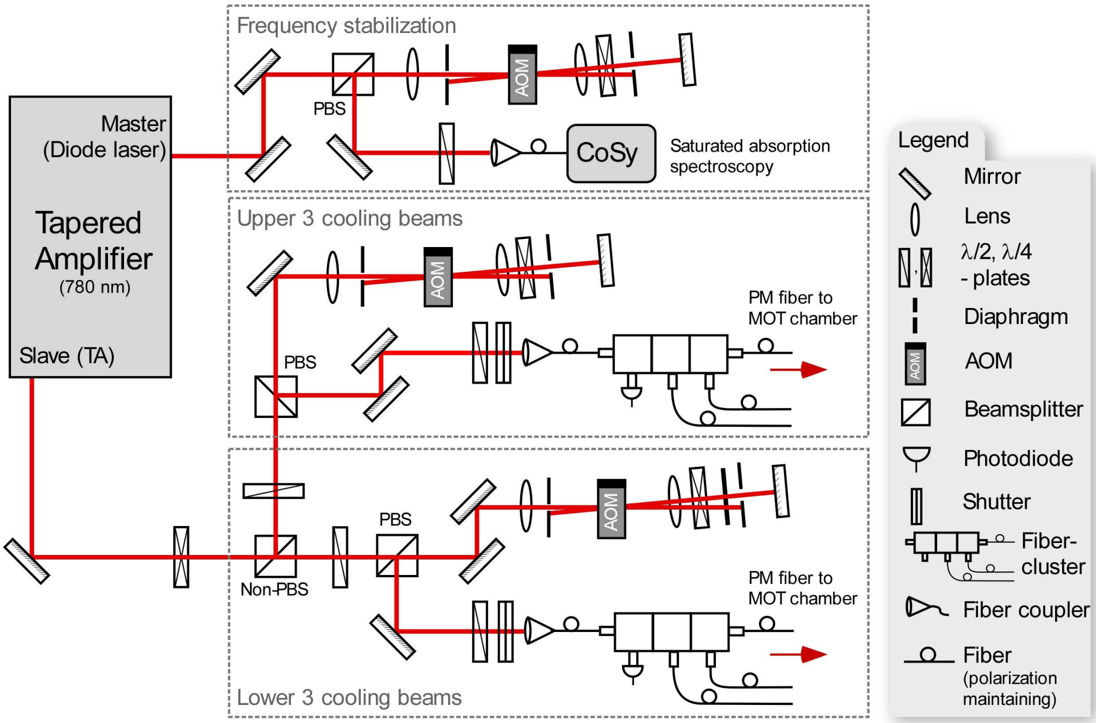
Frequency stabilization
PBS
AOM
Master
(Diode laser)
CoSy
Saturated absorption spectroscopy
Tapered Amplifier
(780 nm)
Slave (TA)
Upper 3 cooling beams
AOM
PBS
PM fiber to MOT chamber
AOM
PBS
Non-PBS
PM fiber to MOT chamber
Lower 3 cooling beams
Legend
Mirror
Lens
λ/2, λ/4
- plates
Diaphragm
AOM
Beamsplitter
Photodiode
Shutter
Fiber-
cluster
Fiber coupler
Fiber
(polarization
maintaining)

Figure 4.15: Laser setup for cooling ^{85}Rb atoms in the MOT. The output light from a Sacher Lasertechnik diode–tapered-amplifier laser system (MOPA) is equally split with 50/50 beamsplitter into two arms – one arm for the three upper cooling beams and the other for the three lower cooling beams. The power and relative frequency detuning of both arms are independently controlled using AOMs driven by two power amplified digital synthesizers. Frequency stabilization is performed using the output from the seeding diode laser (labeled *Master*) which is sent to a saturated absorption spectroscopy module. Adapted from Ref. [88].

is similar in design to the two other laser systems: the laser is locked to a saturation spectroscopy and an array of polarizing beamsplitters divide the laser power between several paths where the -1 order diffracted light from each AOM is fiber coupled. The saturation spectroscopy setup here is identical to the setup described earlier for the cooling laser. This laser is used for a large variety of critical tasks in our experiment which are explained in the following.

Resonator frequency stabilization: Frequency stabilization of the resonator to the $F = 3 \to F' = 4$ transition frequency requires a phase modulated light to implement the Pound-Drever-Hall stabilization scheme (see Chap. 5 for details). Phase modulation is accomplished with a tunable electro-optic phase modulator (EOM, EO-FT43L, Qubig GmbH) operating at an RF frequency.

Since this light couples to a resonator mode having a well-defined polarization, it is critically important to ensure that there are no polarization drifts in the laser light. Even when

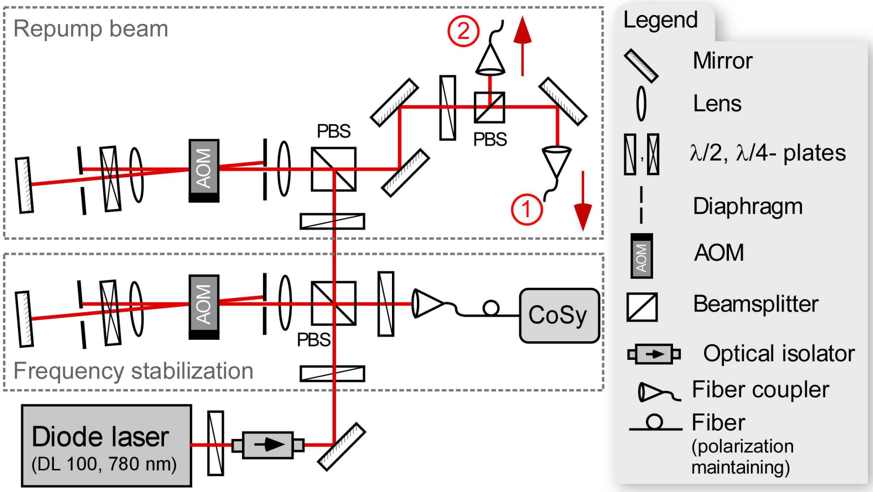

Figure 4.16: Laser setup for repumping cooled ^{85}Rb atoms on the transition $F = 2 \rightarrow F' = 3$. The output light from a Toptica Littrow diode laser (DL100) is split with a polarizing beamsplitter into two arms — one arm for frequency spectroscopy and the other for the actual repump light sent to the MOT chamber. Output ① is sent to the vacuum chamber and the beam overlapped with the MOT using a collimator. Output ② is combined with light used in the light sheet in the science chamber. Adapted from Ref. [88].

using PM fiber this issue can be problematic due to imperfect polarization matching with the incoupling free-space light and slight variations in the birefringence of the fiber caused by the ambient environment. In the setup here, the light is coupled into a 10 m-long PM fiber which transports the light from the laser table to the vacuum chamber table. To minimize this polarization problem, a highly birefringent Berek compensator plate (YVO$_4$ crystal, FOCtek Photonics Inc.) acts as a tunable waveplate that ensures the polarization axis of the free-space light is perfectly matched to the polarization axis of the fiber. In addition, a wire-grid linear polarizer placed before the plate increases the polarization purity to $> 1 : 1000$. Details of the alignment procedure for the Berek compensator, and the associated polarization analyzer device, are documented in Ref. [100]. As an alternative to this polarization setup, a Glan-Taylor polarizer mounted in a rotation mount can equally well serve to ensure the polarization axes are aligned, though this option is typically more expensive.

Distance stabilization: Closed-loop stabilization of the distance of the coupling fiber into the resonator also requires an EOM for phase modulation, however at a different RF frequency. Apart from this, all other optical components are the same.

Atom detection: The experiment must react with sub-microsecond response times to the coupling of an atom to the evanescent field of the bottle resonator. The frequency of the atom detection light is tuned to the resonator frequency and the power level adjusted to achieve maximum sensitivity to atom-induced transmission changes on the output of the coupling fiber, and is set to around 100 fW or equivalently, 0.3 intracavity photons. As with the other beams, polarization is also critical here and a linear polarizer and Berek compensator are again used.

Atom-cavity spectroscopy and light sheet: Following the detection of an atom, the atom-light interaction is a probed with a separate laser frequency having a preset atom–light detuning and power, optimized for the actual cavity QED experiment. This setup (labeled *spectroscopy light* in Fig. 4.17) consists of optical components that are identical to the atom detection path. Additionally, a 50/50 beamsplitter directs light to an optical fiber where it can be used for fountain diagnostics by sending it as a light-sheet through the science chamber.

Furthermore, all light sent to the resonator setup is power stabilized in a similar manner as in the laser cooling setup. Mechanical shutters block the laser light for resonator frequency and distance stabilization during the time-window where the atomic cloud interacts with the resonator. During this time-window, the error signals from both stabilizations are set to zero, thus rendering the stabilizations inactive for times longer than the integration time of the PI controller.

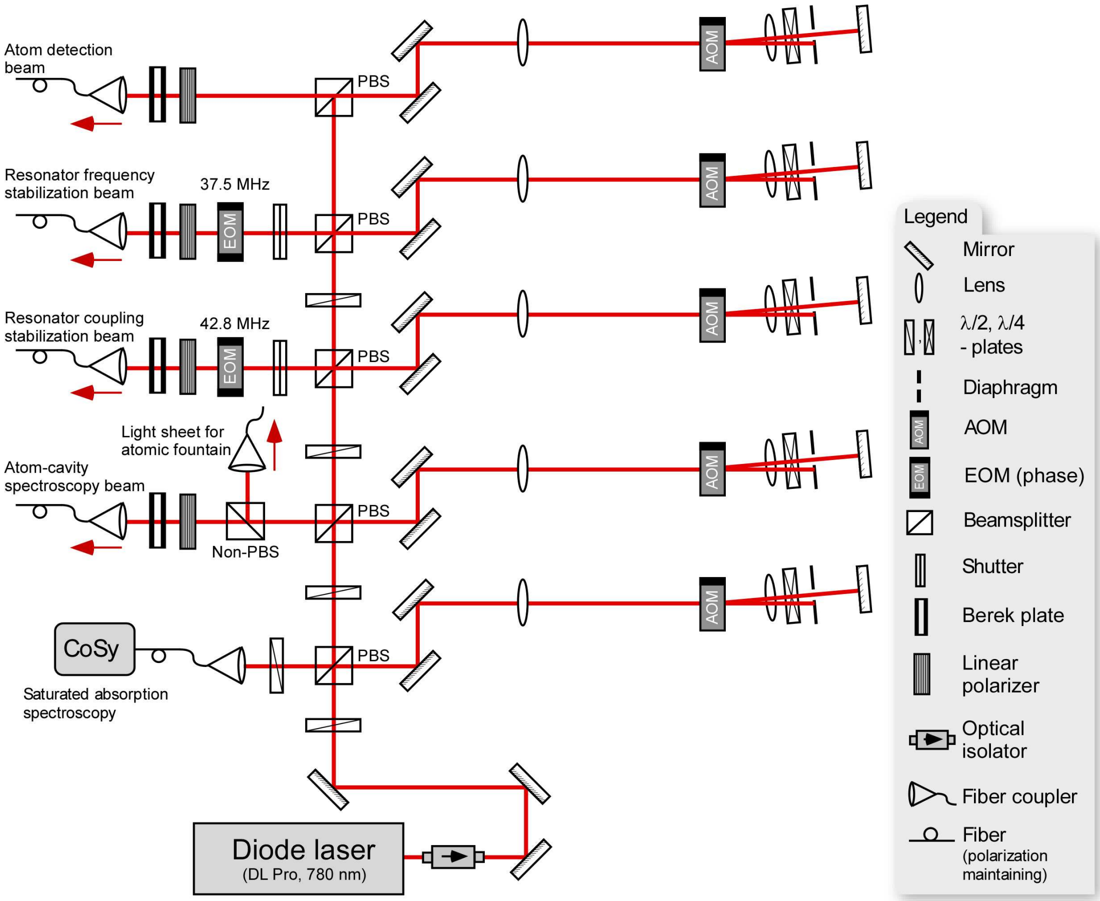
Atom detection beam
PBS
Resonator frequency stabilization beam
37.5 MHz
EOM
PBS
Resonator coupling stabilization beam
42.8 MHz
EOM
PBS
Light sheet for atomic fountain
Atom-cavity spectroscopy beam
Non-PBS
PBS
CoSy
Saturated absorption spectroscopy
PBS
Diode laser
(DL Pro, 780 nm)
AOM
AOM
AOM
AOM
AOM
Legend
Mirror
Lens
λ/2, λ/4 - plates
Diaphragm
AOM
EOM (phase)
Beamsplitter
Shutter
Berek plate
Linear polarizer
Optical isolator
Fiber coupler
Fiber (polarization maintaining)

Figure 4.17: Laser setup for probing the atom-resonator interaction and stabilizing the resonator and coupling fiber. AOMs are used to control both the power and frequency in each beam, while EOMs are used in a Pound-Drever-Hall resonator stabilization scheme (see main text of next chapter).

CHAPTER 5

Realization of Frequency and Distance Stabilization of Ultra-high-Q Modes

In the context of cavity QED experiments as well as other applications, it is important that the resonator can be made resonant with an arbitrary frequency fixed by, e.g., an atomic transition. The ability to tune the resonance frequency of microresonators to other frequency-critical elements is especially important when developing sophisticated optical processing applications. For example, many cavity QED quantum information protocols rely on mapping the quantum state of one two-level system onto an optical field and then transferring it to another, remote two-level system. Such cavity QED quantum networks require multiple resonators to be mutually resonant and to be linked, e.g., by optical fibers [32]. In these situations, it is important to be able to stabilize the resonance frequency of the resonator to an external reference frequency with a high degree of precision. The need for frequency stabilization in the case of ultra-high-Q WGM microresonators is made even more apparent by considering the typical situation where a temperature change of only 1 mK is enough to change the resonance frequency by one linewidth. For example, in a recent cavity QED experiment involving the strong coupling between Cesium atoms and a WGM microtoroid the atom-cavity interaction was hampered by thermally induced drifting of the resonator resonance frequency [48].

Apart from frequency stabilization, the coupling of light from a coupling fiber into a WGM microresonator must also be stable. Light is coupled into such resonators by matching the phase and frequency of the field of the evanescent coupler with the WGM while the coupling strength is set by their spatial overlap [29]. This coupling strength determines the intracavity intensity for a given input power. The latter is maximized in the case of so-called critical coupling. For this reason, the situation of critical coupling is desirable for many microresonator applications. Evanescent coupling of light to WGMs so far has mostly relied on the passive stability of the

---

Parts of this chapter appear in “Active frequency stabilization of an ultra-high Q whispering-gallery- mode microresonator,” *Appl. Phys. B*, 99, 623, (2010), and “All-optical switching and strong coupling using tunable whispering-gallery-mode microresonators,” *Appl. Phys. B*, 105, 1, 129, (2011).

setup, which typically exhibits long-term drifts on the timescale of tens of minutes. However, in order to maintain a stable intracavity intensity, the gap between an evanescent coupler and a WGM microresonator must remain stable within a few tens of nanometers.

In this chapter I describe the implementation of a Pound-Drever-Hall (PDH) stabilization technique to stabilize the resonance frequency of a bottle resonator to an external cavity diode laser which is in turn stabilized to the ^{85}Rb D$_2$-transition. I also introduce a simple technique to actively stabilize the evanescent coupling of light between a WGM bottle microresonator and two optical coupling fibers. The stabilization of a critically coupled resonator yields a residual transmission of $\sim 1 - 2 \times 10^{-2}$ over several days of continuous operation of the cavity QED experiment. Both stabilizations operate simultaneously in our setup. A complementary PDH-based technique to actively stabilize the coupling gap is described in both Ref. [101] and the dissertation of Christian Junge and will not be described here. A major technical achievement of the present setup is its ability to continuously operate in a highly sensitive cavity QED experiment for periods of up to two weeks without any intervention.

In the first part of the chapter, the frequency stabilization scheme is characterized in an ambient air environment. Both the thermal response of the resonator and the performance of the stabilization scheme are then characterized in the vacuum chamber used for the cavity QED experiment. In vacuum, the resonance frequency of the optical mode is observed to be more sensitive to thermal effects arising from the absorption of laser light and the absence of air cooling. In the second part of the chapter, the fiber distance stabilization is demonstrated during actual cavity QED measurements.

5.1 Active frequency stabilization

5.1.1 Introduction

Earlier work has demonstrated the frequency stabilization of a laser to a microtoroid resonator [50], but this is insufficient for applications requiring a resonator (or network of resonators) to be resonant with a given dipole emitter. A large tunable glass sphere, with 0.5 mm diameter and 10^6 Q-factor, was locked to a laser using a lock-in technique [102]. However this method is bandwidth-limited by the intensity build-up time of the resonator. Moreover, the recapture range, i.e., the frequency range over which the resonator remains locked while subject to disturbances, is determined by the resonator linewidth. It has also been demonstrated that the thermal self-stabilization of resonators can be used to maintain a constant power in a resonator [69, 103]. However, apart from the fact that the optical power is a constrained parameter using this technique, it may fluctuate and drift over time due to external perturbations, translating into frequency fluctuations and drifts of the resonator. In addition, it is not possible to directly lock to the center of the resonance using thermal self-stabilization.

As an alternative, the Pound-Drever-Hall technique can be used to achieve frequency stabilization of optical resonators [104, 105]. It offers several advantages, namely, it effectively decouples power fluctuations from frequency fluctuations, has a large recapture range, and is not limited by the resonator bandwidth.

5.1.2 Principle of Pound-Drever-Hall stabilization

Among the various schemes used to stabilize resonators, the PDH scheme is generally the preferred choice for the reasons outlined above. The principle of the scheme relies on the detection of the phase of light transmitted past the resonator–fiber coupling junction, as described in Fig. 5.1.

The transmission amplitude is given by the coherent interference of the uncoupled light transmitted past the resonator with the light leaking out of the resonator after having undergone many revolutions in the resonator via total internal reflection. On resonance, both fields have the same amplitude but the phase shifts by π as the frequency is scanned across the resonance and it follows that there is complete destructive interference, as shown in Fig. 5.1 (a, b). The width of the resonance defines the slope of the phase shift and thus, it is possible to identify a position on either flank of the resonance by observing the phase. However, light detectors measure the intensity and not the phase, and since the intensity varies symmetrically across the resonance, it is not a good error signal for frequency stabilization to the center of the resonance.

The PDH scheme solves this issue by phase modulating the input laser light in order to generate frequency side-bands. The modulation of the light with, for example, an electro-optic modulator (EOM) operating at a frequency ν_{mod} generates frequency sidebands around the resonance at $\nu_0 \pm \nu_{\mathrm{mod}}$, as shown in Fig. 5.1 (c). It is necessary to have ν_{mod} greater than the linewidth of the resonance $\Delta\nu$, otherwise the technique is termed simply as frequency modulation stabilization. Interference of the sidebands with the light from the resonator produces a beat signal with the required phase information, which is extracted by multiplying this signal with the modulation frequency using a mixer.

The amplitude of the PDH error signal for light of frequency ν is given by the relation [105]

$$\epsilon(\nu) = -2\sqrt{P_c P_s}\,\mathrm{Im}\{t(\nu)t^*(\nu + \nu_{\mathrm{mod}}) - t^*(\nu)t(\nu - \nu_{\mathrm{mod}})\}\ . \tag{5.1}$$

The power in the carrier at frequency ν_0 is P_c, and the power in the sidebands is P_s. For a WGM resonator, the transmission amplitude $t(\nu)$ is given by [106]

$$t(\nu) = \frac{-\Delta\nu - 2i(\nu - \nu_0)}{\Delta\nu + 2i(\nu - \nu_0)}\ . \tag{5.2}$$

The slope of the error signal in the normalized plot in Fig. 5.1 (c) is $m = -4/\Delta\nu$, and becomes steeper for narrower linewidths. A more detailed discussion of the PDH scheme can be found in Refs. [52, 105]. We next describe the implementation and characterization of the PDH technique with the bottle resonator.

5.1.3 Setup of the resonator frequency stabilization

Light is coupled into the resonator with the sub-micron diameter waist of a coupling fiber. The coupling fiber is placed at the position of a caustic and perpendicular to the resonator axis. The gap between the coupling fiber and the resonator is controlled with a sub-nanometer resolution using a piezoelectric actuator and is set to a few hundred nanometers, sufficient for the evanescent fields of both to spatially overlap [29]. Following the resonator, the coupling fiber is split

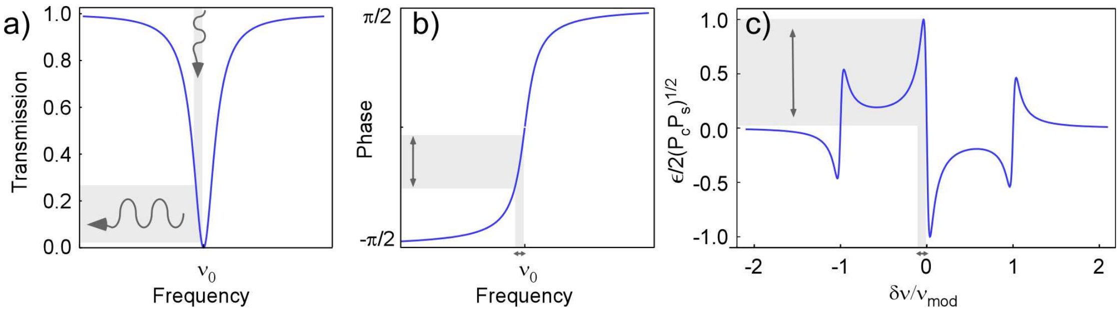

Figure 5.1: Concept of Pound-Drever-Hall frequency stabilization. (a, b) Frequency and phase response of the transmitted light from a WGM resonator. The phase changes by a maximum of π as the frequency is scanned across the resonance. By observing the transmission while modulating the frequency of a laser it is possible to determine if the laser is either red or blue detuned with respect to the resonance. (c) Pound-Drever-Hall error signal as a function of frequency detuning $\delta\nu$. When the modulation frequency Ω_{mod} is much larger than the resonance linewidth $\Delta\nu$, the dispersive error signal ϵ has a distinct shape encoded with phase information, thus making it useful for frequency stabilization.

using a 0.5/99.5 coupler with 99.5% going to a resonant avalanche photodiode (APD, typically 0.5–3 μW) and 0.5% going to a high-gain APD (typically 3–15 nW), having a bandwidth of $\sim$3 MHz.[1] For initial tests, the setup is placed in a box with a regulated, clean air supply.

Pulling on one fiber end with a shear piezo (P-141.10, Physik Instrumente GmbH & Co. KG, mechanical resonance frequency of 100 kHz) elongates the resonator causing the size and refractive index to change, thus shifting the resonance frequency [25]. The spectral properties of the resonator and characteristics of the frequency lock are analyzed using a grating stabilized diode laser (DL Pro, Toptica Photonics AG) around 780 nm with a specified short term ($< 5\ \mu$s) linewidth of 100 kHz.

An EOM (EO-FT43L, Qubig GmbH) phase modulates the laser beam and is driven by a local oscillator running at 42.8 MHz. This frequency is large enough for the sidebands to be distinguishable from the carrier in the resonator spectrum, which has a linewidth of 2–4 MHz, dependent upon the particular resonator mode. Higher modulation frequencies would in principle yield a larger recapture range of the locking scheme but the resulting signal would suffer from interference from ambient noise due to radio signals. The resonant APD is tuned to 42.8 MHz and enables the detection of powers as low as 100 nW at a -3 dB bandwidth of 300 kHz. The signals from the local oscillator and photodiode are mixed, low-pass filtered, and sent to a PI controller where a correction signal is generated. This is in turn amplified and fed back to the resonator shear piezo. Care is taken not to excite resonances in the control loop by using a 4 kHz single-pole low-pass filter before the piezo, thereby fixing the bandwidth of the control loop. The closed-loop characteristics of the lock are analyzed by measuring both the transmitted power with the high-gain APD and the correction signal sent from the PI controller to the piezo.

---

[1] The high-gain APD is exclusively used for PDH stabilization in later experiments in Chaps. 7 and 8 and Secs. 5.1.7 and 5.2.

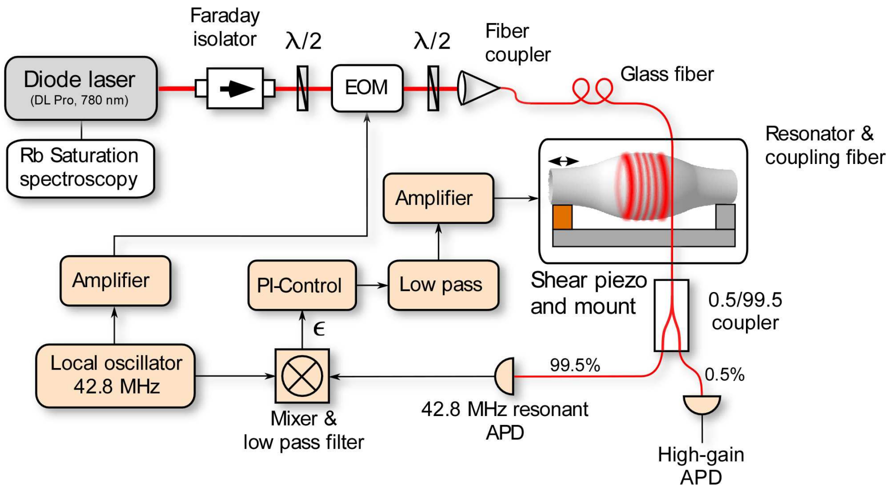
Faraday isolator
λ/2
λ/2
Fiber coupler
Glass fiber
Diode laser
(DL Pro, 780 nm)
EOM
Rb Saturation spectroscopy
Resonator & coupling fiber
Amplifier
Amplifier
PI-Control
Low pass
Shear piezo and mount
0.5/99.5 coupler
ϵ
Local oscillator 42.8 MHz
99.5%
0.5%
Mixer & low pass filter
42.8 MHz resonant APD
High-gain APD

Figure 5.2: Schematic of the Pound-Drever-Hall stabilization setup and resonator geometry. Frequency sidebands at 42.8 MHz are generated in the laser beam spectrum by phase modulating it with an electro-optic modulator (EOM). For clarity, the scale of the resonator is exaggerated with respect to the resonator mount.

Resonator holder design

To achieve active stabilization of UHQ bottle microresonators in the cavity QED experiment, it was necessary to design a special-purpose resonator mount compatible with the requirements of ultra high vacuum (10^{-10} mbar) while maintaining full tunability over 400 GHz and operability with a high bandwidth up to the kHz range. Finite element simulations were critical in ensuring our design was rigid enough to push mechanical resonances up to several kHz. Figure 5.3 shows the resonator mount and the associated support structure with the first six resonances occurring primarily around the shear piezos used for tuning and stabilization. By using only the lower piezo for active stabilization and the top piezo to apply a constant offset voltage, we can neglect the first three resonances (Fig. 5.3 (a) to (c)) because they will not be excited. This assumption is reasonable since external sources of vibration should be minimal because the mount and coupling setup is carefully isolated from external vibrations using viton cushions in the vacuum chamber. The mechanical motion of the fourth resonance is not in the direction of motion of the piezo and may similarly not be excited. The fifth and sixth resonances (Fig. 5.3 (e) and (f)) around 19 kHz show clear oscillations in the direction of piezo motion and set an upper limit on the achievable stabilization bandwidth.

5.1.4 Stabilization performance in air

We stabilize a 50-μm–diameter resonator, with an ultra-high-Q and an axial FSR of 230 GHz, to a laser which is in turn stabilized to the D$_2$-transition of ^{85}Rb using a Doppler-free rubidium spectroscopy set-up (COSY, TEM Messtechnik GmbH). As a reference measurement, the resonator's spectral lineshape is acquired using 2–3 μW of incident power, see Fig. 5.4 (a), suf-

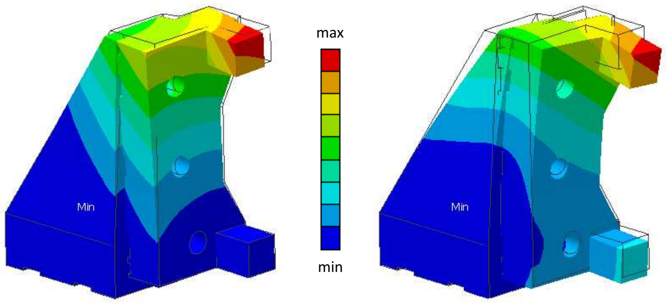

(a) Resonance frequency: 6.5 kHz (b) Resonance frequency: 7.8 kHz

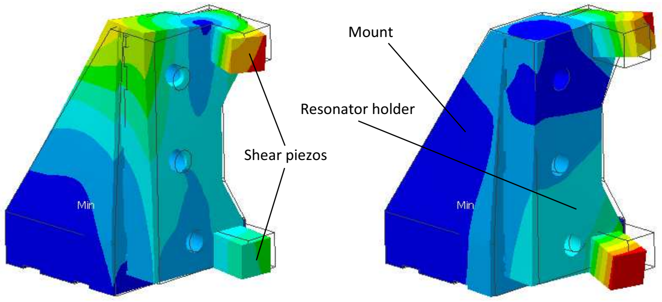

(c) Resonance frequency: 12.6 kHz (d) Resonance frequency: 15.8 kHz

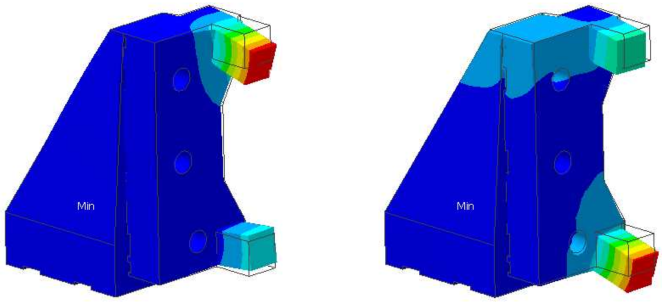

(e) Resonance frequency: 18.6 kHz (f) Resonance frequency: 19.7 kHz

Figure 5.3: Finite element simulations of the six lowest mechanical resonance frequencies of the resonator holder device. The resonator fiber (not shown) is held between two shear piezos that are glued to a resonator holder which is in turn mechanically attached a triangular mount, of which both are made of aluminum. The amplitude of the relative motions is indicated by color coding and is also graphically displayed (displacement is exaggerated).

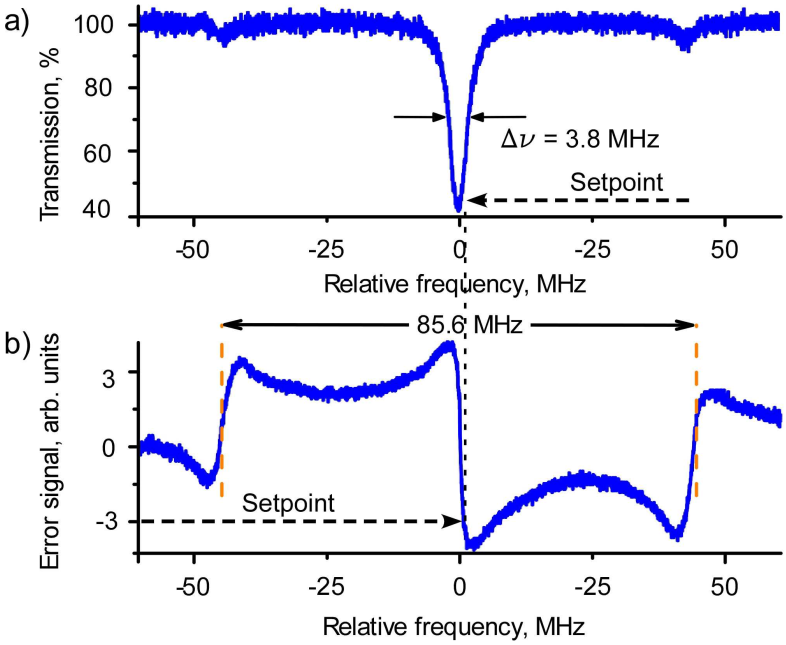

Figure 5.4: Stabilization of an ultra-high Q-factor bottle mode. The mode lineshape (a) reveals a linewidth of 3.8 MHz and is in reasonable agreement with the linewidth of 2.5 MHz estimated from the PDH error signal, see (b). (c) When the resonator is stabilized to the laser, fluctuations are visible around the setpoint of the transmitted power. The rms value of these fluctuations is 206 kHz and is marked with dashed lines. The data is measured with 2–3 μW of launched power. The transmission measurement in (a) is measured with the high-gain APD and the error signal in (b) is measured with the resonant APD.

ficiently low for thermal effects to be neglected. Using the sidebands as frequency markers, the frequency axis is calibrated and the linewidth is estimated to be roughly 3.8 MHz. Based on the slope of the error signal at 0 MHz in Fig. 5.4 (b), the linewidth of the resonance is approximately $\Delta\nu \approx 4U_{\mathrm{m}ax}/m$, where $2U_{\mathrm{m}ax}$ is the peak to peak value of the error signal and m is the slope [105]. Using this method, the linewidth is estimated to be 2.5 MHz, in reasonable agreement with the spectral measurement and confirming the correct operation of the setup. Taking the former measurement this corresponds to a loaded Q-factor of 1.0×10^8 or an intrinsic Q-factor in excess of 2×10^8 [27].

We quantify the performance of the stabilization scheme by measuring the fluctuations of the transmitted power. Since these fluctuations are zero to first order when the resonator–laser detuning fluctuates around zero, we purposefully introduce an offset to the setpoint of the PI controller. This results in a non-zero resonator–laser detuning and relative frequency fluctuations between the laser and the resonator are thus directly converted into intensity fluctuations. The setpoint for the PI controller is indicated by the horizontal dashed lines in Fig. 5.4. With the resonator stabilized in Fig. 5.5 (a), fluctuations around the setpoint correspond to a rms frequency

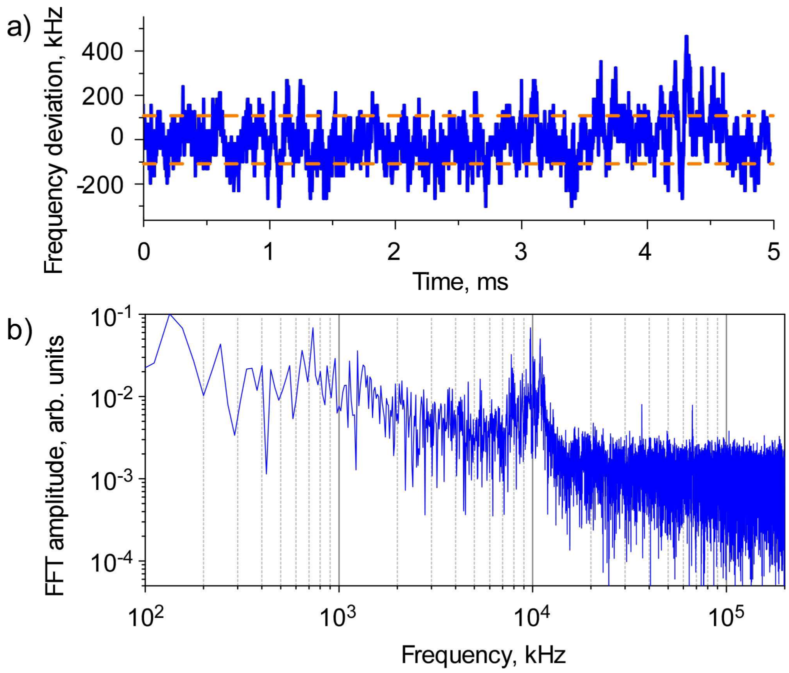

Figure 5.5: Frequency noise of an ultra-high Q-factor bottle mode. (a) When the resonator is stabilized to the laser, fluctuations are visible around the setpoint of the transmitted power. The rms value of these fluctuations is 206 kHz and is marked with dashed lines. (b) FFT of the frequency fluctuations. The data is measured with 2–3 μW of launched power. The measurement in (a) is measured with the high-gain APD.

noise of 206 kHz or 5.4% of the linewidth over a time interval of 5 ms.[2] This time interval is 20 times longer than the response time of the resonator lock, which is limited by the 4 kHz low-pass filter. It is noted that while the resonator is critically coupled, the presence of off-resonant side-bands prevent full extinction of the transmission when on resonance.

There are believed to be two significant sources of frequency noise in these measurements. Electrical noise in the high gain voltage amplifier connected to the shear piezo reduces the signal-to-noise ratio. Also, the linewidth of the laser, at 100 kHz, is comparable to the rms frequency deviation of the stabilized resonator. A Fourier transform of the frequency noise in Fig. 5.5 (b) reveals a strong frequency component at 8–12 kHz, which is beyond the bandwidth of the control loop. Mechanical resonances of the resonator holder at 7.8 kHz and 12.6 kHz, shown in Fig. 5.3 (c,d), may be the cause of these frequency components.

On a longer timescale, the stabilization scheme also has to compensate for slow frequency drifts of the resonator. The magnitude of these drifts can be extracted from the closed loop

---

[2] Interestingly, the fractional frequency uncertainty is 2×10^{-10}, which for a $q = 1$ axial mode would be equal to the fundamental limit of around 2×10^{-10} imposed by the thermorefractive noise of silica [24]. The actual axial mode number used in this measurement is $q \gg 1$ and the mode volume is about a factor of four larger than the $q = 1$ case, but further optimization should make it possible to reach this fundamental limit for $q = 1$.

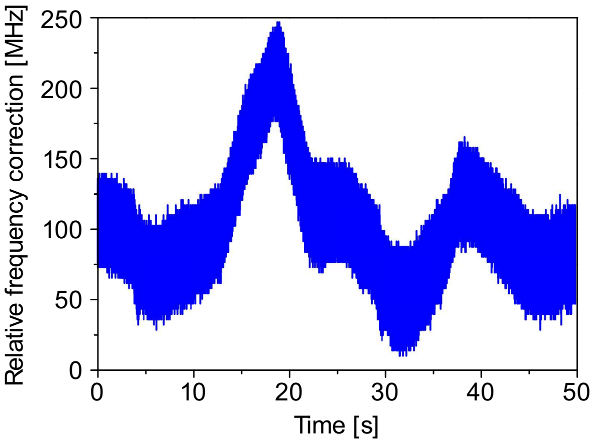

Figure 5.6: Slow frequency drifts of the stabilization scheme. When the resonator is stabilized to the spectroscopy-stabilized laser, the correction signal sent to the piezo is proportional to the compensated frequency drift of the resonator. The signal is measured before the 4 kHz low pass filter.

correction signal. Using the spectroscopy stabilized laser, we monitored the correction signal for 50 seconds in a resonator with a linewidth of 2 MHz (see Fig. 5.6 for a typical trace). Significant frequency corrections over a range of 250 MHz, or over 100 linewidths, are visible despite efforts to passively minimize vibrations and temperature changes. We note that the resonator remained stabilized during the entire measurement.

5.1.5 Thermal bistability

Thermal bistability is a widely studied non-linear effect in microresonators governed by intracavity power and material absorption of light [70]. The large power densities found in microresonators can lead to temperature changes which distort the observed resonance. This effect results in an apparent broadening or narrowing of the resonance, depending upon the resonator–laser scan direction. We investigate this effect by probing another resonator, with the same dimensions and characteristics as the previous one, while simultaneously monitoring the transmitted power and error signal with a standard high bandwidth (130 MHz) photodiode. The resonator is excited with several tens of microwatts and the resonator frequency is scanned at a rate of 220 MHz ms^{-1}. The transmission of the carrier in Fig. 5.7 (a) shows a distinctive triangular lineshape for decreasing frequency, while the lineshape significantly narrows for increasing frequency. This behavior is paralleled in the response of the error signals, see Fig. 5.7 (b). In addition, thermal shifting of the resonance frequency causes uneven spacing of the sidebands; with increasing frequency, the carrier and upper sideband are pushed toward higher frequencies due to the sign of the temperature dependence of the refractive index. The sideband is shifted less than the carrier due to thermal relaxation.

Not surprisingly, in the presence of thermal bistability, it is impossible to stabilize the resonator with zero resonator–laser detuning because this point is an unstable solution to the bista-

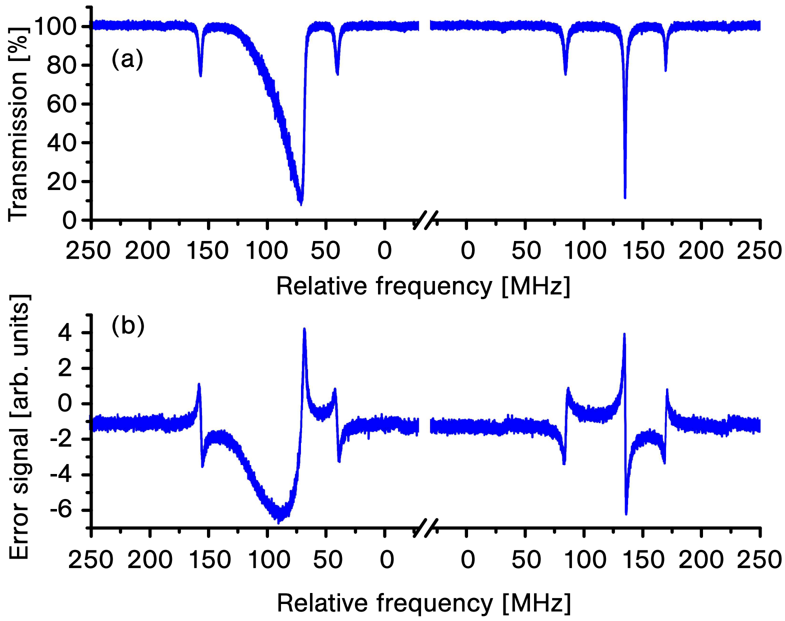

Figure 5.7: Thermal bistability of a resonator mode. (a) With decreasing frequency (left), the transmission of the carrier appears broadened, and with increasing frequency (right), the transmission of the carrier appears narrowed. Correspondingly, the error signals are also distorted, see (b).

bility equation of the system [50]. In the scan with decreasing frequency the zero crossing of the error signal is shifted by -66 MHz with respect to the scan with increasing frequency. Therefore, thermal bistability is an undesirable feature for the purposes of frequency locking which has to be avoided by using low laser powers. In our experiment the intra-cavity power is negligible, but care must be taken during the frequency stabilization phase.

5.1.6 Mode-splitting

Rayleigh scattering caused by surface roughness or inhomogeneities within the glass lifts the degeneracy of clockwise and anti-clockwise propagating modes, see Sec. 3.3.2 [107]. This non-degeneracy, termed mode splitting, can be modeled as two coupled oscillators with scattering mediating the exchange of energy. The magnitude of the mode-splitting is a function of the scattering rate and can range from a fraction of the resonator linewidth to several times the linewidth. While mode-splitting generally does not affect the intrinsic Q-factor, it can severely limit the loaded Q-factor [27]. We investigated the influence of mode-splitting on the error signal. Again, we used resonators with similar dimensions and characteristics as the previous ones. When the splitting between the modes is very small ($\lesssim 1$ loaded linewidth), there is a frequency band between the modes where the transmission is essentially constant. This means that the typically sharp π phase jump at resonance instead has a flattened region where the phase is constant. Figure 5.8 (a) clearly shows these regions on both sidebands and the carrier.

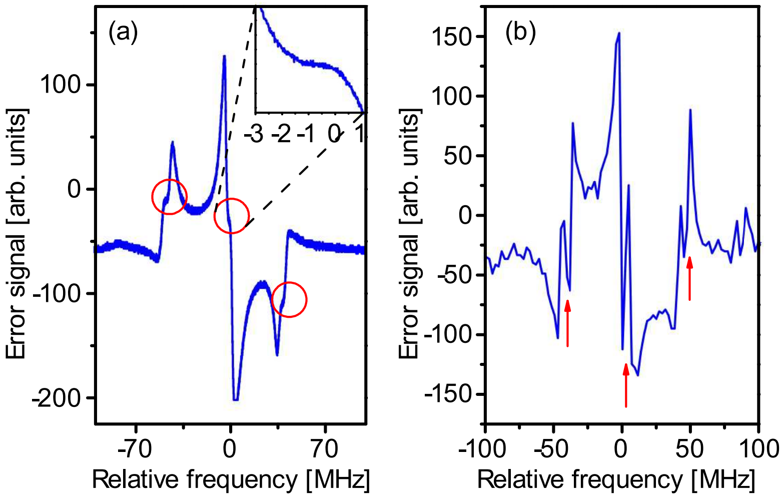

Figure 5.8: Mode splitting in two different resonator modes. (a) Resonances with small mode-splitting cause small plateaus (highlighting circles) in the PDH error signal near critical coupling. (b) Under-coupled resonances with large mode-splitting result in sign changes of the slope (arrows) meaning that the phase changes non-monotonically.

Stabilization to the carrier in this region is problematic because this frequency band acts as a dead-zone. When the mode-splitting is large ($>$ 1 linewidth), and the resonator is under-coupled, the phase changes twice — once for each mode. Figure 5.8 (b) shows large, sharp features on the sidebands and carrier. Again, stabilization is problematic because acoustic and electrical noise makes it difficult to use the PI controller to lock to one of the modes and may induce jumps to the other mode at any time.

5.1.7 Stabilization performance in vacuum

The frequency stabilization measurements have been reproduced in ultra high vacuum. Light, with as little as 15 nW of power, transmitted past the fiber-resonator coupling junction is detected on a high gain APD. The signals from the local oscillator and APD are mixed, low-pass filtered, and sent to a PI controller where a correction signal is generated. This is in turn amplified and fed back to the resonator shear piezo. Care is taken not to excite mechanical resonances in the resonator fiber by using a 100 Hz low-pass filter before the piezo, thereby fixing the bandwidth of the control loop.

We quantify the performance of the stabilization scheme and experimental setup in our ultra-high vacuum chamber, under conditions compatible with the requirements of a single atom cavity quantum electrodynamics experiment. For this purpose, we measure the fluctuations of the transmitted power. We again purposefully introduce an offset to the setpoint of the PI controller. The setpoint for the PI controller is indicated in Fig. 5.9 (a). With the resonator stabilized in Fig. 5.10 (a), fluctuations around the setpoint correspond to a rms frequency noise of ± 209 kHz or around 8% of the resonator linewidth over a time interval of 50 ms. This time interval is 5

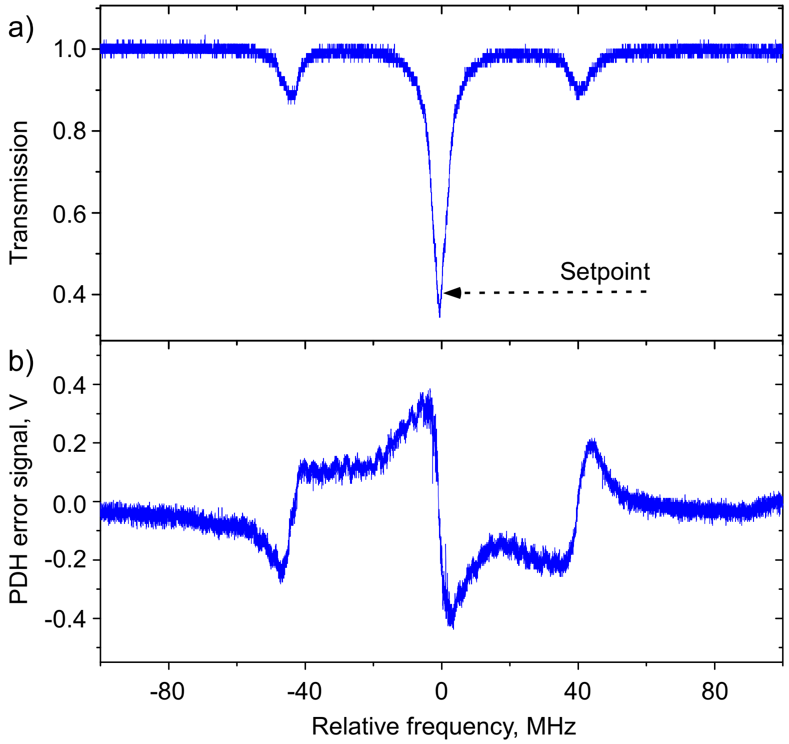

Figure 5.9: Ultra-high Q-factor bottle mode in a vacuum of 2×10^{-9} mBar. The mode lineshape (a) reveals a linewidth of 5.4 MHz ($Q_0 = 1.4 \times 10^8$) which is calibrated using sidebands as frequency markers. The corresponding PDH error signal is shown in (b).

times longer than the response time of the resonator lock. In this setup we have tested the lock for periods of up to one hour without any degradation in performance.

Insight into the response of the lock when operating in vacuum is gained by plotting an FFT spectrum of the frequency deviations, shown in Fig. 5.10 (b).

5.1.8 Thermal response in vacuum

Silica ranks among one of the lowest absorbing materials with as little as 0.2 dB/km loss at 1.5 μm wavelength, and 3.5 dB/km loss at 0.78 μm wavelength. But, nevertheless, the absorbed light is converted into heat. This issue is particularly pertinent to monolithic microresonators where high Q/V ratios facilitate huge power build-up factors and therefore extremely high power densities. For example, with just 1 μW of power coupled into a bottle resonator, the circulating intensity can reach 1 MW cm^{-2}, leading to high power densities and thermal gradients in a very small volume. The heat dissipated in the mode volume influences the resonator radius, R, and refractive index, n, and this in turn shifts the resonance frequency, ν, according to the relation

$$\frac{\delta\nu}{\nu} = \left(\frac{1}{R} \cdot \frac{\partial R}{\partial T} + \frac{1}{n} \cdot \frac{\partial n}{\partial T}\right) \cdot \Delta T, \tag{5.3}$$

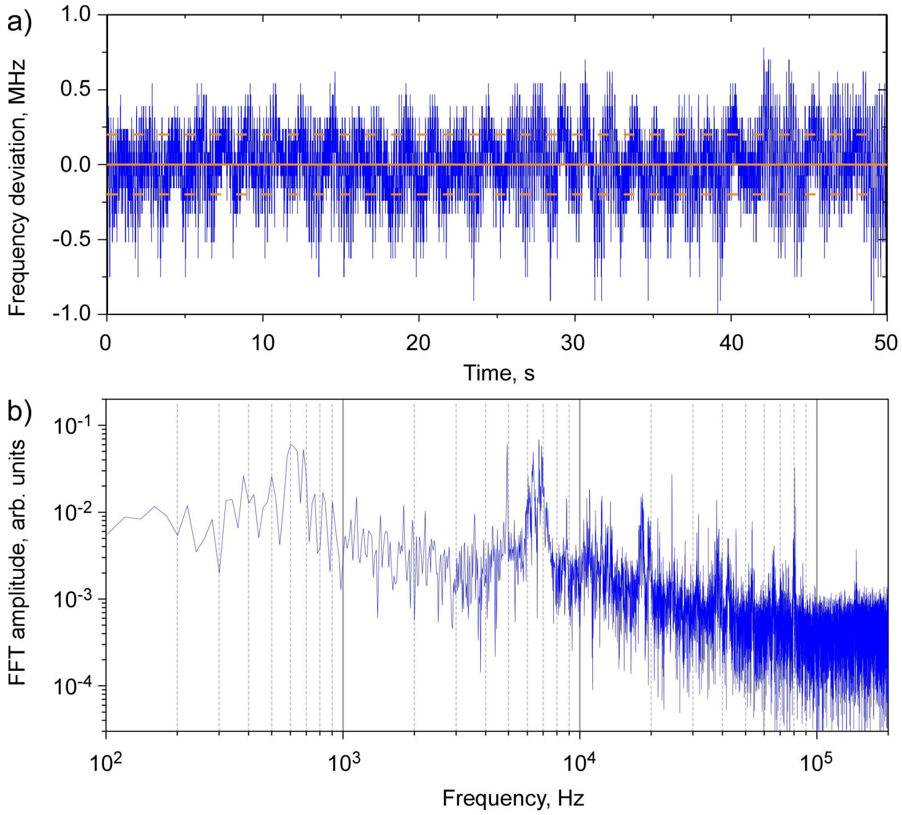

Figure 5.10: Stabilization of an ultra-high Q-factor bottle mode in vacuum. (a) Frequency deviation: when the resonator is stabilized to the laser, which is in turn stabilized to the D_2-transition of ^{85}Rb using a Doppler-free spectroscopy setup, fluctuations are visible around the setpoint of the transmitted power. The rms value of these fluctuations is 418 kHz and is marked with dashed lines. (b) FFT spectrum of the frequency deviations in (a).

where $\frac{1}{R}\frac{\partial R}{\partial T} = 0.6 \times 10^{-6}/°C$ is linear expansion coefficient of silica, ΔT is the change in resonator temperature, and $\frac{1}{n}\frac{\partial n}{\partial T} = 1.3 \times 10^{-5}/°C$ is the thermo-optic coefficient [108, 109]. Placing the resonator in a vacuum exacerbates the issue by denying one of the heat dissipation routes, i.e., convection from the mode volume to the ambient environment. This leaves heat conduction through the resonator material as the dominant dissipation mechanism. In contrast, other experimental and theoretical work in the Rauschenbeutel group has found that thermal radiation is the dominant loss factor in silica nanofibers [110], however we will not focus on nanofibers here. While the resonator will reach a thermal equilibrium if continuously probed with a CW laser light of constant power, many applications, such as the strong-coupling presented in Chap. 7, involve pulsing the power. Accordingly, this causes the resonant frequency to change over time, depending on the operating conditions.

We have investigated the thermal response characteristics of a frequency stabilized bottle resonator having high Q-factor and near critical coupling in vacuum. In particular, the step response of the resonator mode frequency is studied by first locking the resonator and then abruptly turning off the locking laser light. The development of the resonance frequency of the mode follows a typical exponential response according to the equation $\nu(t) = A\left(1 - e^{-t/\tau}\right)$, where A is a pre-factor in units of megahertz and τ is the thermal time constant of the resonator. The setup used here is similar to that used for frequency locking the resonator in Sec. 5.1.7 except for the addition of a sample-and-hold circuit before the shear piezo that maintains the resonator at constant mechanical strain when the locking laser is turned off. An AOM performs the switching of the light with a rise/fall time of a few tens on nanoseconds. The drift of the resonance frequency of the mode is recorded by probing the transmission every 15 ms for a duration of 50 μs when the locking laser light is turned off, see Fig. 5.12. Simultaneously with the probing, the PDH error signal is recorded and reveals the direction in which the frequency of the mode has drifted. Figure 5.11 shows the drift rate, $R = A/\tau$, has a linear dependence with laser power and can be as much as 0.5 MHz/ms for a laser power of just 120 nW. For the resonator mode considered here, this power is enough to shift the resonance by about 10% of the linewidth in 2 ms. Extrapolating the results to higher powers indicates that with 1 μW of power the mode will be shifted by around 40% of the linewidth in 1 ms, thus affecting the transmission very strongly. A thermal time constant of $\tau = 105$ ms was measured from data taken for powers of 15 nW and 20 nW. This is considerably longer than a similar measurement with a bottle resonator in air which found a time constant of 13–15 ms [38].[3] The difference is attributed to the relative importance of conductive and convective cooling mechanisms. For resonators with ultra high quality factor it is thus necessary to use very low powers to lock the resonator. A simple feedforward loop has been implemented for the experiments in Chap. 7 in order to help compensate the drift.

5.1.9 Summary

We have demonstrated active frequency stabilization of a WGM bottle microresonator with an ultra-high Q-factor in excess of 2×10^8 using the Pound-Drever-Hall technique. To the best of our knowledge, this is the first demonstration of active frequency stabilization of an ultra-high Q-factor WGM microresonator using this technique. In particular, our results show that strain tuning of the resonator can be realized with sufficient bandwidth to lock the resonator. The residual rms frequency noise of the lock was 206 kHz, or 5.4% of the resonator linewidth, and represents 3.4% of the natural full width at half maximum of the D_2 line of ^{85}Rb. Our locking scheme thus highly suited with the requirements of cold-atom cavity quantum electrodynamics experiments. Finally, we studied the effects of thermal bistability and mode-splitting on the locking technique. Both effects are shown to interfere with a successful frequency stabilization of the resonator but can be reduced by using low locking laser powers as well as high quality resonators, respectively.

---

[3] The thermal diffusion coefficient, $k_{\mathrm{th}}/(\rho c_p)$, is a factor of 25 times larger for air (2.2×10^{-5} m^2 s^{-1}) than for silica (8.9×10^{-7} m^2 s^{-1}), indicating the dominance of air over silica in cooling. Thermal conductivity: k_{th}. Heat capacity: c_p. Density: ρ.

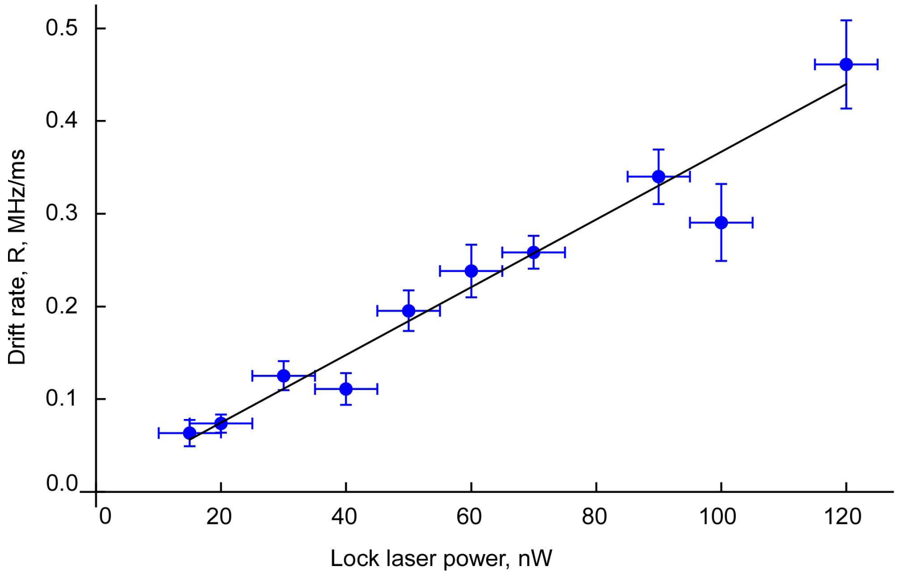

Figure 5.11: Dependence of the drift rate of a resonator mode on lock laser power. Increasing the power causes the absorption and therefore the drift rate to increase linearly.

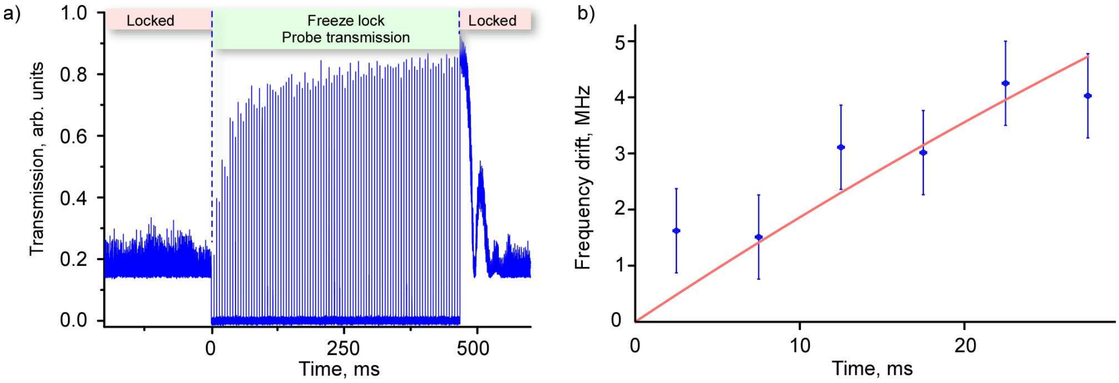

Figure 5.12: Temperature dependent drift of the frequency of the resonator mode. (a) The resonator is first frequency stabilized on resonance. Then, the response of the resonator to a sudden change in power is probed for about 450 ms before turning on the frequency stabilization again. (b) Exponential fit to the data in (a) with a thermal relaxation time constant of $\bar{\tau} = 105$ ms. $Q_{\mathrm{crit}} = 4.2 \times 10^7$, Input laser power = 50 nW.

5.2 Distance stabilization of evanescent coupling

Closed-loop control delivers the greatest benefit when used in noisy environments where it regulates a variable, which in this case is the resonator-fiber gap. Temperature fluctuations around the vacuum apparatus are a major source of drift in the resonator coupling because it causes the mechanical parts within the vacuum chamber to expand and contract. When the experiment was operating in Mainz, we implemented a closed-loop stabilization technique, as described in Ref. [101]. After moving the experiment into a new lab having excellent temperature control we found that the passive coupling stability significantly improved. The changes specifically involved (a) enclosing the optical table supporting the vacuum chamber with a curtain that restricted acoustic noise and air currents, and (b) dedicating an independent temperature control system to the table where temperature fluctuations are now only 100 mK.

With these changes implemented, we decided to switch from closed-loop coupling stabilization to open-loop stabilization, which offered a number of practical benefits. Namely, this enables (a) a reduction in the intra-cavity power since only one stabilization laser is required to actively stabilize the resonator frequency, (b) removal of the closed-loop stabilization electronics, and (c) an improvement in the resistance to long-term polarization drifts since one one laser beam is required for both frequency and open-loop fiber stabilization — previously an additional laser beam for closed-loop stabilization was required. Critical coupling is achieved by simply scanning the coupling fiber over a range of approximately -100 nm to +100 nm around the expected critical coupling position while recording the transmission (see Fig. 5.13 (a, b)). The position where the transmission reaches a minimum as measured on APD 1 corresponds to the critical coupling position. Following this simple routine, the critical coupling position is automatically re-calibrated approximately every 30–40 minutes using a LabView program for data acquisition and control of the Attocube translators.

The stabilization of the position of the second coupling fiber is an equally important issue for optical routing and add-drop filter applications [37]. Early experiments in our group with two coupling fibers ([37]) did not use a feedback signal to correct drifts in the fiber position. These experiments only required the coupling to be stable for a matter of a few seconds or minutes in order to acquire the desired signal, which is feasible in practice without active stabilization. Notwithstanding that, the setup was very prone to acoustic and mechanical noise. In contrast, our cavity QED experiments with one and two coupling fibers require the fiber distances to be stable for hours or days in order to acquire sufficient data. An added benefit of stabilization is that it enables the transfer efficiency of the add-drop filter in Ref. [37] for example, to be completely computer controlled.

It is straightforward to incorporate a second coupling fiber into the stabilization scheme. In this case, we implement the following steps in a software algorithm:

- Similar to the case where only one fiber is used, we first find the critical coupling position, $x_{\rm cc}$, for fiber 1 with fiber 2 pulled back about 2 μm from the resonator so that there is negligible coupling to the resonator. This is measured on APD 1. Fiber 1 is moved to position $x_{\rm cc} + x_{\rm off}$ where $x_{\rm off}$ has been pre-determined to yield critical coupling for fiber 1 when fiber 2 is coupling to the resonator.

- Fiber 2 is brought closer to the resonator while recording the transmission on APD 2. The transmission in Fig. 5.13 (c) has a monotonic trend because only fiber 1 is pumped with light — light from fiber 1 couples into the resonator and out to fiber 2.

- In the example of Fig. 5.13 (c), the coupling of fiber 2 is chosen so as to couple out 10 % of the resonator light. In practice, this is achieved by noting the position of fiber 2 where the photodiode at the output of fiber 2 reaches a particular pre-determined voltage, which is 0.197 in this case.

The scheme, while simple, has proven to be robust against long-term drifts and enables experiments to run continuously for more than many hours as shown in Fig. 5.13 (d). In other experiments, we have achieved the long-term stabilization of two fibers where the coupling efficiency between fiber 2 and the resonator is 90%.

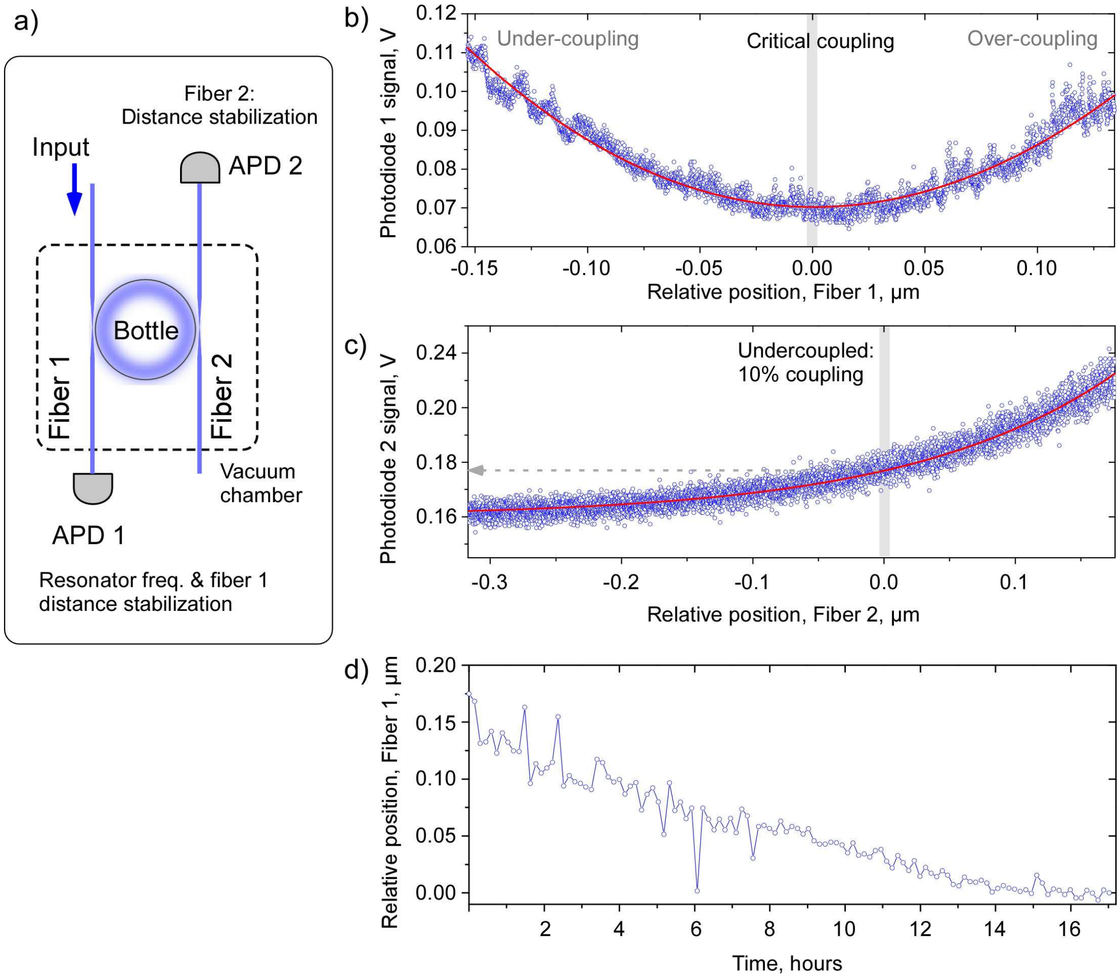

Figure 5.13: Alignment of two fibers to a resonator mode using Attocube translators. (a) Schematic of the setup with two coupling fibers. (b) The transmission of fiber 1 reveals the critical coupling position as the point where the transmission is minimized. This is measured with APD 1. (c) The power coupled from fiber 1 to fiber 2 is a monotonic function when fiber 2 is scanned. The position at 0 μm corresponds to a photodiode signal of 0.197 and marks the point where fiber 2 couples 10% of the light out of the resonator from fiber 1. This is measured with APD 2. For reasons of computational speed, a quadratic fit (solid red line) serves as a good approximation to the transmission response in (b, c). (d) Typical long-term drift of the critical coupling position for fiber 1 over several hours.

CHAPTER 6

Optical Fiber Network and Experimental Control

6.1 Optical Fiber Network

At the heart of the experimental setup is an optical fiber network that interfaces the laser systems with the resonator setup. A fully fledged fiber-based system, rather than free-space optic system, is a natural choice for a fiber-based WGM resonator. This choice facilitates complex optical systems to be constructed by *splicing* together different optical elements using standard fiber-splicing technology. The very low loss of optical fibers is an equally important issue for quantum optics experiments with single-photons since every lost photon means a loss of information on the quantum system under investigation. Moreover, a fiber-based setup naturally lends itself to the development of quantum networks where multiple cavity QED setups can be spliced together [32].

In the experiment, all light sent to the resonator is fiber coupled. The fiber network transports light used in several tasks: resonator frequency stabilization and distance stabilization of the coupling fibers, the detection of atoms interacting with the resonator, and measuring the atom–resonator spectrum with spectroscopy light. In addition, it enables the collection of photons in all four output ports when two coupling fibers aligned with the resonator. In the following, I will give a detailed description of these tasks.

6.1.1 Network layout

Both the detection and the spectroscopy light and, in addition, the frequency and distance stabilization light in Fig. 4.17 must be sequentially launched through the coupling fiber in the vacuum chamber. Figure 6.1 shows the layout of the fiber network with several fiber couplers for combining and splitting the different optical beams.

The detection and spectroscopy light are coupled to two fiber-coupled Mach-Zehnder modulators (NIR-MX800-LN-10, Photline Technologies) for on/off switching of the light at gigahertz modulation frequencies. The modulators are fitted with an internal photodiode used for bias voltage calibration and intensity stabilization and are each capable of providing an optical extinction ratio of 27–30 dB. Such a large extinction ratio is necessary to limit the fast homodyne oscillations to about 10% of the power between the detection and spectroscopy light. Homodyne oscillations arise because light from the same laser source is split and then, after passing through the modulators, recombined on a fiber beam-splitter. For example, during the experimental sequence the spectroscopy modulator transmits light while the detection modulator blocks light, which is equivalent in configuration to a local-oscillator and weak signal in a homodyne setup. The signal measured at the photodetector is $I = E_d^2 \cos^2(\omega_d t + \phi) + E_s^2 \cos^2(\omega_s t) + 2E_s E_d \cos(\omega_d t + \phi) \cdot \cos(\omega t)$, where $E_d(E_s)$ is the electric field of the detection(spectroscopy) fields, ϕ is a phase between the fields, $\omega_d(\omega_s)$ is the frequency of the detection(spectroscopy) field, and t is time. The last term in the relation shows that, in this example, the strong spectroscopy light enhances the signal from the weak detection light. Therefore, our experiment requires a high extinction ratio in order to suppress this effect.

Following the modulators, the polarization can be adjusted to match the polarization of the resonator mode using a linear polarizer, half-wave plate, and quarter-wave plate all placed in a fiber bench (FB, model FB-38W, Thorlabs). The polarization of the stabilization light is similarly aligned using a second FB. Light from four optical fibers (atom detection and spectroscopy light, and frequency and distance stabilization light) is combined with fiber-based power couplers and spliced to coupling fiber 1.

Two coupling fibers can be simultaneously aligned with the resonator mode in an add–drop configuration [37]. As an alternative to sending the detection and/or spectroscopy light through fiber 1, this light can instead be sent through fiber 2 and the transmission in fiber 1 monitored. It is also possible to monitor the transmission in fiber 2. Details of the resonator frequency and distance stabilization with one and two coupling fibers is given in Chap. 5.

6.1.2 Photon detection

Light transmitted past the resonator–fiber coupling junction is either sent to an avalanche photodiode operating in proportional mode for frequency/distance stabilization of the resonator or, alternatively, to two single photon counting modules (SPCMs, model SPCM-AQRH-13FC, Laser Components GmbH/Perkin Elmer Inc.) in a Hanbury-Brown and Twiss configuration. The SPCMs are used for detecting the atom arrival, which is used to measure the transmission and photon statistics during the actual cavity QED experiment. This configuration has three main advantages: the SPCM deadtime is halved, the maximum detectable power is doubled, and it allows us to perform photon correlation measurements (Note: in this case, deadtime is not an issue). Light which is scattered into the counter-clockwise propagating resonator mode is outcoupled in the backward direction and recorded with the aid of two more SPCMs.

Table 6.1 gives the transmission and detection efficiencies for the various parts of the fiber network. The overall detection efficiency of a single photon inside the cavity is a product of the probability of being coupled to the fiber mode (0.5 at critical coupling, assuming only fiber 1 is present), and the efficiencies in Table 6.1, amounting to a total efficiency of 0.24 (i.e., 24%) for transmission and 0.26 for reflection. This efficiency can be almost doubled by using two fibers in an add–drop configuration where fiber 2 is strongly coupled. In this configuration the transfer

Table 6.1: Photon transmission and detection efficiencies.

Section of the fiber network	Efficiency
Fiber 1: Fiber taper transition to the waist	0.96
Fiber 1: Optical elements before detector (transmission)	0.85
Fiber 1: Optical elements before detector (reflection)	0.9
Fiber 2: Fiber taper transition to the waist	0.95
Fiber 2: Optical elements before detector (transmission)	0.9
Detectors at 780 nm (SPCMs)	0.6

efficiency from fiber 1 to fiber 2 can be as high as 0.9 while still maintaining a high Q-factor in the resonator [38]. The total photon detection efficiency for a photon entering the resonator from fiber 1 and being detected in fiber 2 is 0.46, which is about an order of magnitude better than in Fabry-Pérot cavities having similar properties [111] used in cavity QED experiments.

The data pulses from the SPCMs are sent to two data recorder cards (PCI Cobra Compuscope, Gage Applied Technologies Inc.) and a field-programmable gate array (FPGA).[1] The data cards record the transmission and reflection during the 85-ms–long experiment window with a maximum timing resolution of 2 ns. The role of the FPGA is to analyze the detected photons and to control the switching of the Mach-Zehnder modulators/switches in realtime. Further details are given in Sec. 6.2.4. Briefly, the FPGA decides when an atom is coupling to the resonator and subsequently turns off the atom detection light and simultaneously turns on the spectroscopy light for performing the actual experiment using the switches. The FPGA operates with a clock frequency of 100 MHz and controls the experiment on a sub-microsecond timescale, which is much shorter than the typical atom–resonator interaction time of several microseconds.

6.2 Experimental Control and Data Acquisition System

6.2.1 Motivation

Experimental measurements typically range in duration from a single day to several days of continuous operation where the number of experimental runs reaches several tens of thousand. During this time, numerous stabilization loops operate with bandwidths ranging from a few tens of kilohertz to one hour, while at the same time, data acquisition and certain experimental steps require sub-microsecond resolution. At this extreme end, data acquisition speeds of the SPCM pulses momentarily reach 125–500 MHz and the FPGA operates with a clock frequency of 100 MHz. Such a range of timescales from hours to tens of nanoseconds necessitates a multi-layered experimental control and data acquisition system which is outlined here.

---

[1] A Spartan-3 FPGA produced by Xilinx Inc. is mounted on an Opal Kelly board that provides an interface to the FPGA.

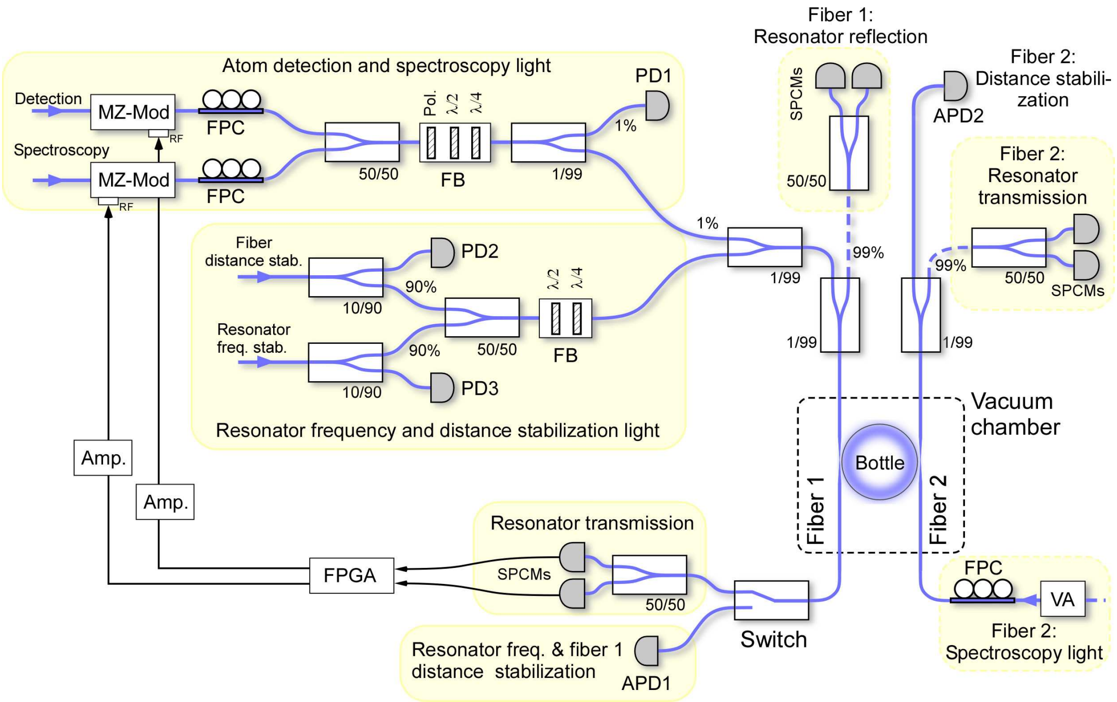
Fiber 1:
Resonator reflection
Fiber 2:
Distance stabili-
zation
Atom detection and spectroscopy light
PD1
Detection
MZ-Mod
FPC
RF
Spectroscopy
MZ-Mod
FPC
RF
Pol.
λ/2
λ/4
50/50
FB
1/99
1%
SPCMs
50/50
APD2
Fiber 2:
Resonator
transmission
1%
99%
1/99
99%
50/50
SPCMs
Fiber
distance stab.
PD2
90%
10/90
λ/2
λ/4
Resonator
freq. stab.
90%
50/50
FB
10/90
PD3
1/99
1/99
Resonator frequency and distance stabilization light
Vacuum
chamber
Bottle
Fiber 1
Fiber 2
Amp.
Amp.
Resonator transmission
FPGA
SPCMs
50/50
Switch
FPC
VA
Fiber 2:
Spectroscopy light
Resonator freq. & fiber 1
distance stabilization
APD1

Figure 6.1: Optical fiber network for atom detection and stabilization of the resonator and coupling fibers. Two coupling fibers (labeled fiber 1 and 2) are aligned with the bottle resonator in the ultra-high vacuum science chamber. Light for stabilization of both the resonator frequency and fiber-to-resonator power coupling are combined and coupled into fiber 1 using fiber-based power couplers. The polarization of the light is matched to that of the mode in the resonator using a fiber bench (FB) with two waveplates. The fiber power before the FB is stabilized using photodiodes (PD2, PD3) and AOMs in Fig. 4.17. The light transmitted past the resonator is detected on an avalanche photodiode (APD1). Light for detecting the presence of atoms interacting with the resonator and light for performing experiments with the system are also combined into fiber 1 (labeled detection light and spectroscopy light, respectively). The polarization in both arms is matched using fiber polarization controllers (FPCs) and aligned to the polarization of the resonator mode using a waveplates in the FB. This light can be routed to two SPCMs using a fiber switch. Reflected photons from the resonator can also be detected using two additional SPCMs. Alternatively, these two SPCMs can be used to monitor the light in fiber 2 (indicated by the dashed lines). For certain experiments, the spectrosopcy light is directly coupled into fiber 2 and the power attenuated using a variable attenuator (VA). See text for details.

6.2.2 Experimental control

A system of four desktop computers (Precision, Dell Inc.) is used for control and data acquisition with two of the computers acting as masters and the other two as slaves.

Two data acquisition and control cards (DAQ, models PCI-6259 and PCI-6733, National Instruments Germany GmbH) in one of the master computers provides analog and digital signals to control various parameters, such as power and frequency setpoints of AOM drivers, setpoints for optical power stabilization in fibers, triggers for mechanical shutters and SPCMs, current setpoints for the anti-Helmholtz MOT coils etc. Internal clocks on both DAQ cards are synchronised over an interconnecting RTSI cable and the timing resolution is variable from 2–10 μs. Custom control software,[2] written in LabWindows C, executes a measurement cycle defining how to control the DAQ cards, and also communicates with the other master computer. The parameters defining various measurement cycles (e.g. voltages and durations) are stored in a text file which is accessed through a user interface. The calibration data for the AOMs and their drivers are stored in the text file and are used in the control program. Various consistency checks are automatically performed in the program to verify correct operation of the measurement cycle before a new sequence is executed. An additional function of this computer is the imaging of the MOT using a custom program, written in LabView, which can simultaneously control and display images from two Pixellink CCD cameras, see Sec. 4.2.2.

The second master computer is exclusively dedicated to three stabilization schemes: (a) stabilization of the bottle resonator frequency to the rubidium spectrum using the Pound-Drever-Hall technique, (b) distance stabilization between the coupling fibers and resonator, and (c) stabilization of the bias voltage of the Mach-Zehnder modulators to ensure a high on/off switching ratio. A hardware-based PI controller was initially implemented in the first two schemes [52, 87, 101, 112], however, a software-based PI controller is capable of providing more flexibility while also providing sufficiently high bandwidth.[3] Control software, written in LabView, is capable of operating with a bandwidth up to 100 Hz and is synchronized with the measurement sequence executed by the other master computer. This synchronization is necessary for the continuous scheduling of (a) when the frequency stabilization should be inactive, i.e. during the 85 ms atom–resonator interaction timewindow, (b) when to execute the open loop stabilization of the resonator–fiber coupling, e.g. every 30 minutes, and (c) when to execute the open loop stabilization of the Mach-Zehnder modulators, i.e. every measurement cycle. All stabilization parameters and variable changes are recorded in the control program for post-analysis.

Data pulses from four SPCMs are timetagged and recorded on two data acquisition cards that are connected to the PCI slots of two slave computers: two computers are required to process the high data rate. Data from each measurement cycle is recorded in files using binary-format for post-analysis. The internal clock of each card is stabilized with an external 10 MHz reference clock giving a stability of 1 ppb. This makes it possible to perform correlation measurements between all four SPCMs even though the data is recorded on separate cards. In addition, one slave computer also has an application programming interface, written in C++, for communicating with the FPGA and reading and storing data on the computer.

---

[2] The control software has its origins in the Quantum Technologies Group of Prof. Meschede.

[3] Results presented in Chap. 5 were preformed with a hardware-based PI controller, unless otherwise indicated. Results in Chaps. 7 and 8 were preformed with a software-based PI controller.

6.2.3 Experimental Sequence

One cycle of the experimental control sequence is shown in Fig. 6.2. The experimental sequence begins by first performing an open-loop stabilization of the bias voltage, V_{bias}, of the Mach-Zehnder modulators and, optionally, open-loop stabilization of the coupling between the fiber(s) and resonator.

Simultaneously, the MOT is loaded with atoms for a duration of 1.5–2.5 s. At this point the anti-Helmholtz magnetic field is switched off and the three upper and three lower cooling beams are detuned at a rate of 0.5 MHz ms^{-1} for 3–4 ms to a final value of $2\Delta\omega$. The optical molasses is now cooled in a moving reference frame. This is followed by a polarization gradient cooling (PGC, see Appendix B) step that further cools the atoms to a sub-Doppler temperature of around 5–6 μK. At this point the light intensity is reduced to $I/I_{\mathrm{sat}} \approx 4$ and all laser light is red-detuned to $\delta/\Gamma \approx 7 - 9$ from the atomic transition. The PGC step finishes once the atom cloud exits the cooling beams after which it takes almost 300 ms to reach the resonator. During this time and the experiment time, the power of the cooling light is set to zero using AOMs and is additionally blocked with mechanical shutters so as to prevent any stray light from reaching the resonator setup and coupling to the SPCMs. The repump light is similarly switched off with an AOM.

A few milliseconds prior to beginning the experiment stage, the errors signals of the resonator frequency and distance stabilization schemes are set to zero and the associated laser light is turned off with AOMs and mechanical shutters. Following this, the SPCMs are gated on and the FPGA begins the atom-detection stage, which is described in more detail in the next section.

6.2.4 Realtime data processing

The arrival of atoms from the fountain in the evanescent field of the bottle resonator is an inherently random process and experimental sequences must be triggered by these events. For detecting an atom arrival, we tune the resonator into resonance with the D_2 cooling transition of ^{85}Rb and operate it under the condition of critical coupling while monitoring the transmission of weak detection light through the coupling fiber [48]. This detection light is resonant with the resonator, meaning that its transmission is low when no atom is present. Experimentally, the detection light transmission is at $\sim$1% in this case. An atom coupling to the resonator results in new eigenmodes and eigenfrequencies for the atom-resonator system, as described by the Jaynes–Cummings model [15]. For the single photon case, this leads to Rabi splitting of the resonance by an amount equal to the vacuum Rabi frequency, $\Omega_0 = 2g$. As a result, the transmission of the weak detection field through the coupling fiber will increase when an atom enters the evanescent field of the resonator.

We find average interaction times on the order of a a few microseconds as shown in Fig. 6.3. Only during the brief interaction time does the SPCM count-rate increase above a low background level of 0.1 counts/bin to 5–6 counts/bin, where a time bin is 500 ns. To study the spectrum and characteristics of the coupled system on this timescale however, it is necessary to have a second (spectroscopy) laser with an independently controlled optical power and frequency, see Fig. 6.1. This second laser is required because it is technically not possible to change the frequency and power of the detection laser light on a microsecond time scale. Realtime pro-

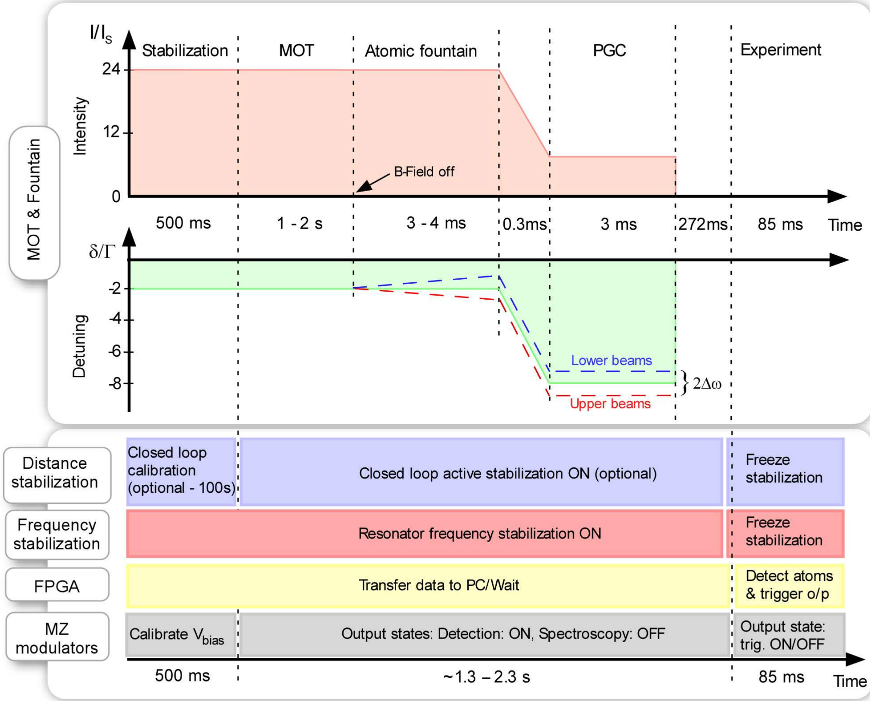
I/I$_S$
Intensity
24
12
0
Stabilization
MOT
Atomic fountain
PGC
Experiment
B-Field off
500 ms
1 - 2 s
3 - 4 ms
0.3ms
3 ms
272ms
85 ms
Time
MOT & Fountain
δ/Γ
Detuning
-2
-4
-6
-8
Lower beams
Upper beams
2Δω
Distance stabilization
Closed loop calibration (optional - 100s)
Closed loop active stabilization ON (optional)
Freeze stabilization
Frequency stabilization
Resonator frequency stabilization ON
Freeze stabilization
FPGA
Transfer data to PC/Wait
Detect atoms & trigger o/p
MZ modulators
Calibrate V$_{bias}$
Output states: Detection: ON, Spectroscopy: OFF
Output state: trig. ON/OFF
500 ms
~1.3 – 2.3 s
85 ms
Time

Figure 6.2: Experiment control sequence. The upper diagram shows the intensity and detuning of the cooling laser light as a function of time. The lower diagram indicates the important steps necessary for operating the resonator and studying the atom–resonator interaction. The stabilization of the resonator frequency and coupling fiber is active always except during the 85 ms experiment time-window. At this time the FPGA searches for atom interactions and correspondingly switches the detection and spectroscopy light. MOT beam intensity: $I_s = 1.6$ mW cm^{-2}: saturation intensity for the D$_2$ cooling transition in ^{85}Rb, $\sigma^{\pm}$ light. See main text.

cessing of the photon stream from the resonator is therefore a critical aspect of the cavity QED experiment since it defines the possible interaction time with the atom.

We have implemented a realtime atom detection scheme using a FPGA operating at a clock frequency of 100 MHz. The FPGA is a hardware device that consists of basic logic elements, such as flip flops, memory units and gates, that can be re-configured to provide the desired functionality. The device is programmed with the hardware description language Verilog in the software environment ISE, provided by Xilinx Inc. An overview of the design and performance is described here, and interested readers will find full details of the implementation documented in Ref. [96].

The principle of the FPGA detection design is to monitor the photon rate and compare it to an expected rate corresponding to an atom coupling event [84]. When the actual rate exceeds a certain predefined rate, the FPGA switches the Mach-Zehnder modulator for the atom detection light off and the modulator for the spectroscopy light on. Figure 6.5 shows a block diagram of the algorithm. First, photon events from two SPCMs are summed together. Since a photon rate

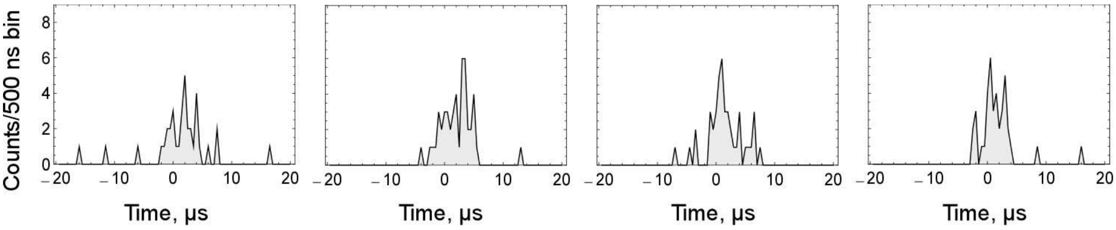

Figure 6.3: Typical transmission traces of single atom transits. Atoms passing through the evanescent field of the resonator mode lift the transmission for several microseconds to a maximum of 5–6 counts/bin, well above a residual background level of 0.1 counts/bin. The time axis is centered to the center-of-mass of the counts. Time bin: 500 ns.

must be calculated, a running time window is implemented using a FIFO memory (first in, first out) with a depth of 128 bits, giving a time-window of 1.28 μs, and a width of 2 bits — there can only be zero, one, or two photons detected per clock cycle. Photon events are written to the FIFO at the rising edge of every clock cycle. A register with the number of photons in the FIFO, $n_{\mathtt{photons}}$, is evaluated by adding the current number of incoming photons, $\Sigma_{\mathtt{SPCM}}$, to the previous register value and subtracting the number of photons leaving the time window, $\Sigma_{\mathtt{FIFO}}^{\mathtt{out}}$. For clarity, we note that the comparison $n_{\mathtt{photons}} \geq n_{\mathtt{thr}}$ in Fig. 6.5, however, is *de facto* a comparison between photon numbers and not rates. The photon rates are trivially determined by dividing the photon numbers by the time window. When this comparison evaluates true, two flags in the FPGA are asserted for switching the modulators and for writing the timetag of the atom coupling event to the computer.

The total loop delay between detecting the presence of an atom at the resonator and probing the coupled system is around 160 ns, and is mainly limited by the propagation delays in the optical fibers and electrical cables ($\sim$ 130 ns, delay: 5.5 ns per meter). A minimum of three and maximum of four clock cycles of the FPGA define the processing time (30–40 ns): one clock cycle is required to read and internally re-shape the SPCM pulses, another for comparing the threshold $n_{\mathtt{photons}} \geq n_{\mathtt{thr}}$, and a third for setting the FPGA outputs for triggering the fiber modulators. A fourth clock cycle may be needed since photon arrival times are not synchronized with the FPGA clock.

A more advanced algorithm has also been implemented which greatly improves our ability to selectively analyze events where the atoms have a stable coupling to the resonator. Before describing this advanced algorithm shown in Fig. 6.4, we first summarize the three steps involved in the simpler algorithm described previously: (a) detect an atom and turn off the detection light, (b) turn on the spectroscopy light for a few microseconds (e.g. up to 20 μs), and (c) turn off the spectroscopy light and turn on the detection light again to search for the next atom. The advanced algorithm has an extra step: (a) same as above, (b) turn on the spectroscopy light for a duration of 0.5–2.0 μs, (c) turn off the spectroscopy light and turn on the detection light to check if the atom is still coupled to the resonator mode, and (d) search for the next atom after 20 μs. While the total number of detected atoms may not drastically change, depending on $n_{\mathtt{thr}}$, the short-lived atoms that crash into the resonator surface can be removed in the post-analysis using information from the second detection phase. In this way, only atoms that have a long and stable

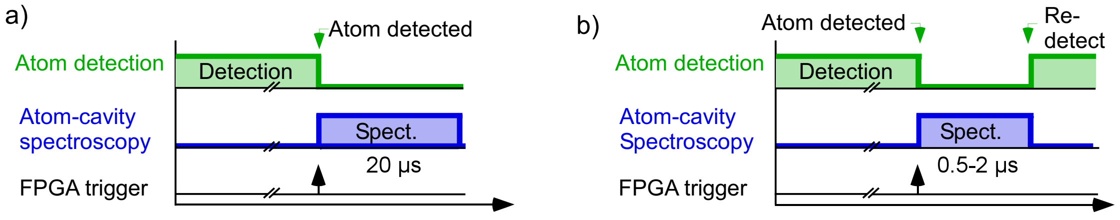
a)
Atom detected
Atom detection
Detection
Atom-cavity spectroscopy
Spect.
20 µs
FPGA trigger
b)
Atom detected
Re-detect
Atom detection
Detection
Atom-cavity Spectroscopy
Spect.
0.5-2 µs
FPGA trigger

Figure 6.4: Atom detection and measurement sequence using two different schemes. (a) Single atom-detection scheme: Detection light is resonant with the cavity and the transmission signal from photon detectors is analyzed in realtime with a FPGA. Once an atom is detected by the FPGA, the detection light is turned off and a second beam is turned on for measuring the atom-resonator spectrum. (b) Double atom-detection scheme: The sequence is the same as the previous scheme except an additional step is added where the atom is re-detected after the spectroscopy step is finished.

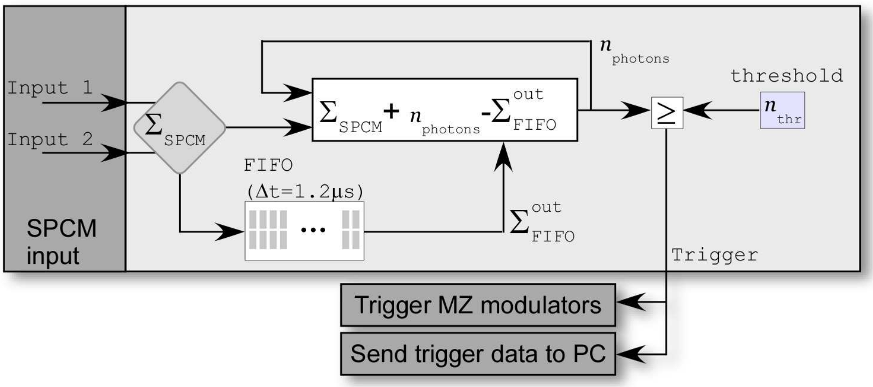
Input 1
Input 2
SPCM input
Σ_{SPCM}
$\Sigma_{SPCM} + n_{photons} - \Sigma^{out}_{FIFO}$
$n_{photons}$
threshold
n_{thr}
≥
FIFO
(Δt=1.2µs)
Σ^{out}_{FIFO}
Trigger
Trigger MZ modulators
Send trigger data to PC

Figure 6.5: FPGA algorithm for detecting the presence of an atom. Photon events from two SPCMs in a Hanbury-Brown and Twiss configuration are summed up in the FPGA. The photon events are stored in a running time window of duration $\Delta\mathtt{t} = 1.2\ \mu$s which is implemented using a FIFO (first in, first out) register. The FIFO has a width of two bits since photon events from the two SPCMs are counted every clock cycle. The number of photons, $n_{\mathtt{photons}}$, is calculated every clock cycle as the sum of the incoming photons $\Sigma_{\mathtt{SPCM}}$ and $n_{\mathtt{photons}}$ from the previous clock cycle minus the sum of photons leaving the time window $\Sigma^{\mathtt{out}}_{\mathtt{FIFO}}$. An output trigger is generated when the photon rate $n_{\mathtt{photons}}/\Delta\mathtt{t}$ is equal to or exceeds $n_{\mathtt{thr}}/\Delta\mathtt{t}$. Adapted from Ref. [96].

coupling to the resonator are analyzed. Further details of the performance of the algorithm, which is important for observing the Rabi spectrum, is provided in the following chapter.

CHAPTER 7

Observation of the Rabi Spectrum of a Coupled Atom–WGM-Resonator System

Cavity-QED systems have the potential to fulfill essential roles in future quantum networks [32] and quantum communication [113], and therefore require controllable and strong coupling of light and quantum emitters. In order to achieve this goal, a number of basic requirements must be fulfilled. Namely, all dissipation rates of the coupled system of light and emitter are negligible compared to the coupling rate g them. This stringent requirement is difficult to satisfy using free-space light and a free-moving emitter because the spontaneous emission rate of the emitter, γ, typically exceeds the coupling rate by a large margin. Our approach to this problem centers on using the bottle microresonator to enhance the electric field of light and thereby propel the coupled system into a regime of strong coupling where $g \gg \gamma$. Additional to this equality is the requirement that the coupling rate also exceeds the dissipation rate of the resonator, i.e., $g \gg (\gamma, \kappa)$.

In this chapter, we investigate the coupling of single atoms to our two-mode WGM bottle resonator. In order to demonstrate that the system operates in the strong coupling regime we measure the transmission properties of the coupled atom and resonator. A clear signature of this regime can be seen as a mode-splitting in the transmission (Rabi) spectrum, as described earlier in Fig. 2.3.

The atom detection scheme, described in Chap. 6, is used to reveal the structure of the resonator transmission spectrum, and shows that single atoms have a much greater effect on the system than predicted by the standard Jaynes-Cummings model presented in Chap. 2. When the frequency of light in the resonator is resonant with the atomic transition, the absolute change in transmission induced by a single atom is measured to be 65% and is more than 35 standard deviations above the theoretically predicted absolute transmission change of 20–25%. The back-reflected light from the resonator similarly shows a significant difference from the theory, being much less than expected by more than 14 standard deviations. Despite WGMs having two orthogonally-polarized modes in the resonator, the atom-resonator response is more indicative of Fabry-Pérot-type behavior with a single mode.

Several possible explanations underlying the observed interaction are discussed, analyzed and tested in Secs. 7.5 and 7.4. In particular, we consider (a) the presence of multiple atoms simultaneously interacting with the resonator, (b) single atoms accelerated by radiation and dipole forces, and (c) asymmetric Rayleigh scattering leading to a modified mode structure that is no longer fully described using either standing-waves or travelling-waves.

We present a detailed investigation of the properties of this novel system:

- Velocity effects (Sec. 7.4): We consider surface Casimir/Van der Waal forces, light-shifts of the energy levels, and dipole forces in simulations of atomic trajectories near the resonator surface. The simulated transmission spectrum is compared to measurements in Sec. 7.2. Signatures of dipole forces on the atoms are observed and described in Sec. 7.4.3.

- Scattering effects (Sec. 7.5): We consider asymmetric scattering in WGM resonators and examine whether this can influence the transmission properties of the coupled atom-resonator system. We find unexpected asymmetries in high Q resonator modes due to asymmetric Rayleigh scattering. This scattering is seen to enhance the effect of splitting in the Rabi spectrum. Finally, using two coupling fibers, we observe atom-resonator interactions that provide evidence that the atom interacts with both standing wave resonator modes (Sec. 7.3).

The chapter is organized as follows: The atom detection scheme is analyzed and the interaction time of the atom with the evanescent field is measured. Transmission spectra are recorded for different experimental conditions and different WGMs. In order to better understand the spectral response, we study velocity effects in Sec. 7.4 and scattering effects in Sec. 7.5. A dramatic and beneficial consequence of these results is that single-atom switching of light in a resonator with one or two coupled nanofibers can be performed with much higher efficiency than previously expected. Our first results demonstrating low-loss, single-atom-controlled switching are presented as an outlook to this work in Chap. 8.

7.1 Characterization of the atom detection schemes

The realtime operation of experiments necessitates the high-speed detection of brief atom transits through the evanescent field. Indeed, this detection step is the central part of the experiment that enables spectral measurements of the coupled system of atom and resonator. The performance of the atom detection scheme described in the previous chapter is first analyzed using pre-recorded transmission data. Afterwards, the realtime performance of the scheme is analyzed in the actual experiment. Work described in Sec. 7.2 (in particular, see Fig. 7.7) and Ref. [96] confirm the consistency of the timing and performance of both the software analysis and realtime response in the experiment.

7.1.1 Realtime performance: Single atom detection scheme

As a first step, continuous time-traces of the photon stream are recorded and time-stamped for post-analysis. The data is recorded in the experiment with only the detection laser light turned on and made resonant with the atomic and cavity frequency, i.e. $\omega_l = \omega_a = \omega_c$, and the FPGA signal to the Mach-Zehnder switches is set inactive and the spectroscopy laser is permanently turned off. A software-based atom detection analysis, similar to that shown earlier in Fig. 6.4 (a) but with the software replacing the role of the FPGA, is used to analyze the time-traces. Around one hundred thousand atom launches are analyzed with the atom detection criterion set to a photon count rate $n_{\rm thr} \geq 7$ counts/1.2 μs. The probability that an atom was detected accidentally due to transmission noise is around 2–4%, depending on the ratio of the power before the resonator to the power transmitted past the resonator, $P_{\rm T}/P_{\rm in}$.

Figure 7.1 (a) shows the detected photon distribution and trigger distribution during the atomic transit. The center-of-mass of the photon distribution for each atom detection event is calculated in a time-window $\Delta t_{\rm win} = \pm 2$ μs around the trigger time and the time axis is aligned so that the center-of-mass is set to $t = 0$ μs. The traces are then summed and normalized to give the number of detected photons per 20 ns bin. The time-window $\Delta t_{\rm win}$ is carefully chosen to yield a low probability (< 5%) of accidentally including photons from the low background transmission (≤ 2% of the incident photon flux) in the center-of-mass calculation. Increasing the time-window to $\pm 10 - 20$ μs erroneously broadens the plots by around a factor of two or more. The photon distribution has a FWHM of 1.6 μs and the distribution of FPGA triggers is centered after the peak in photon transmission (see arrow). Even though we plot the center-of-mass — representing the mean photon distribution — this distribution is necessarily biased due to the atom detection criterion.

The time-dependent transmission following the detection of an atom can reveal information on the characteristic timescales of the transit. To study this, the transmission in Fig. 7.1 (b) is plotted so that the origin at $t = 0$ μs marks the moment the FPGA detects an atom. This alignment makes it possible to clearly identify the time-windows where the distribution is biased due to the atom detection criterion. It is important to note that while the normalized transmission in this time-window can be greater than unity, this should not be directly interpreted as coming from the atom-resonator interaction. Only the transmission outside of these time-windows provide a true measure of the interaction.

Figure 7.1 (b) shows the average transmission of 1.5 million atom transits measured using two photon counters in Hanbury-Brown and Twiss configuration with $n_{\rm thr} \geq 7$ in 1.2 μs. The transmission response in three distinct regions, labeled 1–3, is explained as follows. Region 2, between $-1.2 < t < 0$ μs, shows a significantly elevated transmission relative to the other two regions because we select only atom transits where a minimum of seven photons are detected. The time-bin immediately before $t = 0$ μs marks when the seventh photon was detected for each transit. Immediately following this, a sharp dip of around 40 ns duration is observed and arises due to the deadtime of the photon detectors, which makes one detector (or both, in some cases) briefly inactive during this time. Rather than dipping to a transmission of $0.65/2 \approx 0.32$ during this deadtime, as expected if one detector is inactive, the value drops to around 24%. This is reasonable given the high photon rate just prior to detecting the atom, which is enough to give a non-negligible probability of having two photons at both detectors at $t = 0$ μs.

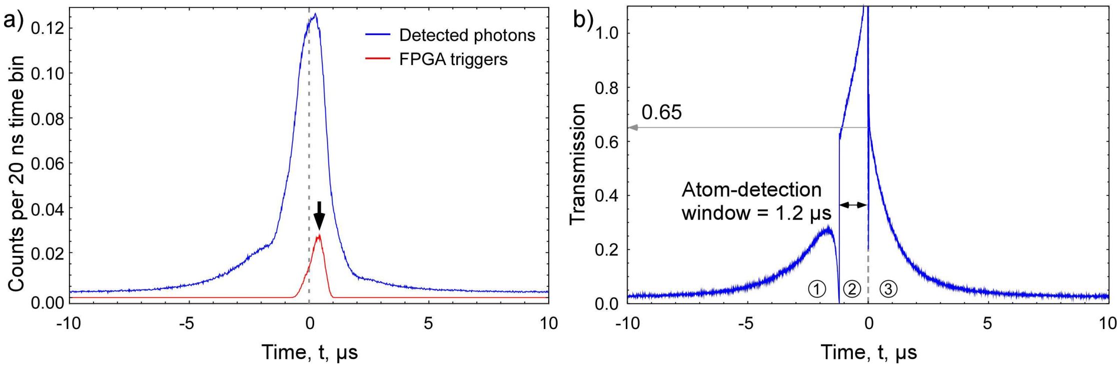

Figure 7.1: Transmission during an atomic transit detected using the single atom-detection scheme. Continuous time-traces of the average transmission from 1,518,023 atom transits are recorded. (a) The mean photon distribution is plotted by aligning the time trace from each transit so that the mean photon arrival time is aligned to $t = 0$ μs. (b) Alternatively, the same data can be re-plotted to calculate the transmission in the fiber after the FPGA detects an atom. Each trace is re-aligned to the time when $n_{\rm thr} \geq 7$ photons are detected in a time-window of 1.2 μs width, which is defined as $t = 0$ μs in the plot. This causes the counts between times -1.2 and 0 μs to be biased. Atom detection criterion: $n_{\rm thr} \geq 7$ photons per 1.2 μs. Bin width: 4 ns. Intra-cavity photon number: ~ 0.2 photons, pump-rate at the coupling fiber: $\sim 10 \times 10^6$ photons/s. FWHM of trigger distribution: 700 ns.

Region 1, from $t = -10$ to -1.2 μs, shows a steady increase in transmission as the atom approaches the resonator. A sharp dip to precisely zero transmission at $t = -1.2$ μs is present because, if a photon was detected at this time, the FPGA would be triggered one time-bin earlier. Therefore, when plotting the data in this manner, there are always zero photons at $t = -1.2$ μs. The transmission for around 200 ns before this time shows a relatively slow decay down to zero. This can be best explained by considering the time reversed process: starting with the moment where there is exactly zero photons, the light is “turned on” again and the transmission exponentially rises to a steady state value with a time constant given by the photon pump rate. The exponential response is due to the Poissonian statistics of light which describes the probability of detecting a photon. From the data we observe a time constant of around 0.12 μs, agreeing well with the expected photon pump-rate of around 0.15 μs.

Finally, region 3 shows a decaying transmission starting from a maximum value of around 0.65, that is much higher than the ~ 0.25 expected from the Jaynes-Cummings Hamiltonian presented in Chap. 2. Figure 7.2 is a plot of the decay on a logarithmic scale for times up to 11 μs following the trigger at $t = 0$ μs. There is an initial fast decay in transmission for the first few microseconds which then slows for longer times. In fact, the effect of the detection event is still noticeable on the 10^{-3} level after 10 μs. Naively assuming a velocity of $\sim$ 3 cm/s for atoms taken directly from the atomic fountain at a temperature of 5 μK, the atom would travel a distance of 300 nm in 10 μs. For reference, the evanescent field decays on a length scale $\sim \lambda/(2\pi\sqrt{n^2-1}) = 118$ nm. A more quantitative understanding requires knowledge of the atomic motion and the dependence of coupling strength with transmission. Of course, since the

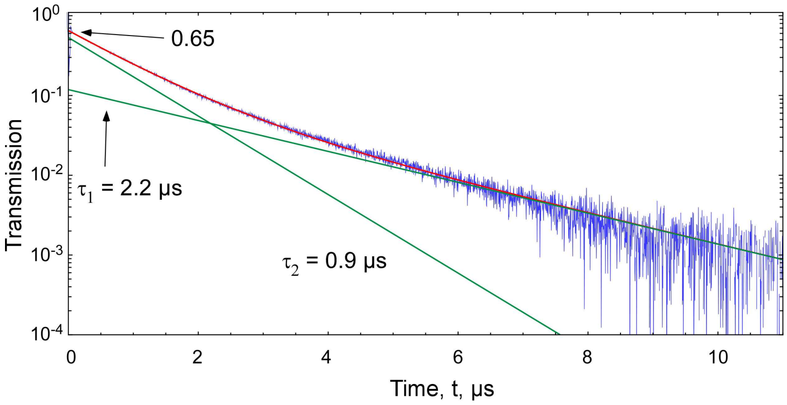

Figure 7.2: Transmission time dependence after FPGA trigger using the single atom-detection scheme. Zoom of the transmission decay after atom detection at $t = 0$ μs in Fig. 7.1 (b) and with a transmission offset of 2.6% subtracted. The red line is a fit to the data using the sum of two exponentials (green lines) with time constants $\tau_1 = 2.2$ μs and $\tau_2 = 0.9$ μs. Bin width: 4 ns.

atoms are not well localized and freely move through the evanescent field, an ensemble average of simulated atomic trajectories in conjunction with the full Jaynes-Cummings Hamiltonian is necessary [84]. However, in this work we limit ourselves to understanding and testing the predictions of the Hamiltonian rather than using it to predict more complicated behavior.

Empirically, however, a double exponential fit reproduces the data well and gives time constants of 2.2 μs and 0.9 μs. This possibly suggests a change in trajectory and/or velocity of the atoms during their transit, which is considered likely due to van der Waals and dipole forces experienced by the atom as it approaches near to the resonator surface. Alternatively, it may also suggest two classes of atoms where one class approaches the resonator perpendicular to the surface, and passes through the exponentially decaying evanescent field, while the second class has a trajectory that is more tangential to the surface and therefore interacts for a longer duration. However, this second class would apparently provide a much smaller transmission change of around 10% compared to the maximum observed value of 65%. Additionally, the probability of detecting such a class of atoms is low since the detection criterion corresponds to around 90–100% of full transmission. The physical response of the motion of an atomic ensemble is left for future studies and will not be studied here.

7.1.2 Realtime performance: Double atom-detection scheme

The success of the previous scheme in detecting atoms coupled to the resonator is well established in experiments [84, 96], however it suffers from a serious drawback. Namely, the coupling/transmission is not constant during the experiment (see Fig. 7.2). Such a situation complicates the data analysis because only photons recorded in the first $\Delta t_{\text{spect}} \approx 100$ ns following the trigger can be used to estimate the transmission. To overcome this problem, a scheme has been implemented to conditionally select only atoms that have a stable and long interaction

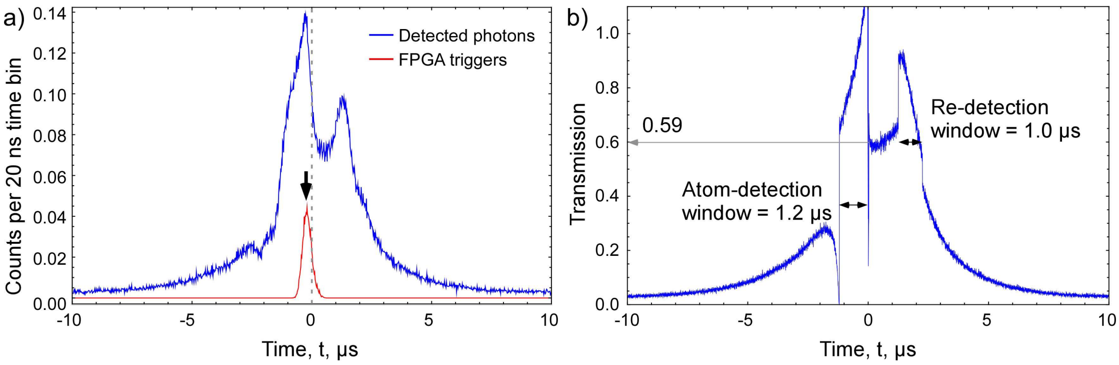

Figure 7.3: Transmission during an atomic transit detected using the double atom-detection scheme. Continuous time-traces of the average transmission from 210,962 atom transits based on the same data from Fig. 7.1. (a) The mean photon distribution is plotted as in Fig. 7.1 (a). (b) The transmission in the fiber after the FPGA detects an atom is plotted as in Fig. 7.1 (b). Double atom-detection criterion: $n_{\text{thr}}^{\text{2nd}} > 3$ photons per 1 μs measured 1.2 μs after the end of the first detection step. Bin width: 4 ns.

time with the resonator. The first part of the scheme is identical to the single atom detection scheme, while the second part involves re-detecting the atom after a spectroscopy measurement interval of $\Delta t_{\text{spect}} = 1$ μs to ensure that it is still strongly coupled to the mode (for reference, see Fig. 6.4 (b) for the timing sequence). In this so-called double atom-detection scheme, the detection criteria are a threshold of $n_{\text{thr}}^{\text{1st}} \geq 7$ counts/1.2 μs for the initial detection and, after an interval Δt_{spect}, a threshold of $n_{\text{thr}}^{\text{2nd}} \geq 3$ counts/1.2 μs for the re-detection step. The probability of accidentally detecting an atom due to transmission noise, $\Delta P_{\text{T}}/P_{\text{in}}$, is negligible ($\sim 0.05$%), and is relatively insensitive for transmission noise up to at least 4%.

In comparison to the first scheme, the double detection scheme in Fig. 7.3 (a) shows a more complex photon distribution. The small spread in trigger times reveals biased regions in the photon distribution corresponding to the two time-windows where the FPGA detects the atom — the first region is around $-1.5 < t < 0$ μs and the second region is around $1 < t < 2$ μs. Interestingly, the photon distribution is ~ 1.6 μs wider, giving a FWHM of ~ 3.2 μs, and the triggers are centered 0.2 μs before the mean photon arrival time. Since the width of the trigger distribution is very narrow (FWHM of 400 ns in this scheme and 700 ns in the first scheme) compared to the FWHM of the photon distribution, we conclude that the photon distribution of all atom transits used in the plot is very similar.

The average transmission is shown in Fig. 7.3 (b), and is plotted in the same manner as Fig. 7.1 (b). With this scheme we now use 13.4% of the total number atoms satisfying the first detection criterion $n_{\text{thr}}^{\text{1st}}$. Importantly, the transmission is almost constant at 0.59–0.65 for the spectroscopy interval $0 < t < 1.2$ μs, unlike with the previous scheme which has an exponential-like decay during spectroscopy measurements. This greatly benefits the operation of complicated experimental protocols where it is desirable to have constant transmission as well as stable and reproducible atom-resonator coupling while performing tasks such as atomic state preparation and manipulation. Apart from that, the longer spectroscopy measurement time increases the

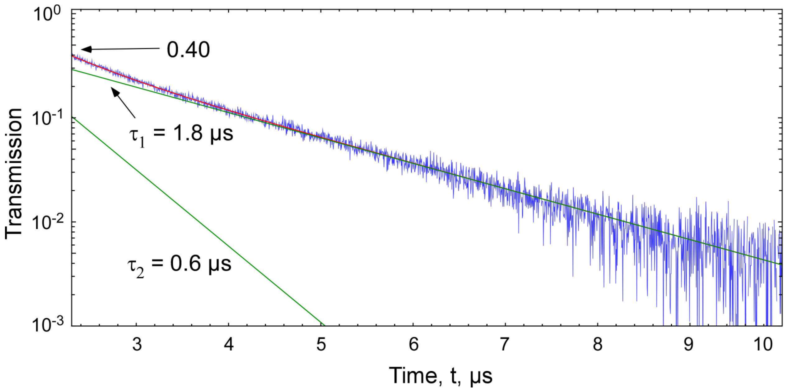

Figure 7.4: Transmission time dependence after FPGA trigger using the double atom-detection scheme. Zoom of the transmission decay after atom detection at $t = 0$ μs in Fig. 7.3 (b). The red line is a fit to the data using the sum of two exponentials (green lines) with time constants $\tau_1 = 1.8$ μs and $\tau_2 = 0.6$ μs. Double atom-detection criterion: $n_{\rm thr}^{\rm 2nd} > 3$ photons per 1 μs measured 1.2 μs after the end of the first detection step. Bin width: 4 ns.

number of photons that can be usefully collected from each atom transit. In this work, we use both detection schemes depending on the particular experiment being performed, which may require a long measurement window (double atom-detection) or simply a high atom detection rate (single atom detection).

Figure 7.4 shows the transmission decay after the re-detection window has ended at $t = 2.2$ μs. Similar to the single atom detection scheme in Fig. 7.2, here we again find that two exponential decays empirically fit the data well, but the time-constants are slightly smaller with $\tau_1 = 1.8$ μs and $\tau_2 = 0.6$ μs.

7.1.3 Observation of single atom events

Proof that we trigger our experiments based on the detection of single atoms, and not multiple atoms coupling at the same moment, is essential to interpreting the observed dynamics. Early cavity QED experiments with Fabry-Pérot resonators featured dense atomic beams from ovens where bunches of atoms interacted with the resonator mode. The Rabi frequency, Ω, scales according to $\Omega\sqrt{N_{\rm atom}}$, where $N_{\rm atom}$ is the number of identically coupled atoms. In the case of WGM resonators, the multi-atom scenario is especially important because different atoms can interact with the two standing-wave WGMs rather than just one mode and thereby change the dynamics considerably.

To verify that our detection schemes do indeed react to single atoms, we have studied the dependence of the number of detected events as a function of the atomic density of the cloud launched towards the resonator. Figure 7.5 shows a linear dependence on atomic density for both schemes as expected for single atoms. If the detection scheme was reacting to two atoms simultaneously coupled to the resonator, a quadratic dependence would be expected. However, since the data shows very good linearity, the contribution of multi-atom events to the measurements is

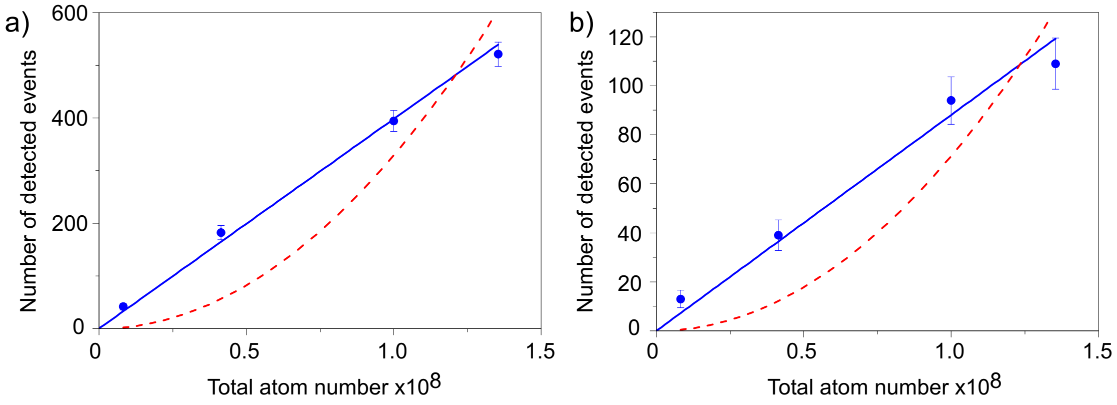

Figure 7.5: Dependence of the number of detected atom-resonator coupling events for different atomic densities. (a) Single detection scheme: single-atom coupling events follow a linear dependence (solid line) while, for comparison, two-atom coupling events follow a quadratic dependence (dashed line). (b) The number of observed events using the double atom-detection scheme similarly follows a linear dependence.

negligible.

The density is varied by varying the Rb partial pressure in the MOT chamber. The atomic density was measured by integrating the fluorescence signal from atoms passing through a light sheet a few centimeters below the resonator in the science chamber (see the setup shown in the inset to Fig. 4.10 and Ref. [88]). This is cross-checked for consistency with a separate measurement of the fluorescence from the MOT. In addition, the cloud temperature is around 5 μK in all measurements.

From each launch of the atomic cloud we typically observe around one coupling event using the double atom-detection scheme during a data acquisition window of 85 ms. Assuming the distribution of events over this time follows Poissonian statistics, the probability of two or more events occurring in the same 3 μs interval is $p(N_{\text{atom}} \geq 2) = 6 \times 10^{-10}$. A more meaningful quantity to consider is the ratio $p(N_{\text{atom}} \geq 2)/p(N_{\text{atom}} = 1) = 1.7 \times 10^{-5}$, where $p(N_{\text{atom}} = 1)$ is the probability to detect one atom in a 3 μs interval. The ratio indicates the probability of detecting two-atom events is negligible compared to the probability of detecting single-atom events. For the single atom detection scheme we typically observe around eight events per 85 ms. This gives a probability of 4×10^{-8} for two or more events in the same 3 μs interval, yielding a ratio $p(N_{\text{atom}} \geq 2)/p(N_{\text{atom}} = 1) = 1.4 \times 10^{-4}$.

Additionally, the observation of eight detected atoms using the single atom detection scheme agrees reasonably well with the expected number of atoms, within an order of magnitude. A simple estimate of the expected number of detected atoms, based on the the total number of atoms in the atomic cloud ($\sim 5 \times 10^7$) and the area overlap of the cloud (radius ≈ 1 cm) with the cross-section of the resonator mode (width ≈ 35 μm, length ≈ 5 μm), and assuming the resonator is located at the center of the Gaussian-shaped cloud, yields a value of around 28 atoms. Considering the use of a conditional atom detection scheme, which presumably is not

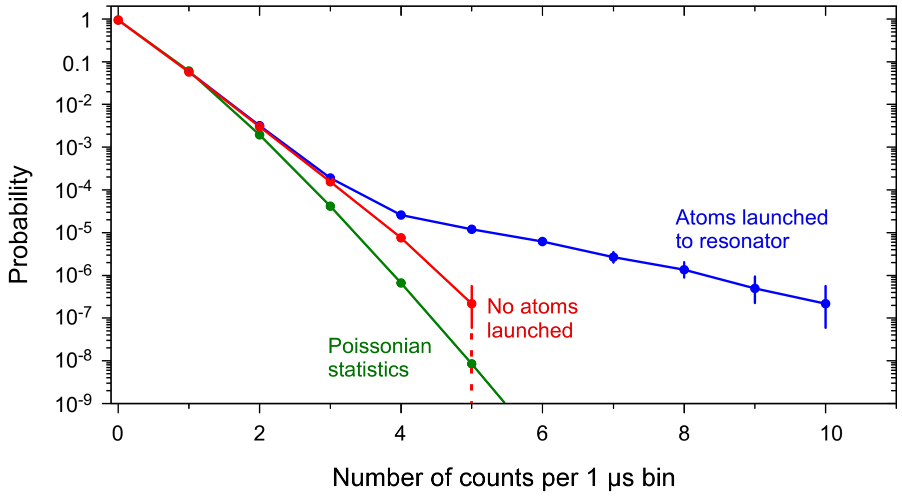

Figure 7.6: Photon detection probability of atom transits.

perfectly efficient at detecting all coupling events, this value is sufficiently small such that the effects of multi-atom events on the resonator transmission and reflection can be ignored.

7.1.4 Photon detection probability

The coupling of atoms to the resonator changes the transmission and reflection properties of the coupled system, especially in the regime of strong coupling — this fact is used for atom detection. As an initial experiment, the number of photon counts per 1 μs time bin are measured for two cases, i.e., with and without atoms, under experimental conditions (i.e., concerning MOT density and photon flux) similar to Sec. 7.1.

An experimental sequence is executed in which an atomic cloud is launched to the resonator every two seconds and the transmission and reflection is recorded for post-analysis. The sequence is run several hundred times and is interleaved with an identical reference sequence in which the atoms are not launched. Photon detection events are binned with 1 μs time resolution for each sequence, as shown in Fig. 7.6 (a). The resonator is probed on resonance with an incident power of $P_{\rm in} \approx 2$ pW, corresponding to 0.18 intracavity photons, and the transmission of the empty resonator is maintained at critical coupling with $P_{\rm out}/P_{\rm in} \leqq 0.02$.[1] In the reference sequence the mean number of photon detection events per time bin is 0.07. Assuming Poissonian statistics, shown in Fig. 7.6, the probability for detecting five photons, for example, in one time bin is thus given by $P_{\rm ref}^{\rm theo}(5) = 0.9 \times 10^{-8}$. Evaluating 1831 experimental sequences, we find $P_{\rm ref}^{\rm exp}(5) = 2.2^{+3.4}_{-1.6} \times 10^{-7}$. The deviation with respect to the theoretical value is due to both frequency noise in the resonator frequency stabilization and mechanical noise in the coupling setup, which both cause super-Poissonian fluctuations of the transmitted intensity. When the atom cloud is launched, however, the photon statistics are significantly modified, yielding a 5-photon detection probability of $P_{\text{atom}}^{\text{exp}}(5) = 1.2^{+0.2}_{-0.2} \times 10^{-5}$, almost two orders of magnitude higher than $P_{\text{ref}}^{\text{exp}}(5)$. The error bars are 95% confidence intervals. The observed change in the counting statistics is a clear indication that atoms from the cloud interact with the resonator mode [48]. Moreover, it confirms the need to have a high threshold of around $n_{\text{thr}}^{\text{1st}} \gtrsim 6 - 7$ for the atom detection scheme using the FPGA.

---

[1] The degree to which the transmission of the empty resonator at critical coupling can be suppressed to zero depends on the stability of the cavity resonance frequency and the frequency of the spectroscopy laser, which must be much narrower than the linewidth of the resonator. Therefore, when the back-scattering rate is large compared to the intrinsic mode decay rate, $h \gtrsim \kappa_i$, the transmission is less sensitive to frequency noise of the stabilization because the FWHM linewidth at critical coupling is broadened by an amount $\sqrt{4\kappa_i^2 + 4h^2}$. For bottle modes with $h/\kappa_i = 2$, we typically find $P_{\rm out}/P_{\rm in} \approx 0.005$.

7.2 Spectroscopy of single atoms coupled to a high-Q WGM resonator

In this section, the frequency spectrum of the atom-resonator interaction is measured and compared with the Jaynes-Cummings prediction. From a quantum mechanical perspective, the new eigenfrequencies of the coupled system should be clearly visible when the condition $g \gg \left(\kappa, \gamma, T_{\text{int}}^{-1}\right)$ is true. Moreover, spectra measured under different experimental conditions, such as variable cavity and laser detunings and different probing schemes, can be directly compared to theoretical predictions. Here we perform a systematic investigation of the system using a range of parameter settings, and reveal a surprisingly strong effect of single atoms on the spectra.

7.2.1 Conditional selection of strongly interacting atoms

The atom detection schemes rely on the conditional selection of only those coupling events where certain threshold conditions are satisfied. It is interesting to consider the different subsets of coupling events depending on changes in the threshold conditions. As demonstrated earlier, the first observed effect is that, with a suitable threshold level chosen, the transmission during the spectroscopy/experiment window remains constant, and also, the subset of short-lived atoms that crash directly into the surface can be removed from the analysis. Thus, long-lived atoms that presumably pass tangentially to the resonator surface are predominantly selected.

Figure 7.7 examines the transition between the selection of short-lived and long-lived atoms. The transmission is plotted using the double-detection scheme with increasing threshold values $n_{\text{thr}}^{\text{2nd}}$. In these measurements the FPGA is connected to the MZ-modulators and the spectroscopy light is active during the spectroscopy window and its power level is set equal to the detection light. Regardless of the threshold, the transmission prior to detecting the atom at $t = 0$ μs always follows the same trend, as expected. The green shaded region, indicating the spectroscopy window used in the data analysis, begins around 264 ns after the FPGA detects the atoms, which is due mainly to electrical and optical delays. Figure 7.7 (a) shows that $n_{\text{thr}}^{\text{2nd}} \geq 2$ is sufficient to ensure a stable transmission during spectroscopy measurements. Also, as the threshold is increased, there is an associated increase in transmission after the second detection step. On the other hand, Fig. 7.7 (b) demonstrates that even increasing the $n_{\text{thr}}^{\text{2nd}}$ from zero to one already produces a significant improvement in the stability of the transmission during spectroscopy, but is still not as good as in Fig. 7.7 (a).

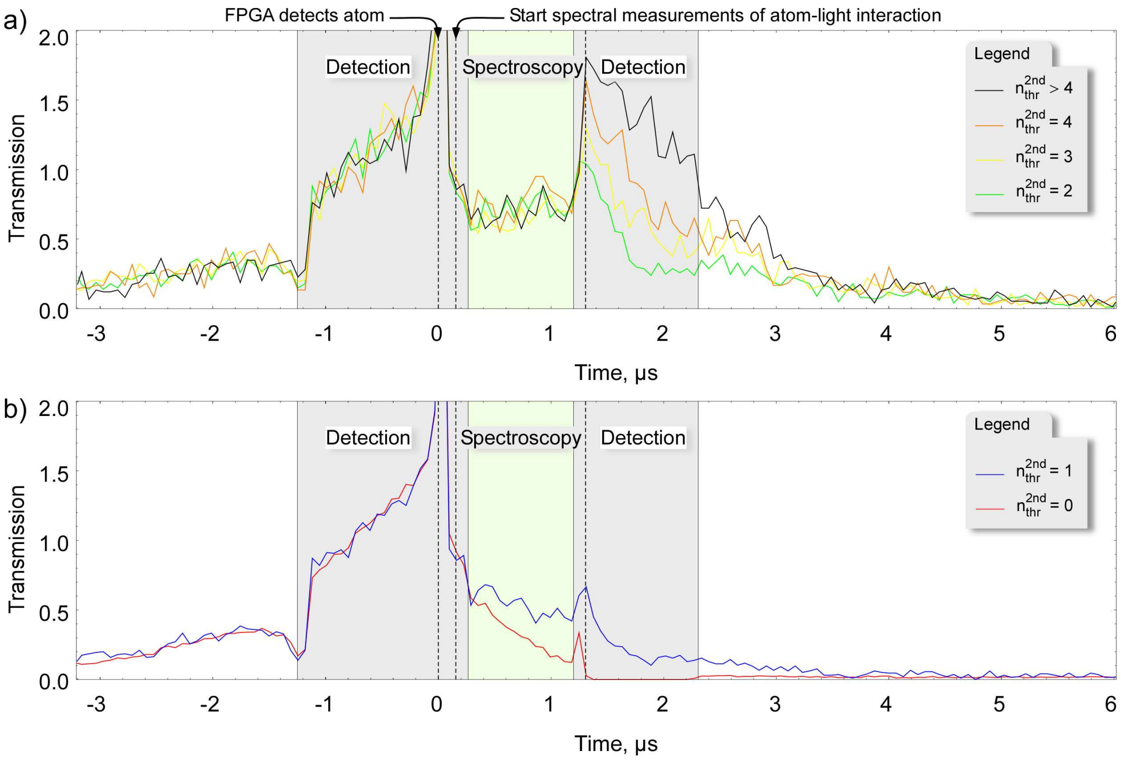

Figure 7.7: Detailed view of the measurement sequence and transmission using the double-detection scheme. (a) Resonator transmission as a function of varying threshold levels for $n_{\text{thr}}^{\text{2nd}}$. The FPGA requires 1.2 μs to first detect an atom, followed ~ 1 μs to probe the atom–light interaction, and finally another 1 μs to re-detect the atom and verify that the atom did not leave the evanescent field before the spectroscopy/experiment is finished. $n_{\text{thr}}^{\text{1st}} \geq 7$. (b) The transmission during spectroscopy is not constant when the threshold $n_{\text{thr}}^{\text{2nd}}$ is too low.

Using the threshold conditions in Fig. 7.7, we measure the transmission and reflection spectra of the coupled atom-resonator system by varying the detuning of the spectroscopy laser, ω_l, with respect to the resonance frequency of the high Q mode, ω_c, as shown in Fig. 7.8 (a–f). The plots show a series of spectra for the empty resonator (grey) and the coupled system (blue) where the threshold condition is progressively increased from low (a) to high (f). Compared to the empty resonance, the transmission with coupled atoms, measured at $\Delta\omega_{\text{cl}}/2\pi = 0$ MHz, changes to an absolute value of 45% when $n_{\text{th}}^{\text{2nd}} = 0$ and increases to 65% when $n_{\text{th}}^{\text{2nd}} \geq 3 - 4$. In reflection, the maximum empty resonance value is only $\sim$ 2% and increases to a maximum of just $\sim$ 5% in the spectra with coupled atoms. When using the single atom detection scheme, the resonant transmission for the coupled system is around 60%, and the reflection value is around $\sim$ 5%. Also, the spectra qualitatively resemble Fig. 7.8 (a) and do not show any spectral splitting.

A pronounced spectral splitting of 28 MHz is measured from the transmission Rabi spectrum, which is shown in more detail in Fig. 7.9. In the reflection spectrum, however, there is no clear splitting despite being measured simultaneously with the transmission spectrum. The peak at around $\Delta\omega_{\rm cl}/2\pi = -8$ MHz is offset from the transmission dip located at around $\Delta\omega_{\rm cl}/2\pi = -16$ MHz. The experimental parameters listed in the caption are the same for all work in this chapter, unless specified otherwise.

A clear deviation is seen in both the measured transmission and reflection spectra when compared to the theoretical prediction in Fig. 2.4, which is plotted for parameters compatible with the resonator mode used in the experiment. Specifically, the model predicts a maximum transmission and reflection of 25% when $\Delta\omega_{\rm cl}/2\pi = \Delta\omega_{\rm ca}/2\pi = 0$ MHz, which does not increase further even when g is larger. Secondly, the distinct absence of any visible eigenmode in the measured spectrum at $\Delta\omega_{\rm cl}/2\pi = 0$ MHz, giving three eigenmodes in the transmission spectrum, disagrees with the theoretical spectrum. (The fact that the resonant transmission does not go to unity indicates that the "missing" eigenmode may be substantially suppressed, though not completely). Thirdly, the spectral features in reflection should more closely mirror the spectral features in transmission, which is not the case in Fig. 7.9.

In order to investigate whether this behavior is a just peculiarity of this particular mode, or instead, is a universal feature in our WGM bottle resonator, we investigate different modes. The Rabi-spectrum is tested further in measurements in the next section with a high-Q mode having large backscattering and a low mode volume, sufficient to be compatible with operation in the strong coupling regime. This test is interesting because it enables a better comparison with other cavity QED experiments with microtoroids and microdisks where the backscattering rate is typically large relative to the intrinsic linewidth.

7.2.2 Rayleigh scattering in a strongly-coupled atom-resonator system

Sub-wavelength scatters on the surface of the resonator can mediate the exchange of energy between the clockwise (CW) and counter-clockwise (CCW) propagating resonator modes via elastic (Rayleigh) scattering, as described in Sec. 3.3.2. The ratio of the inter-mode scattering rate to the intrinsic decay rate of the resonator is given by h/κ_i, and defines an important metric of the system. In a typical resonator where only one travelling mode is pumped, a significant fraction of the light will back-scatter to the other mode when the ratio h/κ_i is large. The fraction of the intra-cavity power that is back-scattered/reflected from the resonator is given by [27]

$$\frac{P_{\rm B}}{P_{\rm in}} = \left(\frac{\Gamma_{\rm scat}}{1+\sqrt{1+\Gamma_{\rm scat}^2}} \right)^2 , \tag{7.1}$$

where $\Gamma_{\rm scat} = h/\kappa_i$, and $P_{\rm (B/in)}$ is the back-reflected/in-coupled power. For the resonator mode used in Fig. 7.9 we get $\Gamma_{\rm scat} \backsimeq 0.2$, which according to Eq. (7.1) gives a back-reflection of 1.2%, roughly consistent with our measurements. In the following, we use a mode with $\Gamma_{\rm scat} = 2$ and a back-reflection fraction predicted by Eq. (7.1) to be as high as 38%, in good agreement with our measurement of 40%.

The Rabi spectrum of the mode with large back-reflection in Fig. 7.10 shows a qualitatively similar structure to the previous mode in Fig. 7.9. The spectra for the transmission and reflection both show the splitting more clearly because it is significantly larger at around 44 MHz,

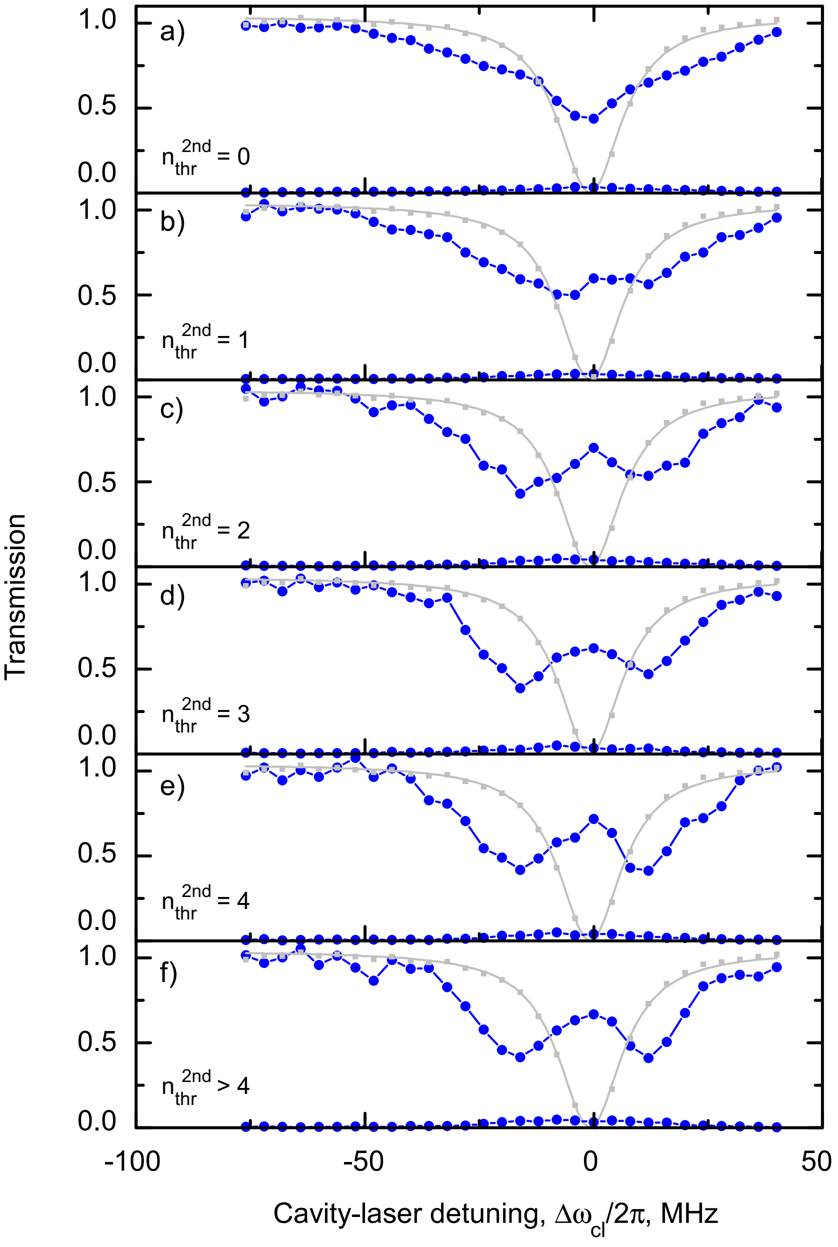

Figure 7.8: Rabi spectra using the double-detection scheme. Increasing the threshold (top to bottom) for re-detecting an atom after the spectrosopcy period reveals the structure in the coupled atom-resonator spectra (blue data points). The grey lines are Lorentzian fits to the empty resonance and the blue lines are a guide to the eye. See main text for details. Cavity-atom detuning: $\Delta\omega_{\mathrm{ca}}/2\pi = 0$ MHz.

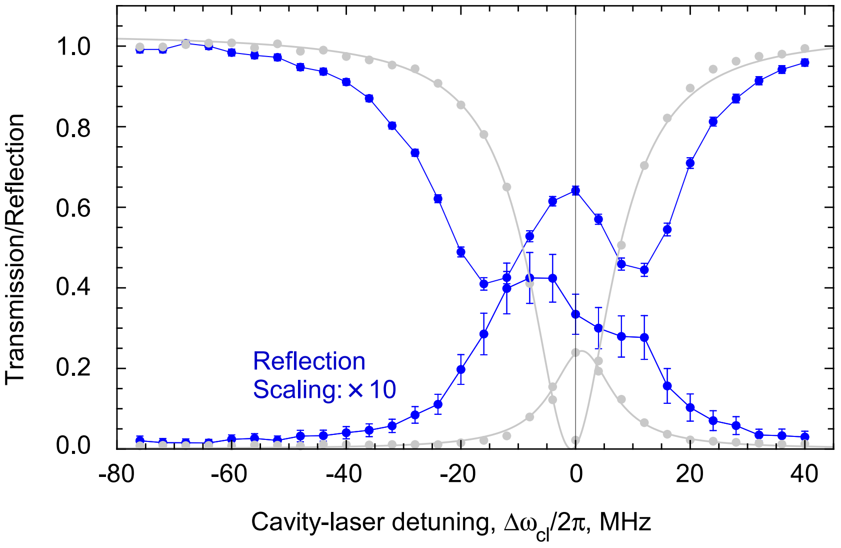

Figure 7.9: Transmission and reflection Rabi spectra. Two distinct dips in the transmission spectrum have a splitting of 28 MHz. Experimental parameters: photon pump-rate at resonator–fiber coupling junction 7.2×10^6 photons/s $\equiv 1.7$ pW, off-resonant photon rate at transmission detectors: 5.9×10^6 photons/s $\equiv 1.5$ pW, ~ 0.14 intracavity photons, residual transmission: $\sim 1 - 2\%$, intrinsic Q-factor: 6×10^7, cavity decay rate at critical coupling: $\kappa/2\pi = 8$ MHz, inter-mode scattering rate of resonator: $h/2\pi = 1.8$ MHz, $\Delta\omega_{\rm ca}/2\pi = 0$ MHz, $n_{\rm thr}^{\rm 2nd} \geq 3$, TM-polarized mode (confirmed using a linear polarizer and CCD camera).

compared to 28 MHz previously. This larger splitting is surprising because both modes are TM-polarized and the axial mode number is $q \leq 5$, giving a very similar mode volume and coupling strength at the surface.

According to calculations using the Jaynes-Cummings model, variations in h have little or no effect on the size of the atom-resonator mode-splitting, which should be simply given by the Rabi frequency $2g/2\pi$. Therefore, the observed Rabi splitting appears to depend on the empty cavity mode-splitting, and therefore masks the true Rabi frequency.

This behavior is expected because measured spectra are composed of typically a few hundred thousand coupling events, not a single event as assumed in the theory calculation. Accordingly, atoms will sometimes couple to standing wave A and other times to mode B, which have an intrinsic splitting of $2h/2\pi$. The atom-resonator splitting in this mode is increased by 16 MHz compared to the previous mode, while for comparison, the mode-splitting of the empty resonator is $2h/2\pi = 15$ MHz. This makes intrinsic mode splitting an additive effect that can, if ignored, lead to an over-estimation of g. To summarize, the Rabi-spectra of two modes with different back-reflection rates show qualitatively similar behavior, but quantitatively, the observed splitting is substantially different.

Comparison to other WGM experiments: Two other similar cavity QED experiments have been performed using WGM resonators and cold atoms and quantum dots. In both cases, spectra

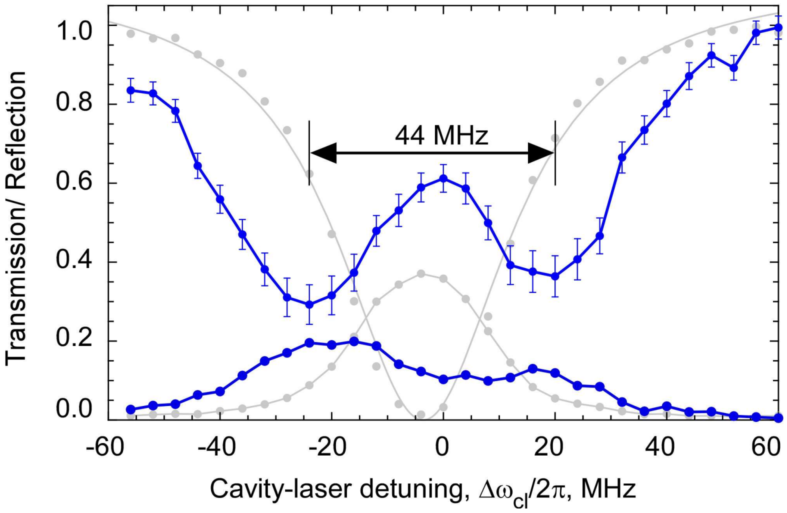

Figure 7.10: Rabi spectra for a resonator mode with large intrinsic mode splitting. An atom coupled to the resonator mode produces large and clearly visible splitting in the transmission spectrum and weaker splitting in the reflection spectrum. Compared to the mode in Fig. 7.9, the two Rabi dips have a broader FWHM approximately given by $2\times(\kappa/2\pi+\gamma/2\pi)\approx 35-40$ MHz [114]. Parameters: resonator decay rate at critical coupling: $\kappa/2\pi = 17.5$ MHz, intrinsic Q-factor: 6×10^7, inter-mode scattering rate: $h/2\pi = 7.5$ MHz, fraction of intra-cavity light backscattered at critical coupling: $\sim 40\%$, axial mode number: $q \leq 5$, photon pump-rate at resonator–fiber coupling junction: 15.8×10^6 photons/s $\equiv 4.0$ pW, off-resonant photon rate at transmission detectors: 12.9×10^6 photons/s $\equiv 3.3$ pW, ~ 0.15 intracavity photons, residual transmission: $\lesssim 1\%$, $\Delta\omega_{\rm ca}/2\pi \leq -3.6$ MHz.

of the coupled quantum emitter and WGM mode were measured. The reflection spectrum for a solid-state microdisk strongly coupled to a quantum dot in Ref. [115] is dominated by intrinsic resonator mode-splitting, which impedes a clear identification of the three eigenstates predicted from the Jaynes-Cummings model. Also, since the waveguide-resonator system was limited to operating in the under-coupled regime, the quantum dot only exhibited a relatively weak effect on the reflection spectrum — a maximum power change of 0.3% was observed between measurements where the coupled quantum-dot–resonator was strongly saturated as compared to when it was not saturated. Spectral measurements on a strongly coupled atom-microtoroid system in Ref. [84] were not able to reveal the three eigenstates predicted from the Jaynes-Cummings model because of excessive “smearing” of the spectral features when $\omega_c = \omega_a$. Interestingly, their data shows an absolute transmission change of $\sim 60\%$ at a detuning of $\Delta\omega_{\rm ca}/2\pi \approx 0$ MHz, in almost exact agreement with our measurement of 62%. Unfortunately, the authors do not investigate this observation. To summarize, a direct comparison of the experimental spectra in Figs. 7.9 and 7.10 to other work with WGM resonators in the literature is difficult because, to date, all have large scattering, $\Gamma_{\rm scat} > 1$ [48, 84, 115], and/or no spectral measurements are available for the resonant case $\omega_c = \omega_a$ [48, 84].

7.3 Spectroscopy with a fiber-coupled three-port resonator

The experiments in the preceding section considered the case where both the in-coupled and out-coupled light is confined to a single fiber. Destructive interference between the intra-cavity light and the transmitted light in the fiber produces the observed transmission response. It is interesting to also consider the response of the atom-resonator system using two fibers where one fiber is used to in-couple light while a second fiber serves to collect light from the coupled system. In this case, the transmission response in the collection fiber is no longer due to the interference of two fields but rather only the intra-cavity field. To this end, we have studied such a configuration using two optical nanofibers as shown in Fig. 7.11 (a, b).

Fiber 1 serves to out-couple 50% of the intra-cavity light which is then measured with four SPCMs. Light is in-coupled to the resonator through fiber 2, which is very weakly coupled to the resonator and causes negligible broadening of the mode linewidth. The distance of both fibers is stabilized using the scheme described in Sec. 5.2.

The transmission field amplitude in fiber 1 is $\hat{a}_{\mathrm{out}} = i\sqrt{2\kappa_e}\hat{a}(t) = i\sqrt{\kappa_e}\left[\hat{A}(t) + \hat{B}(t)\right]$, and the corresponding transmission spectra are shown in Fig. 7.12 (a). The Rabi-split modes in the transmission spectrum are predicted to have a larger splitting compared to both the reflection spectrum and the typical transmission spectrum with one fiber (not shown here, c.f. Fig 7.9). In contrast to the WGM spectrum with one uncoupled mode, the spectrum of a Fabry-Pérot-like resonator with a single mode is dominated by only two Rabi peaks, as shown in Fig. 7.12 (b). Another noticeable feature is the larger amplitude of the Rabi peaks in (b). The coupling of an atom to one of the two standing modes in the WGM resonator results in a re-distribution of energy equally between the two travelling modes a and b. This approximately halves the amplitude of the field in each mode which therefore halves the amplitude of features in the Rabi spectrum in (a) compared to (b) for which there is a single mode of light.

The measured empty resonator (i.e. with no atom coupled) transmission in Fig. 7.12 (c) reaches a maximum of ~ 50%, while the back-reflection is ~ 3%. The transmission spectrum in the coupled-atom case shows two peaks with a splitting of about 36 MHz, which is 8 MHz larger than the 28 MHz splitting measured with a single coupling fiber and which agrees well with the expected value given in Fig. 7.12 (a). The spectrum for the back-reflection is substantially smaller and shows a weak splitting of ~ 20 MHz.

Perhaps tellingly, the measured transmission spectrum is remarkably similar to our expectations for the spectrum from a single-mode atom-resonator system. Not only are these measurements consistent with the previous measurements with a single fiber, they reveal the potential of the resonator to operate as a multi-port device with strongly coupled atoms.

Apart from the two modes investigated here, measurements from other modes at $\omega_l = \omega_c = \omega_a$ all show similar high transmission values. Since these results are highly unexpected, a closer study of the system is warranted.

In the following sections we investigate the experimental conditions required to reproduce the transmission and reflection spectra presented earlier. In particular, we next consider the possibility of a fast-moving atom that couples both standing waves on a timescale shorter than the photon lifetime in the resonator. In order to gain further insight to a possible explanation, we theoretically consider several issues such as the influence of dipole forces and atom-surface

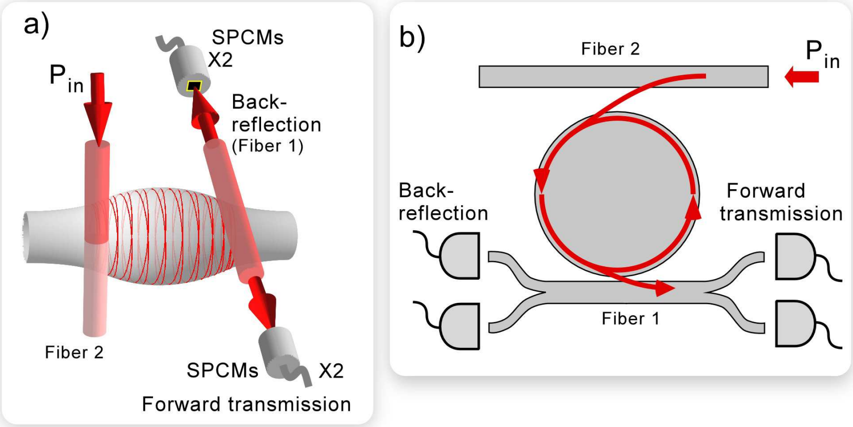

Figure 7.11: Coupling setup using two fibers. (a, b) Light in fiber 2 (also labeled as fiber 2 in the fiber network in Fig. 6.1) is coupled into the empty resonator which itself couples to fiber 1. Fiber 1 is critically coupled to the resonator and couples out $\sim 50\%$ of the light, while fiber 2 is weakly coupled to the resonator and couples in (out) 10% of the pump (resonator) light.

induced level shifts in the following sections. We have performed experiments to study the influence of resonator detuning and atomic forces.

7.4 Forces and velocity effects on atomic motion

In order to reproduce the spectral measurements, we perform simulations assuming only a contribution from atoms that have a high initial velocity. These atoms are assumed to move tangentially along the resonator mode: axial movement along the resonator fiber axis can be safely neglected since the axial extension of the mode is large. If an atom has sufficiently high velocity, such that it can travel from the anti-node of standing wave A a distance of around $\lambda/4n$ to the anti-node of standing wave B within a time $\tau = 1/4\pi\kappa \approx 11$ ns, where τ is the photon lifetime, the atom can be strongly coupled to both modes rather than just one.[2] In effect, the atoms require a velocity of $\lambda\kappa\pi/n \approx 11$ m/s to couple to both modes, where n is the refractive index of glass. This is an overestimate for our measurements since we assume the atom does not perfectly couple to both modes because the resonant transmission does not reach unity.

In our atomic fountain apparatus, a cloud with around 1×10^8 atoms in a diameter of around 1–2 cm passes the evanescent field of the bottle resonator. During the interaction time, the close proximity of the atom to the silica resonator surface can affect its coupling to the mode due to dipole forces. In addition to this, surface interactions via vsn der Waals forces can arise due to shifting of the atomic energy levels. This force is typically of minor importance in Fabry-Pérot resonators since interacting atoms are located many microns away from the mirrors and out of

---

[2] In the definition of τ we define the cavity bandwidth to be the FWHM of the empty cavity resonance, i.e. $2 \times 2\pi\kappa$.

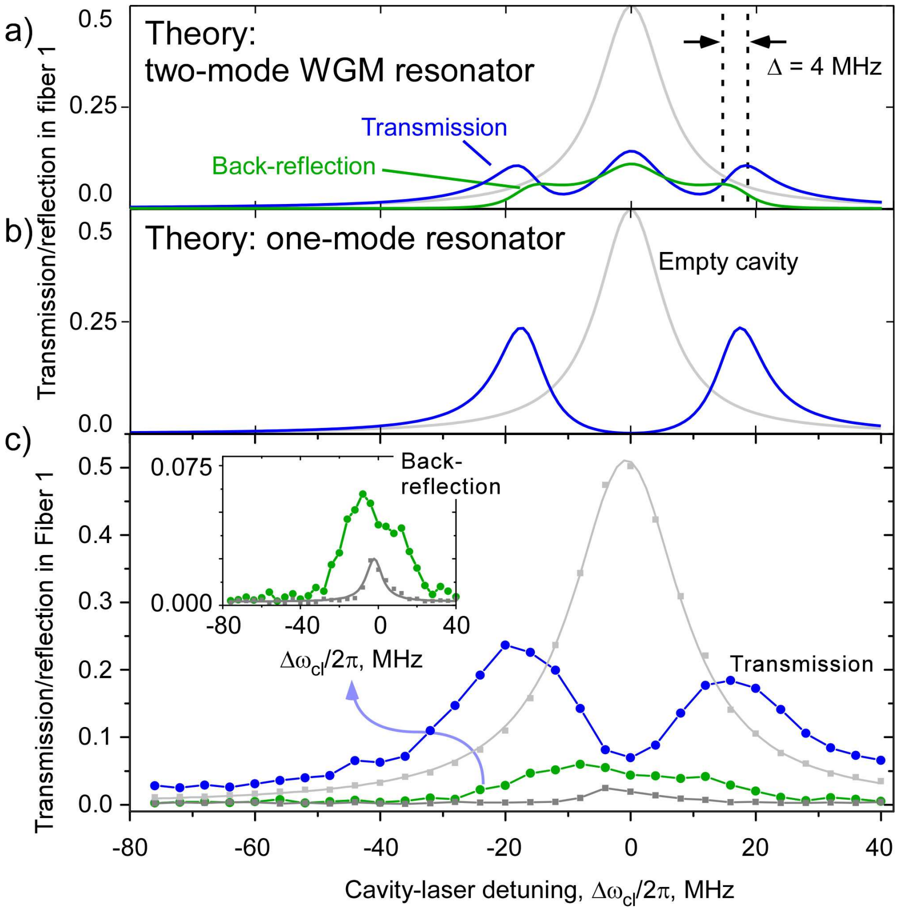

Figure 7.12: Rabi spectrum using two coupling fibers. (a) Theory calculation of the transmission and reflection Rabi spectra from the WGM resonator. The mode splitting in the transmission Rabi spectrum is predicted to be about $2\pi \times 8$ MHz larger compared to the splitting in the spectrum in back-reflection. This apparent increase in g arises because the light in the resonator does not experience destructive interference with light in the fiber, as would be the case in the single-fiber case considered earlier. (b) As a comparison to a WGM resonator, the Rabi spectrum is plotted for a single-mode resonator. (c) Rabi spectra measured on the two ports of fiber 1. The y-axis is normalized so that the transmission of the empty resonance at $\Delta\omega_{\mathrm{cl}}/2\pi = 0$ MHz is equal to 0.5, which is confirmed in separate measurements at critical coupling. Experimental parameters and resonator mode are identical to Fig. 7.9. Calculation parameters: $g/2\pi = 17$ MHz in (a) and $g/2\pi = 17/\sqrt{2}$ MHz in (b), $Q_{\mathrm{crit}} = 0.3 \times 10^8$, $Q_0 = 0.6 \times 10^8$.

range from surface effects. However in our WGM resonator, the regime of strong coupling is achieved when the atom-resonator distance is less than 100 nm, exactly where atom-surface perturbations become important. Combined together, a considerable force on the atom can be expected. More quantitatively, we include the effect of these forces on the atomic trajectory and calculate solutions for the resonant transmission and reflection using the quantum master equation for each time increment.

7.4.1 Theory

Dipole forces

In the quantum mechanical description of light-matter interaction, the energy eigenstates of the atom are replaced by new eigenstates defined by the coupling of the atomic dipole with a light field. This dressed-state picture describes two new eigenstates with an energy gap given by the coupling strength. The potential energy from the energy gap causes a force on the atom affecting its momentum and motion. In a WGM resonator, this force is given by the spatial derivative of the interaction part of the Hamiltonian in Eq. (2.19):

$$\vec{F}_{\mathrm{dipole}} = -\hbar \left[\nabla g_t^*(\vec{r})(\hat{a}^\dagger \hat{\sigma}_- + \hat{b}\hat{\sigma}_+) + \nabla g_t(\vec{r})(\hat{a}\hat{\sigma}_+ + \hat{b}^\dagger \hat{\sigma}_-) \right] , \tag{7.2}$$

The gradient of the electric field (proportional to $g_t(\vec{r})$) in the bottle resonator is very large over a short distance beyond the surface due to the exponential decay of the evanescent wave (see a plot of coupling strength versus distance in Fig. 3.14). Near resonance, $\omega_l \approx \omega_a$, the force is large even if the intra-cavity photon number is less than one. In this section, the influence of the dipole force is seen to have a significant affect on the properties to the atom transits, modifying both the atom interaction time and the number of detected atoms, and is dependent on detuning. To gain a better understanding of this, first the influence of cavity detuning is measured ($\Delta\omega_{\mathrm{ca}}/2\pi = -12$ to +8 MHz, $\Delta\omega_{\mathrm{cl}}/2\pi = 0$ MHz), and then the influence of laser detuning is measured ($\Delta\omega_{\mathrm{ca}}/2\pi = 0$ MHz, $\Delta\omega_{\mathrm{cl}}/2\pi = -76$ to +40 MHz).

Surface forces and atomic level shifts

Quantum fluctuations in the electromagnetic vacuum can induce fluctuations in the electric-dipole moment (EDM) of an atom. This is true regardless of whether or not an atom itself has an intrinsic EDM, such as for the Rb atom which has no EDM. When an atom is placed in front of a surface, radiative interactions with the surface induce a fluctuating image of the atomic EDM in the surface. The radiative exchange in energy between the atom and its image creates a conservative interaction potential that, depending on the atomic and surface properties, is generally attractive.

This potential is termed a van der Waals potential when the distance is small (e.g., several nanometers or less), or a Casimir-Polder potential when the distance is much larger. The exact form of the potential depends of the distance scale relative of the radiation spectrum, but also the material properties of the surface and atomic polarizability. The Lifshitz formalism fully describes the potential using these three parameters. For simplicity, here we use an approximation valid for short distances and which is sufficient to model the essential physics describing the atom-surface interaction.

The approximation uses the Lennard-Jones form of the interaction potential to give $U^{\mathrm{LJ}} = -C_3/d^3$, where d is the atom-surface distance and C_3 is a coefficient proportional to the potential or, equivalently, the energy level shift. It is known that for cesium atoms positioned at a distance of $d = 100$ nm from a silica dielectric surface [84] the difference in frequency shift of the ground-state predicted by the full Lifshitz formalism and the approximation is $\Delta\omega_g^{\mathrm{Lif}} - \Delta\omega_g^{\mathrm{LJ}} = (-1.1 + 0.6)$ MHz $= -0.5$ MHz. For the resonator modes considered in this work, the difference is acceptably small and is expected to be similar for Rb atoms. In addition, there is some variability of the exact value of $\Delta\omega_g^{\mathrm{Lif}}$ for cesium and silica in the literature, with Ref. [84] giving a value 71% larger than Ref. [116]. Calculated values of C_3 for a rubidium atom near a perfectly conducting wall are given in Ref. [117].

We explicitly calculate the value of C_3 for the ground state of ^{85}Rb, $5^2S_{1/2}$, using the measured material constants of silica [109] and the measured and calculated oscillator strengths for Rb [118]. For a real-dielectric with a non-perfect conducting wall, the C_3 coefficient is given by

$$C_3 = \frac{\hbar}{4\pi\varepsilon_0}\int_0^\infty d\xi\alpha(\xi)\frac{\varepsilon(\xi) - \varepsilon_0}{\varepsilon(\xi) + \varepsilon_0}\ , \tag{7.3}$$

where $\varepsilon_0 = 1$ is the permittivity of vacuum, $\varepsilon(\omega)$ is the material permittivity, $\alpha(\xi)$ is the frequency dependent atomic polarizability, and ξ is the Matsubara frequency used in the Lifshitz formalism, which is commonly used in the literature, but is not strictly necessary here.

The dielectric permittivity is calculated along the imaginary frequency axis using the relation [119]

$$\varepsilon(i\xi) = 1 + \frac{2}{\pi}\int_0^\infty d\omega\frac{\omega\mathrm{Im}\varepsilon(\omega)}{\omega^2 + \xi^2}\ , \tag{7.4}$$

where $\varepsilon(\omega) = n^2(\omega) - k^2(\omega) + i2nk$ and includes the real ($n(\omega)$) an imaginary ($k(\omega)$) parts of the refractive index tabulated in Ref. [109] for vitreous SiO_2 glass. The result is plotted in Fig. 7.13 (a) and shows significant contributions in the frequency range $10^{13} \leq \xi \leq 10^{17}$ rad/s. The static dielectric permittivity of SiO_2 can then be directly read from the low frequency end of the plot as $\varepsilon_0 = 3.89$ [120].

To a good approximation, the atomic polarizability of a state in ^{85}Rb is the calculated as the sum over all transitions using the relation [119]

$$\alpha(i\xi) = \sum_n f_n\left(\frac{e^2/m_e}{\omega_n^2 - \xi^2}\right)\ , \tag{7.5}$$

where f_n is the transition oscillator strength, e and m_e is the electron charge and mass in CGS units, respectively. Atomic decay is excluded since the transitions are very narrow compared to the frequency range of the summation.

Equation (7.5) is applied to the $5^2S_{1/2}$ ground state and the $5^2P_{3/2}$ excited state. The total atomic polarizability of the ground state is dominated by the large oscillator strength of transitions $5^2S_{1/2} \rightarrow 5^2P_{1/2}$ and $5^2S_{1/2} \rightarrow 5^2P_{3/2}$, while the polarizability of the excited state is dominated by transitions $5^2P_{3/2} \rightarrow 5^2S_{1/2}$ and $5^2P_{3/2} \rightarrow 6^2S_{1/2}$ [121]. For completeness,

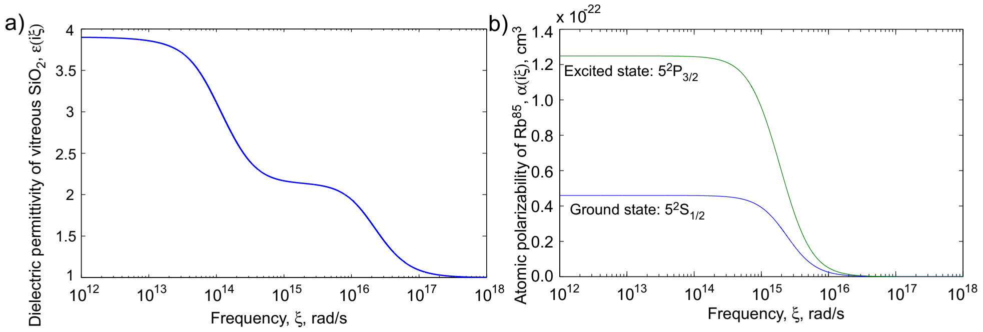

Figure 7.13: (a) Dielectric permittivity of vitreous silica. (b) Total atomic polarizability of ground and excited states of the D$_2$-transition in ^{85}Rb.

the transitions $5^2S_{1/2} \rightarrow N^2P_{1/2}$ and $5^2S_{1/2} \rightarrow N^2P_{3/2}$ for $N = 5 - 10$ are included in the calculation of the ground state polarizability [118, 121]. For the excited state calculation, the transitions $5^2P_{3/2} \rightarrow N^2S_{1/2}$ for $N = 5 - 12$ and $5^2P_{3/2} \rightarrow N^2D_{5/2}$ for $N = 5 - 10$ are included [118, 121]. The result is plotted in Fig. 7.13 (b) and is in agreement with the static dipole polarizabilities (at the low frequency end of the plot) given in Ref. [122].

With the necessary values now at hand, the constant C_3 for the ground state is calculated to be 5.1×10^{-49} J m^3 $\equiv 770 \times h$ Hz μm^3, and for the excited state it is 11.6×10^{-49} J m^3 $\equiv$ $1.7 \times h$ kHz μm^3, where h is Planck's constant. The atomic transition frequency ω_a is shifted by an amount $(U_e^{\mathrm{LJ}} - U_g^{\mathrm{LJ}})/\hbar$, where $U_{(\mathrm{e,g})}^{\mathrm{LJ}}$ is the excited/ground state potential. At an atom-surface distance of 100 nm, the atomic transition frequency is red-shifted by 0.9 MHz, and at distances of 50 nm and 40 nm the red-shift increases to 7.5 MHz and 14.5 MHz, respectively. For reference, the calculated coupling strength $g/2\pi$ at a distance of 50 nm is around 35 MHz for a TM-polarized mode (see Fig. 3.14 (b)). Therefore, energy level shifts can have a measurable effect on the transmission and reflection spectra.

Trajectory calculation

Surface interactions are firstly included in the simulation by including an cavity-atom offset of $\Delta\omega_{ca}/2\pi = 10$ MHz, and secondly, by adding the surface force arising from the surface potential. This force is calculated by

$$\vec{F}_{\mathrm{surf}} = \vec{F}_{\mathrm{surf}}^{g}\sigma_+\sigma_- + \vec{F}_{\mathrm{surf}}^{e}\sigma_-\sigma_+ \ , \tag{7.6}$$

where $\vec{F}_{\mathrm{surf}}^{\mathrm{g,e}} = 2\pi \times \nabla U_{\mathrm{g,e}}^{\mathrm{LJ}}(\vec{r})$, and $\sigma_{+/-}$ is the atomic raising/lowering operator. By adding together the forces ($\vec{F}_{\mathrm{tot}} = \vec{F}_{\mathrm{surf}} + \vec{F}_{\mathrm{dipole}}$) the atom velocity and position can be iteratively calculated for each time step, Δt. The atomic velocity at time t^i is simply

$$v^i = v^{i-1} + a^{i-1}\Delta t \ , \tag{7.7}$$

where $a^{i-1} = F_{\mathrm{tot}}^{i-1}/m$ is the acceleration for the previous time step, and m is the atomic mass. Momentum diffusion due to quantum fluctuations of the optical forces is treated as being negligible and should not change the qualitative results of the simulation. The atom position at time t^i is then simply $r^i = r^{i-1} + v^{i-1}\Delta t$. Lastly, the photon number of the resonator modes is calculated for the transmission and reflection.

Figure 7.14 (a–l) shows the result of three simulated atomic trajectories and the associated data for atomic position, transmission, reflection, and velocity. The top row shows a cross-section through part of the resonator and the atom trajectory near the surface with a starting velocity of $v^{i=0} = 5$ m/s and a starting position ~ 500 nm from the surface on the y-axis. By careful selection of the starting launch angle, interaction times of around 2 μs are observed where the resonant transmission ($\Delta\omega_{\mathrm{cl}} = 0$ MHz) increases to 65% and the reflection increases to 15%, reasonably consistent with our measurements, see Fig. 7.14 (b, c). During this time the atom follows a quasi-stable orbit with a near-constant atom-surface distance of 55 nm while also maintaining constant transmission and reflection. Such orbits are possible when the attractive surface force is balanced by the centrifugal force of the atom trajectory.

While the resonator surface generally has near atomic smoothness Rayleigh scattering by nanometer-sized particles on the surface can mediate the coherent scattering of light between CW and CCW modes. As discussed in Sec. 3.3.2, this mode-scattering can remove the degeneracy of the two resonator modes but it can also affect the spatial mode structure. A standing wave mode structure is then formed with, for example, the node of one standing wave, say A, is located at the position of the scatterer and the anti-node of standing wave B is located at the position of the scatterer. In this case, the intensity of B exhibits a $\cos(\theta)^2$-modulation and A exhibits a $\sin(\theta)^2$-modulation where the phase $\theta = 0$ is defined at the position of the scatter: for reference, see the standing wave picture in Fig. 2.2 (b). As the atom traverses multiple nodes and anti-nodes of the modes, there is a corresponding small modulation in the transmission and reflection. The modulated coupling of the atom to the modes produces an effective coupling strength g when averaged over a section of the trajectory. Starting velocities below 5 m/s are not plotted because the calculated resonant transmission then falls below the measured value.

The transmission spike at 0 μs is an artefact of the simulation due to the abrupt introduction of an atom/photon to the time evolution of the density matrix and can be ignored for times longer than $1/4\pi\kappa \approx 11$ ns.

The sensitivity of the simulation to the starting conditions is visible in the middle and right columns where the starting launch angle is changed by 0.1°. In both cases the interaction time is ≤ 1 μs because the atom either crashes into the surface (e–h) or does not pass close enough for surface forces to significantly modify its trajectory (i–l). Nevertheless, all three cases will be detected by our atom detection scheme, which uses a moving time-window, because the transmission is sufficiently high to exceed the threshold. The double atom-detection scheme will, however, only consider events similar to that in left column because of the requirement for long interaction times.

7.4.2 Experimental results

High-resolution spectrum

To examine if atoms with high-velocity can explain our observed spectrum, we compare the simulated Rabi spectrum with measurements. Figure 7.15 (a) shows a simulated Doppler-shifted

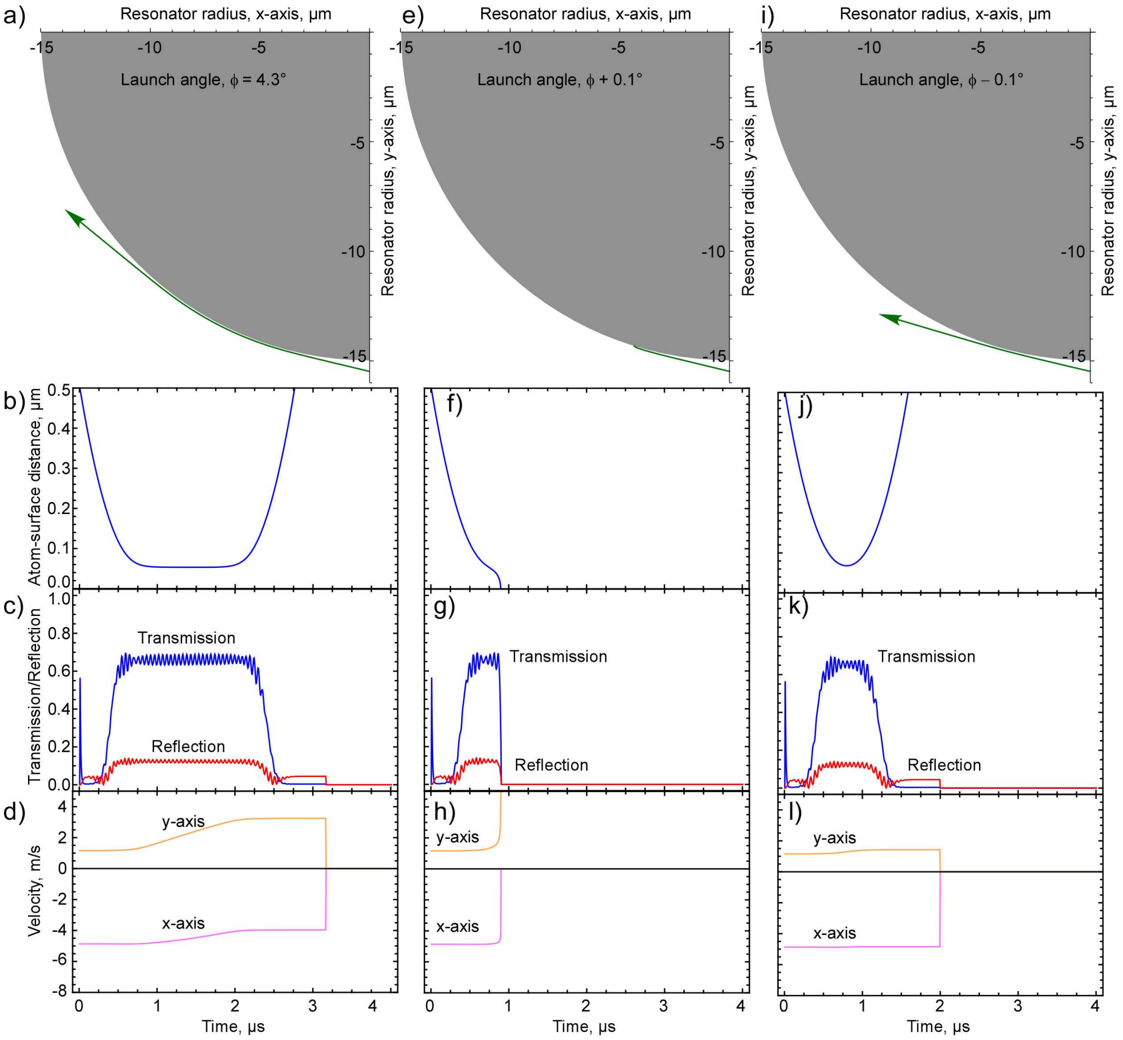

Figure 7.14: Simulated atomic trajectories. Left column (a–d): The atom transit through the evanescent field follows a quasi-stable orbit over a distance of several microns. Surface forces significantly affect the orbit (b, d) and result in a constant transmission and reflection for 2 μs. Middle column (e–h): The launch angle of the atom is increased by 0.1° towards the surface and causes the interaction time to decrease to < 1 μs. Right column (i–l): Similar to the previous case except the angle is decreased by 0.1°. Initial atom velocity $v^{i=0} = 5$ m/s. The simulation ends when the atom crashes on the surface or is more than 1.1 μm away from the surface. Parameters: mode properties identical to Fig. 7.9, $\omega_c = \omega_a = \omega_l$.

Rabi-spectrum averaged over coupling strength ($g_t/2\pi = 15 - 30$ MHz) and positive and negative velocities ($|v| = 4 - 6$ m/s). Two Rabi-split dips due to atoms co- and counter-propagating with the mode are indicated with arrows, but we note also that both central two dips have a contribution from the empty resonator eigenstate and the atom-resonator eigenstates.

Atomic motion leads to a resonance shift of $\vec{k}\vec{v}$. Atoms co-propagating with a velocity of 5 m/s in the direction of the travelling wave mode that is externally pumped by the fiber will be red-shifted by around 6 MHz, measured in the reference frame of the mode. Counter-propagating atoms will result in a blue-shift. A signature of high-velocity atoms moving with respect to the resonator mode is the presence of one or both dips indicated by the arrows in the figure.

Figure 7.15 (b) shows a high resolution spectrum of single atoms coupled to the resonator. A clear qualitative similarity between theory and measurement is evident. In the theory plot, the resonant transmission change is 62%, in good agreement with the measured value of around 65%. The theory plot correctly shows an imbalance in depth between the two main dips, which is also seen in the measured plot, however the imbalance is larger in the theory plot. A close examination of the transmission and reflection in Fig. 7.15 (b) does not clearly indicate the expected dips for a moving atom at the positions of the arrows, which are expected for a moving atom.

Cross-correlation measurements

The transmission of photons in the coupling fiber depends on the dressed states of the coupled atom-resonator system. The photon statistics of the dressed states can show sub-Poissonian (i.e., anti-bunching), super-Poissonian (i.e., bunching), or simply Poissonian statistics, depending on the resonator-laser detuning and the atom-resonator coupling rate g relative to the resonator loss rate κ. Photon cross-correlations measured as a function of detuning in the transmission spectrum can be useful to gain further insight towards identifying which spectral dips correspond to the empty resonator resonance and atom-resonator resonances.

The normalized, time-dependent, second-order photon cross-correlation function for transmission, $g_T^{(2)}(\tau)$, is calculated with the equation

$$g_T^{(2)}(\tau) = \frac{\langle \hat{a}_{\text{out}}^\dagger \hat{a}_{\text{out}}^\dagger(\tau) \hat{a}_{\text{out}}(\tau) \hat{a}_{\text{out}} \rangle}{\langle \hat{a}_{\text{out}} \hat{a}_{\text{out}}^\dagger \rangle^2} \,, \tag{7.8}$$

where the field operators have been defined in Chap. 2. The theoretical cross-correlation for $g_T^{(2)}(\tau = 0)$ as a function of resonator-laser detuning, $\Delta\omega_{\text{cl}}$, is plotted in Fig. 7.16 (b) using the Jaynes-Cummings model where we assume a stationary atom. The spectral features can be understood as follows. At a detuning near the rightmost transmission dip, only single photons can enter the resonator because they are resonant with the single-photon resonance of the Jaynes-Cummings ladder (see the ladder in Fig. 7.16 (a)). When two photons arrive together at the resonator within a time $1/4\pi\kappa$ =11 ns, they cannot efficiently enter the resonator, resulting in an excess of transmitted two-photon events in the fiber and bunching of detected photons in transmission.

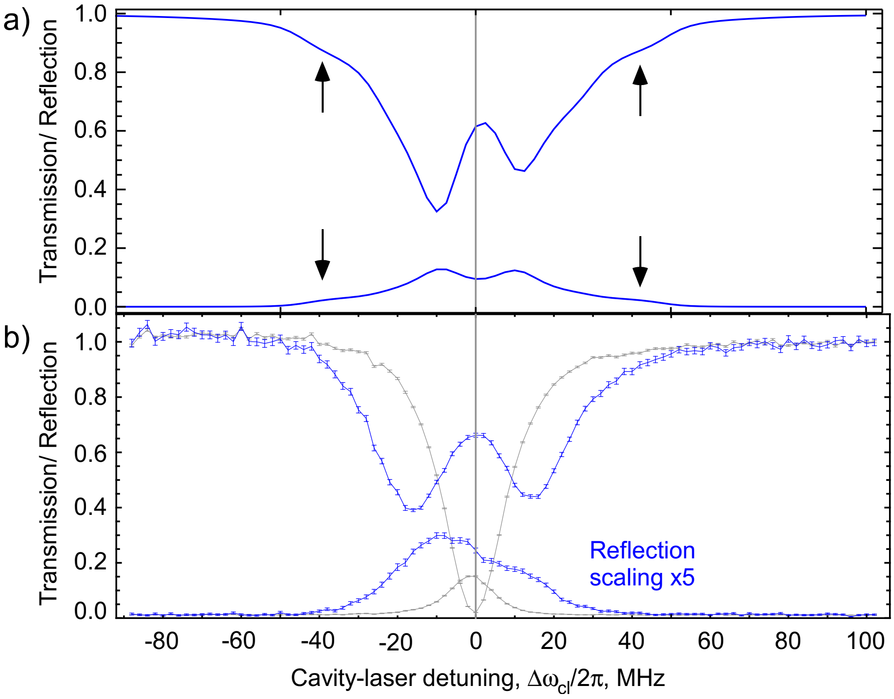

Figure 7.15: High resolution, low noise Rabi-spectra. (a) Simulated spectra assuming a Doppler-shift due to high velocity atoms and with averaging over coupling strengths ($g_t/2\pi = 15-30$ MHz) and positive and negative atomic velocities ($|v| = 4-6$ m/s). The arrows indicate the position of one of the Rabi-split modes. $\Delta\omega_{ca}/2\pi = 5$ MHz. (b) Measured Rabi-spectrum concatenated from two measurements — one mainly covering positive detunings and the other mainly covering negative detunings. Experimental parameters and resonator mode are identical to Fig. 7.9. Error bars are ±1 standard deviation based on the number of photons measured per data point.

On the other hand, when the detuning of incoming photons is reduced to around 11 MHz, two-photon events are more resonant with the two-photon transition (i.e., second step of the Jaynes-Cummings ladder). Both photons can therefore enter the resonator and the atom and resonator eliminate these two-photon events through absorption or other loss processes. This results in a deficiency in two-photon events and anti-bunching of the detected photons in transmission. Such a situation is termed photon blockade because only single photons are transmitted in the fiber while two-photon events are not allowed to be transmitted. We note that this type of photon blockade relies on the quantum nature of the anharmonicity of the Jaynes-Cummings ladder realized in the strong coupling regime of cavity QED. Another type of blockade experimentally demonstrated in Ref. [92] is conceptually and quantitatively different because it relies on the near-resonant saturation of single atoms in the regime of weak-coupling cavity QED. Nevertheless, both photon blockade schemes produce photon anti-bunching with $g_T^{(2)}(\tau = 0) < 1$.

At a detuning $\Delta\omega_{\mathrm{cl}} = 0$ MHz, both one-photon events and particularly two-photon events

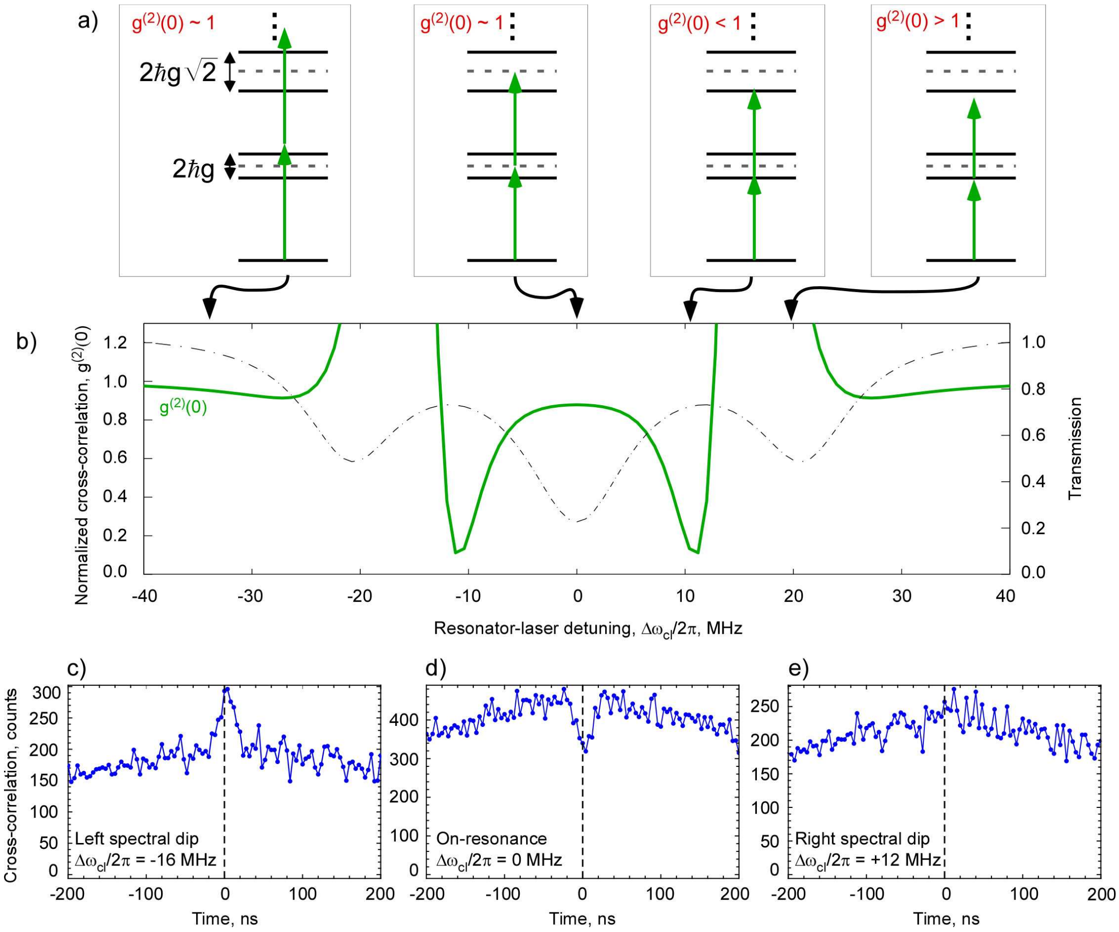

Figure 7.16: Cross-correlation measurements of the Rabi spectrum. (a) Sketch of the ladder of eigenstates given by the Jaynes-Cummings model for different resonator-laser detunings. (b) The normalized second-order cross-correlation (solid line) is calculated as a function of resonator-laser detuning. As an example, the transmission of a coupled system with $g_t/2\pi = 21/\sqrt{2} = 15$ MHz is plotted (dash-dot line). (c–e) Three cross-correlation measurements at three points in the spectrum. Experimental parameters and resonator mode are identical to Fig. 7.9. These mode parameters are used in plot (b).

cannot efficiently enter the resonator because they are detuned far from the resonances of the coupled system. In the limit of large g/κ the normalized cross-correlation is $g_T^{(2)}(\tau = 0) = 1$, but when g/κ is smaller, such as for the resonator modes studied here, the cross-correlation can show weak anti-bunching. This is due to the spectral broadening of the resonances which eventually overlap and results in a non-zero probability of two-photon events entering the resonator. In the limit of large κ for a given g, the normalized cross-correlation approaches zero [92].

Figure 7.16 (c-e) shows cross-correlation measurements at three different detunings chosen to be at the minimum transmission values of the left and right dips in Fig. 7.15 and also on resonance with the empty resonator. As expected from the theoretical prediction for a stationary atom, the left spectral dip (Fig. 7.16 (c)) shows bunching and the resonant point (Fig. 7.16 (d)) shows anti-bunching. The right spectral dip (Fig. 7.16 (e)), however, does not show any features even though it is expected to show bunching.

The $g^{(2)}$ and transmission spectra in Fig. 7.16 (b) will be Doppler-shifted when an atom with high velocity transits the resonator mode. Photon bunching or anti-bunching features in the spectrum may therefore become averaged out over many experimental runs or even individual runs if the atomic transit velocity is strongly time-dependent, as simulated in Fig. 7.14. An interesting future direction for these measurements would be to measure photon cross-correlations for the whole frequency spectrum, though this is very time consuming. The measurement would complement the transmission and reflection measurements and provide a test of the hypothesis that high-velocity atoms are co-propagating (or counter-propagating) in the direction of the travelling mode pumped by the laser. These spectral measurements will also help identify whether both of the split resonances in the transmission spectra are due to the action of atoms, in which case photon bunching is expected, or possibly one resonance is an uncoupled resonance, in which case weak photon anti-bunching or Poissonian statistics is expected.

7.4.3 Properties of atom transits and dipole forces

Dipole forces and cavity detuning

Atoms in a moving molasses are launched on a ballistic trajectory with an average turning point slightly above the bottle resonator. This results in part of the atomic cloud passing the resonator twice — on the upward and downward flights. In each case the atoms have a velocity of around 10 cm/s, determined from the arrival times of the cloud at the resonator. Figure 7.17 (a) shows the temporal distribution of detected events at the resonator as a function of $\Delta\omega_{\mathrm{ca}}$ using the single atom detection scheme. Most atoms are detected on the upward flight in the first 40 ms compared to the downward flight in the final 25 ms of the plot. This is due to the thermal expansion of the atomic cloud which reduces the atomic density.

Distinctly different atom detection statistics are visible when the sign of the detuning $\Delta\omega_{\mathrm{ca}}$ is changed. A repulsive dipole force ($\Delta\omega_{\mathrm{ca}}/2\pi > 0$ MHz) causes a steep but short-ranged potential hill over which only atoms with high enough velocity can overcome. Slower atoms, which arrive late in the first peak and early in the second peak, are simply repulsed by the evanescent field before the atom detection scheme can observe their presence. An attractive dipole force ($\Delta\omega_{\mathrm{ca}}/2\pi < 0$ MHz) adds to the attractive van der Waals force and accelerates more atoms toward the surface where they can couple strongly to the mode and thus be detected.

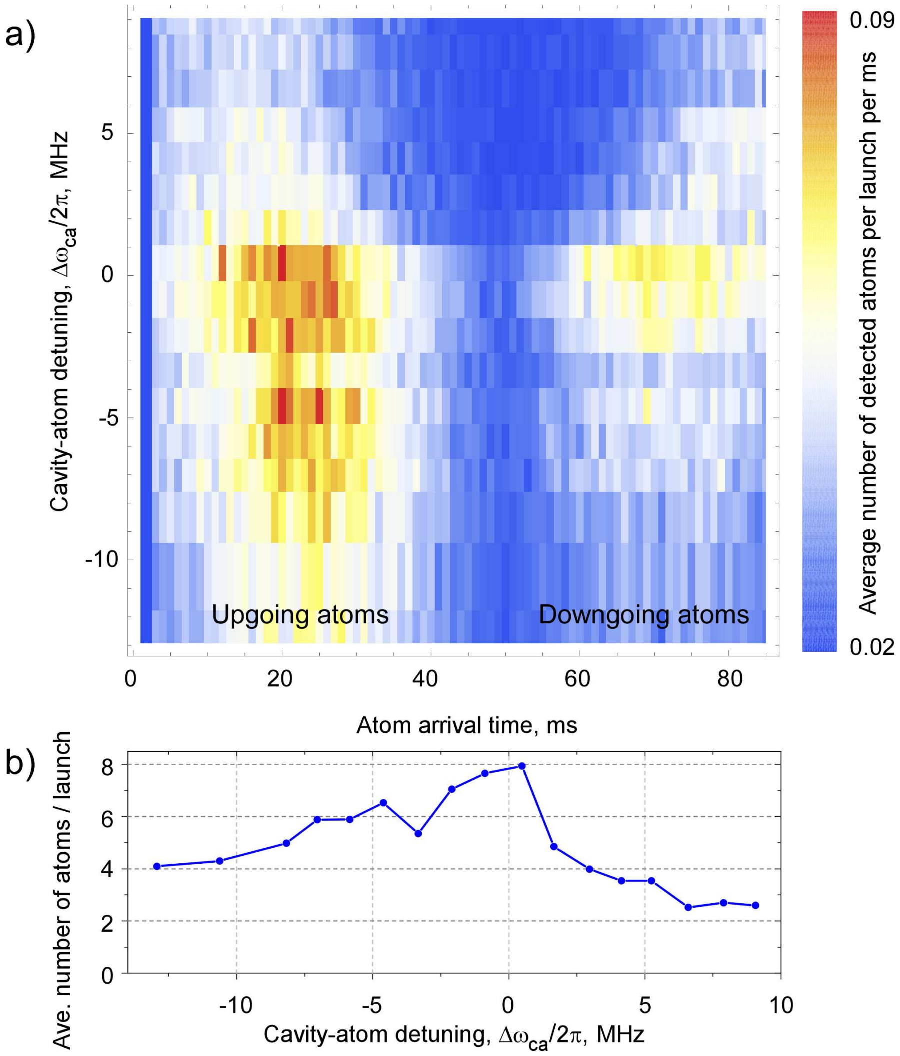

Figure 7.17: Temporal distribution of detected atoms as a function of cavity-atom detuning. (a) Two distinct groups of atoms interact with the resonator mode: when the atomic cloud is launched slightly higher than the resonator, both the upward and downward movement of the cloud can be distinguished. The time axis has been arbitrarily defined to start just before the upward-moving atoms reach the resonator. (b) Average of the data in (a) over all time. Increasing the cavity frequency with respect to the free-space atom transition frequency sharply reduces the number of detected atoms from 8 atoms/fountain launch to 2.5 atoms/fountain launch for $\Delta\omega_{\text{ca}}/2\pi = 6$ MHz. On the other hand, for $\Delta\omega_{\text{ca}}/2\pi > 0$ MHz the number of detected atoms decreases more slowly. See text for details. Parameters: off-resonant photon detection rate is $\sim 10 \times 10^6$ photons/s, $n_{\text{thr}}^{\text{1st}} \geq 7$ and $n_{\text{thr}}^{\text{2nd}} \geq 0$.

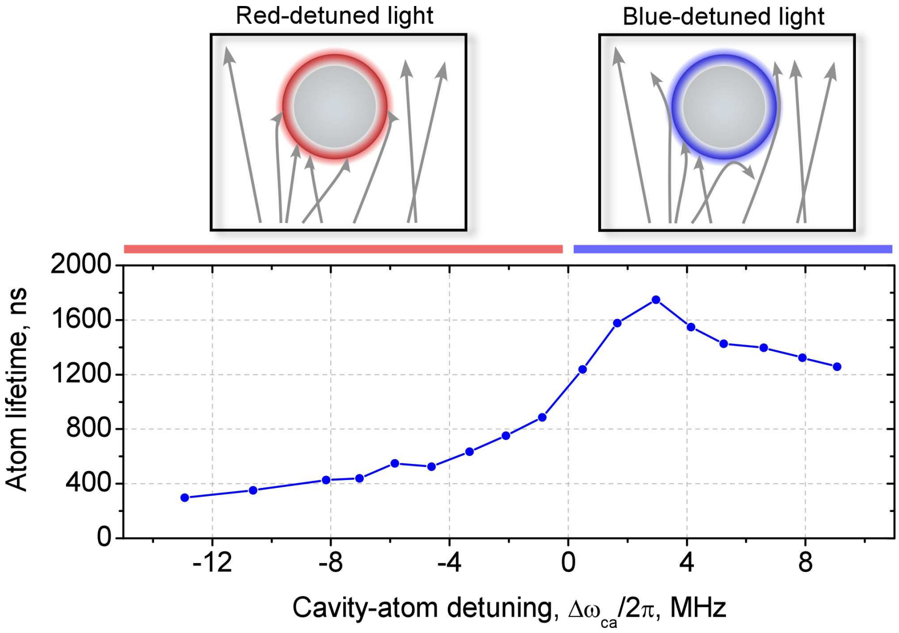

Figure 7.18: Interaction time as a function of cavity-atom detuning $\Delta\omega_{\rm ca}/2\pi$. Attractive dipole forces for $\Delta\omega_{\rm ca}/2\pi < 0$ MHz reduce the lifetime of atoms in the evanescent field, while repulsive dipole forces for $\Delta\omega_{\rm ca}/2\pi > 0$ MHz increase the lifetime. A maximum lifetime of ~ 1750 ns is reached at a detuning of 3 MHz. $n_{\rm thr}^{\rm 1st} \geq 7$ and $n_{\rm thr}^{\rm 2nd} \geq 0$.

Comparing red and blue detuned cases at a value of $\Delta\omega_{\rm ca}/2\pi = \pm 8$ MHz, there is almost a factor of three difference in the number of detected atoms, as shown in Fig. 7.17 (b).[3]

Dipole forces lead to a modification of the interaction time of atoms with the evanescent field, as shown in Fig. 7.18. Using the single atom detection scheme, the time-constant of the quasi-exponential decay of the fiber transmission is measured as a function of $\Delta\omega_{\rm ca}$, similar to that shown in Fig. 7.3 (b). A repulsive dipole force increases the interaction time by $\sim$ 50% at $\Delta\omega_{\rm ca}/2\pi = +3$ MHz compared to when the dipole force is zero at $\Delta\omega_{\rm ca}/2\pi = 0$ MHz. In contrast, an attractive dipole force at a detuning of $\Delta\omega_{\rm ca}/2\pi = -3$ MHz reduces the interaction time by $\sim$ 50% compared to the time at $\Delta\omega_{\rm ca}/2\pi = 0$ MHz.

Dipole forces and laser detuning

It is interesting to study the number of detected atoms as a function of a frequency scan of the atom-resonator system, as shown in Fig. 7.19 (a, b). The influence of dipole forces is again important to consider in the double atom-detection scheme because there is almost a factor of two difference in the number of detected atoms depending on the detuning.

---

[3] As an interesting side note, the dependence of $\Delta\omega_{\rm ca}$ on the number of detected atoms can used to estimate the coupling strength g between an atom and the mode [48]. Indeed, pioneering work in Refs. [48, 123] used this dependence to infer g for cesium atoms coupled to a microtoroid resonator.

A repulsive dipole force due to blue detuned light ($\Delta\omega_{\rm cl}/2\pi < 0$ MHz, $\omega_{\rm c} = \omega_{\rm a}$) counters the attractive van der Waals force, thereby reducing the number of atoms that crash into the resonator surface. Since these atoms have a longer interaction time, the double atom-detection scheme has a higher probability of selecting only these atoms. Note that the opposite is true for the single atom detection scheme, such as in Fig. 7.17. This is because the single atom detection scheme is largely insensitive to the duration of the atom interaction, and most atoms have a short interaction time. A remarkable consequence is this atom detection process is that the number of detected atoms recorded using the single atom detection scheme is essentially constant for all detunings with an average of 9.6 ± 0.9 detection events per fountain launch. Around 10 events/launch are detected with the single atom detection within a ± 30 MHz window around the empty resonance, which then fractionally drops to around 8.5 events/launch when the detuning is large. On the other hand, the double atom-detection scheme has a lower detection rate but, more importantly, it reveals the underlying influence of dipole forces driving the atomic motion with as little as ~ 0.2 intra-cavity photons over sub-micron distances on a microsecond timescale .

Changing the frequency of the spectroscopy light so that it is red-detuned produces an attractive force that reduces the number of detected atoms. These atoms are more likely to crash into the resonator surface and generally have a short interaction time as evidenced through Fig. 7.19 (b).

Atom-resonator detuning

Introducing atom-cavity detuning $|\Delta_{\rm ac}| > 0$ to the coupled system can be used to probe different regions in the transmission and reflection spectra. (Figure 2.4 (a) shows the response of the eigenvalues as a function of atom-cavity detuning). In general, the single-photon Rabi splitting is given by $\sqrt{\Delta_{\rm ac}^2 + 4g^2}$, which is valid for WGM resonators when intrinsic mode splitting is negligible, like in the high Q mode in Fig. 7.9.

Figure 7.20 shows the transmission spectra for red-detuned ($\Delta\omega_{\rm ca} < 0$ MHz) and blue-detuned cases ($\Delta\omega_{\rm ca} > 0$ MHz). Solving for g in the above equation gives $g/2\pi =$ (16.6, 14.0, 16.6, 18.0) MHz for detunings $\Delta\omega_{\rm ca}/2\pi = (-7, 0, +7, +15)$ MHz, respectively. Taking the average we get $\bar{g}/2\pi = 16.3 \pm 1.7$ MHz $\gg$ $(\kappa_e/2\pi = 8, \gamma/2\pi = 3)$ MHz. However, such an estimate must be treated as tentative since we rely on a model that does not reproduce the spectra, and the correspondence between measured mode splitting and Rabi frequency is not fully understood.

The signature of dipole forces is seen to affect the spectra, especially when the resonator is red-detuned from the atomic resonance. Attractive dipole forces pull the atomic trajectories towards the resonator surface and reduce the atom interaction time by a factor of three compared to the blue-detuned cases. Despite the worse photon statistics, a broadened spectrum with a splitting of around 34 MHz is still visible and the transmission change at zero detuning is around 55%. Repulsive dipole forces from blue-detuned light is, in fact, beneficial here because it counters the attractive van der Waals force to ensure fewer atoms crash into the surface.

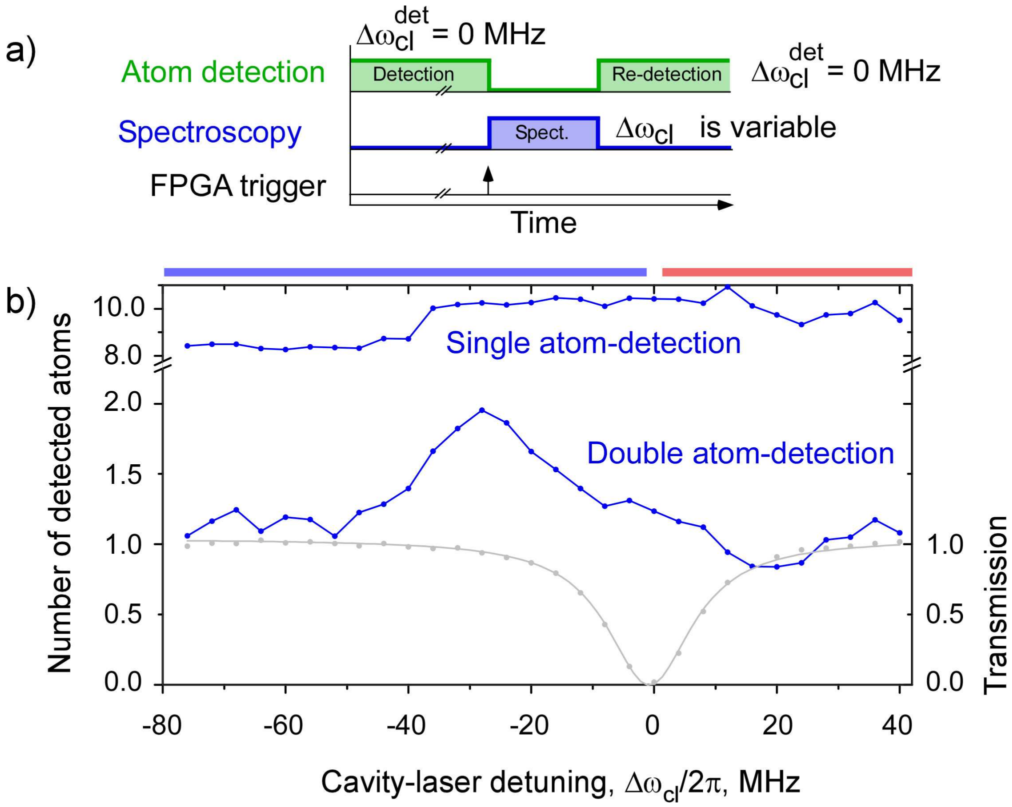

Figure 7.19: Influence of cavity-laser detuning on the number of detected atoms. (a) Experimental sequence using the double detection scheme. (b) The y-axis is the number of detected atoms per fountain launch using the indicated detection scheme. Double atom-detection criteria: $n_{\mathrm{thr}}^{\mathrm{1st}} \geq 7$ and $n_{\mathrm{thr}}^{\mathrm{2nd}} = 2$ photons per 1 μs measured within 2.25 μs after the initial detection trigger. Double atom-detection criterion: $n_{\mathrm{thr}} \geq 7$. The empty resonator spectrum is shown for reference (grey). Blue lines are a guide to the eye. Experimental parameters and resonator mode are identical to Fig. 7.9.

Acceleration of atoms

It remains an outstanding issue to identify a mechanism to produce high-velocity atoms that transit near the resonator surface. One possible mechanism involves atoms that are accelerated by the coupling fiber itself through a chain of momentum kicks from the absorption and emission of photons. Each recoil event adds a recoil velocity of 5 mm/s to the atom, and since the resonator is pumped with a propagating field in the fiber, the net force has directionality. The velocity distribution of the atoms will be very broad since the effect is based on radiation pressure. Unfortunately, neither the photon-rate in the coupling fiber nor the intra-cavity photon number is high enough to accelerate the atoms with sufficient velocity, i.e. 5 m/s. A power of around 1.7 pW in the coupling fiber corresponds to a photon rate of 7.2×10^6 photons/s, while the intensity, according to the calculated field intensity in Fig. 1.7, is less than a quarter of the saturation

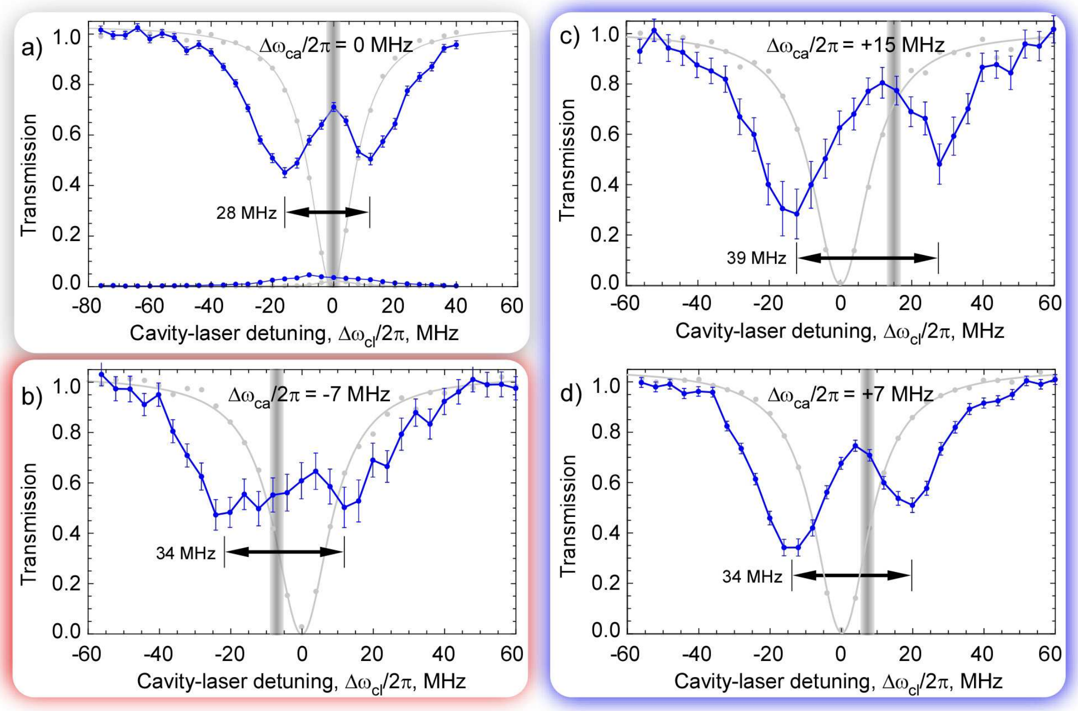

Figure 7.20: Rabi spectra for different resonator-atom detunings. (a) With the resonator and atom on resonance ($\Delta\omega_{\rm ca}/2\pi = 0$ MHz), the mode-splitting in the spectrum is 28 MHz. (c, d) When the resonator is blue-detuned from the atomic transition ($\Delta\omega_{\rm ca}/2\pi > 0$ MHz), the splitting increases and the maximum transmission point between the splitting remains close to the frequency of the atomic transition (vertical grey line). (b) The resonator is red-detuned from the atomic transition. Experimental parameters and resonator mode are identical to Fig. 7.9.

intensity of the atomic transition; the resonant scattering rate scales with $I/(I_{\rm sat} + I)$, where $I_{\rm sat} = 3.1$ mW/cm^2 is the saturation intensity. We conclude that even though atomic motion is an important issue with regard to the spectral properties of an atom coupled to the resonator, such high-velocity atoms are not the principle cause of the large effects we observe.

In the next section we explore another possibility caused not by atoms, but rather the intrinsic properties of the resonator mode itself.

7.5 Light scattering effects in WGMs

7.5.1 Asymmetries in the atom-resonator interaction

The axisymmetric design of the WGM resonator means that the transmission spectrum of the coupled system should be identical when probed in both the CW and CCW directions. The Jaynes-Cummings Hamiltonian, presented in Sec. 2.2.2, is based on the assumption that the coupling strength between the atom and both travelling waves is equal. This assumption has several consequences that are inter-related. Firstly, the symmetric exchange of energy between the atom and both travelling waves should be independent of which mode is excited using the coupling fiber. Secondly, the motion of the atom relative to the travelling waves should be negligible in order to ensure this symmetry and to ignore dynamically coupling terms in the Hamiltonian. Thirdly, the resonator mode structure is assumed to be well described in both travelling-wave and standing-wave bases.

Our results point toward an asymmetry in the interaction between the atom and resonator modes. In the standing wave basis, the atom appears to couple to both modes simultaneously such that there is a total of two (not three) eigenmodes for the coupled system exhibited through mode-splitting in the spectrum. This seems to at least partially remove the uncoupled eigenmode.

We consider asymmetric scatters on the surface of the resonator that have been shown very recently to modify the mode structure of WGMs and result in a non-Hermitian scattering matrix [124]. An atom interacting with such a system can cause non-trivial interference between the scattered waves, and this may lead the atom to couple to both standing waves. Finally, we perform experiments exploring this effect.

7.5.2 Asymmetric WGM mode structure

Asymmetric back-reflection (i.e., unequal back-reflection amplitudes in the CW and CCW directions) implies the Rayleigh scattering process is not time-symmetric because reversing the process yields different field amplitudes for both WGM modes. This is because the scattering rates of both modes are not equal and one mode has higher losses (i.e., $a \neq b^*$ [124]). A very recent theoretical study in Ref. [124] has shown that such non-orthogonal modes should exist in high-Q WGM resonators having a circular cross-section, as opposed to a spiral or limaçon cross-section [125]. Central to this effect is the presence of two (or many) scatterers on the surface that each induce a different frequency shift and loss rate to a respective standing mode. As a result, a situation arises where the amplitude of each travelling wave is unequal, $|a| \neq |b|$. Thus, when the resonator is coupled to a nanofiber, the amplitude of the back-reflected light in the fiber will be higher in one direction than the other, which is clearly shown in measurements in the next section.

Very recent theoretical work on cavity QED in a WGM resonator coupled to multiple quantum emitters (i.e., NV centers in nanodiamonds) has predicted transmission spectra with two resonance dips similar to what is observed in our work [126]. The authors found that by controlling the relative phase between the nanodiamonds and the standing modes they could ensure that no uncoupled mode was present, which thus produced a coupled system with two eigenfrequencies. However, when the phase deviated from this particular situation, either one or two extra transmission dips began to appear in the transmission spectrum due to constructive Rayleigh scattering between the nanodiamonds. In the context of our work, constructive or destructive interference of light between scatters and atomic emitters may equally well play an important role in determining the measured spectra.

In order to investigate if asymmetric back-reflection [124] or interference effects [126] are present in our resonator, and also to better understand the symmetries of the atom-resonator system, we perform experiments to systematically measure the transmission and reflection spectra under four different configurations for atom detection and spectroscopy.

Experimental results

Figure 7.21 (a–d) shows the spectra of the empty resonator and coupled system when scanned with the spectroscopy laser, and the inset figures show the corresponding measurement configurations. Similar to the measurement in Fig. 7.11, two coupling fibers are used in this setup: fiber 2 in the inset is weakly coupled to the resonator and only couples in 10% of the spectroscopy light, and fiber 1 is critically coupled to the resonator and couples out 50% of the intra-cavity light. Fiber 1 then serves to only couple light into the resonator while only weakly perturbing it, while fiber 2 is used to efficiently collect the transmitted and reflected light. Light for the atom detection scheme is sent through fiber 1. The coupling of both fibers is stabilized using the scheme described in Sec. 5.2 by coupling light to the CW propagating mode using fiber 1 and then detecting the transmitted light in fibers 1 and 2.

Empty resonator response: The empty resonator responses when pumping the CW and CCW modes are plotted in Figs. 7.21 (a, c) (grey data). Surprisingly, the reflection amplitude of the resonator strongly changes by a factor of five depending of the pump direction: data in (a/c) has a maximum reflection of $\sim 4/\sim 20\%$ of the intra-cavity power, respectively. If the resonator modes were perfectly symmetric, then the back-reflection should be the same in both directions. On the other hand, the theoretical work in Ref. [124] specifically predicts asymmetric back-reflection from the two modes because the mode amplitudes are different.

An important issue to test is the possibility of excessive losses in the back-reflection measurement in Fig. 7.21 (a), which could alternatively explain the measurements. Independent measurements, where the resonator is removed from the fiber, were performed to measure the transmission of the optical fiber path from right-side photon detectors to the left-side photon detectors shown in the figure inset. These measurements give a transmission efficiency of 75%, which is in agreement with the expected value based on the transmission efficiency of the MEMs switch and coupling fiber, within an error of 10%. Further measurements of the back-reflections of other resonator modes even show the opposite behavior with higher back-reflection in the left-side detectors compared to the right-side detectors: data measured in the configuration (a/c) has a maximum reflection of $\sim 7/\sim 0.4\%$ of the intra-cavity power, respectively. Taken together, there is a high degree of confidence in the accuracy of the asymmetry measurements.

Coupled atom-resonator system: Further asymmetries are observed when an atom is introduced to the resonator mode. Unexpectedly, the transmission spectra measured using the spectroscopy light is dependent on how the atom is detected. If the coupled atom is detected using light in the CW mode and then probed via the same mode, or similarly via the CCW mode, the spectra show two very similar responses with a clear frequency splitting of ~ 36 MHz, see Fig. 7.21 (a, c). This qualitative behaviour is independent of the back-reflection from the empty resonator. On the other hand, Figs. 7.21 (b, d) show that if the coupled atom is detected using a CW mode and probed with the CCW mode, or visa versa, both spectra only show a single large central peak. A closer inspection of the transmission spectra reveals that the effect of the coupled atom is to reduce the transmission near resonance, while the transmission further away from resonance closely follows the empty resonator values. It seems that the coupling g

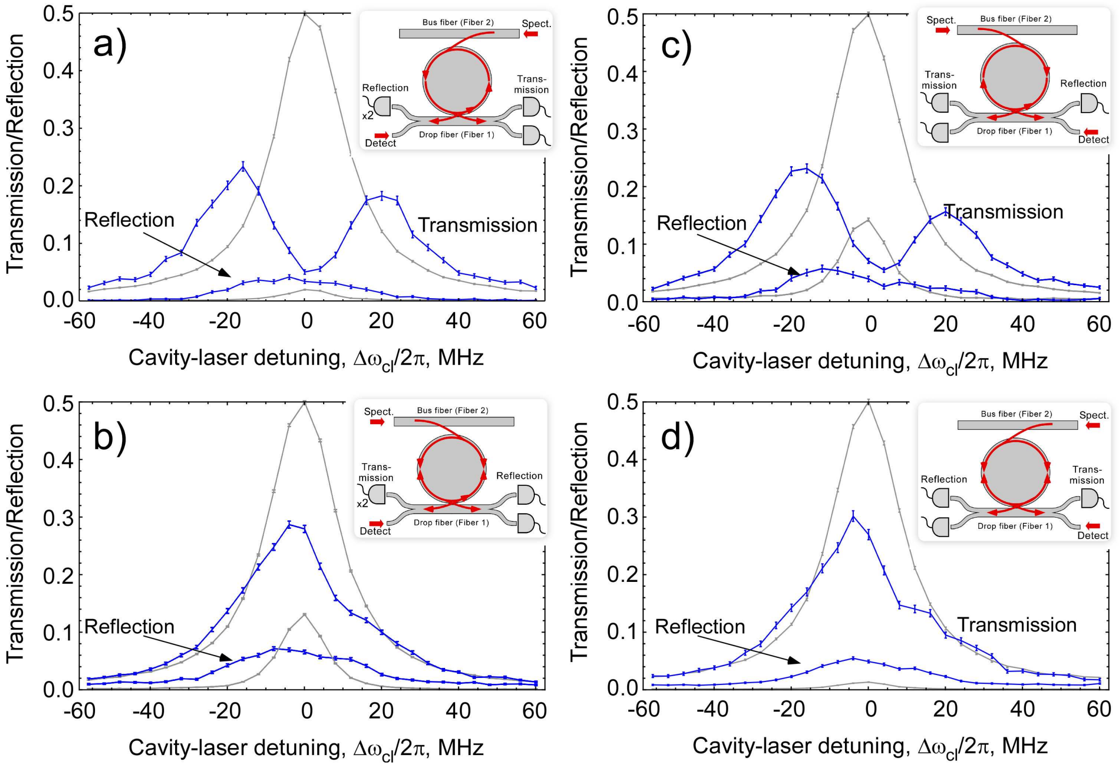

Figure 7.21: Directional dependence of transmission and reflection spectra. Transmission and reflection properties of the empty resonator and coupled atom-resonator system for different configurations of atom detection and spectroscopy. All plots are measured using only the spectroscopy laser, which is weakly coupled to the resonator via the bus fiber (Fiber 2). The y-axis is normalized so that the sum of empty cavity transmission and reflection is 0.5, as expected when fiber 1 is critically coupled using the CCW mode. (a, b) Vastly different responses are seen depending on probing directions. Intracavity photon number: ~ 0.2. (c, d) Reversing the detection direction, the spectroscopy signal again shows a similar response, but on the opposite output ports. See main text.

is much smaller, which is a feature that requires further investigation in order to understand. In addition, we find no time-dependent variation of the Rabi-spectra when dividing the 1 μs-long spectroscopy measurement time into smaller subsets. For example, the spectra produced from the first 500 ns probing interval is qualitatively and quantitatively similar to the spectra produced from the second 500 ns interval.

In summary, the measurements show a strong deviation from predictions of the Jaynes-Cummings model for a stationary atom in which all four configurations should produce the same response. While atomic velocity is in general important to consider, the Rabi spectra cannot be interpreted in terms of this effect.

Empty resonator linewidth: A closer examination of the spectra for the empty resonator in Fig. 7.21 reveals that the mode linewidth measured in transmission is not equal to that measured in reflection. In transmission, the linewidth is 17 ± 1 MHz when pumping the CW mode and 18 ± 1 MHz when pumping the CCW mode. In reflection, however, the linewidth is narrower, being about 10 ± 1 MHz when pumping the CW mode and 11 ± 1 MHz when pumping the CCW mode. The large difference arises because the linewidth measurements using reflected or transmitted light are not equivalent. In the latter case, only a single mode is involved in the measurement, while in reflection two modes are involved — light enters the first mode which is then scattered into the second mode. Therefore, the reflection spectrum is produced from two cascaded modes, which reduces the linewidth by a factor of $\sqrt{2}$ or less.[4] The linewidth narrowing of reflected light in WGMs could be advantageously applied to external cavity diode lasers in order to narrow the emission spectrum (for example, see Ref. [51]). To do this, rather than using a diffraction grating to back-reflect a frequency-selective fraction of the light into the diode laser, the back-reflected light from a WGM could instead replace the function of the grating.

7.6 Summary and outlook

This work has demonstrated the strong coupling of single atoms to high-Q modes of a whispering gallery mode resonator. Spectral measurements of the coupled system show clearly resolved spectra exhibiting mode-splitting, which indicates coherent atom-light interactions in the strong coupling regime of cavity QED. A cooperativity parameter of $g^2/(\kappa\gamma) = 11.0 \gg 1$ is estimated, indicating that single atoms have a strong influence on the transmission properties [127]. This property, combined with the intrinsically low transmission loss of up to two coupling fibers, provides a powerful platform to interface single atoms with the optical mode of an ultra-high-Q resonator in a fully optical fiber-based device.

The transit of each atom through the evanescent field of the mode results in an absolute resonant transmission change of ~ 65%, which may be further increased to 100% if the ratio of Q-factor to mode volume V is further maximized. This amounts to reducing the mode volume so that the coupling strength g is increased ($g \propto 1/\sqrt{V}$) while increasing Q through better fabrication and cleaning procedures. Within the present vacuum chamber setup there are two options to clean the resonator surface of adsorbed rubidium and other unwanted contaminants.

---

[4] In general, the resulting mode profile of two single-mode Fabry-Pérot resonators arranged in series is given by the product of two Lorentizians.

In principle, these contaminants can be evaporated by heating the resonator to several hundred degrees either by sending tens of milliwatts of power through a nanofiber coupled to the resonator where a fraction while be absorbed, or else by illuminating the resonator through two ZnSe viewports with light at a wavelength of around 10 μm using a CO_2 laser (silica is highly absorbing a mid-IR wavelengths). Evaporation of cesium from a nanofiber surface has been successfully demonstrated in another experiment in the group.

The typical atom transit time through the evanescent field is 3–4 μs. Despite this short interaction time, we have developed an atom detection scheme that provides a stable and controllable atom-resonator coupling for around 1 μs, which is long enough to perform experiments. During this time-window, dipole forces are observed to either repulse or attract atoms from/to the resonator surface depending on the detuning of the light and resonator despite a very low average intra-cavity photon number of around 0.2 photons. The dipole force between atoms and single intra-cavity photons has previously been used to trap single atoms in a Fabry-Pérot resonator [21, 22]. While atom trapping with WGM resonators has not been attempted so far, the results shown here suggest that it may be possible in future to similarly harness this force for atom trapping experiments and thereby extend the interaction time to the millisecond timescale as proposed in Refs. [84, 128].

Results in Sec. 7.5 show a remarkable influence of the choice of clockwise or counterclockwise resonator modes for atom detection and spectroscopy. The results show that an atom detected with light propagating in the CW mode, for example, will have a very low coupling strength g when probed in the CCW mode, and visa versa. Once the atom is detected with one travelling wave, it is not clear why a counter-propagating travelling wave should not couple to the atom. The observed asymmetric scattering in the bare CW and CCW modes may suggest a possible link to the asymmetric response in the coupled atom-resonator system.

Finally, we note that nonlinear optical processes in the resonator itself, like surface acoustic waves and Raman lasing, play no role in the atom-resonator interaction because the threshold power for these processes is in the range of several microwatts for our resonator properties, see, for example, Ref. [80].

The high-speed atom detection scheme facilitates a stable and reproducible transmission of $\sim 65\%$ for a duration of 1–1.5 μs at resonance, which is long enough to implement atomic state preparation using optical pumping, for example. In a more advanced setting, the state preparation technique can be used in conjunction with two coupling fibers in order to switch light between the fibers using the internal atomic state rather than using the physical presence of the atom. As described in the next chapter, this may be used to realize a quantum mechanical router that coherently switches photon pulses (< 1 photon on average) between two fibers in which the photon path information is entangled with the strongly coupled atom-resonator router [129–131].

CHAPTER 8

Summary & Outlook – Switching Photons in a Four-Port Device

8.1 Thesis Summary

Within the framework of this thesis, a new experimental apparatus was developed for the investigation of the strong interaction of cold ^{85}Rb atoms with the modes of a whispering gallery bottle (WGM) microresonator. Using an atomic fountain to deliver cold atoms to the evanescent field of the microresonator, we have performed transmission and reflection spectroscopy of the coupled atom-resonator system. The eigenmodes of the system were explicitly revealed through the emergence of Rabi-split resonances in the spectra with a coherent coupling strength $\bar{g}/2\pi = 16.3 \pm 1.7$ MHz $> (\kappa_e/2\pi \approx 8-9, \gamma/2\pi = 3)$ MHz.

The measurements presented in this work represent the first observation of the vacuum Rabi spectrum of single atoms resonantly coupled to a WGM resonator ($\omega_a = \omega_c$). Due to the availability of high-Q modes in our bottle resonator, in conjunction with our experimental protocol, the Rabi spectrum can be clearly resolved in resonator transmission and reflection measurements. Two major observations were made: (a) the transmission and reflection spectra significantly differ from the Jaynes-Cummings model prediction for single atoms coupled to a resonator with two orthogonal modes, and (b) the spectra are strongly dependent on the choice of travelling modes used for atom detection and spectroscopy of the coupled system. We anticipate these observations to be present in other cavity QED systems based on WGM microresonators, such as microtoroids, microdisks and microspheres [10].

Additional spectral measurements with a different resonator mode support our claim that the Rabi spectrum consists of two eigenmodes. Unlike in the first mode ($q \approx 1$) we studied in which the intrinsic back-scattering rate was small ($h \ll \kappa$), the second mode ($q \approx 4$) showed larger mode-splitting by an amount $\sim 2h/2\pi$ because the back-scattering rate was higher ($h \approx \kappa$). Future measurements with different modes with large axial mode numbers q, different polarization (i.e., TE-modes), higher laser powers, and much larger h, should provide more insight into the microscopic processes involved in WGM resonators.

Both atomic motion and asymmetric resonator scattering were investigated as possible explanations for these observations, and routes towards a full understanding were suggested. The influence of dipole and surface forces on the atomic trajectory near the resonator surface was observed, and simulations confirm our assertion that these forces play an important role affecting g as well as the duration of the atom-light interaction. Dipole forces are evident in the asymmetric profiles of resonances in the Rabi spectra. Aided by simulations of atomic trajectories, these forces are shown to affect the atomic motion near the resonator surface at distances below ~ 100 nm. At distances below 50 nm, the van der Wals potential shifts the atomic resonance to such a degree that it becomes far-detuned from the resonator resonance and thus these atomic trajectories play no role in the spectral measurements. When the light is blue detuned, a short but steep potential barrier is formed in front of the resonator surface. This effect is observed in an experiment where atoms with a pre-defined average initial velocity were first launched toward the resonator and then the recorded atom detection events were characterized via the detection rate and interaction duration. In the future, it may even be possible to control these forces using the existing FPGA feedback system in order to manipulate the atomic trajectory of the atoms at will. However, it remains a task to examine if there are solutions to the atomic center of mass wavefunction that permit (quasi) stable localization of an atom in a highly confined potential.

Atoms transit the evanescent field of the resonator at random intervals over an ~ 85 ms-long measurement window. Furthermore, the precise trajectory $\mathbf{r}(t)$ is characterized in terms of the atom-surface distance, which affects the coupling strength $g(\mathbf{r}(t))$, but also in terms of the duration of the interaction, which ranges anywhere from tens to hundreds of nanoseconds up around 3–4 μs. A major achievement of this thesis has been to overcome these obstacles by selecting only coupling events where the coupling is stable. In particular, our realtime atom-detection protocol enables the identification of only those atoms that strongly couple to the resonator for a sufficiently long duration. The detection protocol relies on continuous transmission measurements of the coupling fiber to determine when the photon count rate exceeds a threshold due to the coupling of an atom, i.e., $n_{\mathrm{photons}} \geq n_{\mathrm{thr}}^{\mathrm{1st}} \simeq 6$ in a time window $\Delta t = 1.2$ μs. The criterion enforces the conditional selection of only those atoms that approach very close to the resonator having an estimated atom-surface gap of $> 50 - 100$ nm. Of course, some weakly coupled events satisfy this criterion by virtue of statistical fluctuations on the scale of $\sqrt{n_{\mathrm{photons}}} \approx 2$. However, these weak coupling events can be efficiently removed from the set of analyzed coupling events by applying a second criterion $n_{\mathrm{photons}} \geq n_{\mathrm{thr}}^{\mathrm{2nd}}$ around 2 μs after the first criterion. Weakly coupled atoms, false detection events, and atoms that quickly crash into the surface, do not satisfy this condition.

Despite the very high Q-factor of WGMs, the measured back-reflection amplitudes in clockwise and counter-clockwise directions are not always equal, i.e., CW and CCW modes do not back-scatter light with equal strength. This behavior is predicted in a very recent theoretical investigation [124] that relied on the interference between scatters on the surface of the resonator, and is likely to also apply to our experiments both with and without rubidium atoms [126]. This unexpected observation challenges conventional expectations of high-Q WGMs as dielectric structures that back-scatter light equally in both directions. While unequivocal confirmation of the cause of the asymmetry is left for future work, the present results from the bare resonator are consistent with the model in Ref. [124].

Finally, we verified that individual coupling events correspond to single atoms rather than multiple atoms. As such, a multi-atom Jaynes-Cummings model proposed in Ref. [126] cannot be used to explain the eigenstructure in our spectra.

The mode asymmetries due to Rayleigh scattering as well as the atom-light asymmetries characterized in this thesis can be expected to improve our present understanding of how particles such as atoms and biochemical molecules interact with WGM resonators, see, for example, experimental and theoretical work in Refs. [10, 39, 48, 61, 84, 114, 115, 123, 128, 132].

8.2 Future Applications: Atom-controlled optical switching

The development of technologies capable of practical, robust, yet highly efficient control of photons is essential to future quantum communication applications [32]. In a large-scale quantum network, for example, this will require quantum information to the transmitted using photonic qubits to multiple nodes for storage or processing. Several technologies have been proposed for processing light at the single photon level using, for example, electromagnetically-induced transparency (EIT) in ensembles of atoms or other quantum emitters [32, 133], surface plasmons in nanowires [134], and single atoms in cavity QED [32, 135]. Experimental work in Ref. [133] recently demonstrated that EIT in a quasi-1–D ensemble of cold Rydberg atoms can be used to slow down single photons which can then be transmitted or absorbed, depending on the presence of a second (or multiple) photon(s). For other theory and experimental work toward quantum optical switching devices see Refs. [92, 114, 129, 131, 136].

To move beyond simple on/off switching, a "quantum switch" should ideally control the propagation of photons by routing incoming photons to physically separate output channels, similar to the function of a classical optical router in standard communication technology. By contrast to a classical optical switch, fundamentally new phenomena are possible with a quantum switch wherein a photonic qubit can itself be entangled with the switch. This requires the switch to be prepared in arbitrary superposition states using, e.g., the hyperfine ground states $F = 2$ and $F = 3$ in ^{85}Rb. When the atom is prepared in an arbitrary superposition of these states using, e.g., a suitable microwave field or adiabatic passage using an optical light field, the light can be routed to the two output ports labelled 2 and 3, as shown in Fig. 8.1. If the atom is prepared in an equal superposition of both hyperfine states, this results in an entangled Bell state between the atom and the routed photon on ports 2 and 3.

This switch should preserve the quantum state of an optical signal and also enable the redistribution of quantum information to different nodes in a large quantum network. On the other hand, classical optical switches cannot be prepared in a quantum mechanical superposition of states, nor do they show quantum correlations. This is because the states in a classical switch strongly decohere due to coupling to the environment, and are therefore unsuited for applications in a quantum network.

The bottle resonator is a promising technology that can solve this problem. To date, it has already been experimentally demonstrated to operate as a classical optical switch and add-drop filter using the Kerr effect at ultra-low powers [35, 37, 38]. Crucially, the bottle resonator has an advantageous mode geometry that can be interfaced with two coupling fibers. The transfer efficiency of a light field from a single fiber to the resonator is greater than 0.99 in experiments

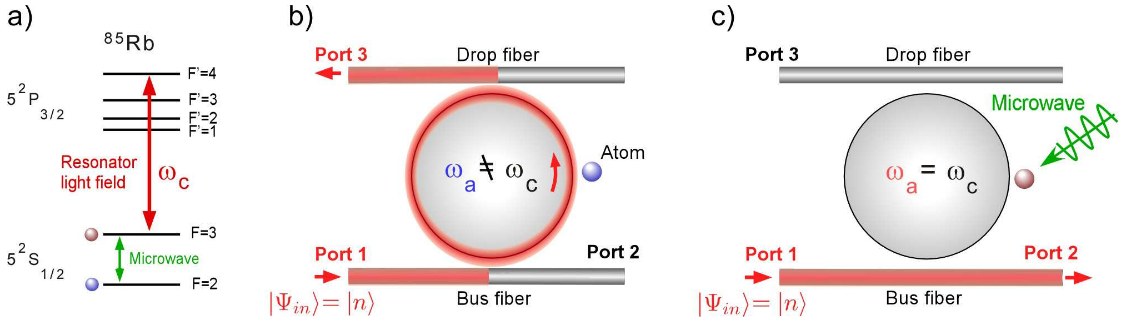

Figure 8.1: Sketch of the quantum switch using a bottle resonator. (a) Energy level diagram of ^{85}Rb showing the atomic transition resonant with the resonator light field ($F = 3 \rightarrow F' = 4$), and the hyperfine ground states ($F = 2, 3$). (b) Routing configuration when the atom is off-resonant with the resonator. The output state is $|\psi\rangle_{\text{out}} = |F = 2\rangle|n_{\text{port2}} = 0, n_{\text{port3}} = n\rangle$, where n_{port} is the number of photons at a port. (c) Routing configuration when the atom is resonant with the resonator. The output state is $|\psi\rangle_{\text{out}} = |F = 3\rangle|n, 0\rangle$.

[26, 36], while the transfer efficiency from one fiber to the second fiber via the resonator is as high as 0.93 while maintaining a loaded quality factor compatible with the strong coupling regime of cavity QED [38]. Apart from this issue, both the resonance frequency of the resonator and the in-coupled light power to the resonator mode can be actively stabilized [35, 101, 112]. In the next section, we demonstrate the classical switching of photons between two optical fibers using the interaction of individual atoms.

8.2.1 Single-atom switching in a bottle resonator

A long-term goal of the bottle resonator experiment is the realization of a quantum switch. Several stringent requirements must be fulfilled to achieve a fully functional device, including (a) the preparation of atomic states must be performed with sufficiently high speed due to the limited atom-resonator interaction time of a few microseconds, (b) and the atom-light interaction must be coherent. Another important issue relates to the maximum atom-induced transmission change achievable when two coupling fibers are well coupled to the resonator. Ideally, an optical switch is capable of transferring 100% of the light from the input port to either of the output ports without causing signal loss. For a quantum switch based on the coupled atom-resonator system studied here, the maximum transmission change is dependent on the condition $g \gg (\kappa, \gamma)$ as well as the exact nature of the WGM fields in the empty and coupled resonator. Here, we present an initial step towards a quantum switch and verify that our four-port bottle resonator is capable of efficiently switching light in a process that is mediated by the coupling of single atoms.

The addition of a second fiber of the resonator reduces the quality factor by the fraction $(\kappa_{e,1} + \kappa_{e,2})/\kappa_0$, where $\kappa_{e,1(2)}$ is the external coupling rate with fiber 1 (2), and κ_0 is the intrinsic decay rate of the resonator mode. This ratio determines the transfer efficiency between the fibers, η, which can be written in terms of Q-factors as [137]

$$\eta = 1 - 2\frac{Q_{\mathrm{load}}}{Q_0} \, , \tag{8.1}$$

where Q_{load} is the loaded Q-factor at critical coupling, and Q_0 is the intrinsic Q-factor. Therefore, the efficiency of the add-drop switch improves when the two fibers are strongly coupled to the resonator. At the same time, however, the single atom cooperativity, $g^2/(\kappa\gamma)$, proportionately decreases and this reduces the effect of single atoms on the transmission.

To gain insight into the operation of the resonator with a second coupling fiber, we repeat the spectral measurements in Chap. 7, but now with a transfer efficiency increased to $\eta = 0.56$ (measured for the empty resonator). The resonator setup is operated in an add-drop configuration similar to Fig. 8.1 (b). Unlike in earlier add-drop experiments with a bottle resonator in Ref. [38], the nonlinear element here is a single atom rather than the Kerr nonlinearity in silica glass. The bus fiber is critically coupled to the mode, which is required for the atom detection scheme.

It is sufficient to measure the transmission on output ports 2 and 3 because the results from Chap. 7 indicate that the back-reflection arising from the atom-resonator interaction is very small for this mode (for example, see Fig. 7.9).

Figure 8.2 (a, b) shows the Rabi spectra measured in both the bus and drop fibers demonstrating the operation of the single-atom *classical* switch. Prior to an atom coupling to the resonator, the light flows from the bus fiber to the drop fiber with a transfer efficiency $\eta = 0.56$. The corresponding transmission in the bus fiber is 3% and the back-reflection is $\sim 0.5\%$. Following the coupling of atoms, the new frequency-shifted eigenstates of the coupled system mostly block light with frequency $\omega_l = \omega_a = \omega_c$ from entering the resonator. Consequently, the absolute transmission in the drop fiber decreases by 42% while the absolute transmission in the bus fiber increases by almost an equal amount to 46%.

Based on the experimental parameters demonstrated in Fig. 8.2, we can evaluate the classical fidelity of the switching operation on a single photon input state in the bus fiber. For this, we assume that the same switching performance is possible when using the internal hyperfine states of the atom rather than the physical presence or absence of the atom. In this proposed scheme, an atom in the $F = 2$ ground state is not resonant with the resonator, and thus the photon is transmitted to port 3 of the drop fiber with the output state $c_0|F = 2\rangle \otimes |n_{\mathrm{port2}} = 0, n_{\mathrm{port3}} = 1\rangle$, where c_0 is a constant measuring the coupling efficiency from resonator to drop fiber, and $|0, 1\rangle$ is the state of the field in the transmission ports of the fibers. Here we neglect the small amount of light in the reflection port of the drop and bus fibers. The state of the coupled system of atom and field is then $|\Psi\rangle = (c_0|F = 2\rangle \otimes |0, 1\rangle + c_1|F = 3\rangle \otimes |1, 0\rangle)/\sqrt{2}$, where $c_0 = \sqrt{0.56}$ and $c_1 = \sqrt{0.46}$. The fidelity of the system is $|\langle\Psi|\Psi^+\rangle|^2 = (0.56 + 0.46)/2 = 0.51$, where $|\Psi^+\rangle$ is the same as $|\Psi\rangle$ except $c_0 = c_1 = 1$. If resonator losses are excluded since only photons that leave the resonator can be detected, the fidelity increases further to a maximum of 0.8. These values are already very promising and there are excellent prospects for improving them further by increasing the Q-factor of the resonator by almost an order of magnitude to 4×10^8, as demonstrated for a bottle resonator in Ref. [25].

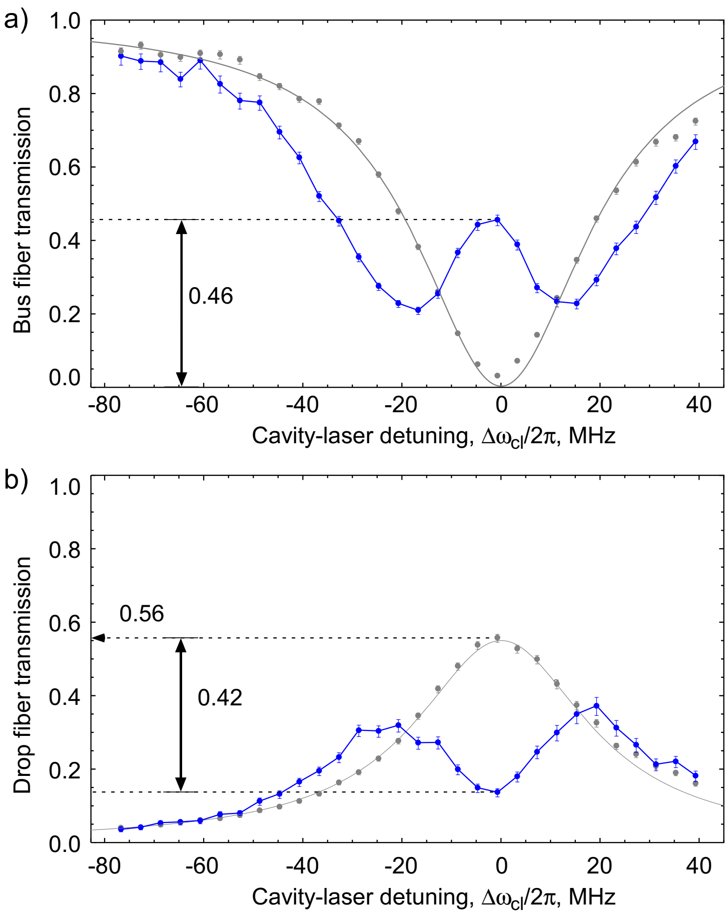

Figure 8.2: Rabi spectra of the bottle resonator optical switch. (a,b) Empty resonator (grey): 97% of the light in the critically coupled bus fiber is transferred to the empty resonator, of which 56% is transferred across to the drop fiber. The FWHM linewidth measured in the bus fiber transmission is 45 ± 1 MHz, and is in reasonable agreement with a FWHM linewidth of 48 ± 1 MHz measured in the drop fiber transmission. Atom coupling (blue): The bus fiber transmission increases to an absolute value of 46%. Correspondingly, the transmission in the drop fiber decreases to an absolute value of 14%. Experimental parameters and resonator mode are the same as in Fig. 7.9 with $\kappa/2\pi = 18$ MHz.

Appendices

APPENDIX A

Electric Fields in Optical Fibers

The resonance conditions for optical modes in an optical fiber are given by a transcendental equation for the propagation constant β_{fiber},

$$\left[\frac{J\prime_n(ha)}{haJ_n(ha)} + \frac{K\prime_n(qa)}{haK_n(qa)}\right] \cdot \left[\frac{n_{\text{core}}^2 J\prime_n(ha)}{haJ_n(ha)}\right] = \left[\frac{n\beta_{\text{fiber}}}{k}\right]^2 \cdot \left[(qa^{-1}) + (ha^{-2})\right]^2 , \tag{A.1}$$

for HE and EH modes. The functions $J_n(K_n)$ are the Bessel function (modified Hankel function of the second kind) of order n, the prime in $J\prime_n$ indicates differentiation, $k = 2\pi/\lambda$ is the free space propagation constant of light of wavelength λ, n_{core} is the refractive index of the core, n_{clad} is the refractive index of the cladding, $h = \sqrt{n_{\text{core}}^2 k^2 - \beta_{\text{fiber}}^2}$ is the radial propagation constant in the core, and $q = \sqrt{n_{\text{clad}}^2 k^2 - \beta_{\text{fiber}}^2}$ is the radial propagation constant in the cladding. Similar equations also exist for TE and TM modes [56], however only the so-called HE_{11} mode propagates in the optical nanofibers used in this work.

The electric field distribution for these modes in a nanofiber is given in cylindrical coordinates (radial: r, azimuthal: ϕ, axial: z) as [56, 138]

$$\begin{aligned}
E_r &= -\frac{a_1 J_0(2ahr) + a_2 J_2(2ahr)}{J_1(2ah)} f_1(\phi) , \\
E_\phi &= -\frac{a_1 J_0(2ahr) - a_2 J_2(2ahr)}{J_1(2ah)} g_1(\phi) , \\
E_z &= -i \frac{2ah}{a\beta_{\text{fiber}}} \cdot \frac{J_1(2ahr)}{J_1(2ah)} f_1(\phi) ,
\end{aligned} \tag{A.2}$$

for fields inside the fiber of radius a. The fields outside the fiber are given as

$$\begin{aligned}
E_r &= -\frac{2ah}{2aq} \cdot \frac{a_1 K_0(2aqr) + a_2 K_2(2aqr)}{K_1(2aq)} f_1(\phi) \ , \\
E_\phi &= -\frac{2ah}{2aq} \cdot \frac{a_1 K_0(2aqr) - a_2 K_2(2aqr)}{K_1(2aq)} g_1(\phi) \ , \\
E_z &= -i \frac{2ah}{a\beta_{\text{fiber}}} \cdot \frac{K_1(2aqr)}{K_1(2aq)} f_1(\phi) \ ,
\end{aligned} \tag{A.3}$$

where the polarization is given by $f_1(\phi) = \sin(\phi)$ and $g_1(\phi) = \cos(\phi)$. The propagation constant β_{fiber} must be solved numerically [53] before calculating the electric field distribution. See Fig. 1.7 for a plot of the nanofiber field.

APPENDIX B

Trapping and Cooling Atoms

With the advent of the first demonstration of trapped and cooled neutral atoms in 1985 [139,140], and the subsequent developments since then, neutral atoms are now accepted as an indispensable tool in quantum optics. Their long coherence times as well as their well-defined energy structure which exhibit narrow linewidth optical transitions make them an ideal quantum emitter.

B.1 Magneto-optical trap

The principle of a magneto-optical trap is to cool atoms using near-resonant laser light in an inhomogeneous magnetic field. Doppler cooling is achieved by red-detuning the laser light with respect to the transition frequency of a two level atom. Cooling is complemented by a superimposed magnetic field gradient at the location of the atoms, and also by polarized laser light, to create both velocity and position dependent forces for cooling and trapping, respectively.

Scattering forces

Neutral atoms interact with light through absorption and emission processes. Laser light with intensity I impinging on an atom with absorption cross-section σ_{abs} will exert a radiation force given by

$$F_{\text{rad}} = -\frac{I\sigma_{\text{abs}}}{c} \,, \tag{B.1}$$

where c is the speed of light.[1] This is a direct consequence of the momentum imparted on the atoms by the photons ($\hbar\vec{k}$) and momentum conservation.

The momentum of an atom moving in a trajectory against a counter-propagating laser beam is reduced in units of $\hbar\vec{k}$ due to absorption as shown in Fig. B.1. Photon emission occurs at a

---

[1] The on-resonance absorption cross-section is $\sigma_{\text{abs}} = \hbar\omega\Gamma/2I_{\text{sat}}$, where I_{sat} is the saturation intensity, ω is the resonance frequency, and Γ is the atomic decay rate. I_{sat}=3.89 mW cm^{-2} for the D$_2$ cooling transition in ^{85}Rb used in this experiment, $5^2S_{1/2}(F=3) \rightarrow 5^2P_{3/2}(F'=4)$, assuming isotropic polarization.

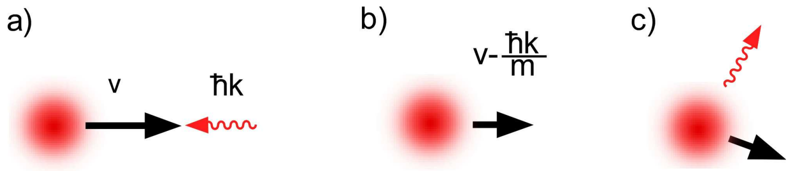

Figure B.1: Concept of light scattering by atoms. (a) An atom with velocity v along a particular axis absorbs a counter-propagating photon having momentum $\hbar\vec{k}$. (b) The net momentum and velocity is reduced. (c) Spontaneous emission of a photon in a random direction thereby reduces the atom velocity after many such cycles of absorption and emission. Reproduced from Ref. [88].

rate Γ and is, however, directionally random. From the optical Bloch equations for a two level atom, it can be shown that the steady state scattering force is [99]

$$\vec{F}_{\text{sca}} = \hbar\vec{k}\frac{\Gamma}{2}\frac{I/I_{\text{sat}}}{1 + I/I_{\text{sat}} + 4(\Delta_{la}/\Gamma)^2} , \tag{B.2}$$

where Δ_{la} is the laser-atom detuning ($\omega_l - \omega_a - \vec{k}\vec{v}$) including the Doppler shift $\vec{k}\vec{v}$. The saturation intensity is defined as $I/I_{\text{sat}} = 2(\Omega/\Gamma)^2$ where $\Omega = -\mathbf{d}\mathbf{E}/\hbar$ is the Rabi frequency which defines the interaction strength. Using this definition we get

$$I_{\text{sat}} = \frac{c\epsilon_0\gamma^2\hbar^2}{4|\hat{\epsilon}\mathbf{d}|^2} , \tag{B.3}$$

where $I = (1/2)c\epsilon_0 E^2$ and $\hat{\epsilon}$ is the unit polarization vector. In the experiments with ^{85}Rb atoms described here, the Rabi frequency is ~18 MHz for a typical cooling beam intensity of 16 mW cm^{-2} on the cooling transition $5^2S_{1/2}(F = 3) \rightarrow 5^2P_{3/2}(F' = 4)$.

In the limit of large I, a maximum force is experienced at a detuning of $\Gamma/2$,

$$\vec{F}^{\text{max}}_{\text{sca}} = \hbar k\Gamma/2 .$$

At this detuning, a ^{85}Rb atom has a maximum acceleration of 1.1×10^5m s^{-2}, some ten thousand times greater than the gravitational acceleration.[2] This identifies scattering forces as being a fast and effective means of decelerating fast-moving atoms, with the net force countering the initial atomic motion.

Doppler cooling & optical molasses

Using the scattering forces described above, the velocity of thermal atoms having an initial value of hundreds of meters per seconds can be reduced by orders of magnitude. This can be achieved in a 1D arrangement with two counter-propagating laser beams sightly red-detuned with respect to the atomic transition. The total force $\vec{F}_{\rm mol}$, is just the sum of the forces from each beam

---

[2] A related quantity, the atomic recoil velocity ($v_{\text{rec}} = \hbar\vec{k}/m$, m: mass), is 6.0 mm s^{-1} for the same transition as above.

$$\vec{F}_{\rm mol} = \vec{F}_{+} + \vec{F}_{-} \, , \tag{B.4}$$

where $\vec{F}_{\pm}$ is defined using Eq. (B.2) as

$$\vec{F}_{\pm} = \pm \hbar \vec{k} \frac{\Gamma}{2} \frac{I/I_{\rm sat}}{1 + I/I_{\rm sat} + 4[(\omega_l - \omega_a \mp \vec{k}\vec{v})/\Gamma]^2} \, . \tag{B.5}$$

There is no damping force for a stationary atom as shown in the plot of $\vec{F}_{\rm mol}$ in Fig. B.2 (a). In the frame of the atom, both beams have equal detuning and this causes the contribution from each beam to exactly cancel, see Fig. B.2 (b). The resonance frequency of an atom with a positive velocity experiences a large scattering force because it is closer to resonance with a counter-propagating beam due to the Doppler shift as shown in Fig. B.2 (c). A co-propagating beam, however, is tuned further from resonance. Similar arguments also hold for atoms with negative velocities. In the regime of low velocities, $\vec{k}\vec{v} \ll \Gamma$, the force given in Eq. (B.4) has a linear dependence with velocity and is written as $\vec{F}_{\rm mol} \approx -\beta_{\rm damp}\vec{v}$.[3] The damping coefficient $\beta_{\rm damp}$ is given by the gradient of the force around zero in Fig. B.2 (a). The negative sign in the equation is due to the fact that the lasers are red-detuned and this ensures that the force has a damping effect. Hence the term *optical molasses* is used to describe the viscous damping effect of the light.

The width of the distribution in Fig. B.2 (a) also sets the range of atomic velocities over which $\vec{F}_{\rm mol}$ is appreciable. The so-called *velocity capture range* is $v_{\rm cap} \approx \Gamma/\vec{k}$ and measures just 5 m s^{-1} for the D$_2$ transition in ^{85}Rb. Since atoms released from the atomic source in the vacuum chamber have a large rms velocity of at least $v = \sqrt{k_B T/m} = 170$ m s^{-1}, only atoms in the low velocity wing of the Boltzmann distribution are captured.

Spontaneous emission of photons at a rate Γ ultimately sets the temperature limit of Doppler cooling, which is 145.6 μK in our case [121]. Each absorption and emission process results in a momentum exchange equal to a single recoil. Furthermore, this process is stochastic around zero average momentum. The Doppler temperature limit is therefore

$$T_D = \frac{\hbar\Gamma}{2k_B} \, , \tag{B.6}$$

while the Doppler velocity limit is

$$v_D \simeq \left(\frac{\hbar k}{m}\frac{\Gamma}{k}\right)^{1/2} = (v_{\rm rec}v_{\rm cap})^{1/2} \, . \tag{B.7}$$

The Doppler velocity is 0.17 m s^{-1} for D$_2$ transition in ^{85}Rb. These limits are also valid for other laser beam geometries, such as the common six-beam arrangement used in the experiments described later.

---

[3] Here we make the assumption that the Doppler effect is small ($\vec{k}\vec{v} \ll \Gamma$) in order to illustrate the linear dependence of force with velocity. In reality, however, Doppler cooling is effective at larger Doppler shifts ($\vec{k}\vec{v} \sim \Gamma$) and polarization gradient cooling is dominant in the low velocity regime, c.f. Sec. B.1.

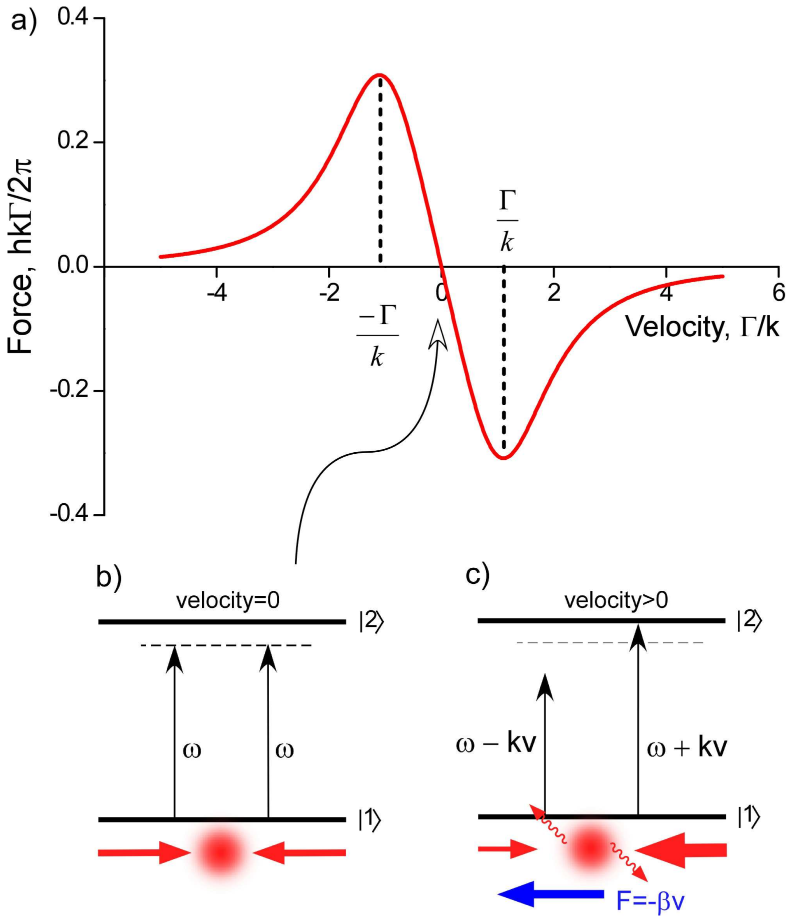

Figure B.2: Doppler cooling in a one dimensional optical molasses. (a) Light force on an atom with two red-detuned, counter-propagating beams shown in (b,c). An atom with zero velocity experiences no force because the net force of the two beams cancels to zero. (c) An atom with positive velocity experiences a negative force because the Doppler effect causes the atom to become more resonant with the left-propagating beam. The atom preferentially absorbs atoms in this beam, but spontaneously emits photons in a random direction, thereby experiencing a velocity dependant restoring force given by Eq. (B.4). The force in (a) is the sum of two Lorentzian-shaped forces centered at $v = \pm\Gamma/k$. Adapted from Ref. [88].

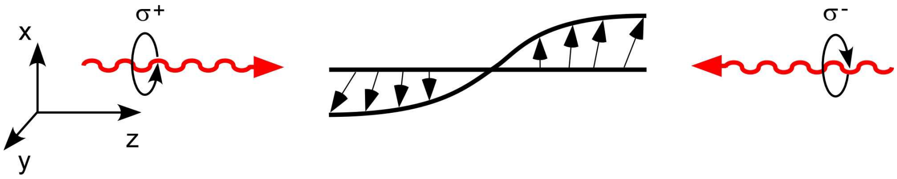

Figure B.3: Polarization gradient cooling with circularly polarized light. Two counter-propagating beams with polarizations σ^- or σ^+, respectively, combine to form a linear-polarized beam where the electric field rotates around the z-axis with a period of λ, where λ is the light wavelength. Adapted from Ref. [88]

Polarization gradient cooling

So far, we have considered an idealized two-level atom interacting with a light field, but in reality atoms have a multi-level structure. Rather than having a negative effect on the atomic temperature, Dalibard and Cohen-Tannoudji explained [141] in 1989 how this multi-level structure can result in sub-Doppler temperatures that were first observed in experiments the previous year.

As mentioned already, Doppler cooling relies on the velocity-dependent imbalance in the atomic absorption due to two counter-propagating beams. Other effects should also be considered, namely, the polarization gradient of the light and the recycling of energy between the hyperfine magnetic states, m_F. In the work described here, circularly polarized light in the $\sigma^+\sigma^-$-configuration is used for polarization gradient cooling (PGC), as shown in Fig. B.3. In this configuration, the light polarization is linear along the polarization axis (z-axis in the figure) around which it rotates in a helical pattern with a period λ.

We consider an atom moving along the z-axis and we introduce a rotating coordinate system for the atom rotating with the laser polarization. The Hamiltonian of the atomic evolution in the rotating frame has terms that are proportional to the atomic velocity, $\vec{v}$, and the coupling between the m_F sub-levels. For an atom moving towards the σ^+ light, which is also red-detuned, the positive m_F sub-levels will be more highly populated than the negative m_F sub-levels.[4] Optical pumping thus causes an imbalance in the ground state populations, leading to an imbalance in the radiation forces exerted by the $\sigma^\pm$ light and an imbalance in the scattering of the $\sigma^\pm$ light. Small differences in the ground state population yield a large damping force in the regime $\vec{k}\vec{v} < \Gamma$ [141].

In this experiment, temperatures of 5–6 μK are typically reached by first applying Doppler cooling and then PGC, giving an rms velocity of around 50 mm s^{-1}. This low velocity is beneficial because it ensures that the atomic cloud does not greatly expand before traveling to the location of the resonator: the atomic cloud expands from an initial diameter of about 2 mm to a final diameter of 1 cm at the resonator.

---

[4] The probability of absorbing a photon on a particular transition is proportional to the square of its dipole matrix element. For example, in the considered case, the $5^2S_{1/2}(F = 3, m_F = 3) \rightarrow 5^2P_{3/2}(F' = 4, m_F = 3)$ transition is 28 times more likely to absorb a σ^+ photon than a σ^- photon.

Magnetic confinement

Magnetic confinement of a molasses was proposed and demonstrated in initial works by Dalibard and Raab in 1987, respectively. An atomic molasses in itself is not well confined, and atoms will diffuse away from the cooling region in less than a second. The solution to this problem is to superimpose a spatially inhomogeneous magnetic field to shift the Zeeman sublevels which are normally degenerate. This has the effect of producing a position dependent force which, when combined with the radiation forces, traps the atoms [99].

The concept of a MOT is explained in Fig. B.4 where the transition $F = 0 \rightarrow F' = 1$ is considered. (Note the rules: $F = 0 \nleftrightarrow F' = 0$ and $\Delta F = \pm 1$). The quadrupole magnetic field B_z is zero at $z = 0$ and varies linearly in z, and linearly shifts the m_F states via the Zeeman effect by an amount

$$\Delta E_{|F,m_F\rangle} = g_F \mu_B m_F B_z \ . \tag{B.8}$$

The constant g_F is the Landé factor, μ_B is the Bohr magneton, m_F is the magnetic quantum number, and a typical magnetic field gradient for alkali atoms is 10 G cm^{-1}.

Two counter-propagating beams, with one having σ^+ polarization and the other σ^- polarization, preferentially couple to the $m_{F'} = +1$ and $m_{F'} = -1$ states, respectively.[5] An atom displaced from the origin located at $z = 0$, e.g. say an atom placed at $z > 0$, will be more resonant with the σ^- laser light and less so the σ^+ laser light due to the selection rules in Fig. B.4 (a). Similar to the optical molasses damping described above, the atomic motion will be affected by the enhanced scattering from the σ^- light and return to the trap origin. The σ^+ light, on the other hand, is far off-resonant when the atomic position is $z > 0$. More quantitatively, we can re-write Eq. (B.2) as

$$\vec{F}_\pm = \pm \hbar \vec{k} \frac{\Gamma}{2} \frac{I/I_{\text{sat}}}{1 + I/I_{\text{sat}} + 4(\delta_\pm/\Gamma)^2} \ , \tag{B.9}$$

where

$$\delta_\pm = \omega_l - \omega_a \mp \vec{k}\vec{v} \pm \mu B_z/\hbar \ ,$$

and where $\mu = (g_{F'} m_{F'} - g_F m_F)$ is the effective magnetic moment between the excited and ground states. Similar to the case the optical molasses, the force in a MOT can be re-written using the assumption of small Zeeman shifts $\alpha_{\text{damp}} z \ll \Gamma$ and small velocities $\beta_{\text{damp}} v \ll \Gamma$ [99]

$$F_{\text{MOT}} = -\beta_{\text{damp}} \vec{v} - \frac{\beta_{\text{damp}} \alpha_{\text{damp}}}{\vec{k}} z \ . \tag{B.10}$$

The damping coefficient α_{damp} is given by the gradient of the magnetic field in the center of the trap, $(g_F \mu_B/\hbar)(\mathrm{d}B/\mathrm{d}z)$. The resulting force is therefore a linear function of velocity and position. Finally, the capture range in a MOT is greater than in an optical molasses — due to the very high damping rate of the MOT (hundreds of kilohertz) — with $v_{\text{cap}} \approx 20 - 40$ m s^{-1} in this experiment [88].

A schematic of the actual 3D implementation of a MOT is shown in Fig. B.5. Three pairs of counter-propagating laser beams are arranged in a mutually orthogonal configuration. The

---

[5] It is important to note that the light polarization labels $\sigma^\pm$ refer to rotation about the quantization axis of the atom.

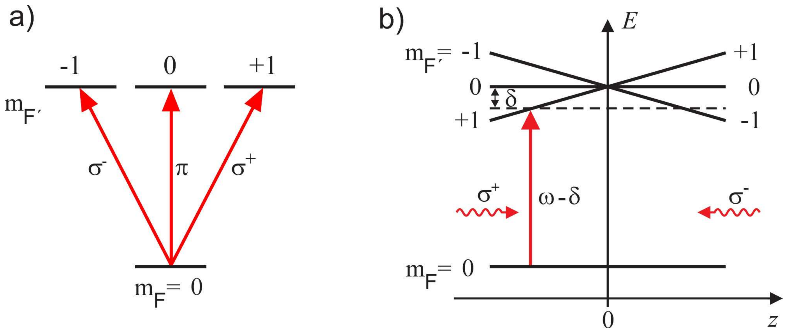

Figure B.4: Polarization-dependent absorption of light. (a) The transition $m_F \rightarrow m_{F'}$ is dependent on the polarization of the light with transitions $\Delta m_F = -1, 0, +1$ being allowed for polarizations σ^-, π, σ^+, respectively. (b) A quadrupole magnetic field linearly shifts the magnetic hyperfine levels so that the transition frequency spatially varies along the z-axis. Atoms moving out of the trap center at $z = 0$ preferentially absorb either σ^- or σ^+ light depending on their position. The atom position is thereby pushed towards the trap center. For simplicity, we use the $F = 0 \rightarrow F' = 1$ transition but in the experiment the actual transition is $F = 3 \rightarrow F' = 4$.

intersection point is at the point of zero magnetic field in the center of a quadrupole magnetic field created by two circular magnetic coils in anti-Helmholtz configuration. The gradient in the x-axis and y-axis is half the gradient in the z-axis:

$$\frac{\mathrm{d}B_x}{\mathrm{d}x} = \frac{\mathrm{d}B_y}{\mathrm{d}y} = -\frac{1}{2}\frac{\mathrm{d}B_z}{\mathrm{d}z} \, . \tag{B.11}$$

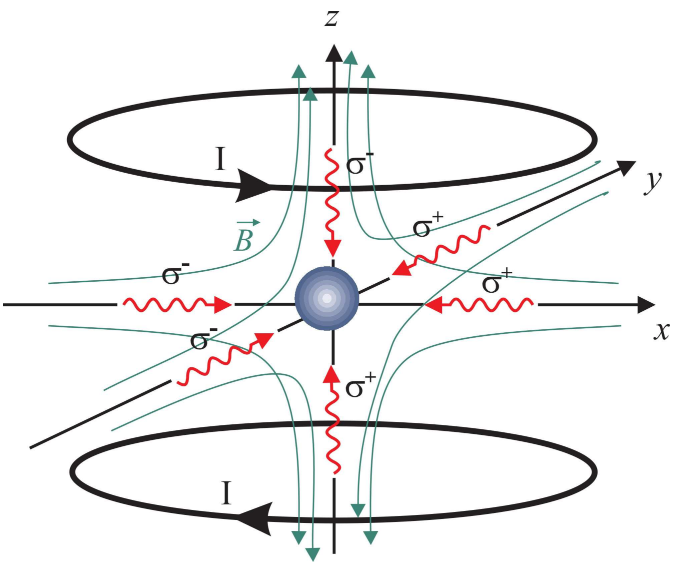

Figure B.5: Sketch of the magnetic fields and light fields in a 3D MOT. Current, I, flows in two coils in anti-Helmholtz configuration and produces the magnetic field $\vec{B}$. Three pairs of counter-propagating beams are arranged to all be mutually perpendicular, to have circular polarization, and are red-detuned from the atomic transition. The beams in the xy-plane have left-handed helicity while the beams in the z-axis have right handed helicity. Reproduced from Ref. [57].

Bibliography

[1] D. Hanneke, S. Fogwell, and G. Gabrielse. New measurement of the electron magnetic moment and the fine structure constant. *Phys. Rev. Lett.*, 100:120801, 2008.

[2] W. Lamb and R. Retherford. Fine structure of the hydrogen atom by a microwave method. *Phys. Rev.*, 72:241, 1947.

[3] H. Bethe. The electromagnetic shift of energy levels. *Phys. Rev.*, 72:339, 1947.

[4] P.A.M. Dirac. The quantum theory of the emission and absorption of radiation. *Proc. Roy. Soc. Lond. A*, 114:243–265, 1927.

[5] J. Schwinger. On quantum-electrodynamics and the magnetic moment of the electron. *Phys. Rev.*, 73:416–417, 1948.

[6] E. M. Purcell. Spontaneous emission probabilities at radio frequencies. *Physical Review*, 69:681, 1946.

[7] E. Yablonovitch. Inhibited spontaneous emission in solid-state physics and electronics. *Phys. Rev. Lett.*, 58:2059–2062, 1987.

[8] P. Goy, J.-M. Raimond, M. Gross, and S. Haroche. Observation of cavity-enhanced single-atom spontaneous emission. *Phys. Rev. Lett.*, 50:1903–1906, 1983.

[9] O. Benson. Assembly of hybrid photonic architectures from nanophotonic constituents. *Nature*, 480:193–199, 2011. and references therein.

[10] K. J. Vahala. Optical microcavities. *Nature*, 424:839–846, 2003.

[11] H. Walther, B. T. H. Varcoe, B.-G. Englert, and T. Becker. Cavity quantum electrodynamics. *Rep. Prog. Phys.*, 69:1325, 2006.

[12] The nobel prize in physics 2012. `http://www.nobelprize.org/nobel_prizes/physics/laureates/2012/advanced-physicsprize2012.pdf`, Oct 2012.

[13] T. Wilk, S. C. Webster, A. Kuhn, and G. Rempe. Single-atom single-photon quantum interface. *Science*, 317:488–90, 2007.

[14] K. M. Birnbaum, A. Boca, R. Miller, A. D. Boozer, T. E. Northup, and H. J. Kimble. Photon blokade in an optical cavity with one trapped atom. *Nature*, 436:87–90, 2005.

[15] E. Jaynes and F. Cummings. Comparison of quantum and semiclassical radiation theories with application to the beam maser. *Proc. IEEE*, 51:89–109, 1963.

[16] P. Meystre and M. Sargent III. *Elements of Quantum Optics*, volume 4. Springer-Verlag, New York, 2007.

[17] D. Meschede, H. Walther, and G. Müller. One-atom maser. *Phys. Rev. Lett.*, 54:551–554, 1985.

[18] C. J. Hood, M. S. Chapman, T. W. Lynn, and H. J. Kimble. Real-time cavity QED with single atoms. *Phys. Rev. Lett.*, 80:4157–4160, 1998.

[19] R. J. Thompson, G. Rempe, and H. J. Kimble. Observation of normal-mode splitting for an atom in an optical cavity. *Phys. Rev. Lett.*, 68:1132–1135, 1992.

[20] T. Kampschulte, W. Alt, S. Brakhane, M. Eckstein, R. Reimann, A. Widera, and D. Meschede. Optical control of the refractive index of a single atom. *Phys. Rev. Lett.*, 105:153603, 2010.

[21] P. W. H. Pinkse, T. Fischer, P. Maunz, and G. Rempe. Trapping an atom with single photons. *Nature*, 404:365–368, 2000.

[22] C. J. Hood, T. W. Lynn, A. C. Doherty, A. S. Parkins, and H. J. Kimble. The atom-cavity microscope: Single atoms bound in orbit by single photons. *Science*, 287:1447–1453, 2000.

[23] S. Gleyzes, S. Kuhr, C. Guerlin, J. Beru, S. Deléglise, U. Busk Hoff, M. Brune J.-M. Raimond, and S. Haroche. Quantum jumps of light recording the birth and death of a photon in a cavity. *Nature*, 446:297–300, 2007.

[24] A.B. Matsko, A.A. Savchenkov, N. Yu, and L. Maleki. Whispering-gallery-mode resonators as frequency references. I. fundamental limitations. *J. Opt. Soc. Am. B*, 24:1324–1335, 2007.

[25] M. Pöllinger, D. O'Shea, F. Warken, and A. Rauschenbeutel. Ultra-high-Q tunable whispering-gallery-mode microresonator. *Phys. Rev. Lett.*, 103:053901, 2009.

[26] S. M. Spillane, T. J. Kippenberg, O. J. Painter, and K. J. Vahala. Ideality in a Fiber-Taper-Coupled Microresonator System for Application to Cavity Quantum Electrodynamics. *Phys. Rev. Lett.*, 91:043902, 2003.

[27] T. J. Kippenberg, S. M. Spillane, and K. J. Vahala. Demonstration of ultrahigh-Q small mode volume toroid microcavities on a chip. *Appl. Phys. Lett.*, 85, 2004.

[28] V. S. Ilchenko A. B. Matsko. Optical resonators with whispering-gallery modes - part I: basics. *IEEE J. Sel. Top. Quantum Electron.*, 12:3–14, 2006. and references therein.

[29] J. C. Knight, G. Cheung, F. Jacques, and T. A. Birks. Phase-matched excitation of whispering-gallery-mode resonances by a Fiber taper. *Opt. Lett.*, 22:1129, 1997.

[30] Lord Rayleigh. The problem of the whispering gallery. *Philos. Mag.*, 20:1001–1004, 1910.

[31] E. Vetsch, D. Reitz, G. Sagué, R. Schmidt, S. T. Dawkins, and A. Rauschenbeutel. Optical interface created by laser-cooled atoms trapped in the evanescent field surrounding an optical nanofiber. *Phys. Rev. Lett.*, 104:203603, 2010.

[32] H. J. Kimble. The Quantum Internet. *Nature*, 453:1023, 2008. and references therein.

[33] T. Schröder, M. Fujiwara, T. Noda, H.-Q. Zhao, O. Benson, and S. Takeuchi. A nanodiamond-tapered fiber system with high single-mode coupling efficiency. *Opt. Express*, 20:10490–10497, 2012.

[34] J. Klinner, M. Lindholdt, B. Nagorny, and A. Hemmerich. Normal mode splitting and mechanical effects of an optical lattice in a ring cavity. *Phys. Rev. Lett.*, 96:023002, 2006.

[35] D. O'Shea, C. Junge, M. Poellinger, A. Vogler, and A. Rauschenbeutel. All-optical switching and strong coupling using tunable whispering-gallery-mode microresonators. *Appl. Phys. B*, 105:129–148, 2011.

[36] A. Vogler. Kopplung zweier optischer Mikroresonatoren ultrahoher Güte über eine makroskopische Distanz. Master's thesis, Johannes Gutenberg Universität, Mainz, Germany, 2009.

[37] M. Poellinger. *Bottle microresonators for applications in quantum optics and all-optical signal processing*. PhD thesis, Johannes Gutenberg Universität, Mainz, Germany, 2010.

[38] M. Pöllinger and A. Rauschenbeutel. All-optical signal processing at ultra-low powers in bottle microresonators using the Kerr effect. *Opt. Express*, 18:17764–17775, 2010.

[39] M. Rosenblit, P. Horak, S. Helsby, and R. Folman. Single-atom detection using whispering-gallery modes of microdisk resonators. *Phys. Rev. A*, 70:053808, 2004.

[40] T. Tanabe, M. Notomi, E. Kuramochi, A. Shinya, and H. Taniyama. Trapping and delaying photons for one nanosecond in an ultrasmall high-Q photonic-crystal nanocavity. *Nature Photonics*, 1:49–52, 2007.

[41] Y. Louyer, D. Meschede, and A. Rauschenbeutel. Tunable whispering-gallery-mode resonators for cavity quantum electrodynamics. *Phys. Rev. A*, 72:031801, 2005.

[42] M. Sumetsky. Whispering-gallery-bottle microcavities: the three-dimensional etalon. *Opt. Lett.*, 29:8, 2004.

[43] J. M. Ward, D. G. O'Shea, B. J. Shortt, M. J. Morrissey, and S. G. Nic Chormaic K. Deasy. Heat-and-pull rig for fiber taper fabrication. *Rev. Sci. Inst.*, 77, 2006.

[44] C. Strelow, H. Rehberg, C. M. Schultz, H. Welsch, C. Heyn, D. Heitmann, and T. Kipp. Optical microcavities formed by semiconductor microtubes using a bottlelike geometry. *Phys. Rev. Lett.*, 101, 2008.

[45] V. Sandoghdar, F. Treussart, J. Hare, V. Lefèvre-Seguin, J. M. Raimond, and S. Haroche. Very low threshold whispering-gallery-mode microsphere laser. *Phys. Rev. A*, 54:R1777–R1780, 1996.

[46] W. von Klitzing, E. Jahier, R. Long, F. Lissillour, V. Lefèvre-Seguin, J. Hare, J. M. Raimond, and S. Haroche. Very low threshold green lasing in microspheres by up-conversion of IR photons. *J. Opt. B: Quantum Semiclass. Opt.*, 2:204–206, 2000.

[47] D. O'Shea. Optical characterisation of rare-earth doped fluoride and phosphate glass microsphere resonators. Master's thesis, University College Cork, Cork, Ireland, 2008. and references therein.

[48] T. Aoki, B. Dayan, E. Wilcut, W. P. Bowen, A. S. Parkins, T. J. Kippenberg, K. J. Vahala, and H. J. Kimble. Observation of Strong Coupling between One Atom and a Monolithic Microresonator. *Nature*, 443:671, 2006.

[49] K. J. Vahala T. Carmon. Visible continuous emission from a silica microphotonic device by third-harmonic generation. *Nature Physics*, 3:430–435, 2007.

[50] T. Carmon, T. Kippenberg, L. Yang, H. Rokhsari, S. Spillane, and K. Vahala. Feedback control of ultra-high-Q microcavities: application to micro-Raman lasers and microparametric oscillators. *Opt. Express*, 13:3558, 2005.

[51] V. S. Ilchenko and A. B. Matsko. Optical resonators with whispering-gallery modes-part II: applications. *Selected Topics in Quantum Electronics, IEEE Journal of*, 12:15 – 32, 2006. and references therein.

[52] A. Rettenmaier. Aktive Frequenzstabilisierung eines durchstimmbaren Flüstergaleriemoden-Mikroresonators ultrahoher Güte. Master's thesis, Johannes Gutenberg Universität, Mainz, Germany, 2009.

[53] F. Warken. *Ultradünne Glasfasern als Werkzeug zur Kopplung von Licht und Materie*. PhD thesis, Rheinischen Friedrich-Wilhelms-Universität Bonn, Bonn, Germany, 2007.

[54] J. U. Nöckel. *Resonances in Nonintegrable Open Systems*. PhD thesis, Yale University, Connecticut, USA, 1997. `http://pages.uoregon.edu/noeckel/eikonals/`.

[55] L. G. Guimar aes and H. M. Nussenzveig. Uniform approximation to mie resonances. *J. Mod. Optic.*, 41:625–647, 1994.

[56] A. W. Snyder and J. D. Love. *Optical Waveguide Theory*. Kluwer Academic Publishers, London, 2000.

[57] G. Sague. *Cold atom physics using ultra-thin optical fibres*. PhD thesis, Rheinischen Friedrich-Wilhelms-Universität Bonn, Bonn, Germany, 2008.

[58] E. Vetsch. *Optical Interface Based on a Nanofiber Atom-Trap*. PhD thesis, Johannes Gutenberg Universität, Mainz, Germany, 2010.

[59] A. Kubanek, A. Ourjoumtsev, I. Schuster, M. Koch, P. W. H. Pinkse, K. Murr, and G. Rempe. Two-Photon Gateway in One-Atom Cavity Quantum Electrodynamics. *Phys. Rev. Lett.*, 101:203602, 2008.

[60] B. W. Shore, P. Meystre, and S. Stenholm. Is a quantum standing wave composed of two traveling waves? *J. Opt. Soc. Am. B*, 8:903–810, 1991.

[61] K. Srinivasan and O. Painter. Mode coupling and cavity-quantum-dot interactions in a fiber-coupled microdisk cavity. *Phys. Rev. A*, 75:023814, 2007. and references therein.

[62] C. W. Gardiner and M. J. Collett. Input and output in damped quantum systems: Quantum stochastic differential equations and the master equation. *Phys. Rev. A*, 31:3761–3774, 1985.

[63] L. Tong, R. Gattass, J. Ashcomand, S. He, J. Lou, M. Shen, I. Maxwell, and E. Mazur. Subwavelength-diameter silica wires for low-loss optical wave guiding. *Nature*, 426:816, 2003.

[64] G. Brambilla, V. Finazzi, and D. Richardson. Ultra-low-loss optical fiber nanotapers. *Opt. Express*, 12:2258, 2004.

[65] K. Karapetyan, 2011. Universität Bonn, private communication.

[66] F. Warken and H. Giessen. Fast profile measurement of micrometer-sized tapered fibers with betterthan 50-nm accuracy. *Opt. Lett.*, 29:1727–1729, 2004.

[67] S. Kozaki. Scattering of a gaussian beam by a homogeneous dielectric cylinder. *J. Appl. Phys.*, 53:7195, 1982.

[68] D.J. Butler and G. Forbes. Fiber-diameter measurement by occlusion of a gaussian beam. *Appl. Opt.*, 37:2598, 1998.

[69] T. Carmon, L. Yang, and K. Vahala. Dynamical thermal behavior and thermal selfstability of microcavities. *Opt. Express*, 12:4742, 2004.

[70] V. S. Ilchenko and M. L. Gorodetskii. Thermal nonlinear effects in optical whispering gallery microresonators. *Laser Phys.*, 2:1004, 1992.

[71] M. L. Gorodetsky, A. A. Savchenkov, and V. S. Ilchenko. Ultimate q of optical microsphere resonators. *Opt. Lett.*, 21:453–455, 1996.

[72] M. L. Gorodetsky, A. D. Pryamikov, and V. S. Ilchenko. Rayleigh scattering in high-Q microspheres. *J. Opt. Soc. Am. B*, 17:1051–1057, 2000.

[73] D. W. Vernooy, V. S. Ilchenko, H. Mabuchi, E. W. Streed, and H. J. Kimble. High-Q measurements of fused-silica microspheres in the near infrared. *Opt. Lett.*, 23:247–249, 1998.

[74] A. A. Savchenkov, A. B. Matsko, V. S. Ilchenko, and L. Maleki. Optical resonators with ten million finesse. *Opt. Express*, 15:6768–6773, 2007.

[75] M. Borselli, K. Srinivasan, P. E. Barclay, and O. Painter. Rayleigh scattering, mode coupling, and optical loss in silicon microdisks. *Applied Physics Letters*, 85:3693–3695, 2004.

[76] M. Soltani, S. Yegnanarayanan, and A. Adibi. Ultra-high Q planar silicon microdisk resonators for chip-scale silicon photonics. *Opt. Express*, 15:4694–4704, 2007.

[77] M. Sumetsky, Y. Dulashko, and R. S. Windeler. Optical microbubble resonator. *Opt. Lett.*, 35:898–900, 2010.

[78] G. S. Murugan, J. S. Wilkinson, and M. N. Zervas. Selective excitation of whispering gallery modesin a novel bottle microresonator. *Opt. Express*, 17:11916–11925, 2009.

[79] D. S. Weiss, V. Sandoghdar, J. Hare, V. Lefèvre-Seguin, J.-M. Raimond, and S. Haroche. Splitting of high-Q Mie modes induced by light backscattering in silica microspheres. *Opt. Lett.*, 20:1835–1837, 1995.

[80] S. M. Spillane. *Fiber-coupled Ultra-high-Q Microresonators for Nonlinear and Quantum Optics*. PhD thesis, California Institute of Technology, California, USA, 2004.

[81] J. Poirson, F. Bretenaker, M. Vallet, and A. Le Floch. Analytical and experimental study of ringing effects in a Fabry-Perot cavity. Application to the measurement of high finessees. *J. Opt. Soc. Am. B*, 14:2811, 1997.

[82] A. Polman, B. Min, J. Kalkman, T. J. Kippenberg, and K. J. Vahala. Ultralow-threshold erbium-implanted toroidal microlaser on silicon. *Applied Physics Letters*, 84:1037–1039, 2004.

[83] M. Cai, O. Painter, K. J. Vahala, and P. C. Sercel. Fiber-coupled microsphere laser. *Opt. Lett.*, 25:1430–1432, 2000.

[84] D. J. Alton, N. P. Stern, T. Aoki, H. Lee, E. Ostby, K. J. Vahala, and H. J. Kimble. Strong interactions of single atoms and photons near a dielectric boundary. *Nature Physics*, 7:8, 2010.

[85] D.A. Barber and N.H. Rizvi. Characterization of the effects of different lasers on the tensile strength of fibers during laser writing of fiber Bragg gratings. *Proc. SPIE*, 4876:321, 2003.

[86] P. Nisbet, J. Dilley, and A. Kuhn. Highly efficient source for indistinguishable photons of controlled shape. *arXiv:1106.6292v1*, 2011.

[87] S. Nickel. Kopplung, Charakterisierung und aktive Frequenzstabilisierung von Flaschenresonatoren ultrahoher Güte innerhalb einer Ultrahochvakuum-Apparatur. Master's thesis, Johannes Gutenberg Universität, Mainz, Germany, 2010.

[88] C. Hauswald. Aufbau und Charakterisierung eines Atom-Springbrunnens für ein Resonator-QED-Experiment mit Flüstergaleriemoden-Mikroresonatoren. Master's thesis, Johannes Gutenberg Universität, Mainz, Germany, 2010.

[89] M. Khudaverdyan, W. Alt, I. Dotsenko, T. Kampschulte, K. Lenhard, A. Rauschenbeutel, S. Reick, K. Schörner, A. Widera, and D. Meschede. Controlled insertion and retrieval of atoms coupled to a high-finesse optical resonator. *New J. Phys.*, 10:073023, 2008.

[90] J. A. Sauer, K. M. Fortier, M. S. Chang, C.D. Hamley, and M. S. Chapman. Cavity QED with optically transported atoms. *Phys. Rev. A*, 69:051804, 2004.

[91] H. J. Metcalf and P. Van der Straten. *Laser cooling and trapping*, volume 1. Springer-Verlag, New York, 1999.

[92] T. Aoki, A. S. Parkins, D. J. Alton, C. A. Regal, B. Dayan, E. Ostby, K. J. Vahala, and H. J. Kimble. Efficient routing of single photons by one atom and a microtoroidal cavity. *Phys. Rev. Lett.*, 102:083601, 2009.

[93] N. F. Ramsey. History of atomic clocks. *J. Res. Natl. Bur. Stand.*, 88:301–320, 1983.

[94] K. M. Birnbaum. *Cavity QED with Multilevel Atoms*. PhD thesis, California Institute of Technology, California, USA, 2005.

[95] G. Lamporesi. *Determination of the gravitational constant by atom interferometry*. PhD thesis, Università degli studi die Firenze, Florence, Italy, 2006.

[96] K. Friebe. Strong coupling of single atoms to a whispering-gallery-mode resonator of ultrahigh quality. Master's thesis, Johannes Gutenberg Universität, Mainz, Germany, 2011.

[97] A. I. Oliva, Victor Sosa, R. de Coss, Raquel Sosa, N. López Salazar, and J. L. Pe na. Vibration isolation analysis for a scanning tunneling microscope. *Rev. Sci. Inst.*, 63:3326–3329, 1992.

[98] A. I. Oliva, M. Aguilary, and V. Sosa. Low- and high-frequency vibration isolation for scanning probe microscopy. *Meas. Sci. Technol.*, 9:383–390, 1998.

[99] C. J. Foot. *Atomic Physics*, volume 1. Oxford University Press, 2005.

[100] M. Fürst. Hilfsmittel zur Einstellung einer polarisationserhaltenden Glasfaser, 2012. unpublished.

[101] C. Junge, S. Nickel, D. O'Shea, and A. Rauschenbeutel. Bottle microresonator with actively stabilized evanescent coupling. *Opt. Lett.*, 36:3488–3490, 2011.

[102] J. Rezac and A. Rosenberger. Locking a microsphere whispering-gallery mode to a laser. *Opt. Express*, 8:605, 2001.

[103] P. Del-Haye, O. Arcizet, A. Schliesser, R. Holzwarth, and T. J. Kippenberg. Full Stabilization of a Microresonator-Based Optical Frequency Comb. *Phys. Rev. Lett.*, 101:053903, 2008.

[104] R. W. P. Drever, J. L. Hall, F. V. Kowalski, J. Hough, G. M. Ford, A. J. Munley, and H. Ward. Laser phase and frequency stabilization using an optical resonator. *Appl. Phys. B*, 31:97, 1983.

[105] E. D. Black. An introduction to Pound-Drever-Hall laser frequency stabilization. *Am. J. Phys.*, 69:79, 2001.

[106] H. A. Haus. *Waves and fields in optoelectronics*, volume 1. Prentice-Hall New Jersey, 1984.

[107] D. S. Weiss, V. Sandoghdar, J. Hare, V. Lefèvre-Seguin, J.-M. Raimond, and S. Haroche. Splitting of high-Q Mie modes induced by light backscattering in silica microspheres. *Opt. Lett.*, 20:1835, 1995.

[108] Certificate for standard reference material 739: Fused-silica thermal expansion. NIST certificate, `https://www-s.nist.gov/srmors/certificates/archive/739.pdf`, 1991.

[109] E. D. Palik. *Handbook of Optical Constants of Solids*, volume 1. Academic Press, New York, 1985.

[110] C. Wuttke and A. Rauschenbeutel. Probing planck's law for an object thinner than the thermal wavelength. *arXiv:1209.0536*, 2012.

[111] A. Kubanek. *Two-photon gateway and feedback control of a single atom in a cavity*. PhD thesis, Technische Universität München, Munich, Germany, 2010.

[112] D. O'Shea, A. Rettenmaier, and A. Rauschenbeutel. Active frequency stabilization of an ultra-high Q whispering-gallery-mode microresonator. *Appl. Phys. B*, 99:623, 2010.

[113] E. Knill, R. Laflamme, and G. J. Milburn. A scheme for efficient quantum computation with linear optics. *Nature*, 409:46–52, 2001.

[114] S. Rosenblum, S. Parkins, and B. Dayan. Photon routing in cavity QED: Beyond the fundamental limit of photon blockade. *Phys. Rev. A*, 84:033854, 2011.

[115] K. Srinivasan and O. Painter. Linear and nonlinear optical spectroscopy of a strongly coupled microdisk-quantum dot system. *Nature*, 450:862–865, 2007.

[116] F. Le Kien, V. I. Balykin, and K. Hakuta. Atom trap and waveguide using a two-color evanescent light field around a subwavelength-diameter optical fiber. *Phys. Rev. A*, 70:063403, 2004. and references therein.

[117] W. R. Johnson, V. A. Dzuba, U. I. Safronova, and M. S. Safronova. Finite-field evaluation of the Lennard-Jones atom-wall interaction constant C_3 for alkali-metal atoms. *Phys. Rev. A*, 69:022508, 2004.

[118] J. E. Sansonetti. Wavelengths, Transition Probabilities, and Energy Levels for the Spectra of Rubidium (Rb I through Rb XXXVII). *J. Phys. Chem. Ref. Data*, 35:301–421, 2006.

[119] J. F. Babb, G. L. Klimchitskaya, and V. M. Mostepanenko. Casimir-Polder interaction between an atom and a cavity wall under the influence of real conditions. *Phys. Rev. A*, 70:042901, 2004.

[120] B. Geyer, G. L. Klimchitskaya, and V. M. Mostepanenko. Thermal quantum field theory and the Casimir interaction between dielectrics. *Phys. Rev. D*, 72:085009, 2005.

[121] D. A. Steck. Rubidium 85 D line data, 2008. revision 0.1.1.

[122] J. Mitroy, M. S. Safronova, and Charles W. Clark. Theory and applications of atomic and ionic polarizabilities. *J. Phys. B: At. Mol. Opt. Phys.*, 43(20):202001, 2010.

[123] B. Dayan, A. S. Parkins, T. Aoki, E. Ostby, K. J. Vahala, and H. J. Kimble. A photon turnstile dynamically regulated by one atom. *Science*, 319:1062–1065, 2008.

[124] J. Wiersig. Structure of whispering-gallery modes in optical microdisks perturbed by nanoparticles. *Phys. Rev. A*, 84:063828, 2011.

[125] J. Wiersig, S. W. Kim, and M. Hentschel. Asymmetric scattering and nonorthogonal mode patterns in optical microspirals. *Phys. Rev. A*, 78:053809, 2008.

[126] X.-C. Yu, Y.-C. Liu, M.-Y. Yan, W.-L. Jin, and Y.-F. Xiao. Coupling of diamond nanocrystals to a high-q whispering-gallery microresonator. *Phys. Rev. A*, 86:043833, 2012.

[127] P. R. Berman. *Cavity quantum electrodynamics*. Academic Press, Inc., Boston, 1994.

[128] D. W. Vernooy and H. J. Kimble. *Phys. Rev. A*, 55:1239, 1997.

[129] X.-Y. Chang, Y.-X. Wang, C. Zu, K. Liu, and L.-M. Duan. Experimental demonstration of an entanglement-based quantum router. *arXiv:1207.7265v1*, 2012.

[130] K. Lemr and A. Černoch. Linear-optical programmable quantum router. *arXiv:1208.3556v1*, 2012.

[131] I.-C. Hoi, C. M. Wilson, G. Johansson, T. Palomaki, B. Peropadre, and P. Delsing. Demonstration of a single-photon router in the microwave regime. *Phys. Rev. Lett.*, 107:073601, 2011.

[132] A. M. Armani, R. P. Kulkarni, S. E. Fraser, R. C. Flagan, and K. J. Vahala. Label-free, single-molecule detection with optical microcavities. *Science*, 317:783, 2007.

[133] T. Peyronel, O. Firstenberg, Q.-Y. Liang, S. Hofferberth, A. V. Gorshkov, T. Pohl, M. D. Lukin, and V. Vuletić. Strongly interacting rydberg excitations of a cold atomic gas. *Nature*, 2012.

[134] D. E. Chang, A. S. Sorensen, E. A. Demler, and M. D. Lukin. A single-photon transistor using nanoscale surface plasmons. *Nature Physics*, 3:807–812, 2007.

[135] P. Bermel, A. Rodriguez, S. G. Johnson, J. D. Joannopoulos, and M. Soljačić. Single-photon all-optical switching using waveguide-cavity quantum electrodynamics. *Phys. Rev. A*, 74:043818, 2006.

[136] L. Davidovich, A. Maali, M. Brune, J. M. Raimond, and S. Haroche. Quantum switches and nonlocal microwave fields. *Phys. Rev. Lett.*, 71:2360–2363, 1993.

[137] H. Rokhsari and K. J. Vahala. Ultralow loss, high q, four port resonant couplers for quantum optics and photonics. *Phys. Rev. Lett.*, 92:253905, 2004.

[138] L. Tong, J. Lou, and E. Mazur. Single-mode guiding properties of subwavelength-diameter silica and silicon wire waveguides. *Opt. Express*, 12:1025–1035, 2004.

[139] S. Chu, L. Hollberg, J. E. Bjorkholm, A. Cable, and A. Ashkin. Three dimensional viscous confinement and cooling of atoms by resonance radiation pressure. *Phys. Rev. Lett.*, 55, 1985.

[140] S. Chu, J. E. Bjorkholm, A. Ashkin, and A. Cable. Experimental observation of optically trapped atoms. *Phys. Rev. Lett.*, 57, 1986.

[141] J. Dalibard and C. Cohen-Tannoudji. Laser cooling below the doppler limit by polarization gradients: simple theoretical models. *J. Opt. Soc. Am. B*, 6:2023–2040, 1989.

Acknowledgements

Text here

Curriculum Vitae

Personal Data

Danny O’Shea
Eelke Meinertswei 24
9295 KC Westergeest
The Netherlands

Tel.: (0031) 5 11 44 41 87
E-Mail: doshea@ati.ac.at

Born on 05. 01. 1984 in Cork, Ireland

Nationality: Irish

Education

10/2007 – Present	Doctoral dissertation: Cavity QED experiments with a whispering-gallery-mode bottle resonator Vienna University of Technology, Vienna, Austria (12/2010 – Present), and University of Mainz, Mainz, Germany (10/2007 – 12/2010)
9/2005 – 8/2007	MSc. thesis: Optical characterisation of rare-earth doped fluoride and phosphate glass microsphere resonators University College Cork, and Tyndall National Institute, Cork, Ireland
9/2001 – 7/2005	Undergraduate studies in Applied Physics and Instrumentation Cork Institute of Technology, Cork, Ireland

Groningen, The Netherlands, 14. March 2013